

Energy Recovery and Storage from Aircraft Taxiing Operations

Thesis submitted to the University of Nottingham for the degree of

Doctor of Philosophy, September 2022

Milos Lukic

14318998

Supervised by:

Michael Galea

Christian Klumpner

Paolo Giangrande

Signature _____

Date 27/09/2022

Abstract

This thesis focuses on the model-based design and analysis of the entire aircraft electric taxiing system, emphasising battery energy storage. The versatile model of the whole system (batteries, power converters, and electric machine) is developed which also includes aircraft dynamics and road loads in addition to the control algorithms, both at system and component levels. The developed model is primarily used for preliminary sizing and analysis of battery energy storage. However, the model is also used to gain insights into interactions between different components and between control and components through closed-loop control, outline requirements specifications, and analyse system operations.

Acknowledgment

First of all, I would like to thank my supervisors Michael Galea, Christian Klumpner and Paolo Giangrande for giving me the opportunity to work on this interesting project at the University of Nottingham, within the Power Electronics Machines and Control group and within the Institute for Aerospace Technology (IAT). I am grateful for valuable ideas, discussions, and your diligent supervision. I would also like to express my gratitude to the European Commission's Marie Skłodowska-Curie Actions which partially funded the doctoral programme. I am immensely grateful to IAT team members Helen, Serhiy and Tao, for coordinating the programme and giving support when needed.

I would like to thank all colleagues that I have met in IAT for their assistance and enthusiasm. Especially, I want to thank Daniela, Sarah, Mahnaz, Sharmila, Angel, Ahmed, Hery, Jay, Sam, and Tanvir for making my PhD experience unforgettable and enjoyable. Outside of IAT, I want to thank Ivan for his endless support and for being a good friend. The last two years of PhD due to pandemic were very challenging so I would also like to thank my flatmates for being very understanding, tolerable and making work from home enjoyable. Also, my gratitude and appreciation go to my cousin Vladimir who made my settling in Nottingham easier and who was always there for me.

Last but not least, I want to thank my family for cheering and love. I will forever be grateful to my parents, sister and grandparents who never stopped encouraging me and believing in me, even when I did not. Despite the distance, they helped me go through the ups and downs that come with PhD studies. Thank you for everything.

Table of contents

Contents

Abstract 2

Acknowledgment 3

Table of contents 4

List of figures 8

List of Abbreviations 19

1 Chapter: Introduction 22

1.1 Aviation impact on environment 22

1.1.1 Background on More Electric Aircraft 22

1.1.2 Emissions at airport level 23

1.1.3 Improved taxiing procedures and Electric taxiing 24

1.2 Research rationale and problem scope 25

1.3 Aim and objectives of the thesis 26

1.4 Methodology 28

1.4.1 Modelling Methods of Vehicular Traction Electrified Powertrains 28

1.5 Outline of the thesis 31

2 Chapter: Aircraft Electric Taxiing 33

2.1 Review of Electric Taxiing Systems 33

2.1.1 Problems of conventional taxiing 33

2.1.2 General benefits and disadvantages of ETS 36

2.1.3 Electric taxiing systems development up to date 38

2.1.3.1 Electric pushback systems 39

2.1.3.2 TaxiBot 40

2.1.3.3 EGTS 41

2.1.3.4 Wheeltug 43

2.1.3.5 DLR 44
2.1.3.6 Summary of ET systems 45
2.1.4 Comparison of different system topology and their benefits 45
2.1.4.1 Differences between on on-board and external systems 45
2.1.4.2 Differences between different on on-board systems (MLG vs NLG; geared vs direct) 47
2.2 Electric Taxiing Aircraft Dynamics modelling 48
2.2.1 Aerodynamic drag resistance ($Faero$) 49
2.2.2 Grade resistance ($Fgrade$) 50
2.2.3 Rolling resistance (Frr) 50
2.2.4 Inertial force 51
2.2.5 Analysis of the resistive forces and total traction force 52
2.2.6 Power and Energy at the wheel 56
2.3 Future trends, recommendations, and conclusions 61
3 Chapter: Battery Literature Review and Modelling 64
3.1 Literature Review 64
3.1.1 Terminology 64
3.1.2 Lithium-ion batteries 67
3.1.2.1 Electrolyte and Separator 69
3.1.2.2 Positive electrodes 69
3.1.2.3 Negative electrodes 75
3.1.3 On power and energy density 77
3.1.4 Conclusions on lithium-ion batteries and future trends 78
3.2 Battery modelling 80
3.2.1 Physical models 80
3.2.2 Empirical models 82

3.2.3 Equivalent Circuit Models 83
3.2.4 OCV 83
3.2.4.1 Continuous methods 84
3.2.4.2 Discrete methods 85
3.2.4.3 Software implementation 87
3.2.5 Impedance 88
3.2.5.1 Analysis of the impedance in the frequency domain 88
3.2.5.2 Time-domain impedance analysis 95
3.2.6 State of Charge 97
3.2.7 Conclusion on battery modelling 99
4 Chapter: Dynamic modelling of ETS's drive and model's employment 100
4.1 The TM description 101
4.2 2D Finite Element Model of TM 103
4.3 Performance analysis of the TM and parameters calculation 105
4.3.1 No-load analysis 105
4.3.2 Torque versus current 107
4.3.3 Efficiency map 109
4.3.4 Inductances and resistance 109
4.4 QD Model development 112
4.5 Verification of the QD model 115
4.6 3-phase voltage source inverter modelling 116
4.7 Control system development 120
4.8 Employment of the model and interim conclusions 124
4.8.1 A320 analysis 127
4.8.2 Power demands and energy consumption analysis 130
5 Chapter: Battery modelling 136

5.1 Battery selection....136
5.2 Test rig description and experiment sequence explanation....138
5.2.1 Test rig description....138
5.2.2 Sequence explanation....140
5.2.2.1 EC Lab implementation of the sequences....142
5.3 Post-processing and data analysis....144
5.3.1 OCV engineering....145
5.3.2 RC network voltage calculation ($V\tau$)....148
5.4 Curve fitting procedure....151
5.4.1.1 Fitting procedure....153
5.4.1.2 Fitting results and battery cell parameters....157
5.5 Model validations....159
5.6 Conclusion....166
6 Chapter: The full model of ETS....167
6.1 The battery rating selection....167
6.1.1 BMS considerations....169
6.2 The battery results and discussion....170
6.2.1 HE batteries....170
6.2.2 MEP batteries....174
6.2.3 HP batteries....177
6.3 Discussion summary....178
6.3.1 Battery replacement cost vs extra fuel cost....180
6.4 Conclusions....183
7 Chapter: Conclusions and Future Work....185
7.1 Conclusions....185
7.2 Future Work....187

List of references.....190

List of figures

Figure 1.1 Quasi-static approach in modelling vehicular power trains, adapted from [41]. ...29

Figure 1.2 Dynamic approach in modelling vehicular power trains, adapted from [39], [41].29

Figure 2.1 Generic architecture of external ETS, adapted from [60]. 35

Figure 2.2 Generic architecture of on-board ETS, adapted from [60]. 36

Figure 2.3 Process charts of conventional, external electric, and on-board electric taxiing....37

Figure 2.4 Mototok and its operator. 39

Figure 2.5 Taxibot towing KLM aircraft at Amsterdam Schiphol airport. 40

Figure 2.6 Architecture of EGTS's electric drive system [74]. 41

Figure 2.7 Wheeltug's demonstrator aircraft. 43

Figure 2.8 Block fuel savings versus flight distance and taxiing time, adapted from [63]. 46

Figure 2.9 Differences between conventional and on-board ETS pushback [60]. 47

Figure 2.10 Resistive forces acting on the aircraft. 49

Figure 2.11 The load forces range of a Boeing 737-400 ($cdo = 0.055, m = 68\,t$ and $A = 105.4\,m2$) and Airbus A321ceo ($cdo = 0.07, m = 93.5\,t$ and $A = 122.4\,m2$) during electric taxiing. 53

Figure 2.12 (a) The $Ftraction$ against aircraft mass for $ieq, \% \in (0.9\% - 5.6\%)$ (b) The maximum and minimum breakaway force. 55

Figure 2.13 Power requirements at the wheel for Embraer E Jet family for four different speeds. 57

Figure 2.14 Power requirements at the wheel for Boeing B737, B767 and Airbus A320 families for four different speeds. 58

Figure 2.15 Power requirements at the wheel for Boeing B777 family for four different speeds. 59

Figure 2.16 Power requirements at the wheel for Boeing B787 family for four different speeds. 60

Figure 2.17 Expected future development of on-board ETS. 62

Figure 3.1 Schematic configuration of lithium-ion in discharge mode [114]..... 66

Figure 3.2 Difference between OCV and cell terminal for different current rates [115]. 67

Figure 3.3 Lithium-ion cell during charge (above) and discharge (below). 68

Figure 3.4 Potentials vs. Li/Li+ and specific capacities of some of the positive and negative active materials for lithium-ion cell, adapted from [118]. 69

Figure 3.5 Crystal structure of the three lithium-insertion compounds in which the Li cations are mobile through the 2D (layered), 3D (spinel) and 1D (olivine) frameworks [121]..... 70

Figure 3.6 Layered crystal structure of LCO [121]. 70

Figure 3.7 Typical charging/discharging voltage of LCO. 71

Figure 3.8 Spinel crystal structure of LMO [121]. 73

Figure 3.9 Typical charging/discharging cycles of LMO [118]. 73

Figure 3.10 Olivine crystal structure of LFP [121]..... 74

Figure 3.11 Typical charging/discharging cycles of LFP [118]. 74

Figure 3.12 Charge and discharge potentials vs. Li/Li+ of graphite material [139]..... 76

Figure 3.13 Charge and discharge potentials vs. Li/Li+ of LTO material [139]. 77

Figure 3.14 Typical discharge characteristics of LFP, LMO and NMC chemistries [148]..... 78

Figure 3.15 Schematic of P2D model. 81

Figure 3.16 Schematic of SPM. 81

Figure 3.17 General representation of ECM with OCV and $zbat$. 83

Figure 3.18 Battery terminal voltage response after discharge [166]. 86

Figure 3.19 Voltage evolution during OCV characterisation with 1 minute relaxation with respect to time [167]. 87

Figure 3.20 Voltage evolution during OCV characterisation with 1 minutes relaxation with respect to SoC [167]..... 87

Figure 3.21 Spectrum of lithium-ion battery [169]. 89
Figure 3.22 Spectrum of inductor, capacitor, and resistor. 90
Figure 3.23 Spectrum of Warburg impedance and CPE. 90
Figure 3.24 Spectrum of FSW and FLW impedance. 91
Figure 3.25 Effect of series resistance to impedance spectrum. 92
Figure 3.26 Spectrum of parallel RC circuit (left) and parallel RQ circuit, i.e., ZARC (right). 93
Figure 3.27 The ECM model using CPEs. 94
Figure 3.28 Randless model of battery and its approximation [172]. 94
Figure 3.29 Reduced ECM (above) and CPE approximation (below). 94
Figure 3.30 Thevenin ECM with n parallel RC pairs. 95
Figure 3.31 Incremental SoC identification [174]. 96
Figure 3.32 General Kalman filter iteration diagram. 99
Figure 4.1 The direct drive ETS system developed by the University of Nottingham and Co. 100
Figure 4.2 The test bed for analysis of electric drive system at the UoN. 101
Figure 4.3 Wheel hub of the A320 MLG [179]. 101
Figure 4.4 Magnetisation direction of PMs inside five-stage Halbach array configuration. 102
Figure 4.5 Construction slice line/arcs of the 2D FE model. 104
Figure 4.6 Construction slice surfaces of the 2D FE model. 104
Figure 4.7 A 1/3 of the 2D FE model illustrating magnetisation directions and phase windings arrangement. 105
Figure 4.8 PM flux linkage during no-load analysis. 105
Figure 4.9 Back-emf of phase a for eight different speeds. 106
Figure 4.10 Back-emf of all six phases for fixed speed of 120 rpm. 107
Figure 4.11 Torque (left) and torque constant (right) versus iq for $id = 0$ for symmetrical operation. 107

Figure 4.12 Torque (left) and torque constant (right) versus iq and $id = 0$ for single-star operation. 108

Figure 4.13 Torque (left) and torque constant (right) versus iq for different id values during symmetrical operation. 108

Figure 4.14 The efficiency map of the TM. 109

Figure 4.15 *qd0* frame orientation. 112

Figure 4.16 The *qd0* equivalent circuit of machine used for ETS. 115

Figure 4.17 3-phase 2-level voltage source inverter. 117

Figure 4.18 The procedure of obtaining *qd0* duty cycles form modulation signals in time domain. 118

Figure 4.19 Averaged *qd0* model of 3-phase 2-level VSI. 119

Figure 4.20 Electrical waveforms and generated losses. 119

Figure 4.21 Physical layer of the ETS model. 120

Figure 4.22 The acceleration profiles with $ieq, \%$=0.8% and three different values of MTOW. 121

Figure 4.23 The acceleration profiles with MTOW=79 t and three different values of $ieq, \%$. 122

Figure 4.24 Control layer of the ETS model. 123

Figure 4.25 The full forward-facing model of the ETS including aircraft dynamics. 124

Figure 4.26 AMS T-O and LHR T-I reference drive cycles. 125

Figure 4.27 Speed curves during testing of control system for Cleansky project SOG [195]. 126

Figure 4.28 TXL T-O drive cycle [196]. 126

Figure 4.29 TXL T_O reference cycle adapted from Figure 4.28 126

Figure 4.30 Mask of the created model in PLECS 4.4. 127

Figure 4.31 The speed profile of an A320 with 69 t under AMS T-O and maximum regeneration scenario. 128

Figure 4.32 The TM's torque profile of an A320 with 69 t under AMS T-O and maximum regeneration scenario. 128

Figure 4.33 The slope profile of AMS T-O drive cycle. 128

Figure 4.34 The DC link and wheel power profiles of an A320 with 69 t under AMS T-O and maximum regeneration scenario. 128

Figure 4.35 The energy profiles of an A320 with 69 t under AMS T-O and maximum regeneration scenario. 129

Figure 4.36 The speed profiles of an A320 under AMS T-O and minimum regeneration scenario for three different aircraft mass. 129

Figure 4.37 The DC link power profiles of an A320 under AMS T-O and minimum regeneration scenario for three different aircraft mass. 130

Figure 4.38 The typical taxi-out route at AMS. 131

Figure 4.39 Typical TXL T-O route. 132

Figure 4.40 The prolonged unrestricted TXL-TO in comparison to TXL-TO. 133

Figure 4.41 Typical taxi-in route at LHR. 134

Figure 5.1 Biologic SP-150 (left) and 20 A VMP3 booster. 138

Figure 5.2 Four wire connection: correct (left) and incorrect (right). 138

Figure 5.3 Cylindrical cell holder for currents up to 200A from Arbin instruments. 139

Figure 5.4 The holder's connector (top) and its side view connection to the cell (bottom). . 139

Figure 5.5 Cell, holder, and its connection to the booster wires. 140

Figure 5.6 The overall test procedure for one cell. 143

Figure 5.7 Flowchart of the Charging, OCV GCPL5 and Impedance GCPL5 sequences in more detail. 143

Figure 5.8 GPW test procedures in more detail. 144

Figure 5.9 The voltage and current waveforms and their significant points during 1.5C rate pulse experiment for the Samsung INR35E cell. 145

Figure 5.10 Identifying the non-linearities in OCV curves. 146

Figure 5.11 Engineering of the OCV points. 147

Figure 5.12 Difference between engineered and non-engineered OCV for LG HG2 cell. ...147

Figure 5.13 Engineered OCV curves for all the eight selected cells. 148

Figure 5.14 Process of finding OCV(t) from OCV(Q) and Q(t).....148

Figure 5.15 Cell terminal voltage and OCV during 1C pulse experiment for A123 M1B....149

Figure 5.16 The instantaneous resistance at the beginning of pulse period for Samsung INR20S. 149

Figure 5.17 $V\tau$ waveform for 4C pulse rate for A123 M1B cell. 150

Figure 5.18 The flowchart of the developed algorithm for ECM parametrisation [174]. 153

Figure 5.19 The fitting procedure shown using waveforms. 153

Figure 5.20 Relaxation waveform and auxiliary line used for initial voltage estimation.....154

Figure 5.21 The pulse fitting loop procedure of the slowest RC circuit.....155

Figure 5.22 Experimental and fitted $V\tau$ with three RC waveforms for INR30Q cell with 1C pulse. 156

Figure 5.23 Absolute error between experimental and fitted $V\tau$ for INR30Q cell with 1C pulse. 156

Figure 5.24 The experimental and fitted voltage at cell terminals of the INR30Q cell during 1C pulse experiment. 157

Figure 5.25 Value of the three RC parameters extracted during the pulse for LG MJ1 cell. 158

Figure 5.26 Value of the three RC parameters extracted during the relaxation for LG MJ1 cell. 159

Figure 5.27 Implementation of battery cell model in Simulink/MATLAB using ECM with 3 RC pairs and 1D and 2D lookup tables.....159

Figure 5.28 Voltage at the cell terminals of the model and experiment during dynamic power profile for INR35E.....161

Figure 5.29 Dynamic power profile applied to the INR35E cell discharging it from 90% to 20% SoC.....161

Figure 5.30 Voltage at the cell terminals of the model and experiment during dynamic power profile for INR35E (zoomed 4000s to 9000s). 162

Figure 5.31 Relative error of terminal voltage during dynamic power profile for INR35E (zoomed 4000s to 9000s). 162

Figure 5.32 Current of the INR35E cell model during the power profile. 162

Figure 5.33 SoC of INR35E cell during power profile. 163

Figure 5.34 Voltage at the cell terminals of the model and experiment during two dynamic power profiles for INR20S. 163

Figure 5.35 The two dynamic power profiles applied to the INR20S cell. 164

Figure 5.36 Voltage of the model and experiment during dynamic power profiles for INR20S (zoomed). 164

Figure 5.37 Relative error of terminal voltage during dynamic power profiles for INR20S. 164

Figure 5.38 Current of the INR20S cell model during the power profiles. 165

Figure 5.39 SoC of INR20S cell during power profiles. 165

Figure 6.1 The mask of the battery pack block. 167

Figure 6.2 SoC (left) and terminal voltage (right) during AMS T-O for blend braking strategy for three HE batteries employed in 69t A320. 171

Figure 6.3 SoC (left) and terminal voltage (right) during TXL T-O for blend braking strategy for 69t A320. 172

Figure 6.4 SoC (left) and terminal voltage (right) during LHR T-I for blend braking strategy for 69t A320. 172

Figure 6.5 SoC (left) and terminal voltage (right) during AMS T-O for blend braking strategy for three MEP batteries employed in 69t A320. 175

Figure 6.6 $I_{d,ref}$ (left) and aircraft speed (right) during AMS T-O for blend braking strategy for three MEP batteries employed in 69t A320. 175

Figure 6.7 SoC (left) and terminal voltage (right) during TXL T-O (unrestricted) for blend braking strategy for three MEP batteries employed in 69t A320. 176

Figure 6.8 SoC (left) and terminal voltage (right) during LHR T-I for blend braking strategy for three MEP batteries employed in 69t A320. 176

Figure 6.9 SoC (left) and terminal voltage (right) during TXL T-O (unrestricted) for blend braking strategy for three HP batteries employed in 69t A320. 178

Figure 6.10 SoC (left) and terminal voltage (right) during LHR T-I for blend braking strategy for three MEP batteries employed in 65t A320. 178

List of tables

Table 2.1 Fuel Flow indices during taxiing and relevant times. 38

Table 2.2 Summary of Et system developments up to date. 45

Table 2.3 Estimated zero lift drag coefficient during taxiing for different aircraft. 50

Table 2.4 Range of electric taxiing kinematic parameters. 53

Table 2.5 Introduced acceleration error using equivalent slope approach. 54

Table 2.6 Torque requirements for narrow- and wide-body aircraft considering MLG and NLG configurations and different grades. 55

Table 2.7 The rating of APU S/G for different aircraft families [94], [103], [104]. 57

Table 3.1 Summary of electrode positive active materials. 78

Table 3.2 The complex impedance of the essential circuit elements for ECM. 89

Table 3.3 Comparison of battery models. 99

Table 4.1 The parameters of the designed TM. 103

Table 4.2 Comparison of FE and *qd0* model for 80.8 rpm and id=0A. 116

Table 4.3 Comparison of FE and *qd0* model for 40 rpm and id=-100A. 116

Table 4.4 Energy consumption for A320 with 69 t under AMS T-O cycle 131

Table 4.5 Energy consumption for A320 with 75 t under AMS T-O cycle 131

Table 4.6 Energy consumption for A320 with 79 t under AMS T-O cycle 131

Table 4.7 Energy consumption for A320 with 69 t under TXL T-O cycle. 132

Table 4.8 Energy consumption for A320 with 75 t under TXL T-O cycle. 132

Table 4.9 Energy consumption for A320 with 79 t under TXL T-O cycle. 132

Table 4.10 Energy consumption for A320 with 69 t under prolonged TXL T-O cycle. 133

Table 4.11 Energy consumption for A320 with 75 t under prolonged TXL T-O cycle. 133

Table 4.12 Energy consumption for A320 with 79 t under prolonged TXL T-O cycle. 133

Table 4.13 Energy consumption for A320 with 65 t under LHR T-I cycle. 134

Table 4.14 Energy consumption for A320 with 71 t under LHR T-I cycle. 134

Table 4.15 Energy consumption for A320 with 75 t under LHR T-I cycle. 134

Table 5.1 Datasheet characteristics of the selected cells. 136

Table 5.2 Positive and negative electrode materials of the selected cells [198], [199]. 137

Table 5.3 The average instantaneous resistance for all selected cells. 150

Table 5.4 Accuracy of the fitting procedure for all battery cells during impedance estimation tests. 157

Table 5.5 The accuracy of HG2 cell model for five pulse tests. 160

Table 5.6 The accuracy results of INR20S cell model for five pulse tests. 160

Table 5.7 The accuracy results of INR35E cell for four pulse tests. 160

Table 5.8 Errors for three representative power profiles. 166

Table 6.1 Battery specifications. 169

Table 6.2 Panasonic NCRB battery performance for A320 69t during AMS T-O for three braking strategies. 171

Table 6.3 HE battery performance for A320 69t during AMS T-O for blend braking strategy. 171

Table 6.4 HE battery performance for A320 69t during TXL T-O (unrestricted) for blend braking strategy. 172

Table 6.5 HE battery performance for A320 65t during LHR T-I for blend braking strategy. 172

Table 6.6 MEP battery performance for A320 69t during AMS T-O for blend braking strategy. 175

Table 6.7 MEP battery performance for A320 69t during TXL T-O for blend braking strategy. 176

Table 6.8 MEP battery performance for A320 65t during LHR T-I for blend braking strategy. 176

Table 6.9 HP battery performance for A320 69t during TXL T-O for blend braking strategy. 178

Table 6.10 HP battery performance for A320 65t during LHR T-I for blend braking strategy. 178

Table 6.11 The expected DoD and reserve for taxiing mission consisting of TXL T-O and LHR T-I. 180

Table 6.12 Extra cost of fuel per flight needed for carrying more weight due to battery addition. 181

Table 6.13 Number of cycles before reaching EOL for commercial 18650 cells and different DoDs. 181

Table 6.14 Cost of battery installation and replacement per flight over five years period. 182

Table 6.15 Cost of electricity per flight. 182

Table 6.16 Total extra cost per flight. 182

List of Abbreviations

AMS	IATA Code for Amsterdam Airport Schiphol
AEA	All Electric Aircraft
AET	All Electric Taxiing
APU	Auxiliary Power Unit
ATM	Air Traffic Management
ATRU	Active Transformer Rectifier Unit
BCF	Brake Cooling Fan
BLDC	Brushless Direct Current
BMS	Battery Management System
CDM	Collaborative Decision Making
CO	Carbon monoxide
CP	Current pulse
CPE	Constant Phase Element
CT	Conventional Taxiing
CV	Constant Voltage
DC	Direct Current
DLR	German Aerospace Centre (Deutsches Zentrum für Luft- und Raumfahrt)
EASA	European Union Aviation Safety Agency
ECDT	Engine Cool Down Time
ECM	Equivalent Circuit Model
ECS	Environmental Control System
EDL	Electrical Double Layer
EDS	Energy Dispersive Spectroscopy
EDX	Energy Dispersive X-ray Spectroscopy
EGTS	Electric Green taxiing Systems
EHA	Electrohydraulic Actuator
EIS	Electrochemical Impedance Spectroscopy
EMA	Electromechanical actuator
EMS	Energy Management Strategy
EOL	End of Life
EPS	Electric Pushback System
ESS	Energy Storage System
ESUT	Engine Start Up Time
ET	Electric Taxiing
ETS	Electric Taxiing System
EU	European Union
EV	Electric Vehicle
FAA	Federal Aviation Authority
FEA	Finite Element Analysis
FLW	Finite Length Warburg
FOD	Foreign Object Damage
FSW	Finite Space Warburg

GCPL	Galvanostatic Cycling with Potential Limitation
GEIS	Galvanostatic Electrochemical Impedance Spectroscopy
GHG	Green House Gasses
GPS	Global Positioning System
GPW	Power Profile Importation
HC	Hydrocarbons
HE	High Energy
HET	Hybrid Electric Taxiing
HEV	Hybrid Electric Vehicle
HP	High Power
IATA	International Air Transport Association
ICAO	International Civil Aviation Organization
LCO	Lithium Cobalt Oxide
LESS	Local Energy Storage System
LFP	Lithium Iron Phosphate
LHR	IATA Code for London Airport Heathrow
LMO	Lithium Manganese Oxide
LNO	Lithium Nickle Oxide
LTO	Lithium Titanate Oxide
MAE	Mean Absolute Error
MEA	More Electric Aircraft
MLG	Main Landing Gear
MTOW	Maximum Take-Off Weight
MTPA	Maximum Torque Per Ampere
NAS	National Aerospace
NCA	Nickel Cobalt Aluminium
NCM	Nickel Cobalt Manganese
NEDC	The New European Driving Cycle
NLG	Nose Landing Gear
NM	Nautical Mile
NMC	Nickel Manganese Cobalt
NOx	Nitrogen Oxides
NYCC	New York City Cycle
OCV	Open Circuit Voltage
OEM	Original Equipment Manufacturer
PAS	Paris Air Show
PEIS	Potential Electrochemical Impedance Spectroscopy
PID	Proportional Integral Derivative
PM	Permanent Magnet
PMSM	Permanent Magnet Synchronous Machine
RMSAE	Root Mean Square Absolute Error
RMSE	Root Mean Square Error
RMSRE	Root Mean Square Relative Error

RP	Relaxation Period
SC	Super Capacitor
SEI	Solid Electrolyte Interphase
SEM	Secondary Equipment Manufacturer
SHE	Standard Hydrogen Potential
SOC	State of Charge
SPM	Single-Particle Model
T-I	Taxi In
T-O	Taxi Out
TM	Traction Motor
TXL	Code for Berlin Airport Tegel
UDDS	Urban Dynamometer Driving Schedule
VSD	Vector Space Decomposition
VSI	Voltage Source Inverter
XRD	X-ray Diffraction

1 Chapter: Introduction

1.1 Aviation impact on environment

The air transport industry is undoubtedly one of the most vital links in the global economy, bringing numerous social and economic benefits to nations [1]. As such, aviation is one of the rare sectors that continuously grows on average every year. The projections at the end of 2019 were very optimistic. According to the Airbus Global Market Forecast from 2019, the traffic and the number of aircraft are expected to have doubled by 2033 and 2040, respectively [2]. However, this growth posed justified fears regarding the environment. Namely, the aircraft jet engines are responsible for emitting pollutants such as carbon dioxide (CO_2), nitrogen oxides (NO_x), unburnt hydrocarbons (HC) and carbon monoxide (CO) [3]. In the EU in 2016 the aviation was accountable for 13.4% of all emissions generated from the transport sector, being the second most significant source of greenhouse gas (GHG) emissions after road transport [4]. Hence, the environmental concerns became critical and urgent, and many policies were introduced to counter the impact. However, the events from March 2020 significantly disturbed the aviation industry with worldwide borders closure due to the ongoing COVID-19 pandemic. The global passenger traffic dropped by an incredible 60%, back to the levels of the early 2000s [5]. Even though aviation has experienced many challenges and shocks since the beginning of the 21st century, such as the 9/11 attack, 2008 financial crisis, and SARS epidemic, it managed to recover quickly and keep a constant growth trend over the years [6]. The International Air Transport Association (IATA) and EUROCONTROL forecast that aviation will fully recover to pre COVID-19 times in 2024 with even noteworthier growth resulting from the confinement and desire to travel [7], [8]. Therefore, all the policies that were put forward to mitigate the impact should not be neglected. Arguably, the most famous document Flight Path 2050 strategy, suggested by European Commission, presents significant milestones such as a 75% reduction of CO2 and 90% of NOx compared to the new aircraft from 2000 [9]. In addition, numerous policies worldwide on a national level are implemented to suppress the impact. For example, all flights where a rail alternatives under two and a half hours exist are to be banned in France [10]. This example perfectly illustrates the role and impact that regulatory bodies have on this issue.

1.1.1 Background on More Electric Aircraft

Pollution emission is in direct relation to fuel consumption, so it is not surprising that most efforts are put into enhancing and advancing how aircraft use their fuel. For instance,

significant improvements can be achieved from more efficient aircraft operation since current operational practices are not always optimal from a fuel consumption point of view [11]. For example, Air Traffic Management (ATM) providers can improve the use of air space and route design, such as continuous descent approach or an optimised profile descent which allows for less noise and pollution during the approach phase of the flight with immediate effect on towns on the approach line [12], [13]. Simultaneously, aircraft manufacturers, original and secondary equipment manufacturers (OEM and SEM) are constantly advancing the technology. The examples, to name a few, are more efficient jet engines, more optimised aircraft structures such as lighter materials like composites and sandwich structures, new aircraft designs, all resulting in a better fuel efficiency [14]. From an electrical engineering perspective, the more electric aircraft (MEA) program approaches the problem from a different angle [15]. Its goal is to substitute traditional devices that use hydraulic, pneumatic, and mechanical power with electrical ones, translating into more efficient use of onboard energy, reduced system weight and consequently fuel consumption [16].

The two most ‘’electrified’’ aircraft are Boeing B787 Dreamliner and now discontinued Airbus A380. Both have adopted the concept of electro-hydraulic actuators (EHA) or electro-mechanical actuators (EMA) as replacement of traditional hydraulic systems for control of primary and secondary control flight surfaces, landing gear braking, significantly reducing excessive piping systems [17], [18]. In terms of electrification of pneumatic systems, B787 advanced the most. The functions and systems that are now successfully electrified are environmental control system (ECS), de-icing of wings, and starting of the main engines, so-called bleedless engine start [19], [20]. The mentioned changes result in numerous advantages such as reduced system weight, ease of maintenance, and increased engine efficiency [21]. Consequently, the introduction of more electrical loads resulted in a higher installed generated electrical capacity of 1MVA for B787 and 600kVA for A380 [22].

1.1.2 Emissions at airport level

Even though the airborne flight phases have been traditionally targeted for fuel efficiency improvement, the airports have become substantial sources of noise and emissions due to the increased congestion and traffic in recent years. Significant measures are jointly adopted by airports, airlines, and aircraft manufacturers to alleviate those problems and improve air quality at and around airports [23]. Carbon emissions at airports arise from many different sources. For example, the vehicle fleet, energy used by the buildings, and similar are all emissions that

airports can control directly, and which are at acceptable levels [24]. On the other hand, there are emissions that the airport has no contractual responsibility to, such as emissions from the aircraft or passenger and staff transport to the airport [24]. Numerous studies have shown that a greater part of emissions actualises from the latter class, particularly from the aircraft in the Landing and Take-off (LTO) cycle [25]. According to [26], 64% of total carbon emissions at Heathrow airport in 2018 originated from aircraft in the LTO. Defined by the International Civil Aviation Organisation (ICAO), an LTO cycle consists of four different flight phases differentiated by the percentage of full thrust (F_{oo}) used: take-off (100% F_{oo}), climb (85% F_{oo}), approach (30% F_{oo}), and taxi (7% F_{oo}, i.e., idle state) [27]. In [28], it is mentioned that the taxiing phase consumes 36% of LTO fuel. Additionally, it is stated that 12% of NOx, 89% of CO, and 91% of HC come from taxiing. Heathrow airport also estimates that taxiing is accountable for 40% of their total ground emissions [29]. The reason taxiing is responsible for this high environmental impact is that nowadays, main engines in idle thrust are used for ground movement, which is a highly inefficient operating point. In addition, they are very noisy and cannot be used for pushback due to safety reasons, so additional tractors and tugs are required, which reduces the autonomy of the aircraft and increases total taxiing time. Therefore, it is no surprise that most of the innovative measures that have been introduced concentrate on limiting the use of main engines and even eliminating their use during taxiing.

1.1.3 Improved taxiing procedures and Electric taxiing

In general, the undertaken actions regarding aircraft taxiing can be divided into operational and technological solutions [30]. Operational solutions such as single-engine taxiing and active routing are implemented both by airlines and airports [31]. However, even if considerable fuel savings and pollutions reduction can be obtained, the main engines are still operational and contribute to the airport's carbon footprint. On the other hand, technological solutions assume engineless taxiing and they are mainly adopted by aircraft OEMs and SEMs. Engineless taxiing can be broadly divided into dispatch towing, and electric taxiing (ET) and more details will be provided throughout the thesis. In a broad sense, ET can be defined as a movement of the aircraft while it is still on the ground using means of an electric or hybrid-electric traction propulsion system. For example, if aircraft is towed with an electric or hybrid-electric tractor, the procedure is called external ET. In this option, only minor modifications are made on the aircraft, mainly in avionics. Conversely, on-board ET is based on the concept of powered wheel [32], where electric motors are installed inside the wheels of nose or/and main landing gears (NLG or/and MLG) and are used for traction while aircraft is on the ground,

excluding take-off and landing. In Chapter 2, different ET systems (ETSs) are explained in detail, comparing their performances, advantages, disadvantages, and discussing challenges that impede the implementation of these innovative systems.

Since the first proof of concept of on-board ETS in 2006, many companies have tried to enter this lucrative market of ET. However, since then, only five have managed to demonstrate fully operational systems or electric drive units:

- Taxibot: external ETS, a semi-autonomous series hybrid-electric tractor with diesel engines.
- Wheeltug: on-board ETS in NLG, powered from the auxiliary power unit (APU).
- EGTS: on-board ETS in MLG, geared, powered from the APU.
- DLR: on-board ETS in MLG, geared, fuel cells powered.
- Nottingham-Safran-DLR: on-board ETS in MLG, direct, powered from the APU.

1.2 Research rationale and problem scope

As already mentioned, airports are not exempt from FlightPath 2050 requirements, and probably the strictest commitment is that all ground movements are required to be carbon-free by 2050 [9]. To date, most commercially developed on-board and external ETS are relying on the hybrid-electric propulsion concept. In the case of on-board ETS, the APU drives the Starter/Generator (S/G) which produces electric energy needed for the ET drive unit and other systems. This solution is coming as a logical choice, as APU already must be turned on during engine-free taxiing in order to provide the essential powers (pneumatic, hydraulic, and electrical) to ECS, lighting, and infotainment systems. Unfortunately, these hybrid electric taxiing (HET) solutions do not guarantee carbon-free taxiing. Even if ETS's power comes at minimal cost and brings many benefits, as discussed later, it does not bring us closer to the milestone of carbon free aircraft taxiing.

For this to be achieved, the ET drive unit must be powered from a non-carbon producing source. The DLR ET drive unit is the only one from the developed ETS powered by a non-carbon source, i.e., fuel cells. Although hydrogen is very energy dense, this system is unsuitable for this application due to the weight and complexity of associated systems, such as a hydrogen tank, compressors, pumps and similar [33]. Even if the system's weight were acceptable, the procedure would still be emitting pollutants, as the APU would have to be turned on to power other systems. Zero-carbon taxiing can be achieved, for example, by installing APU that uses

hydrogen fuel [34], or using even more sustainable aviation fuel than what is available today [35], together with increasing the rating of aircraft's S/G. Another option is installing an electrochemical local energy storage system (LESS) device which will exclusively power the ET drive unit. Of course, in this scenario, it is also assumed that other systems operational during taxiing are powered from zero-emitting sources. This option will be named all electric taxiing (AET). Compared to fuel cells, traction batteries reached certain technological maturity thanks to the electric vehicle's development. Therefore, in this thesis, only batteries, in particular lithium-ion, will be considered as a potential option for LESS. Battery powered ET drive unit option has multiple benefits compared to being powered from APU S/G.

The main benefit of installing battery type energy storage is the possibility of energy recuperation during aircraft breaking. Taxiing drive cycles typically exhibit few stop and go patterns which provide an excellent opportunity for energy regeneration. This implementation improves the efficiency of the drive because, typically, the braking energy would be dissipated in a braking resistor in case of APU driven ETS. The LESS can also be charged during landing and take-off, but this falls outside the scope of this work. Another benefit is the reduction of the cabling complexity. If the ET drive unit is powered from the APU S/G at the rear of the aircraft, lengthy cables are needed. Not only that the cabling complexity would be reduced, but also weight savings would be achieved for using shorter cables.

On the subject of weight, the main disadvantage of this solution is the increase of aircraft's weight. Consequently, aircraft might end up heavier and spend more fuel during flight, which could offset savings obtained while taxiing electrically on the ground. Finally, the introduction of high energy and power rating batteries to the aircraft can potentially prolong the certification of these systems due to safety issues that the aviation sector already had with lithium-ion batteries [36].

1.3 Aim and objectives of the thesis

This project aims to analyse a dedicated optimal battery energy storage device intended as a future system in a new generation of more electric narrow-body aircraft that will solely power the ETS [37]. The assumption is made that by 2050, the existing APU will be replaced by more sustainable solution such as hydrogen or biofuel powered APU and that other systems such as ECS, starting of main engines, lighting and de-icing will be powered from zero carbon producing sources. Therefore, the investigated LESS and ETS are not considered to be

retrofitted to the existing aeroplanes, as is the case with current conventional developments of ETS, the so-called HET.

The potential of improving ground propulsion technologies and procedures has been recognised, and the corresponding efficiency increase has become an attractive opportunity. Hence, many projects and collaborations were announced, but unfortunately, most of them without any news or updates on the development and with uncertain future. The latest unsuccessful collaboration is of Airbus and Safran, which ended in 2020, only two years after the partnership had been established [38]. Out of the five developed ETS prototypes, four were fully demonstrated by fitting to the actual aircraft, whereas one was demonstrated in a laboratory environment up to TLR5 standards [21]. Of those four, EGTS and DLR decided to halt the programme after successful demonstrations, Wheeltug is in the process of certification and accepting orders, and only one external ETS managed to complete certification being operational since 2015 (Taxibot). Adopting on-board ETS is paved with challenges and obstacles, which can best be seen from the fact that as of 2022, no on-board ETS are operational, 16 years after the first proof of concept. Despite this fact, the prospects of on-board ETS remain promising still.

The focus of the previous studies was on individual parts of the ETS, such as electric machines or power electronics. However, to expedite ETS's introduction and reach the goal of zero-carbon taxiing by 2050, timely studies at the system level are needed. We hope that this thesis will stimulate further research on this vital topic, which will lead to faster market adoption of ETS. In this thesis, a model-based design approach was adopted, where whole ETS is modelled including aircraft dynamics, propulsion system (machine and power converters), and several commercially available cylindrical lithium-ion cells. The model's simulation data are then used to inform system architecture decisions, to validate battery energy storage selections (in terms of chemistry and ratings) against drive cycle performance requirements and analyse system-level trade-offs. This approach is contrary to the traditional methods in which battery chemistry is selected beforehand, and the whole system is designed and modelled considering only one type of battery. The primary outcome of this work is a versatile system level model of the on-board ETS that serves as a platform for model driven development which supports battery cell selection to drive optimised designs. The model can be adapted depending on the airport taxiway conditions, aircraft specifications and demanded drive cycle. Additionally, the model utilises a database of models of commercially available lithium-ion

cells of different chemistries that can be co-simulated and analysed in conjunction with the rest of the ET drive unit.

The main objectives and contributions of this work are:

1. Comprehensive literature review of ET operations and ETS which explains benefits, challenges, and future developments of these novel systems.
2. Development of dynamic model of a voltage source inverter-driven double-star permanent magnet synchronous machine with outer rotor.
3. Development of aircraft ET speed control, including the limitations of power train components, such as field weakening and regeneration limitations.
4. Development of commercially available lithium-ion battery cell models database that are used for analysis of all electric taxiing. The parametrisation and verification of the models was done experimentally.
5. Performance analysis of different LESS in terms of chemistry and rating for several typical taxiing drive cycles.
6. Analysis of HET for different energy management strategies (EMSs) and different types of LESS.

1.4 Methodology

In this section a brief review of modelling techniques is presented and based on the desired aims and objectives a suitable method is selected. Even though ET is an aerospace-based application, it essentially can be classified as traction application as the ETS is only utilised while being on the ground.

1.4.1 Modelling Methods of Vehicular Traction Electrified Powertrains

The two most common modelling approaches of vehicular traction electrified power trains, depending on research purpose, are:

- Backward facing modelling (i.e., quasi-static)
- Forward face modelling (i.e., dynamic)

The schematic of the quasi-static method, also called backward facing, is shown in Figure 1.1. The input to the model is the desired vehicle's speed, i.e., drive cycle. The primary assumption when using this methodology is that the desired drive cycle is followed precisely by the vehicle speed. Therefore, this approach does not consider the limitations of the

powertrain, and it assumes that the vehicle can carry out any given kinematic profile [39]. Thus, the input to the model is better said to be the actual speed of the vehicle rather than the desired one, i.e., the reference. Due to this constraint, this method is suitable for energy consumption evaluation (and fuel consumption in terms of hybrid electric drivelines), preliminary design of energy management strategies, assessment of emissions and performance [40].

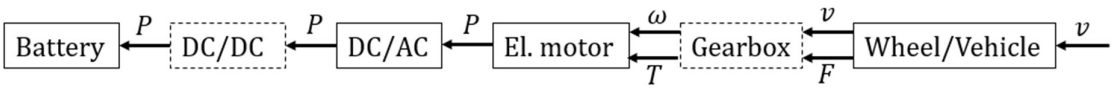


Figure 1.1 Quasi-static approach in modelling vehicular power trains, adapted from [41].

As shown in Figure 1.1, the model's input is fed to the vehicle dynamics block, which calculates the necessary traction force needed for that operating point, neglecting whether the electric machine can provide it. Going backwards, traction force acts as input to the gearbox and electric machine blocks outputting the needed electric power at the terminals of the electric machine. As most of the models are based on the efficiency, power, and loss maps, the final result is then power needed from the battery or/and engine for the given drive cycle.

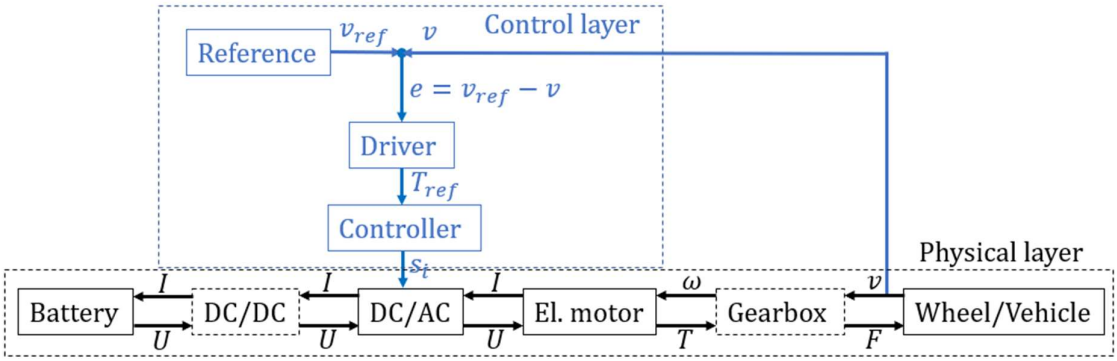


Figure 1.2 Dynamic approach in modelling vehicular power trains, adapted from [39], [41].

Compared to the backward approach, which does not follow the causality principle, a dynamic approach, i.e., forward face modelling, is based on the first principle description of power train components with dynamics equation describing the evolution of its state [39]. Thus, it is used when dynamics and control of the system are of importance. As shown in Figure 1.2, the input to the system is the reference speed compared to the actual vehicle speed. The error is fed to the driver, modelled as proportional integral derivative (PID) controller, whose output is needed torque at the wheel to achieve the reference speed. That reference is passed on in a forward manner to the machine and inverter controller. On the physical level, the mechanical output of the electric machine model (torque at the shaft) is connected to the vehicle dynamics block (and gearbox if it is present). Therefore, compared to the previous method, the

tractive force is input to the vehicle dynamics block rather than its output. This results in acceleration and consequently speed change, which acts as a feedback signal. On the other side, the electrical machine model is connected to the inverter and battery models. In Figure 1.2, the flow of relevant states is depicted, clearly showing the difference from the backward-facing approach. Consequently, the forward-facing method is used for: drivability, stability, and handling studies, acceleration capability analyses, development of control methods and similar [40].

Therefore, as one of this thesis's objectives is developing a practical and functional model for multiple studies and considering the limitations of backward face modelling, the forward approach is selected. Even though the forward face method seems superior, its main drawback is lower computational efficiency, i.e., the longer time needed to simulate a given drive cycle [42]. The most critical element in the performance simulation of vehicles, simulation time wise, are switching devices that operate at kHz and above frequencies. For capturing this high frequency dynamics, a simulation time step should be at least ten times less than switching frequency, i.e., in the range of microseconds. In a device and even some system level simulations switching models of power converters are used. However, the behaviour of the system is simulated only for few seconds. Considering that the maximum duration of the taxiing drive cycle is 30 minutes, a detailed model would require practically unapproachable GB of random-access memory with standard computer's usual configurations. Thus, measures must be taken to reduce the model complexity of switching models and make them suitable for system-level simulation whilst keeping the satisfying level of model accuracy. Therefore, all power electronic models in this thesis are developed using average models where switching dynamics are neglected, and low frequency dynamics are considered [43]. As a result, a simulation time step can be increased and increase the simulation speed.

When considering electric machines, the most common dynamic model is the *qd* model. However, for developing a working *qd* model parameters of the machine such as self and mutual inductances, winding resistances, and flux of permanent magnets (PMs) must be known by the modeler. Those parameters are obtained either through experiments or finite element analysis (FEA) and using transformation matrices parameters' can be converted to the *qd* frame values. Fortunately, the average model of 3-phase power electronics can also be transformed to a *qd* model so two models can easily exchange information. Therefore, practically, 3-phase inverter and 3-phase machine can be combined into one block with physical input and output

as DC link voltage and shaft torque, respectively. A control input to the block is the desired duty cycles of the switches. More details are presented in Chapter 4.

Finally, in order to complete the model of ETS, batteries are represented as equivalent circuits. This is the most convenient solution as *qd* model of machine and inverter can also be represented via electric circuits, and thus easily be connected to the battery model [44]. This concludes the system's forward dynamic model, which can be used for assessing the battery and drive performance, control of the components, energy management strategies, etc. The aircraft dynamics modelling will be explained in more detail in Chapter 3, the traction motor model is developed in Chapter 4, including the inverter model and its control. In Chapter 5, dynamics models of commercialised lithium-ion batteries are shown.

1.5 Outline of the thesis

This thesis is organised into seven chapters. It focuses on ET concepts, modelling of electric drives and batteries, performance analysis and design by simulation.

In Chapter 1, motivation for the research and research rationale have been explained. The aim of the thesis and contributions have been clearly defined. Finally, the accepted methodology has been described.

Chapter 2 presents an extensive literature review of ETS. Commercially available systems are presented and analysed, and the differences between topologies are outlined. Additionally, aircraft taxiing dynamics is also presented in this chapter with emphasis on the road load resistances calculation, power and torque requirements at the wheel, and acceleration performance.

The literature review of battery technologies is discussed in Chapter 3. First, battery terminology and the basic operating principles of various pre-lithium batteries are briefly discussed. Then, the lithium-ion batteries, as the most-used battery type in traction application applications, are thoroughly discussed, including working principles, benefits and disadvantages of each type, shape of the cells and similar. Finally, an extensive literature review on battery modelling procedures is also given.

The model of traction machine (TM) is developed in Chapter 4. First, the TM is modelled in finite element software from which the machine's parameters were obtained. The acquired parameters are then used to develop a dynamic machine model in the *qd* reference frame. Also, in this chapter, the averaging procedure of three-phase inverters is explained, and the developed

inverter's model is combined with the TM's model. Finally, the control system is also explained, including design of current and voltage PI controllers, design of Maximum Torque Per Ampere (MTPA) strategy etc. The chapter is concluded with the simulation of two typical drive cycles with deriving power and energy requirements at the DC link.

Chapter 5 introduces the characteristics of the selected commercial lithium-ion cells, and it describes the experimental technique whose measurements are used to derive parameters of the selected cells. The post-processing, such as data preparation, data analysis, curve fitting, and interpolation methods, is explained. Finally, the developed models are verified not only to the experiments used for parametrisation but also to the applied taxiing power profile to the cells.

In Chapter 6, the batteries' models are combined with the model from Chapter 4 and are simulated for typical taxiing duty cycles. Several battery ratings and drive cycles were selected to analyse the aircraft performance. The results are compared in terms of availability, energy content, power rating, and ability to accelerate. Chapter 7 presents additional findings using the developed model. Also, the lifetime and charging options were analysed for the case of AET.

Finally, Chapter 7 concludes the thesis with final remarks and opportunities for future work.

2 Chapter: Aircraft Electric Taxiing

This chapter is envisaged to give insight of aircraft ET procedures from different points of view, such as operations, technology, challenges, and future trends. In the first part of this chapter, a detailed review of ETS is presented. The problems of conventional taxiing are outlined with a focus on increased congestion and fuel consumption, and it is explained how ETS can alleviate those problems. Developed ETS to date are described, and their benefits and disadvantages are shown. The second important part of this chapter deals with the modelling of aircraft dynamics during taxiing. In this part all limitations of the ETS are analysed from the kinematic performance perspective, providing the reader with knowledge to understand the reasoning behind different design choices of ETS. The given model is used in Chapter 4 in which the performance of the whole drive is simulated. Finally, the chapter is concluded with recommendations and the author's opinion on the possible future development trends of these systems.

2.1 Review of Electric Taxiing Systems

In this part of Chapter 2 the extensive literature review of ET procedures and ETSs is given. The problems of conventional taxiing presented in Chapter 1 and solutions to those problems are explained in more detailed. Then, benefits and disadvantages of electric taxiing, as one of the most promising solutions, and its implementation challenges presented. Five developed systems up to date are thoroughly described in 2.1.3 and their differences in 2.1.4.

2.1.1 Problems of conventional taxiing

As outlined in the previous chapter, taxiing is one of the most critical ground procedures targeted for efficiency improvements. According to ICAO, taxiing is defined as the movement of the aircraft while it is still on the ground that happens under its own power [45]. Taxiing is divided into two distinct phases: taxi-out and taxi-in. Taxi-out commences when the aircraft begins to move under its own power, leaving the gate, ramp, apron, or parking area, and terminates upon reaching the runway. In contrast, taxi-in begins upon exiting the landing runway and terminates upon arrival at the gate, ramp, apron, or parking area when the aircraft ceases to move under its own power [46]. In between taxi-in and taxi-out, there is a pushback phase. Pushback means reversing an aircraft from a nose-in parking stand using the power of a specialised ground vehicle attached to or supporting the nose landing gear [47]. Even though aircraft can use reverse thrust for backward movement, this procedure is prohibited at the gate

due to safety issues, such as jet engine blast and foreign object damage (FOD). Once the aircraft is pushed back and the tractor is disconnected, main engines can safely be turned on, and taxi-out can begin. In this thesis, the pushback will be considered as an integral part of taxiing as specified by EUROCONTROL [48].

In Europe, narrow-body aircraft spend 2.5 hours on the ground, equivalent to 30% of their time and 10% of fuel consumption [49], [50]. With expected increased traffic and congestion trend taxiing and queuing times will only rise in the future. For example, the average taxi-out time at London Heathrow airport in the summer of 2019 was 22 min, whereas the average taxi-in time at Amsterdam was 8 minutes [51], compared to around 60 minutes of airborne time between those two airports. Thus, 360 kg of fuel is burnt during dual-engine taxiing for the worst-case scenario of 30 min, taking into account the typical burn rate of 6 kg/min per engine at 7% idle thrust [52]. For every kg of burnt fuel during taxiing, 3.115 kg of CO2 is emitted [53], amounting to 1.19 tons of CO2 per taxiing cycle.

Some operational measures such as Advanced Surface Movement Guidance and Control System (A-SMGCS), Airport Collaborative Decision Making (A-CDM) system, and Active Routing (AR) improve the movement of aircraft for minimal fuel consumption and minimum delay through a set of optimisation algorithms [54], [55]. Another operational measure is single-engine taxiing, during which only one engine is used and effectively almost halving the fuel consumption and emissions. Even though these measures improve the carbon footprint, they still use main engines. In the case of single-engine taxiing, due to asymmetrical thrust, problems occur during manoeuvring, particularly in turns [56]. In addition, single-engine taxiing operations highly depend on the weather conditions and it has proven unpopular among pilots [57].

Technological solutions, on the other hand, assume engineless taxiing. The most notable, dispatch towing, uses conventional pushback tractors for towing tractors even during taxiing procedures. Even though jet fuel consumption is significantly reduced, the consumption of tugs will increase. Depending on the fuel used, the actual emissions can increase despite engines being turned off. This is due to the fundamental differences in fuel burn processes of jet, diesel, and gasoline engines. In [58] was shown that the use of diesel tugs for dispatch towing could increase by up to 100% NOx emissions, and in the case of gasoline tugs, CO emissions can increase by up to 500%. An additional problem with this option is NLG fatigue, as the tow bars are not designed for prolonged periods of high force, in addition to the low maximum achievable speed [59].

Another and novel idea of aircraft ground movement is electric taxiing. Electric taxiing is the movement of the aircraft while on the ground using means of electric traction. The reason behind the name is that electricity is involved in the last stage of the energy conversion process, i.e., electric motor, despite the fact what it is the primary energy source. Suppose the primary energy source uses fuel consuming device, e.g., genset. In that case, the word hybrid will be used as a prefix calling these systems hybrid electric taxiing (HET) as explained in Chapter 1. If primary source uses only a zero-carbon emitting device, it will be called all-electric (AET). If both sources are used, the system is called HET plus, shortly HET+. Electric taxiing can further be divided into external and on-board systems. External ETS assume an external tug connected to the NLG of the aircraft that tows the aircraft to the runway for take-off and connects to it after landing for towing it from the runway. On the other hand, on-board ETS are installed in the wheel/s of the landing gear/s either main or nose (MLG or NLG). The general architecture of external ETS is shown in Figure 2.1. Both fuel-based engine and electrochemical sources are shown, where dashed box indicates that system is hybrid. External HET+ system can take form of series, parallel or series-parallel combination, thus the representation in Figure 2.1 is only of the descriptive character. The general architecture of on-board ETS is shown in Figure 2.2 where TM stands for traction motor (i.e., electric motor) and n for the number of motors installed in the corresponding landing gear. For narrow-body aircraft, NLG can host maximum two motors whereas each MLG can host up to two motors meaning that total maximum number of TMs in MLG on-board ETS can be four. APU S/G is lined with dash lines meaning that it represents a HET system. Similarly, TM can be connected to wheel through gearbox mechanism (i.e., geared on-board ETS) or without (i.e., direct drive on-board ETS). Compared to external systems which can have multiple hybrid powertrain configurations, on-board HET+ always takes form of series hybrid powertrain configuration. General advantages and disadvantages of ETSs, regardless of the configuration, are presented in the next section. The differences between specific ETSs are presented in section 2.1.4.

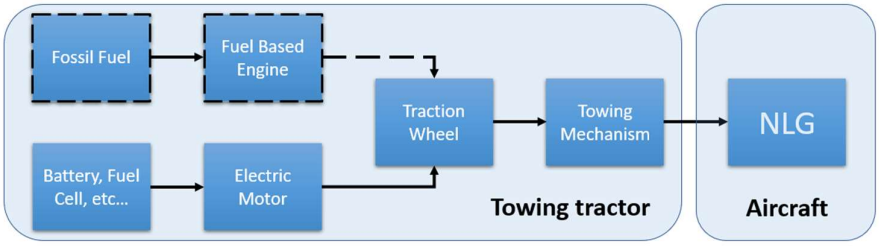


Figure 2.1 Generic architecture of external ETS, adapted from [60].

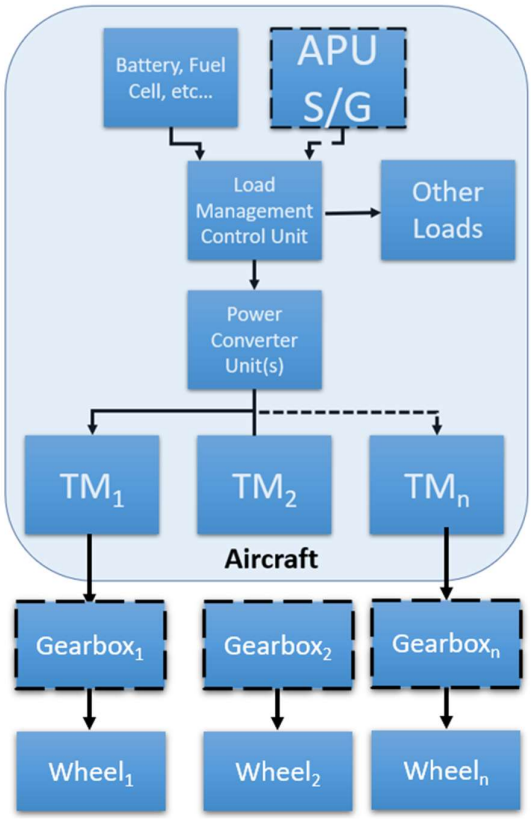


Figure 2.2 Generic architecture of on-board ETS, adapted from [60].

2.1.2 General benefits and disadvantages of ETS

All developed ETS, whether external or on-board, HET or AET, have several aspects in common. Most important of all is that ET procedures do not require the use of main engines for taxiing. As already mentioned, this results in numerous direct benefits, the most notable ones being reducing taxiing fuel, pollution, and noise emissions. Some indirect advantages include lower risk of engine FOD and consequently lower engine maintenance cost. Similarly, as the brakes are not used extensively during ET, the maintenance cost of brakes is reduced [61]. Of course, depending on the system, there are specific benefits and disadvantages. After introducing technical aspects of the developed ETS in section 2.1.3, their advantages and drawbacks will be compared in detail in section 2.1.4.

Another common aspect for all ETS is their main disadvantage, the main barrier towards wider implementation. Namely, prior to take-off, a specific start-up procedure must be followed in which engines are warmed for a pre-defined time, so-called Engine Start-Up Time (ESUT). Similarly, after landing, the engines should cool down for a period called Engine Cool Down Time (ECDT) before shutting them off. ESUT is usually between 5 and 7 minutes,

whereas ECDT is around 3 minutes [62]. During conventional taxiing, these conditions are automatically fulfilled. However, during engineless taxi-out, after the aircraft has reached the runway, the engines would not be ready for take-off. This problem represents one of the most significant operational hurdles, which ET disputants always bring up when standing up against these systems. Therefore, this problem should carefully be addressed. The aircraft can turn on their engines for the last 5 minutes of taxiing, but this might pose safety issues for the aircraft taxiing behind due to jet engine blast. On the other hand, a place similar to the de-icing platform can be built near the runway where aircraft can safely warm up their engines for take-off, which will undoubtedly increase the time aircraft spend on the ground. In Figure 2.3, a process charts for conventional double-engine taxi (top), external ETS (middle), and on-board ETS (bottom) are shown.

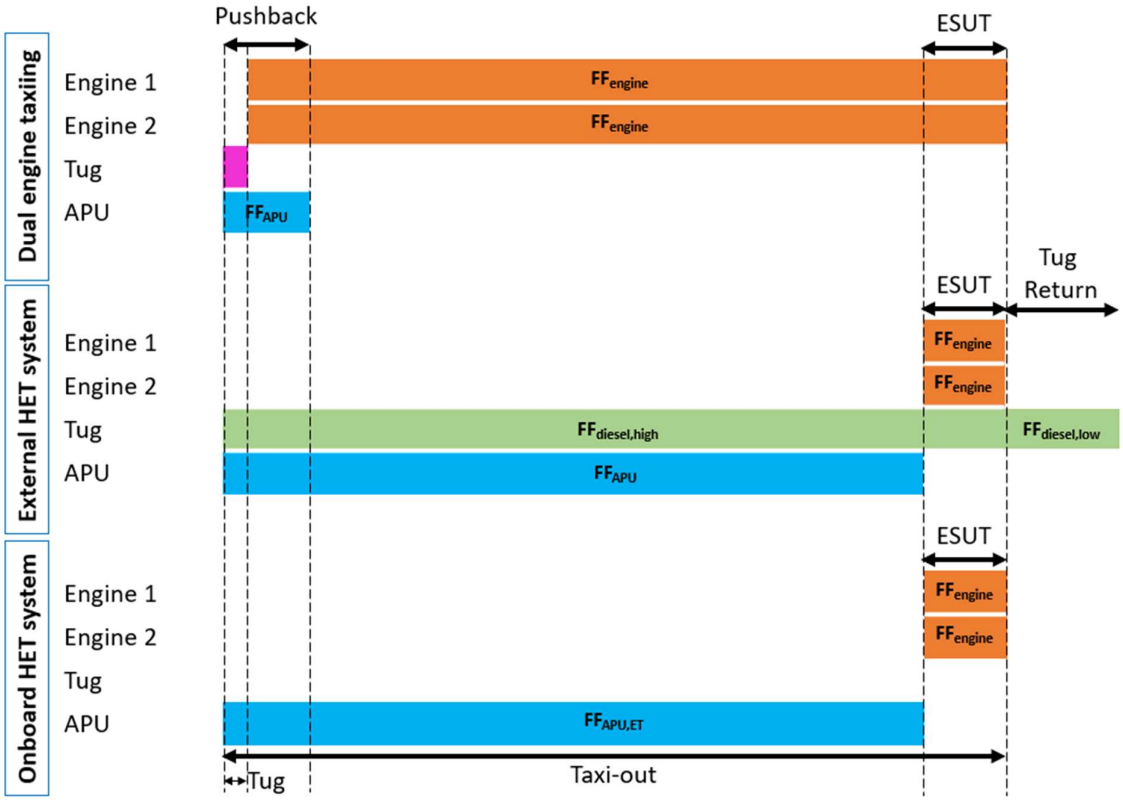


Figure 2.3 Process charts of conventional, external electric, and on-board electric taxiing.

Process charts are useful for comparing procedures from operational point of view and for rough estimations on fuel consumption and greenhouse gas emission. Using fuel flow indices usually found in the literature for jet engines and APU during taxiing, APU during ET, diesel tug with high and low load, savings can be predicted using (2.1)-(2.3).

$$F_{dual} = 2FF_{engine}(t_{taxi-out} - t_{tug}) + FF_{diesel,high}t_{tug} + FF_{APU}t_{pushback} \quad (2.1)$$

$$F_{external} = FF_{APU}(t_{taxi-out} - ESUT) + FF_{diesel,high}t_{taxi-out} + 2FF_{engine}ESUT + FF_{diesel,low}t_{return} \quad (2.2)$$

$$F_{onboard} = FF_{APU,ET}(t_{taxi-out} - ESUT) + 2FF_{engine}ESUT \quad (2.3)$$

Table 2.1 Fuel Flow indices during taxiing and relevant times.

FF_{engine} [kg/min]	FF_{APU} [kg/min]	$FF_{APU,ET}$ [kg/min]	$FF_{diesel,high}$ [gal/h]	$FF_{diesel,low}$ [gal/h]	$ESUT$ [min]	t_{t-o} [min]	$t_{pushback}$ [min]	t_{tug} [min]	t_{return} [min]
6	1.8	2.1	35.7	11	5	30	3	1.5	5

Assuming fuel flow indices and times as in Table 2.1 a rough approximation of fuel savings can be derived. Therefore, in this scenario dual engine taxiing consumes 330.3 kg of jet fuel and only 2.9 kg of diesel fuel. On the other hand, external ETS burn 105 kg of jet fuel and 60.4 kg of diesel, representing 68% decrease and almost 2000% increase in diesel fuel. When it comes to on-board HET, only jet fuel is used. In the given scenario 112.5 kg of jet fuel is consumed. These are just the rough estimates assuming that taxiing time remains the same in all the situations which is not always the case. For a more accurate study, a set of flight movements must be considered each of them with different taxiing times as performed in [63].

Finally, both on-board and external ETS have operational challenges when it comes to their successful implementation. For example, implementation of the on-board ETS is airlines' responsibility, and at the same time it needs close collaboration with airports [64]. However, the same applies to external ETS. As primary users of those tractors, airports would invest in tractors, but the benefits would be going to airlines. So, in both cases, a compromise must be reached if these novel systems are to be seen operating at airports worldwide. In the case of external systems, Lufthansa proposed that ground handling companies of major airlines purchase tugs that will operate at their hub airports [65]. This proposal would have to put all major airlines in the agreement, which is highly unlikely, and not to mention that small airports would be left out from the initiative [60].

2.1.3 Electric taxiing systems development up to date

After first proof of on-board ETS concept by Wheeltug back in 2005, many companies recognised the ET market's potential and decided to develop their own systems. Some companies concentrated their focus on external ETS in form of tugs. Interestingly, some developed tugs are only used for pushback and will be called electric pushback systems (EPS) herein. As they are also electric, external, and as pushback is part of taxiing these systems EPS are considered under external ETS category. Naturally, on-board systems, as one of the most

interesting MEA concepts, gained the most interest which resulted in development of several prototypes of which most were demonstrated implemented on actual aircraft. It is also fair to mention that only one on-board ETS project is still active and aiming to enter service in 2022. Despite this fact, it is worth mentioning other systems as they gave insight and laid foundations for future research of ETS.

2.1.3.1 Electric pushback systems

EPS are external systems designed to replace conventional tugs used for pushback. The most notable manufacturers and their models are Mototok (Spacer 8600), Charlatte (CPB35E), and Lektro (AP8950SDB-AL-250). Due to their low maximum cruising speeds when towing aircraft with maximum take-off weight (MTOW), 2-4 knots (1.03-2.06 m/s), they are not suitable for the taxiing phase. Nonetheless, compared to the traditional tractors, the new vehicles have numerous benefits:

1) They are all battery-powered, which practically classify them as AET (although they are only used for pushback) with emissions and noise from this procedure being eliminated.
2) They help optimise the hangar space because they are smaller than conventional tractors, most notably Mototok [66].
3) The licensed driver is not required for Mototok, which is controlled remotely by the operator, allowing for better viewing angle and more flexibility in staff selection as the operator does not need driving or special licenses.

Mototok can perform 25 pushbacks on one charge, which is enough for 2-3 days of operation, and it is charged in 3 hours [66]. There are 45 operational Mototok at Heathrow and British airways recently celebrated 100000th pushback [67].



Figure 2.4 Mototok and its operator.

2.1.3.2 TaxiBot

TaxiBot is a hybrid-electric pilot-controlled towbarless towing vehicle used both for pushback and taxiing procedures. It was developed by Israeli Aerospace Industries in collaboration with TLD group and Siemens which manufactured the vehicle and electric driveline respectively. Compared to the dispatch towing, TaxiBot uses a unique interface mechanism to clamp to the NLG, which resolves the problems of increased NLG fatigue and low lifecycle [68]. The clamping system is designed in such a way that it allows the tractor to slightly lift the front wheel, lock it up in position, and place it on a turret that can rotate [65]. This solution allows the pilot to control the TaxiBot using brakes and tiller, same as throughout conventional taxiing with engines. The wheel's movement is captured by the sensors and transmitted to TaxiBot's wheels, which turns the same way as the aircraft would. Although the pilot steers and brakes the aircraft, the TaxiBot still needs a driver, who takes over control for the pushback and for driving the TaxiBot back to the gate after it has decoupled from an aircraft or to collect a plane that has just landed [69].



Figure 2.5 Taxibot towing KLM aircraft at Amsterdam Schiphol airport.

The powertrain of TaxiBot consists of two diesel generators (combination of a diesel engine and an electric generator), producing electricity for eight electric motors, each driving one wheel of the tractor. The total power to the road is estimated to be 500 kW, which is enough to tow Boeing B737 with MTOW at 23 knots (11.83 m/s) [70]. It is estimated in [65], [69], [71] that the introduction of TaxiBot can have positive effects such as:

- 50-65% reduction of fuel during taxiing
- 50% reduction in Foreign Object Damage (FOD)
- 5.4 million USD savings per year per aircraft

As already mentioned, TaxiBot is presently the only certified taxiing alternative. It gained certification approval from the European Aerospace Agency (EASA) for the Boeing B737

classic family in 2014, which was complemented by B737 new generation certification in 2016. In May 2017, Airbus A320 family obtained certification from EASA and Federal Aviation Administration (FAA), including neo variants. The same year, FAA certified TaxiBot for the B737 classic and new generation [60]. At the moment, there are ten operational TaxiBots worldwide [72], operating at Frankfurt International Airport for Lufthansa LEOS (launch customer), Delhi and Bangalore Airports, and since April 2020 at Schiphol Airport where extensive feasibility study is being conducted.

2.1.3.3 EGTS

Notably, the most prominent developed ETS was Electric Green Taxiing Systems (EGTS), a joint venture between Safran and Honeywell announced at Paris Air Show (PAS) in 2011 [73]. EGTS was foreseen as an on-board ETS with one traction motor per MLG. The system was powered from the APU S/G, making it a type of HET, and its electrical architecture is shown in Figure 2.6.

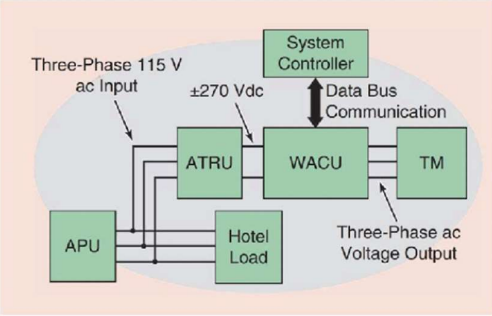


Figure 2.6 Architecture of EGTS's electric drive system [74].

As it can be seen, the APU's generator is connected to the Autotransformer Rectifier Unit (ATRU), which feeds the $\pm$270V DC bus. The motor controller (WACU), i.e., active 3-phase bride 2-level inverter, is connected to the traction machine (TM). A surface mount permanent magnet synchronous machine (PMSM) was used with rated and peak torques of 130Nm and 200Nm, respectfully [75]. Low torque values suggest that the system used gearboxes, as the torque requirements for taxiing are in the order of kNm magnitude, which will be later demonstrated and calculated in section 2.2.5. The total weight of two motors with cooling fans is 72 kg [74], whereas the total EGTS weight is estimated to be 300-400 kg [76]. The system was successfully demonstrated at PAS in 2013 but due to safety requirements only with a maximum speed of 10 knots (5.14 m/s). Soon after, EGTS was successfully demonstrated with 20 knots (10.28 m/s) at Toulouse airport [74]. Other kinematic requirements for which the system was designed are [77]:

1) Maximum taxiing speed of 20 knots achieved in 90 s.
2) 10 knots speed in 45 s for active runway crossing
3) Breakaway at MTOW with 1.5% slope

The requirements stated above, especially maximum speed, might seem at first low compared to the conventional taxiing speeds of 30 knots (15.43 m/s). However, these are in line with the study [78], in which 19 knots (9.77 m/s) is identified to be the optimal speed for ETS, which would not cause further delays for the aircraft taxiing behind. As argued in [78], [79], these requirements cannot be achieved with the existing APU of B737 and A320 families which employ 90 kVA S/G. Thus, for a high-speed electric taxiing of 20 knots, the generator, or entire APU, would have to be modified to accommodate higher taxiing loads. This aspect is analysed and explained in more detail in the following subsection 2.2.6.

The expected benefits of introducing a system like EGTS are stated below [60], [77]:

1) 61% reduction of CO2, 51% of NOx, 62% HC and 73% of CO
2) EGTS reported that their system could achieve 4% of block fuel savings per flight. It is important to notice that compared to TaxiBot, which quantify fuel savings relative to the taxiing fuel, EGTS's savings are quantified in terms of block fuel, i.e., fuel for the entire mission which includes ground and airborne operations.
3) All indirect and direct benefits translate into $250k per aircraft per year in profits

Despite the successful demonstration, the companies decided to halt the project in 2016. As explained in [80], numerous factors led to this resolution which was not in favour of EGTS. However, the most considerable justification was the oil price which at that time reached a historical minimum. Even though the project is terminated, Safran continued being devoted to the electric taxiing idea. In 2017, one year after the split with Honeywell, Safran and Airbus announced a collaboration targeting 2022 as the expected entry year of their ETS. However, at the end of 2019, Airbus decided to halt the program due to the undisclosed reasons [38]. Safran also collaborated with the German Aerospace Centre (DLR), University of Nottingham, and Adeneo to develop a direct drive for MLG on-board ETS, demonstrating operations in laboratory environments up to TLR 5 standards [21]. As this drive is at the focus of this thesis, it is thoroughly explained in dedicated Chapter 4. More recently, Safran became the topic leader in Clean Sky 2 initiative project ,, High-density energy storage module for an electric taxi" that started in 2018 and it is still ongoing [81].

2.1.3.4 Wheeltug

Wheeltug is a Gibraltar based company that first demonstrated the concept of on-board ETS in 2005 [82]. Wheeltug opted for NLG configuration, having two patented AC induction motors installed in each landing gear wheel [60]. The weight of the motors is 136 kg, whereas the whole system is just about 200 kg [79], [83]. The system is envisaged to be retrofitted to the existing aircraft with only landing gear and cockpit control modifications. Thus, being powered from the unmodified APU and due to the traction limitations of NLG, Wheeltug can achieve a maximum speed of only 9 knots (4.63 m/s). Additionally, due to the lower tractive effort, its possible operation in critical weather conditions such as snow, ice, and rain would be debatable.

Even though low taxiing speed can result in longer taxiing times, Wheeltug creators emphasise that most savings (both in time and money) come from more efficient gate operations than taxiing fuel savings. Therefore, Wheeltug is marketed as system which provides autonomous pushbacks and low-speed taxiing. According to Wheeltug, most taxiing patterns are indeed low-speed with stop-and-go patterns for which it can be used beneficially [79]. However, if there is a clear path to the runway and if high-speed taxiing is needed, the aircraft would taxi with main engines [83]. Therefore, one can argue that Wheeltug is more of an on-board EPS rather than ETS.



Figure 2.7 Wheeltug's demonstrator aircraft.

In terms of the gate, apron, and pushback operations, Wheeltug and EGTS offer similar advantages, which are attributes of all on-board ETS. However, in terms of block fuel utilisation and kinematic performances, the EGTS concept is advantageous. Nonetheless, Wheeltug has already more than 2000 orders even though it still awaits certification. The reason for this impressive and respectful number of logged orders might be due to the attractive power by hour lease arrangement, which reduces the financial risk that airlines have to take. Moreover, airlines can benefit from this agreement allowing for more efficient and flexible fleet utilisation planning. For example, airlines can only install Wheeltug at selected aircraft

that fly the routes with the most potential for cost savings. Finally, With the last test run in 2020 at Memphis airport, Wheeltug expects its entry date to be at the beginning of 2022 [84].

2.1.3.5 DLR

DLR and Lufthansa Technik joined forces in creating an interesting on-board NLG system for Airbus A320. The developed system has two motors integrated into the NLG wheels through a double stage planetary gearbox (1:12) [85]. PM brushless DC (BLDC), with a maximum torque output of 400 Nm, are used as TMs, resulting in almost 10 kNm torque at the road [86]. With maximum power from the fuel cells of 50 kW, the maximum speed that can be developed using this system is 13.5 knots [87]. The DLR ETS was tested in 2011 at Hamburg Finkerwerder airport on an Airbus A320 [88]. However, after that, the company has not updated the public about its future, and ten years after, it can only be assumed that DLR gave up on the electric taxiing idea.

The major disadvantage of the proposed system is also its main benefit - the fuel cells system. This demonstration showed that it is possible to have an AET system independent of APU power generation, reducing the taxiing fuel consumption only to the necessary APU's power for the ECS, lighting and similar. However, even though fuel cells are slowly gaining interest and market share in mobility applications such as Toyota Mirai or hydrogen-powered trains in the Netherlands, their safety and weight concerns are major bottlenecks for aerospace applications. Up to date, the most efficient way to store hydrogen is in high compressed metal tanks at 700 bars. For this to be achieved, tanks must be cumbersome, leading to a very low gravimetric density (m_{H_2}/m_{tank}) of only 5.5 wt%. [89] For example, for storing 5 kg of hydrogen, approximately a 100 kg tank must be used. Moreover, storing highly explosive gas at very high pressure require strict safety measures to be in place. On a more system-level, fuel cells require multiple other devices for a normal operation compared to a battery system. Compressors and pumps are needed to transfer hydrogen from the tank and pump water as waste to other storage tanks [33]. In addition, the response rate of fuel cells is slow, so it cannot cope with quick speed reference changes and acceleration demands. Therefore, a battery or supercapacitor should be installed to aid fuel cells during these tasks. Finally, a DC/DC converter is almost always present due to the fuel cells stack's low voltage, which was also the case in DLR's system where the voltage is boosted from 50 V to 300 V [86].

2.1.3.6 Summary of ET systems

In this section several ET systems developments up to date have been introduced. Some of the systems are already in service such as Mototok and Taxibot, whereas Wheeltug is in the process of certification. Other projects are halted or haven't updated public leading to assumptions those projects are stopped as well. The presented systems cover the spectrum of different configurations. They differ in terms of the application (either used only for pushback or also for taxiing), different maximum achievable speeds (low, medium or high), the source of energy (battery, APU, or fuel cells), location and type of the TM installation (MLG vs NLG and geared vs direct). The summary of these systems is given in Table 2.2 below.

Table 2.2 Summary of Et system developments up to date.

System	Type	Source	Speed	Status
Motok	External (pushback)	Battery	Low (<5 knots)	Operational
Taxibot	External	Diesel engine	High (< 23 knots)	Operational
Wheeltug	On-board; NLG; geared	APU	Low (<10 knots)	Certification
EGTS	On-board; NLG; geared	APU	High (<20 knots)	Halted
DLR	On-board; NLG; geared	Fuel cells	Medium (<13.5 knots)	Halted
Safran/ UoN	On-board; MLG; direct	APU	High (<20 knots)	Research

Comparison of different systems is given in section 2.1.4 below, whereas the future developments and potential road maps are discussed in section

2.1.4 Comparison of different system topology and their benefits

2.1.4.1 Differences between on on-board and external systems

One of the most significant downsides of the on-board systems is that they require changes to be made to the aircraft, and consequently, the certification procedure of those systems is more prolonged and more detailed. At the moment, only Wheeltug remained as a potential representative of the on-board ETS, and it is in the certification process since 2017 [90]. From the press releases, it can be observed that the entry date has been postponed many times, indicating potential difficulties during certification. On the other hand, external ETS certification is more straightforward, and they are already operational since 2017.

The second drawback is that on-board ETS increase the weight of the aircraft. Therefore, aircraft will almost certainly burn more fuel when airborne, so there is a possibility of offsetting the savings obtained on the ground while taxiing electrically. Many studies were conducted, and it has been demonstrated that total block fuel savings depend on the flight distance, total taxiing time and weight of the ETS system. In [63], the potential savings are calculated based on actual flight missions of US domestic carriers within national airspace (NAS) in 2007 with

A320/B737 families. The results presented in Figure 2.8 are for a baseline scenario that assumes 600 kg weight of ETS and moderate APU fuel flow, ESUT and ECDT. For example, for a flight with 30 minutes of taxiing and sector lengths of 1000 NM and 500 NM, 3% and 6% block fuel savings can be achieved respectively. The same study also showed that 78% of analysed flights would result in fuel savings. This number jumps to 99% for the optimistic scenario (ETS weight of 200 kg, low APU fuel burn, small ESUT and ECDT) and drops to only 47% for the pessimistic scenario of 1000 kg and high APU fuel burn. As an illustration, London Heathrow to Amsterdam Schiphol flight is just short of 200 NM, with 30 minutes taxiing time, as explained in 2.1.1. According to Figure 2.8, the potential fuel savings for this route could be high as 7.5%. Therefore, the on-board ETS are only beneficial for narrow-body aircraft that fly short-haul routes between airports with high taxiing times [77]. Additionally, the airlines would schedule aircraft equipped with on-board ETS only for specific flights in order to maximise the benefits, which would reduce the flexibility that airlines have when optimising fleet utilisation. However, with a power-by-hour lease agreement and retrofit option, which Wheeltug offers, airlines would not lose as much flexibility as if all aircraft would be equipped with on-board ETS. Finally, the mechanical shock during landing imposes a significant engineering challenge and so far, it hasn't been address in the literature. Even the EGTS and Wheeltug test drives for the public included only taxiing performance.

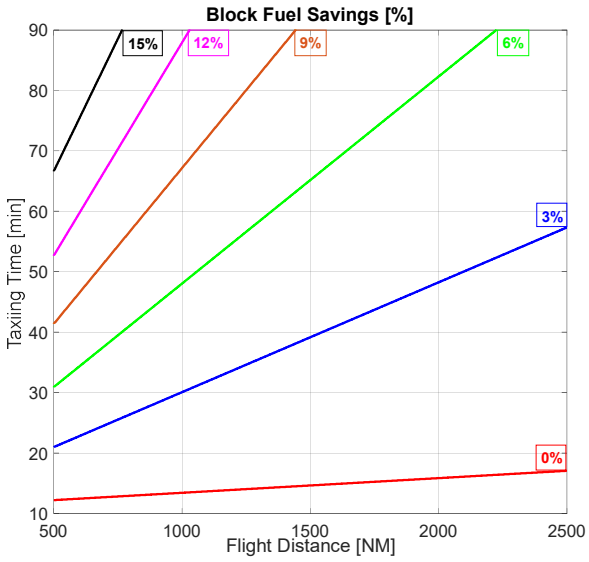


Figure 2.8 Block fuel savings versus flight distance and taxiing time, adapted from [63].

On the other hand, the on-board systems are advantageous when it comes to the autonomy of the aircraft. Namely, compared to the external systems, where the availability of

tractors causes increased waiting time at the gate, the on-board systems can perform pushback whenever the boarding is completed. Wheeltug compared in detail two pushback procedures, and the differences can be seen in Figure 2.9 [60]. Even though the picture is courtesy of Wheeltug, this applies to all on-board ETS.

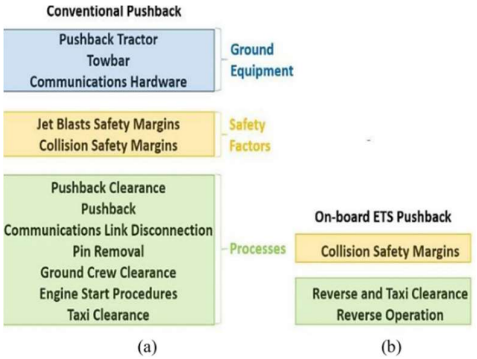


Figure 2.9 Differences between conventional and on-board ETS pushback [60].

Even though the external systems require little or no changes to the aircraft, significant changes must be made to the airport infrastructure. A feasibility study from Schiphol airport in 2020 showed that infrastructure is not yet ready for TaxiBot [91]. Extra roads must be built, and the existing infrastructure at Schiphol had to be modified as TaxiBots are wide for some manoeuvres. In order to reduce waiting time at the gate, a realistic number of tractors must be operational. Considering that TaxiBots are three times more costly than regular pushback tractors, their introduction will represent significant airport expenditure. Furthermore, ensuring that a tug is available to meet an aircraft a few minutes after it lands is operationally complex [92], thus making this procedure seamless for taxi-in, considering that the aircraft already has initial speed and that it needs a cool-down period for engines.

2.1.4.2 Differences between different on on-board systems (MLG vs NLG; geared vs direct)

As seen already, MLG systems offer higher taxiing speeds because 90% of aircraft weight is supported by MLG, resulting in higher available traction effort [93]. Furthermore, MLG can accommodate four motors in total. In this option, four motors would be providing the necessary high torque, easing the design requirements of TM. On the other hand, the implementation and fitting of electric motors inside MLG wheels is more complicated due to the presence of brakes and strict spatial requirements. In addition to the confined available space, brakes produce a lot of heat, especially during landing. Thus, special cooling considerations should be devoted in this case. Most narrow-body aircraft are equipped with

brake cooling fans (BCF) within MLG, so they can potentially be integrated with the cooling system of TM, making this a viable option that can be exploited in the future.

Due to high torque requirements, some ETS manufacturers prefer a geared system. In a geared system a motor is connected to the wheel of landing gear through a step-down gearbox. The gearbox reduces the speed applied to the wheel while increasing the applied torque to the road. Taxiing is a high torque low-speed application and therefore, the introduction of gearboxes can relax the design of the machine. However, at the same time, it introduces additional component count, which reduces the reliability on a system level due to potential jamming. On the other hand, the direct on-board ETS are connected directly to the wheel. This means that the motor will spin during the landing and take-off, so precautions must be taken, especially if the machine uses permanent magnets. The presence of magnets is also a problem of geared systems, so a clutch is used to disconnect the machine from landing gear during take-off and landing. The clutch installation is more manageable in a geared system, as seen with DLR ETS, where double stage gearbox acts as reduction mechanism and clutch, which allows wheel free rotation during take-off and landing. If the clutch is not used and the machine has PMs, a high voltage back emf will be generated, causing potential hazards and faults. One of the solutions is to keep the switches of the inverter open or short circuit them. In the first option, insulation must be designed to withstand high voltage levels. In contrast, the short-circuit will generate braking torque in the second option that must be assessed in detail along with the short-circuit current amplitude.

2.2 Electric Taxiing Aircraft Dynamics modelling

This subsection deals with theoretical modelling of aircraft dynamics during taxiing. As already mentioned in Chapter 1 and at the beginning of this chapter, the analysed kinematic parameters are integral parameters of the whole ETS model, and as such are investigated in more detail. Additionally, the developed kinematic model is used to explain the limitations of HET and to give more insight of various on-board ETS configurations.

Compared to slower Wheeltug NLG ETS., the on-board MLG ETSs are designed to develop relatively high traction torque values to meet kinematic requirements, such as maximum speed, maximum acceleration, and breakaway force at zero speed. As seen, defined prerequisites of EGTS are namely 1.) 20 knots speed in 90 s, 2) 10 knots speed in 20 s for active runway crossing and 3) breakaway torque at 1.5% slope at MTOW.

The aircraft's longitudinal kinematic performance is highly dependent on the taxiway's conditions. When an aircraft is taxiing, the required power at the wheel should match the road load resistances for desired kinematic profile. Therefore, it is essential to estimate road resistances for various aircraft before specifying power and energy, and torque requirements at the wheel. Thus, a mathematical model of aeroplane taxiing dynamics was developed, and it is presented in this section. A simplified two-dimensional longitudinal dynamics model can be used for the ET application, as shown in Figure 2.10. To achieve desired kinematic performance, the force provided to the wheels by the ET drive, i.e., traction force ($F_{traction}$), should overcome all resistive forces that act on the aircraft, which are namely:

- The road load, which is the sum of aerodynamic drag resistance (F_{aero}), grade resistance (F_{grade}) and rolling resistance (F_{rr}), as depicted in Figure 2.10.
- Inertial force (F_{in})

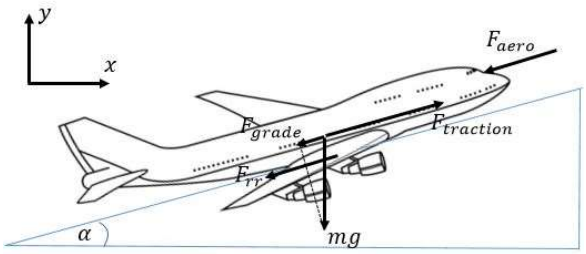


Figure 2.10 Resistive forces acting on the aircraft.

2.2.1 Aerodynamic drag resistance (F_{aero})

Aerodynamic drag occurs due to the flow of the air over the aircraft surface. Since only aircraft ground movement is considered, the lift induced drag is ignored and thus F_{aero} can be modelled as:

$$F_{aero} = 0.5\rho_{air}c_{d0}Av^2 \tag{2.4}$$

where ρ_{air} is the air density, c_{d0} is the zero-lift drag coefficient, A is the wing area, and v is the aircraft's velocity. For a more accurate estimate, it is convenient to breakdown the zero-lift drag coefficient, as in (2.5), accounting for structural variations introduced by landing gears, flaps, and slats:

$$c_{d0} = c_{d0,clean} + \Delta c_{d0,gear} + \Delta c_{d0,flaps} + \Delta c_{d0,slats} \tag{2.5}$$

where $\Delta c_{d0,gear}$, $\Delta c_{d0,flaps}$ and $\Delta c_{d0,slats}$ represent a drag coefficient's increase due to landing gears, flaps, and slats, respectively [94]. Exact values of c_{d0} are hardly ever explicitly given by aircraft manufacturers since they depend on many factors (e.g., Mach number, angle of attack

etc.), and besides, they are difficult to measure [95]. However, in [95] c_{d0} values have been estimated for some commercial jet aircrafts and different flight phases. For instance, estimated clean zero lift drag coefficient of Airbus A320 is 0.023, whereas taxiing zero lift is estimated to be 0.055 (with only gear effect considered), as shown in Table 2.3. Later it will be demonstrated that this force is an order of magnitude smaller than other resistive forces and that it can be neglected in most studies.

Table 2.3 Estimated zero lift drag coefficient during taxiing for different aircraft.

Aircraft Type	Aircraft name	$c_{d0,clean}$	$\Delta c_{d0,gear}$	$c_{d0,taxiing}$
A319	Airbus A319	0.020	0.031	0.051
A320	Airbus A320	0.023	0.032	0.055
A321	Airbus A321	0.033	0.037	0.070
B734	Boeing 737-400	0.021	0.034	0.055
B737	Boeing 737-700	0.024	0.029	0.053
B738	Boeing 737-800	0.021	0.032	0.053
B739	Boeing 737-900	0.024	0.034	0.058
E75L	Embraer E175	0.022	0.031	0.053
E190	Embraer E190	0.020	0.030	0.05
E195	Embraer E195	0.032	0.030	0.062

2.2.2 Grade resistance (F_{grade})

This gravitational resistive force occurs if the aircraft is taxiing on the taxiway with angle α and it is always directed downward. This force is given by:

$$F_{grade} = mg\,sin(\alpha) \tag{2.6}$$

where m is the mass of the aircraft and g the gravitational constant. According to the ICAO rules, the maximum allowable taxiway slope is 1.5% [46], which is equivalent to the maximum slope angle of 0.86° or 0.015 rad. Therefore, $sin(\alpha)$ can be approximated as $tan(\alpha)$ and hence grade resistance can be written in more usable form as:

$$F_{grade} \approx mg\,tan(\alpha) = mg\,i_{\%}/100 \tag{2.7}$$

where $i_{\%}$ is the taxiway slope in percentage.

2.2.3 Rolling resistance (F_{rr})

Rolling resistance force (also called rolling friction) is a force required to overcome the friction between a tyre and road. It can be calculated using (2.8) where c_{rr} is the rolling resistance coefficient (considering $cos(\alpha) \approx 1$ for small slope angles).

$$F_{rr} = c_{rr} mg\,cos(\alpha) \approx c_{rr} mg \tag{2.8}$$

Rolling resistance coefficient depends on many factors such as taxiway and weather conditions (dry, wet or ice), the tyre's inflation pressure, and similar [96]. In the literature,

numerous values have been used, c_{rr} normally ranging between 0.009 and 0.015 for normal operating conditions [97], [85], but even using as high value as 0.2 [76]. Another aspect to be considered is static rolling friction. As for most types of friction forces, c_{rr} coefficient also has a static value that is higher than the aforesaid dynamic values, and it is associated with the static rolling resistance force. This force must be overcome to move the aircraft from the standstill. Hence it is called breakaway rolling resistance force, with associated breakaway rolling resistance coefficient c_{br} which ranges between 0.015 and 0.022 [78], [98].

In order to model the transition between the breakaway and continuous rolling resistance coefficient, several speed models are considered. For example, in [98], c_{rr} is modelled as:

$$c_{rr} = c_{rr,0} + \Delta c_{br}\left(1 - \frac{v}{v^*}\right), v < v^* \tag{2.9}$$

$$c_{rr} = c_{rr,0}, v > v^* \tag{2.10}$$

where incremental breakaway part $\Delta c_{br}\left(1 - \frac{v}{v^*}\right)$ linearly reduces with the speed increase. After certain speed v^* the c_{rr} equals to its dynamic value $c_{rr,0}$. On the other hand, in [31], the exponential model is used:

$$c_{rr} = c_{rr,0} + \frac{c_{br} - c_{rr,0}}{1 + e^{m_r|\omega| - a_r}} \tag{2.11}$$

where m_r and a_r are tunable parameters. Finally, in some studies, the value of Δc_{br} (and consequently c_{br}) depends on the time that aircraft spends at a standstill [31], [94]. In [31], the following model was used

$$c_{br} = c_{br,min} + \frac{c_{br,max} - c_{br,min}}{1 + e^{m_b(-t^{p_b} + a_b)}} \tag{2.12}$$

with five degrees of freedom ($c_{br,min}$, $c_{br,max}$, m_b, p_b and a_b) to shape the characteristic S-curve.

2.2.4 Inertial force

The sum of the aforementioned three resistive forces is called road load, as they represent resistances coming from the road. However, to achieve a certain demanded acceleration, traction force should also overcome the inertial force $m_i \frac{dv}{dt}$, where m_i is the aircraft's inertial mass, which includes the inertia of rotating parts such as wheels and electric motors, and it is described by:

$$m_i = m + \frac{n_{NLG} J_{w,NLG}}{r_{NLG}^2} + \frac{n_{MLG} J_{w,MLG}}{r_{MLG}^2} + \frac{n_m J_m i_g^2}{r_i^2} = km \tag{2.13}$$

In (2.13) $n_{NLG}, J_{w,NLG}, r_{NLG}, n_{MLG}, J_{w,MLG}$ and r_{MLG} are number of landing gear wheels, wheel inertia and tyre radius of NLG and MLG, respectively. Number of the installed in-wheel motors is n_m, motor inertia J_m, gearbox ratio i_g, k is the inertial coefficient, and r_i is the tyre radius of LG in which the motor is installed.

On the other hand, in applications where rotational and translational motion are coupled, such as traction application, it is not uncommon to describe the dynamics in terms of rotation by reflecting translational mass and forces to the rotating shaft [99]. In this case, the equation of motion becomes:

$$J_{eq}\frac{d\omega}{dt} = T_m - T_{res} \tag{2.14}$$

where J_{eq} and T_{res} are the equivalent moment of inertia and torque calculated as:

$$J_{eq} = J_m + J_{wheel} + \frac{mr_i^2}{n_m} \tag{2.15}$$

$$T_{res} = \frac{r_i F_{res}}{n_m} \tag{2.16}$$

The typical expected accelerations can be calculated from the desired kinematic performance using simple formulas:

$$v = at \tag{2.17}$$

$$s = \frac{at^2}{2} \tag{2.18}$$

For example, considering EGTS's requirements maximum expected average acceleration is 0.26 $\mathrm{m/s^2}$ during active runway crossing (10 knots over 20 s). In [87], [100], [101], active runway crossing is also selected as an event with the highest acceleration. In those studies, it is required for aircraft to cross the width of runway (230 m according to the Canadian aviation authority) in 45 s. This corresponds to an acceleration of 0.23 $\mathrm{m/s^2}$. However, in those studies, the length of aircraft is not considered. For the longest single-aisle aircraft, i.e., A321, that acceleration rises to 0.27 $\mathrm{m/s^2}$ which is similar to 0.26 $\mathrm{m/s^2}$ of EGTS. Therefore, kinematic design requirement of EGTS can be adopted as a standard.

2.2.5 Analysis of the resistive forces and total traction force

Taking into account the resistive forces acting on the aircraft during taxiing, the total needed force at the wheels can be calculated using (2.19):

$$F_{traction} = m_i\frac{dv}{dt} + F_{rr} + F_{grade} + F_{aero} \tag{2.19}$$

In this subsection, traction force and resistances will be analysed for different parameters and various aircraft types. In Table 2.4, the minimum and maximum values of the resistance forces' parameters are summarised. In order to analyse the magnitude of each force, a Boeing 737-400 and Airbus A321ceo with MTOW of 68 t and 93.5 t are selected, and the breakdown of forces is shown in Figure 2.11.

Table 2.4 Range of electric taxiing kinematic parameters.

Parameter	Value
c_{rr}	0.009 - 0.015
c_{br}	0.015 - 0.022
i [%]	0 - 1.5
v [$knots$]	0 - 20
a [$\frac{m}{s^2}$]	0 - 0.26
k	1.01

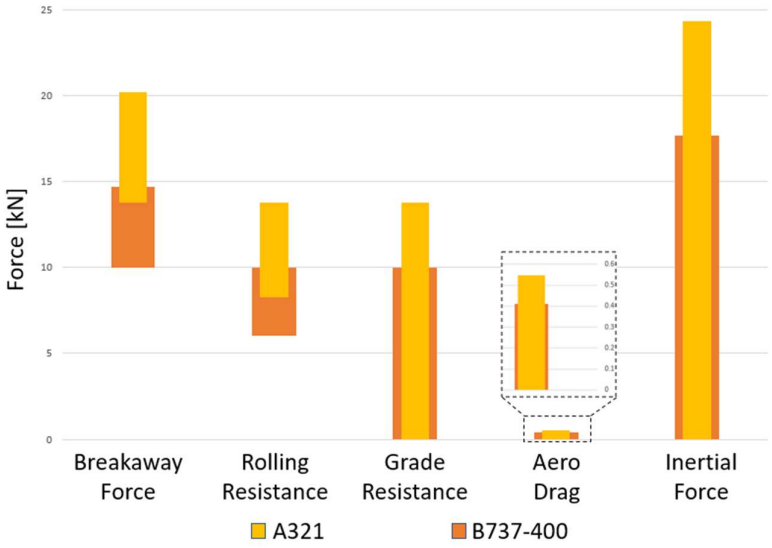


Figure 2.11 The load forces range of a Boeing 737-400 ($c_{do} = 0.055, m = 68\ t$ and $A = 105.4\ m^2$) and Airbus A321ceo ($c_{do} = 0.07, m = 93.5\ t$ and $A = 122.4\ m^2$) during electric taxiing.

It can be seen that aerodynamic drag is contributing the least to the total resistive force, and in most of the studies, this force had been neglected [93]. It is important to notice that rolling resistance is always present, in contrast to grade and inertial forces that are existent only if the taxiway is sloped or if the aircraft is accelerating/decelerating. Finally, breakaway rolling resistance is present only during standstill, and once it is overcome, it subsides in favour of dynamic rolling resistance.

Figure 2.11 provides information about the traction for only two aircraft type and their mass. In order to analyse traction sensitivity on MTOW, current data display in form of bars is

not acceptable. Even though it seems many parameters can be varied, equation (2.19) can be rewritten more insightfully (considering $F_{aero} = 0$ and $g \approx 10\ m/s^2$)

$$F_{traction} = mg\left(\frac{a}{g} + c_{rr} + \frac{i_{\%}}{100}\right) = mg\left(\frac{10a}{10g} + \frac{c_{rr,\%}}{100} + \frac{i_{\%}}{100}\right)$$
$$\approx mg\left(\frac{10a}{100} + \frac{c_{rr,\%}}{100} + \frac{i_{\%}}{100}\right) = mgi_{eq,\%} \tag{2.20}$$

where $i_{eq,\%}$ is the equivalent slope, and it is calculated as:

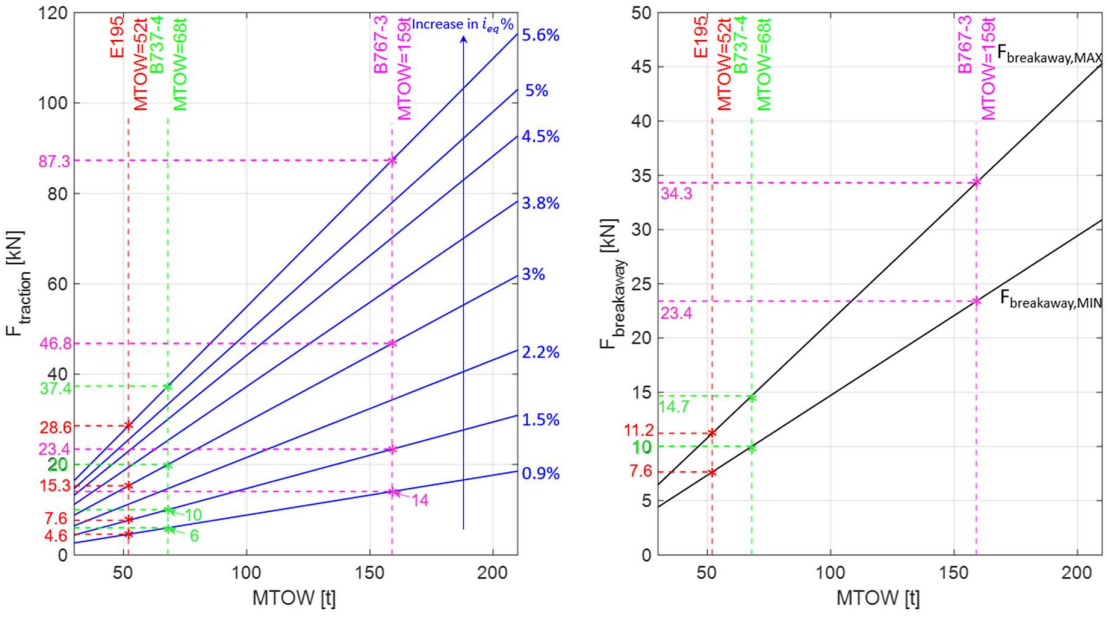
$$i_{eq,\%} = \frac{10a}{100} + \frac{c_{rr,\%}}{100} + \frac{i_{\%}}{100} \tag{2.21}$$

Thus, acceleration of $1\ \mathrm{m/s^2}$ can be considered as the equivalent of adding a slope of 10%. In Table 2.5 the introduced error for expected acceleration range is calculated. With low accelerations during taxiing, the errors are practically negligible.

Table 2.5 Introduced acceleration error using equivalent slope approach.

$a[m/s^2]$	0.1	0.15	0.2	0.26
$i_{real,\%}$	1.02	1.53	2.04	2.65
$i_{eq,\%}$	1	1.5	2	2.6

As previously explained, the maximum expected acceleration during electric taxiing is $0.26\ \mathrm{m/s^2}$ which is, therefore, equivalent of taxiing on a 2.6% slope. Hence, the traction force against mass variation will be considered only with different equivalent slopes, as shown in Figure 2.12. The minimum $i_{eq,\%}$ value occurs with the lowest rolling resistance coefficient on a dry level taxiway and no acceleration ($c_{rr} = 0.9\%, i_{\%} = 0; a = 0$) compared to the worst-case scenario of 5.6% ($c_{rr} = 1.5\%, i_{\%} = 1.5\%, a = 2.6\%$).



(a) (b)

Figure 2.12 (a) The $F_{traction}$ against aircraft mass for $i_{eq,\%} \in (0.9\% - 5.6\%)$ (b) The maximum and minimum breakaway force.

With the aim of explaining the mass sensitivity in more detail, two narrow-body (single aisle) and one wide-body (double aisle) aircraft are taken as a point of reference. The two most representative aircraft from Boeing are selected, B737-400 (147 passengers) and B767-300 (261 passengers) and the most representative regional jet, Embraer E195 (117 passengers). Both traction forces and breakaway rolling resistances are shown in Figure 2.12 for selected equivalent slopes and breakaway coefficients. It is evident that forces are very sensitive to the weight, meaning that requirements of wide body aircraft are more demanding. Moreover, during analysis, difference in weight during taxi-out and taxi-in should be considered, due to the burnt fuel during airborne phase. During taxi-in planes are lighter hence naturally taxi-out requirements with MTOW are more stringent.

In case of the on-board ETS torque is important parameter, so traction and breakaway torque are also shown in Table 2.6 for both MLG and NLG configuration. Traction force is computed assuming 1.5% rolling resistance coefficient. Due to different radii values of landing gears [102], torque requirements differ for MLG and NLG configuration. Since MLG radius is bigger, torque requirements are higher, and thus more difficult to achieve in case of MLG configuration. For instance, almost 13 kNm is needed for breakaway of B737-4 on a 1.5% slope, which indicates that each MLG should provide at least 6.5 kNm. In case of direct drive on-board ETS with one TM per MLG, an electric machine would have to able to provide this torque alone without any assistance from gear box, which represents a challenging design requirement. However, installation of the on-board MLG systems has multiple advantages compared to the NLG ones as seen in section 2.1.4.2.

Table 2.6 Torque requirements for narrow- and wide-body aircraft considering MLG and NLG configurations and different grades.

Aircraft model	**Embraer E195 (narrow-body; regional jet)**			
MTOW [t]	52			
Grade [%]	0		1.5	
On-board ETS	NLG	MLG	NLG	MLG
Diameter [m]	0.61	1.04	0.61	1.04
$F_{breakaway}$ **[kN]**	11.28	11.28	18.97	18.97
$F_{traction}$ **[kN]**	7.69	7.69	15.38	15.38
$T_{breakaway}$ **[kNm]**	**3.44**	**5.88**	**5.78**	**9.89**
$T_{traction}$ **[kNm]**	**2.34**	**4**	**4.68**	**8**

Aircraft model	**Boeing 737-400 (narrow-body; short haul)**
MTOW [t]	68

Grade [%]	0		1.5	
On-board ETS	NLG	MLG	NLG	MLG
Diameter [m]	0.69	1.02	0.69	1.02
$F_{breakaway}$ [kN]	14.68	14.68	24.69	24.69
$F_{traction}$ [kN]	10.00	10.00	20.01	20.01
$T_{breakaway}$ [kNm]	**5.04**	**7.45**	**8.47**	**12.54**
$T_{traction}$ [kNm]	**3.43**	**5.09**	**6.86**	**10.18**

Aircraft model	Boeing 767-300 (wide body; long haul)			
MTOW [t]	159			
Grade [%]	0		1.5	
On-board ETS	NLG	MLG	NLG	MLG
Diameter [m]	0.94	1.17	0.94	1.17
$F_{breakaway}$ [kN]	34.31	34.31	57.71	57.71
$F_{traction}$ [kN]	23.4	23.4	46.8	46.8
$T_{breakaway}$ [kNm]	**16.12**	**20.03**	**27.12**	**33.7**
$T_{traction}$ [kNm]	**11**	**13.66**	**22**	**27.32**

2.2.6 Power and Energy at the wheel

Once kinematic requirements of the ET are defined, required power can be calculated using (2.22) where t is the taxiing time.

$$P_{traction}(t) = F_{traction}(t)v(t) \tag{2.22}$$

Using equation (2.21), $P_{traction}(t)$ can be expressed as function of aircraft mass, equivalent slope, and aircraft velocity:

$$P_{traction}(t) = mgi_{eq,\%}v(t) = f(m, i_{eq,\%}, v) \tag{2.23}$$

By keeping speed constant, $P_{traction}$ becomes function of two variables $f(m, i_{eq,\%})$, and thus it can conveniently be illustrated and analysed via contour plots. Thus, in Figure 2.13 - Figure 2.16 the required power is presented as contour plot for four different constant speeds ($v = 5, v = 10, v = 15$ and $v = 20\ knots$). Each figure corresponds to different aircraft family which are grouped by the same APU S/G rating. Equivalent slope does not depend on the family and its range is kept the same for each case study (0.9%-5.6%). Ratings of APU's electric generator for each family are given in Table 2.7, and for the convenience they are also presented in Figure 2.13 - Figure 2.16 with two bolded black curves (normal and overload rating). The generator of A320 and B737 (90 kVA rated) is allowed to operate in overload condition with 120 kV (133% load) for 30 s. Due to the scarce of data for other APU's, it is assumed that they can also operate with 133% load for 30 s. B737 and A320 families include B737 classic (B737-400, B737-500, B737-600), B737 new generation (B737-700, B737-800, B737-900), B737 MAX (MAX7, MAX8, MAX9, MAX10), Airbus A320ceo (A318ceo, A139ceo, A320ceo,

A320ceo, A321ceo) and Airbus A320neo (A319neo, A320neo, A321neo). The lightest of them is B737-5 with only 60.5 t MTOW, and the heaviest A321neo with MTOW of 97 t. Both neo and MAX generations use same APU as their ceo and classic and new generation counterparts with various improvements. To the best of authors knowledge, the rating of generator also remained the same, so they are all included in the same category. Similarly, is with the Embraer's E jet family which uses the Pratt & Whitney APS2300 APU with 40 kVA generator rating [103]. The updated version used for E2 Jet family, the APS2600 APU, is derived from an old one so it is assumed that electrical generation is the same [104].

Table 2.7 The rating of APU S/G for different aircraft families [94], [103], [104].

Aircraft Family (min; max)	S/G [kVA(kVA/s)]	MTOW [t]	(S/G Rating)/MTOW [kVA/t]
Embraer E and E2 Jet (E170; E2-195)	1 x 40(53.5/30)	38.6-62.5	0.64-1.04
Boeing 737 and Airbus A320 (B737-5; A321neo)	1x 90(120/30)	60.6 -93.5	0.96-1.48
Boeing 767 (B767-3; B767-4ER)	1x 90(120/30)	142.9-204.1	0.44-0.63
Boeing 777 (B777-2; B777-3ER)	1x 120(160/30)	247.2-351.5	0.34-0.49
Boeing 787 (B787-9; B787-10)	2x 225(300/30)	227.9-254	1.97-2.19

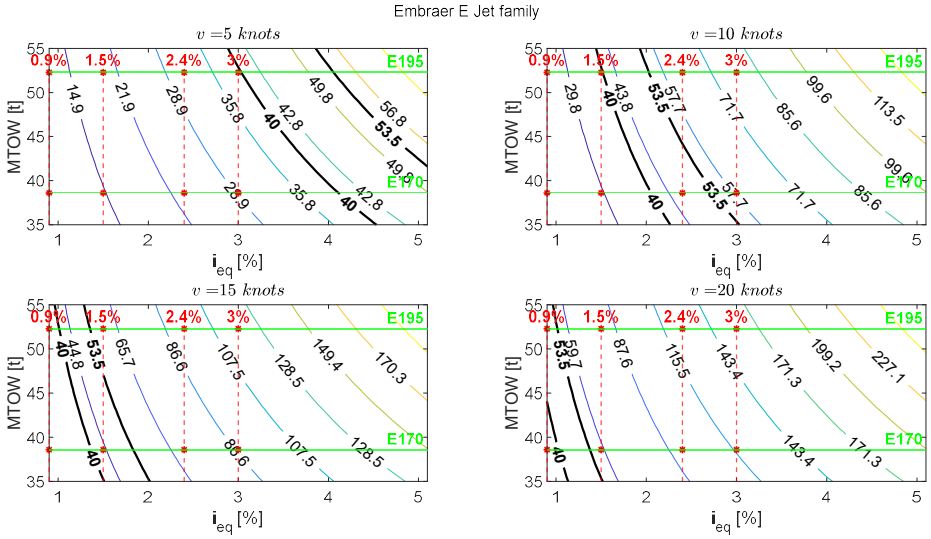


Figure 2.13 Power requirements at the wheel for Embraer E Jet family for four different speeds.

In Figure 2.13, the power requirements at the wheel for Embraer E Jet family are shown. As expected, it is evident that the power requirements become more stringent when speed increases. At 5 knots both E175 and E195 can sustain high equivalent grade (i.e., loads). However, at 20 knots E175 can sustain only 0.9% which is enough to overcome rolling friction with the lowest coefficient value. At this speed it is highly unlikely to request accelerations but if slope of 1.5% is encountered the drive wouldn't be able to cope as it would operate about its

53.5 kVA overload threshold. On the other hand, E195 would operate in overload regime even with 0.9% of equivalent slope.

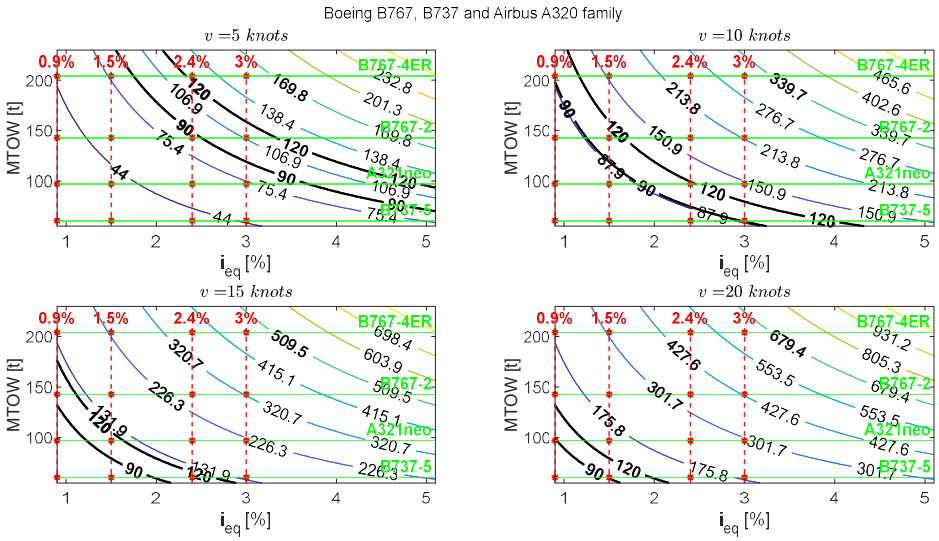


Figure 2.14 Power requirements at the wheel for Boeing B737, B767 and Airbus A320 families for four different speeds.

Power requirements at the wheel for Boeing B737, B767 and Airbus A320 families are shown in Figure 2.14. They all have the same APU rating, but B767 family is heavier spanning range of 140 t to 205 t compared to its short haul counterpart of 60 t to 93.5 t (or 95). It is evident that APU S/G of the heaviest B767-400ER would operate at the limit for 2.4% equivalent slope for speed of 5 knots and in overload for 3% road load. Therefore, the margins for acceleration, which are highly likely to occur at 5 knots, are practically non-existent. As the speed increases, even the smallest B767-200 wouldn't be able to maintain speed of 15 knots at lowest 0.9% load, without exceeding the power rating. Therefore, for this APU rating, B767 family is not suitable for HET due to very small kVA/t ratio.

Conversely, the short-haul A320 and B737 families show better compliance with the 90 kVA generator. For example, at 5 knots both B737-5 and A321neo can sustain 3% slope (1.5% rolling and 1.5% grade), having enough margin for acceleration (B737-5 2.6% and A321 0.9%). Expectedly, as the speed increases those margins reduce. For example, at 15 knots, the maximum equivalent slope that can be sustained is around 1.8% for A321 and 2.8% for B737-5. However, at 20 knots, an A321 can maintain continuously only 0.9% equivalent slope load with the 0.4% margin, whereas a B737-5 can sustain load of 1.5% with 0.5% margin for grade (as acceleration is unlikely at this speed). Therefore, even the lightest aircraft wouldn't be able to sustain maximum load without acceleration of 3%.

Nonetheless, compared to long haul and regional jet, this family showed so far, the best compliancy with the installed APU, namely for aircraft with lower MTOW, i.e., older generations aircraft such as Boeing 737 classic. As it is expected that Boeing 737 MAX and Airbus A320neo become dominant type in the future with lightest in each category being A139neo of 75.5 t and B737 MAX 7 with 80 t, it is evident that ETs would reach its limitations at lower speeds, compromising advantage of MLG on-board systems which are advertised as high-speed taxiing. If the APU is not upgraded, or additional energy storage device installed, the ETS performance could be reduced, such as not achieving 20 knots, or reducing maximum allowed acceleration which due to active runway crossing remains unlikely. Alternatively, significant reductions of MTOW can be achieved using innovative composite materials as mentioned in Chapter 1.

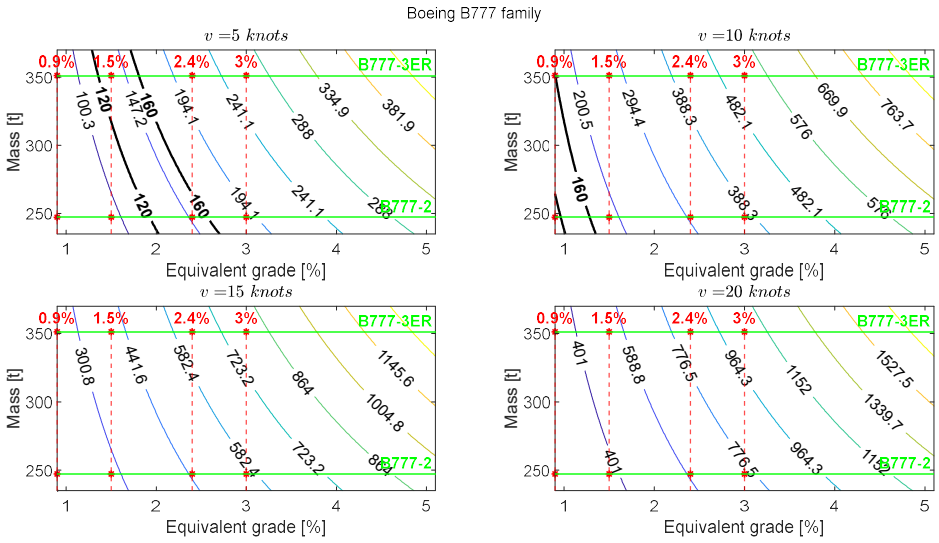


Figure 2.15 Power requirements at the wheel for Boeing B777 family for four different speeds.

In Figure 2.15 the requirements of the heaviest B777 family are presented. Although their APU S/G rating is higher, it is not sufficient for electric taxiing. Already at 10 knots the power would not be sufficient to overcome minimum rolling resistance. This is due to the fact of very low kVA/t ratio of only 0.34-0.49.

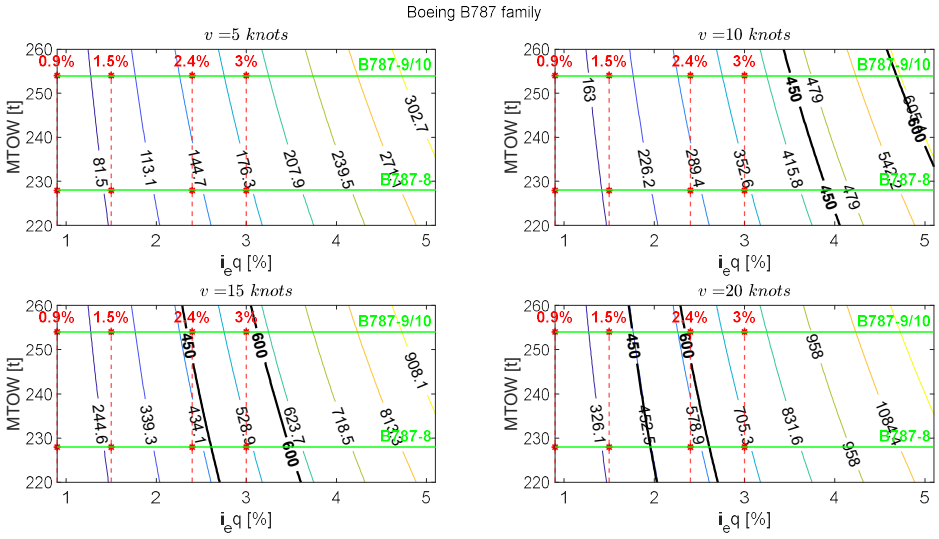


Figure 2.16 Power requirements at the wheel for Boeing B787 family for four different speeds.

Finally, in Figure 2.16 the requirements of B787 Dreamliner family with two 225kVA generators is shown. Due to very high power rating and lower MTOW, the starter/generator would be able to sustain cruising at 1.5% at any speed plus to have enough margin for acceleration at low speed and enough margin for slope at high speeds. However, as B787 Dreamliner family is the aircraft that use most electricity, the APU S/G electrical power wouldn't be used only for taxiing. There should be enough power for ECS and bleedless start of the main engines. Even though, engine start can be performed when aircraft is at still (i.e., no power required for ET), the ECS requires significant amount of which would further reduce the ETS capability. Nonetheless, this example showed that kVA/t rating of 1.97 would result in satisfying electric taxiing operations. Considering that 1.48 kVA/t of Boeing 737-4 is close to meet the requirements, the aimed kVA/t ratio should not be less than 2 kVA/t.

This analysis showed that HET, i.e., ETS powered solely from APU S/G, would struggle to meet the required demands for most of the aircraft families with different MTOW and APU S/G rating, as mentioned in 2.1.3.4. The heavy wide bodies, such as B777 and B767, showed the least flexibility due to unproportionally low APU rating compared to their weight. Contrary, the B787 with high APU power rating and lower MTOW would be a suitable candidate if the APU S/G power was used for taxiing only, which would not be the case. In terms of short haul aircraft, the most promising are A320 and B737 families. The APU generator can sustain cruising at any speed for 0.9% equivalent slope, but the margins might not be satisfying especially at high speed. This problem can be rectified by either one or combination of following things:

- installing small energy storage device that would provide necessary power boost when necessary, i.e., upgrading to HET+ systems.
- upgrading the APU S/G rating.
- reducing the expected ET kinematic performance.
- using lightweight materials such as composites which can result in a lower MTOW and more favourable kVA/t ratio, same as in B787 family.

Finally, the regional jets, even though the lightest of all, show less satisfying performance than A320 and B737 due to highly lower rating APU of only 40 kVA.

2.3 Future trends, recommendations, and conclusions

Regarding external ETS, many obstacles must be resolved before their broad adoption, mainly improving airport infrastructure, in addition to airports and airlines reaching the comprehensive agreement regarding the ownership. As an improvement from a hybrid system TaxiBot, the next development phase should see AET tractors. Also, future trends involve completely autonomous tractor which is being investigated by NASA in a project called SafeTug [105].

Concerning the drive unit of on-board systems, many studies focused on electric motors. The preferred TM's topology in all developed systems was the radial flux machine. However, in [106], the adoption of axial flux machines for an on-board geared MLG ETS with four motors was explored. Other studies focused on the clutch problem and researched conical motors. Conical motors have two degrees of freedom and can also move in the axial direction of the machine. This axial movement can detach TM from the wheel during landing and take-off, acting practically as a clutch system. One of these motors was investigated in particular for ET applications in studies [107]–[109]. Despite the fact that TM represents only one part of the system, albeit very important, the research of other parts was neglected. For example, TM weight is only 25% of the total EGTS system weight. This fact shows that even though most efforts to create high torque and power dense TM, the rest of the system accounts for majority of the weight such as power electronics, cooling, cabling etc.

When it comes to propulsion techniques, electric propulsion, more precise AEA, will eliminate the need for ETS as the generated thrust will come from a carbon-free source. However, it is uncertain if the all-electric narrow-body aircraft with more than 100 seats will be developed by 2050. The expected future development trend of the ETS is shown in Figure 2.17. At the moment, taxiing is performed using main engines with operational measures in

place to reduce its environmental impact. As a next step, the industry will likely see the introduction of HET systems that can be retrofitted to the existing aircraft without modifying the APU generator, similar as Wheeltug. Therefore, they will be used for low-speed ET (up to 10 knots) and autonomous pushback, whereas high-speed taxiing will be performed with jet engines. The gap of low traction performance can be bridged by introducing an energy storage system that will assist APU, practically enhancing it to HET+ system. This development is already in the research phase in CleanSky 2 project that was mentioned in section 2.1.3.3. Besides allowing higher cruising speeds and acceleration demands, the LESS will also absorb energy during taxiing stop-and-go patterns. HET+ has a similar mode of operation as in a series hybrid electric vehicle, where energy storage and fuel powered APU work in combination to provide the best possible efficient operation. Alternatively, high-speed ET can be achieved with APU generator modification, which remains unlikely. The most recent addition from Airbus and Boeing, A320neo and 737MAX families, utilise the same APU as their predecessors. Therefore, the APU upgrade will probably be in the next development phase of new short-haul aircraft. It is expected that how battery technology advances that LESS' rating will increase and further reduce the dependency on APU. Finally, by 2050 it is envisaged that ETS will entirely be powered from batteries and that MEA technology will also apply to narrow-body aircraft and not only to widebodies such as B787 and A350. Therefore, the APU improvements shouldn't be aligned with ET requirements, but instead with the need to power without emissions more electric systems in new narrow-body aircraft.

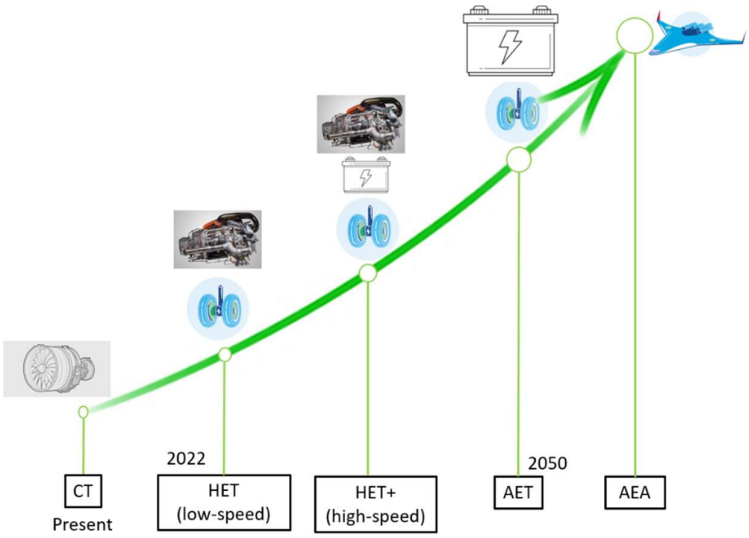


Figure 2.17 Expected future development of on-board ETS.

Unquestionably, ET brings more benefits than disadvantages. However, the main problem in its implementation is in the lack of coordination and talks between authority bodies,

airlines, and airports. In order to see further progress, an agreement must be reached. When it comes to the on-board systems, their successful implementation will depend on many factors such as airlines fleet type, airport operations, type of the on-board system and most important, regulations. At this point, Wheeltug's system seems like the most logical option that airlines would opt for. It is retrofittable, leased on a power-by-hour basis, can perform electric pushback and low-speed electric taxi if needed. If high-speed taxiing is needed or if taxiing time is less than ESUT, main engines will be used. Taking these into account, Wheeltug appears to be an essential addition to the operations of short-haul flights, which face aggressive competition from trains aided by national governments. Therefore, Wheeltug in the nearest future can act as a transition system to high-speed ET. Hopefully, with the introduction of Wheeltug in 2022, more things will be clear, and ET will gain much-needed momentum.

3 Chapter: Battery Literature Review and Modelling

In this chapter, battery chemistries that are often used in electric vehicle industry are presented. Historically, lead-acid and nickel-based batteries were used initially in the automotive sector. However due to their superior energy and power densities, lithium-ion batteries are almost exclusively used nowadays for electric traction, and naturally emphasis is put on them in the forthcoming discussion. Second part of this chapter deals with battery modelling. Three possible approaches are presented, each of them having benefits and drawbacks. More focus is given to the equivalent circuit models as they appear the most suitable for system-level simulations of this project.

3.1 Literature Review

3.1.1 Terminology

Batteries are electrochemical devices that convert electrical energy into potential chemical energy during charging and convert chemical energy into electrical energy during discharging [110]. It is essential to distinguish the difference between the terms electrochemical cell and battery. A cell is the basic electrochemical unit, whereas a battery comprises multiple cells electrically connected in series and/or parallel stacked together to form an integrated pack. Therefore, it can be anticipated that the behaviour of the individual cell and battery pack will differ in certain aspects, for instance, in thermal management. Moreover, batteries in most applications require a battery management system (BMS) and cannot be operated without it. Cells/batteries that can only be discharged are called primary cells/batteries while the rechargeable cells/batteries are called secondary cells/batteries.

The primary chemical process that occurs during energy conversion is called the reduction-oxidation (redox) reaction. Redox reaction is a type of reaction in which the electrons are exchanged between species/materials. Oxidation is a reaction in which electrons are lost, and it is said that specie has been oxidised. Contrary, electrons are gained/accepted in the reduction reaction, and it is said that specie has been reduced. Substances that have the ability to oxidize other substances (cause them to lose electrons) are known as oxidizing agents, oxidants, or oxidizers. Substances that have the ability to reduce other substances (cause them to gain electrons) are said to be reductive or reducing and are known as reducing agents, reductants, or reducers. There are two types of electrochemical cells, namely: galvanic and electrolytic cells. In a galvanic cell, the redox reactions occur spontaneously, whilst reactions in an electrolytic cell are driven by an external energy source (usually applied voltage or current).

Therefore, secondary batteries behave as galvanic cells when discharged and electrolytic cells when charged [111]. Each half-reaction happens at the positive and negative electrodes. A path for electrons to move between electrodes must be provided to have a sustainable reaction, and externally connected electrodes do that. More about the discharge and charge process will be explained in the following chapters.

The most important parts of the cell are:

- Electrodes (positive and negative)
- Electrolyte
- Separator
- Current collector

Electrodes are made of metal. The positive electrode always has a higher potential than the negative electrode. Usually, negative electrodes are pure metals or metal alloys while positive electrode is generally in the form of metal oxide, sulphide or oxygen [112]. Many authors equate the terms cathode and anode with positive and negative electrodes respectively. However, this is not entirely true. A cathode is an electrode at which reduction occurs, and an anode is an electrode at which oxidation happens. Since during charge and discharge reactions are reversed, the positive electrode is cathode during discharge and anode during the charging process. Therefore, by using the terms cathode and anode, we cannot be sure about the electrode's polarity, and hence those terms will not be used.

An electrolyte is used to provide ion transportation, i.e., it behaves as an ionic conductor. The electrolyte usually comprises a solvent containing dissolved chemicals (the solute). Usually, the solvent is water, and solvate can be acid, salt or base [113]. The role of the separator is to isolate electrodes electrically and to prevent their short-circuiting. Although it is an isolator, it allows the movement of ions through it.

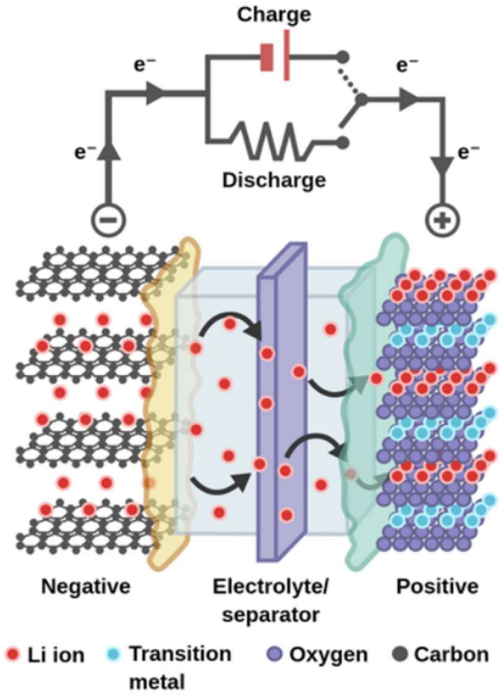


Figure 3.1 Schematic configuration of lithium-ion in discharge mode [114].

An illustration of the cell's parts mentioned above in the discharge mode can be seen in Figure 3.1. Electrons flow from the negative to positive electrode via external circuit, where they are combined with positive ions that flow through the electrolyte. In general, each electrode generates a potential and in electrochemistry it is common to refer that potential to standard hydrogen electrode (SHE). In equilibrium, i.e., when no current is applied, a potential difference between electrodes can be measured and it is called open-circuit voltage (OCV) or no-load voltage. No-load battery terminal voltage is not always constant. It is dependent on the amount of stored charge in it, in other words, on the state of charge (SoC) or depth of discharge (DoD). When a battery is under load conditions, being discharged, the actual battery voltage will differ from the theoretical OCV due to the loss in ohmic resistance, diffusion process (mass transport) and the loss in electrochemical reaction (activation losses) (Figure 3.2). The theoretical explanation of mass transport and activation losses is out of the scope of this thesis. However, in section 3.2.1, the vital electrochemical processes are mentioned from the battery physical modelling standpoint.

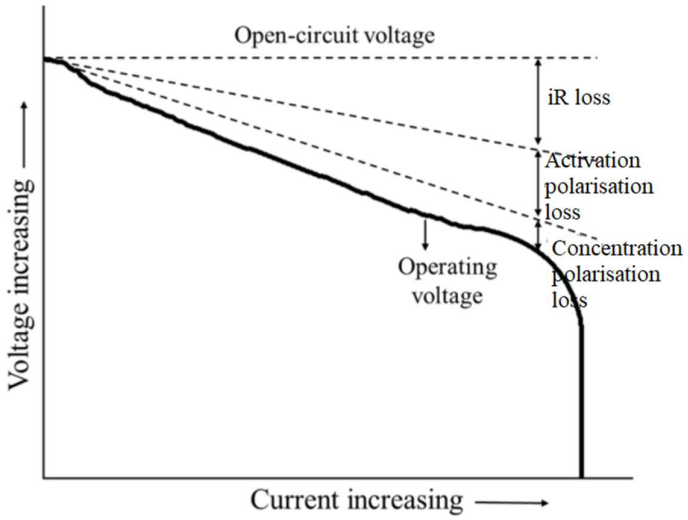


Figure 3.2 Difference between OCV and cell terminal for different current rates [115].

3.1.2 Lithium-ion batteries

As NiMH batteries, Li-ion batteries work on the principle of solid-state reaction mechanisms. The mechanism in Li-ion batteries is insertion reaction or in other words, intercalation (xA+BX=AxBX). This means that lithium ions are removed or inserted into the host without a significant change to the host [116].

Positive electrode materials are generally prepared in the lithiated state to be paired with negative electrode in de-lithiated state, so when the two electrodes are combined for the first time the cell is fully discharged [112]. Thus, during charge, positive electrode material is oxidized since lithium atom diffuses towards surface of active material in the processes of de-intercalation, where it loses electron and becomes lithium ion, Li^+ (Figure 3.3). Li^+ further diffuses through electrolyte and separator reaching negative electrode. At the same time, through conductive binder, electrons reach current collector and via external circuit are brought to negative electrode where they meet again with Li^+ creating lithium atom. Lithium atom diffuses from the surface of negative electrode active material towards its centre in the processes of intercalation. Thus, names rocking chair, shuttlecock and sponge process are equally used to describe the operation of Li-ion batteries.

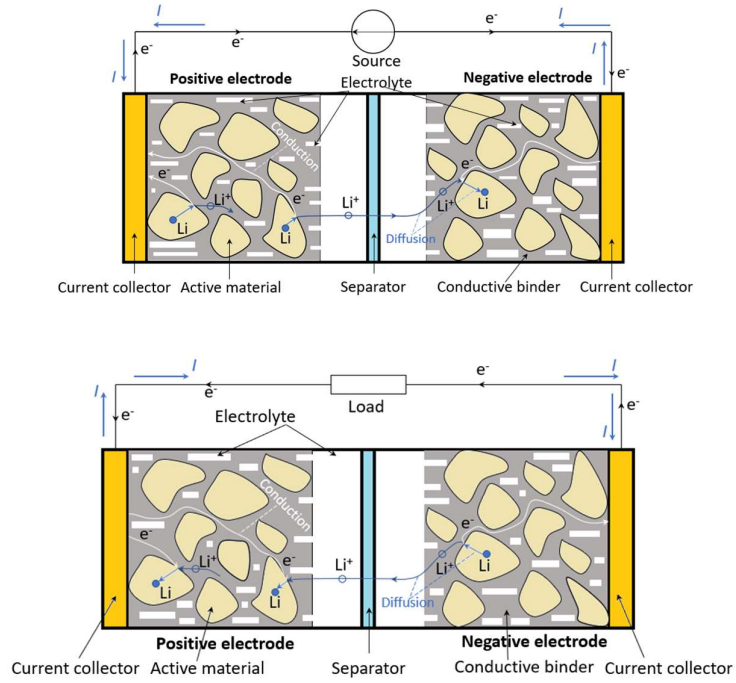


Figure 3.3 Lithium-ion cell during charge (above) and discharge (below).

In the following subsections lithium-ion cell's materials are analysed. It is common when studying and testing materials of lithium-ion batteries to refer to metallic lithium (Li/Li+) electrode instead of to the SHE. The metal lithium has potential of -3.05 V towards hydrogen, so material M's potential vs. SHE ($E_{M\to SHE}$) is converted to potential vs Li/Li+ ($E_{M\to Li/LI^+}$) using $E_{M\to Li/LI^+} = 3.05 + E_{M\to SHE}$. The materials are usually represented in graph where x-axis has a specific capacity in $mAhg^{-1}$ or $Ahkg^{-1}$ and ordinate has a potential towards Li/Li+ as shown in Figure 3.4. The cell voltage is calculated as difference. For example, pairing $LiFePO_4$ with $Li_4Ti_5O_{12}$ gives ~1.9V cell voltage whereas pairing with carbon results in ~3.3V cell voltage [117].

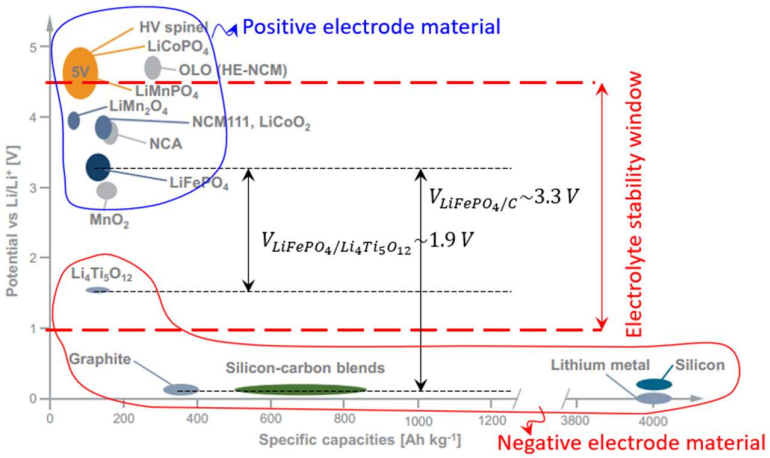


Figure 3.4 Potentials vs. Li/Li+ and specific capacities of some of the positive and negative active materials for lithium-ion cell, adapted from [118].

3.1.2.1 Electrolyte and Separator

Electrolyte is very important component of Li-ion batteries and since lithium reacts violently with water the solvent in li-ion batteries' electrolyte is non-aqueous liquid organic substance [112]. Common solvents are ethylene carbonate (EC), propylene carbonate (PC) and dimethyl carbonate (DMC). The solute is lithium salt, most common one being $LiPF_6$ (Li^+, PF_6^-), $LiBF_4$ and $LiClO_4$ [119]. As already mentioned, lithium-ion cells are manufactured in completely discharged state (all the lithium is in the positive electrode) and they must go through precise first charge cycle, so called formation process. Conventional organic electrolytes are stable within a potential window of 1.5 V to 4.3-4.5 V vs. Li/Li^+ [113]. Unfortunately, if the electrode is exposed to voltages outside this window, all of the mentioned conventional electrolytes will react violently with electrode materials [120]. As it can be inferred from Figure 3.4, a conventional negative electrode material is outside the stability window and graphite undergoes through side reaction during formation process of the cell. This process, during which a solid electrolyte interphase (SEI) is created, will be explained in more detailed in section on graphite materials for negative electrodes.

3.1.2.2 Positive electrodes

In general, positive electrode materials are created of lithiated metal oxides or lithiated metal phosphates. Typical representative materials are $LiCoO_2$, $LiMn_2O_4$, $LiFePO_4$ each of them having different spatial crystal structure namely, layered, spinel and olivine respectively (Figure 3.5). Difference between associated chemistries is due to the diversity of crystal structures. For instance, in spinel structures Li^+ can move in three directions (3D) while in olivine only in one linear direction (1D) which will eventually have consequences on the

dynamics of the cell if additional precautions are not to be taken. Another materials of interest are $Li(NiMnCo)O_2$ and $Li(NiCoAl)O_2$.

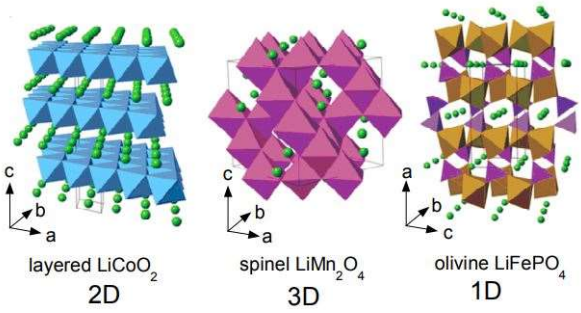


Figure 3.5 Crystal structure of the three lithium-insertion compounds in which the Li cations are mobile through the 2D (layered), 3D (spinel) and 1D (olivine) frameworks [121].

3.1.2.2.1 Layered structure

Lithium cobalt oxide ($LiCoO_2$ or LCO) was the first material to be used in commercial Li-ion batteries. In 1980, Goodenough discovered that LCO was a viable intercalation compound, and it was successfully commercialised and brought to market by Sony in 1991 [122], [123]. LCO is a compound that has a layered type of crystal structure like the one of carbon (Figure 3.6). Intercalation reaction during discharge is described by:

$$\text{Positive electrode: } Li_{1-x}CoO_2 + xLi^+ + xe^- \xrightarrow{discharge} LiCoO_2 \; ; E^+ \sim 4\,V \tag{3.1}$$

$$q = nF/M \tag{3.2}$$

where $x = 0$ stands for maximum amount of lithium that can be stored in the material.

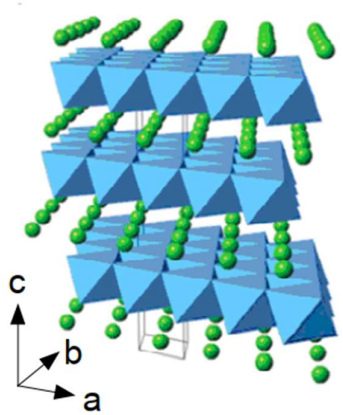


Figure 3.6 Layered crystal structure of LCO [121].

Voltage profile of LCO is rather sloped compared to other non-lithium chemistries, and its charge and discharge potentials vs Li/Li+ are shown in Figure 3.7. Theoretical specific capacity of LCO can be calculated using (3.2) where F is Faraday's constant (26.8 Ah/mol) and M is the molar mass of the material, in case of $LiCoO_2$ is 97.97 g/mol. Therefore, theoretical capacity

of LCO is around 272 $mAhg^{-1}$ assuming all the lithium participates in reaction and that can be extracted from crystal lattices. Unfortunately, not all lithium can be reversibly intercalated and de-intercalated from $LiCoO_2$. Lithium behaves as pillars of LCO structure, keeping the oxide layers apart [112]. If during de-lithiation too much lithium is removed (x>0.5), the LCO crystal undergoes structural changes which leads to reduced capacity and cyclability [112]. Therefore, x is equal to 0 for fully lithiated state, and 0.5 for what can be considered as the limit of the de-lithiated state which occurs at 4.2V vs. Li/Li+ resulting in a practical maximum reusable capacity of around 140-150 $mAhg^{-1}$ [124]. Additionally, charging above 4.2V at 200°C results in release of oxygen that can react with electrolyte causing exothermal reaction and lead to thermal runaway, fire and explosion [125]. However, research has proven that by coating LCO particles capacity of 180 $mAhg^{-1}$ with cut-off voltage of 4.5V can be achieved [126]. Finally, cobalt is rare element and thus expensive in addition to being highly toxic. Nonetheless, LCO is still preferable choice for consumer electronics that require high capacity and energy density such as notebooks, mobile phones etc [127]. Due to the aforementioned problems of LCO cells, economics of scale cannot be applied and that is one of the reasons why they haven't found application in transportation industry (if being used for automotive products in larger volumes, a shortage and a price increase would be the consequence [127]).

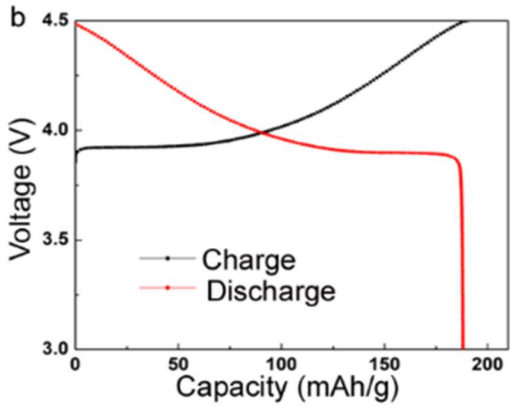


Figure 3.7 Typical charging/discharging voltage of LCO.

Therefore, material engineers are trying to either replace Co with more viable option or to reduce its percentage in the positive electrode with the aim of developing suitable batteries for traction applications. A cheaper alternative to Co is nickel ($LiNiO_2$ or LNO). LNO has similar theoretical capacity as LCO of 275 $mAhg^{-1}$, but it has higher reversible capacity of 200 $mAhg^{-1}$ [118]. Although being responsible for higher practical specific capacity, Ni is more thermally unstable and it is accountable for faster capacity fade, i.e., lower cycle life, and thus this chemistry is not commercialised today despite significant research efforts [128], [129]. The

shortcomings of Ni and Co are nowadays alleviated by introducing aluminium and manganese to compounds of Ni and Co, in so called NMC and NCA. They also have benefits of layered structure but introducing properties of other metals used in compound, Mn or Al.

NMC is a compound consisting of Ni, Mn and Co ($Li(Ni_xMn_yCo_z)O_2$). Since each of the metals introduces their own advantages and disadvantages, the properties of NMC cell depend on the amount of metal and their ratio and thus are difficult to generalise. The most common compound, and first developed, is $Li(Ni_{0.33}Mn_{0.33}Co_{0.33})O_2$ with equal ratios of Ni, Co and Mn, also abbreviated as NMC 111. This cell has improved safety compared to LCO and LNO and slightly higher capacity (~150 $mAhg^{-1}$ [130]) than LCO. As already seen Ni is responsible for high capacity and thus higher ratios of Ni can increase specific capacity up to 200 $mAhg^{-1}$ (for x=0.8; NMC 811) but at the same time it lowers the thermal capability and increases capacity fade compared to NMC 111 [131].

NCA is compound consisting of Ni, Co and Al ($Li(Ni_{1-x-y}Co_xAl_y)O_2$). Aluminium is added with the purpose of offsetting the thermal stability problems of LCO and LNO and improving electrochemical properties [125]. Typical compound used nowadays is $Li(Ni_{0.8}Co_{0.15}Al_{0.05})O_2$ and it offers practical capacity between 180 and 200 $mAhg^{-1}$, the most of all commercialised layered structure compounds [124], [132]. Consequently, NCA cells are with high energy density. However, those cells are expensive due to the synthesis of NCA and due to the presence of both Ni and Co in high ratios, their safety is main challenge.

3.1.2.2.2 Spinel structure (LMO)

Two years after LCO breakthrough, in 1983, Goodenough and Thackeray presented another intercalation compound, namely lithium manganese oxide ($LixMn_2O4$ or LMO). LMO has the lowest theoretical specific capacity of all lithium-ion chemistries 148 $mAhg^{-1}$ with practical capacities ranging between 100 and 120 $mAhg^{-1}$ [116]. Typical charge/discharge characteristic is flatter compared to LCO and it has two plateaus (Figure 3.9) with midpoint potential of 4.05 V vs Li/Li+ [118], resulting in the lower specific energy compared to LCO. On the other hand, LMO has a 3D spinel crystal structure depicted in Figure 3.8 which allows for three-dimensional lithium diffusion significantly improving rate capability compared to its 2D layer counterparts [133]. On the other hand, cost of LMO is lower than LCO, LNO, NMC and NCA since it doesn't consist of expensive cobalt and nickel. Consequently, LMO is safer compared to nickel and cobalt layer compounds but exhibits poor cycling stability at temperatures above 50 degrees [117]. Thus, LMO is viable alternative to LCO and its congeners, where energy density

and lifecycle aren't of the prevailing importance, and it is widely used today. With electrode coating, cyclability problems can be overcome and LMO cells were even used in electric vehicles and are also used in mixed electrodes mainly with NMC [117], [133].

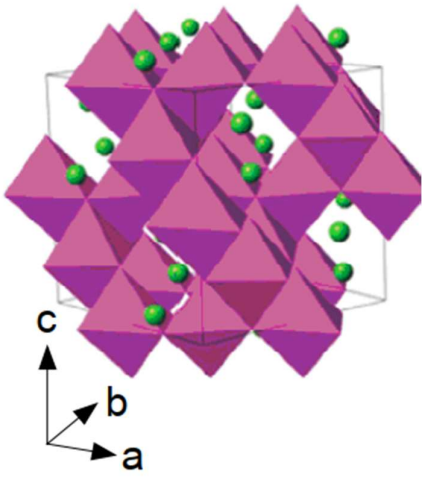


Figure 3.8 Spinel crystal structure of LMO [121].

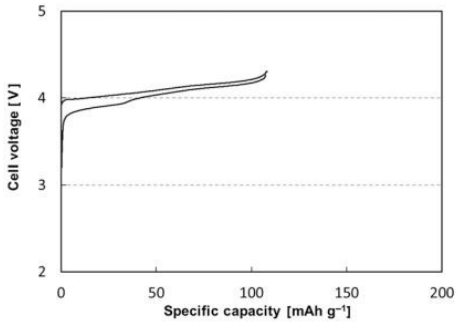


Figure 3.9 Typical charging/discharging cycles of LMO [118].

3.1.2.2.3 Olivine structure (LFP)

Third major positive electrode material produced in Goodenough's laboratory (with Padhi) is lithium iron phosphate ($LiFePO_4$ or LFP) [123]. The greatest advantage of this material is that it is not prone to thermal runaways, i.e., it has very high thermal stability and safety [134]. LFP is virtually unreactive with electrolytes up to 350°C [116]. This is due to its 1D olivine structure (Figure 3.10) and strong covalent P-O bonds that offer not only a thermal but also a structural stability resulting in excellent cyclability [118]. Additionally, LFP material is popular because of its environmental friendliness and low cost due to the use of abundant elements.

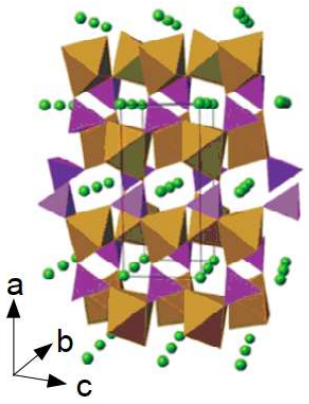


Figure 3.10 Olivine crystal structure of LFP [121].

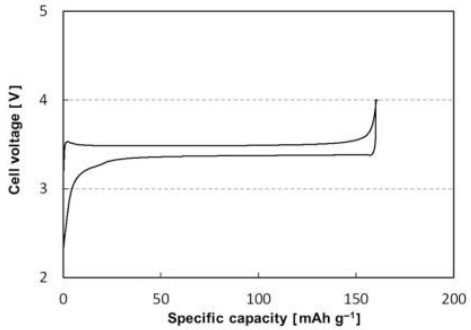


Figure 3.11 Typical charging/discharging cycles of LFP [118].

However, the main drawback of this chemistry is low theoretical capacity of around 170 $mAhg^{-1}$ in addition to the average potential vs Li/Li of around 3.45 V vs. Li/Li+, resulting in low energy density. Also, LFP is prone to high self-discharge rates especially at elevated temperatures which can cause balancing problems with aging [117]. Unfortunately, the LFP olivine structure intrinsically exhibits low ionic and electronic conductivity resulting in low rate capability causing the material to initially be thought only applicable for low cost applications [135]. It has been proven that high rates of LFP can be achieved by reducing the particle size to nano levels and by surface modification through carbon coating and at the same time increasing practical specific capacity [136]. To date nano-size carbon coated LFP electrodes have been successfully commercialised by A123 and BYD and thus these cells found their use in power tools and transportation where high discharge rates and power levels are required [135]. Typically, continuous discharge rates of 20 C are possible whereas 10 s 48 C pulse discharge rates can be achieved [137]. Furthermore, capacity is the same for all discharge rates, in other words it has very low Peurket's coefficient close to 1 which slightly simplifies certain SoC estimation methods [138].

3.1.2.3 Negative electrodes

Similarly, as with the positive electrodes, the materials that host lithium ions in negative electrodes are intercalation based. While there is more variation in positive electrodes, negative electrodes are usually carbon based or transit metal oxide.

3.1.2.2.4 Carbon based electrodes

The most common negative electrode of lithium-ion batteries is graphite (C_6). Graphite can store one lithium ion per six carbon atoms which results in high specific capacity of 372 $mAhg^{-1}$ and very low potential vs. Li/Li^+ (0.04-0.2 V) with characteristic two plateaus shape (Figure 3.12) [139]. Therefore, from the energy density perspective graphite is the preferable choice, even though it has comparably lower density then other materials such as silicon because its manufacturing process is perfected and its behaviour well-researched. Additionally, graphite is non-toxic, abundant and it appears as low-cost option. However, graphite electrodes have shortcomings which are mainly associated with the SEI layer. As already mentioned, during formation process electrolyte and graphite react violently in creating a passivating film layer on negative electrode surface. However, fortunately, the reaction is self-limiting in a sense that when SEI layer is created on the surface of the graphite, it prevents further reaction of lithium and electrolyte. SEI layer thus chemically insulates graphite from the electrolyte whereas at the same time is conductive for Li^+. SEI also contains lithium, which means that some capacity is lost at the first charging cycle besides increasing the resistance of the cell leading to power fade [140]. Additionally, graphite experiences 10% volume strain between charging and discharging cycles which lead to mechanical structural problems such as cracks in SEI layer exposing again graphite to electrolyte. Because of this more lithium is lost in regenerating the layer and becomes inactive which with time leads to capacity fade. It is obvious that Li-ion cells cannot operate safely without SEI and even though growth of it is slow after first charge cycle, it is still considered as main aging mechanism of the Li-ion batteries [141]. Another shortcoming of graphite is lithium plating which occurs near or below 0 V vs Li/Li+. When battery with graphite electrode is charged with high rates, graphite potential gets close to 0 V and thus metal lithium deposits in form of dendrites that can grow which not only causes capacity loss, but it presents a safety issue as they can grow across separator and short-circuit electrodes. Therefore, among other limiting factors, fast charging is also hindered by graphite.

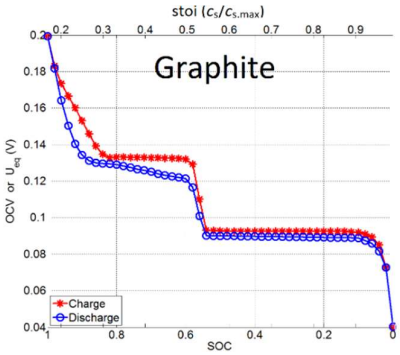


Figure 3.12 Charge and discharge potentials vs. Li/Li+ of graphite material [139].

3.1.2.2.5 Lithium-titanite

Another successfully commercialised negative electrode is lithium-titanite, i.e., lithium titanium oxide ($Li_4Ti_5O_{12}$) with spinel crystal structure, abbreviated as LTO. The redox reaction that occurs in this material is shown in (3.3) and it involves three lithium ions. Therefore, theoretical specific capacity of the LTO is 175 $mAhg^{-1}$. The reaction is also characterised with 1.5 V vs. metal lithium which is constant throughout the whole reaction and exhibit very small hysteresis between charge and discharge (Figure 3.13). Therefore, LTO cells are typically low voltage cells with low energy density. For example, Altairnano cell has nominal voltage of 2.22 V and specific energy of 82 $Whkg^{-1}$ [142] with positive electrode not disclosed, although most likely it is layered structure NMC or NCA [143].

$$Li_4Ti_5O_{12} + 3Li^+ + 3e^- \rightarrow Li_7Ti_5O_{12} \qquad (3.3)$$

However, introduction of LTO instead of graphite brings a lot of benefits. First of all, the volume change during discharge and charge is practically inconsiderable of only 0.25%, compared to 10% of graphene [144]. Contrary to graphite, LTO electrodes do not react with electrolyte as they operate under voltage higher than 1 V and hence don't have SEI layer. The zero-strain property in combination with high voltage towards Li/Li^+ translate into enhanced safety and stability. As a result, LTO cells have high cyclability of more than 10000 cycles, high charging rates and excellent thermal stability.

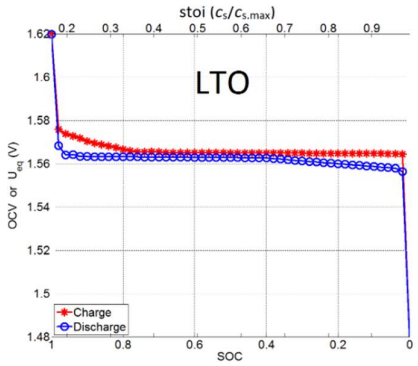


Figure 3.13 Charge and discharge potentials vs. Li/Li+ of LTO material [139].

3.1.3 On power and energy density

Energy density of the cell can be calculated using total cell capacity q_{cell} and positive and negative electrode potentials using following formulas:

$$q_{cell} = \frac{1}{\frac{1}{q^+} + \frac{1}{q^-}} \tag{3.4}$$

$$e_{cell} = q_{cell}(E^+ - E^-) \tag{3.5}$$

where q^+ and q^- are specific capacities of positive and negative electrode respectively. For example, theoretical energy density of NCA/graphite cell is 605 Whkg^{-1} using theoretical values for specific capacity ($q^+ = 272\ \mathrm{mAhg^{-1}}$, $q^- = 372\ \mathrm{mAhg^{-1}}$) and 3.85 V as cell voltage. However, taking into consideration practical reversible capacities, the energy density drops to 437 Whkg^{-1} [145]. Then, when the weight of current collectors, electrolyte, separators, binders, 18650 battery housings and tabs is included it drops to 264 Whkg^{-1} which is only 46% of theoretical value and close to advertised value of the most famous NCA chemistry, Panasonic NCR 18650B. This example illustrates that in theory novel chemistries can have promising densities (good capacity and voltage), but equally important is to find acceptable way of housing all the materials without deteriorating density too much. Similar happens when battery pack is assembled. First cells are assembled to module, and its energy density is lower than single cell due to presence of battery holders, welding strips, BMS etc. Then when modules are integrated into pack the weight increases due to presence of cooling system and battery casing which prevents mechanical abuse. As a result, the battery of Tesla, which uses Panasonic NCRB, is 120 Whkg^{-1} [120].

As already seen, the properties of lithium-ion batteries not only depend on the selected material, but also whether the material is coated, the size of the particles and similar. Each selected chemistry can be optimised for either power or energy depending on the ratio of active

to passive materials [146]. As expected, the energy optimised cells have thicker electrodes, i.e., more active material at the expense of passive materials. On the other hand, power optimised cells have thinner electrodes and more passive material to enhance the electro-kinetics and reduce the impedance. For example, Kokam offers selection of NMC cells that range from low energy density and high rates (e.g., 120 $Whkg^{-1}$ and 20C continuous) to high energy density and low rate (e.g., 186 $Whkg^{-1}$ and 2C continuous) [147].

3.1.4 Conclusions on lithium-ion batteries and future trends

As it was seen, different positive and negative electrode materials result in distinct properties, sometimes completely contradictory. The differences arise from the unique crystal structure (layered, spinel and olivine) and from the materials used. Most used material types of positive electrode are LCO, NMC and NCA for layered, LMO for spinel and LFP for olivine structure. For some chemistries it is difficult to generalize characteristic and behaviour. For instance, a behaviour and characteristic of NMC cell depends on the ration of Ni, Co, and Mn used. Additionally, every cell can be optimised as ‘’energy’’ or ‘’power cell’’. Nonetheless, for the sake of convenience Table 3.1 summarises these chemistries. Typical discharge characteristics of these materials summarised in Figure 3.14.

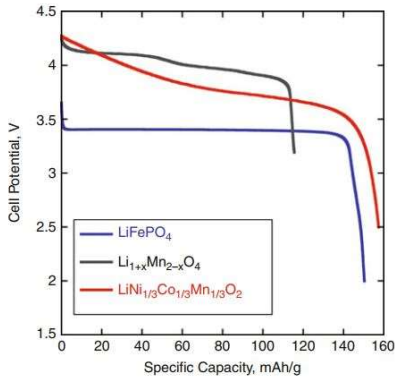


Figure 3.14 Typical discharge characteristics of LFP, LMO and NMC chemistries [148].

Table 3.1 Summary of electrode positive active materials.

	Theoretical capacity	Practical capacity	Mid-point voltage vs Li/LI+	Safety	Cost
LCO	274	140 - 150	3.9 - 4	+	$$$
LNO	274	150 - 200		+	$$
LMO	148	100 - 120	4.05 - 4.1	+++	$
NMC 111	280	163 - 170	3.7 - 4	++	$$$
NMC 811	275	206	3.7 - 4	+	$$$
NCA	279	180 - 200	3.7-3.9	+	$$
LFP	170	120-160	3.45	++++	$

From the automotive perspective LFP/LTO cells offer fast charging times and very high lifecycles at very high rates. Therefore, these cells can be suitable for public transportation where fast charging times are very important. In terms of improvements, they can be made to existing materials to improve safety, high-rate capability, cyclability etc using already mentioned techniques such as nanoparticulation, coating etc. In terms of negative active materials, silicon is pursued as interesting topic due to high capacity (Figure 3.4) but its volume strain of 270% makes it far from acceptable 10% of carbon. New electrolytes are looked for which have higher stability window which means they have to be in solid state [128]. But also, solid state active materials are researched. Behind lithium-ion chemistry sodium-ion, florid-ion as well as metal batteries are all researched.

Looking beyond battery technology, which are based on faradaic processes, energy storage systems based on non-faradaic processes exist. Most notably they are electrochemical capacitors (EC), also called supercapacitors and ultracapacitors. Albeit like conventional capacitors, ECs differ in certain key aspects. The main one is that ECs have higher capacitance than conventional electrolytic and dielectric capacitors. This is obtained by utilising porous materials as an electrode material, which guarantee high surface area, and relying on the phenomenon of the electrical double layer (EDL), which intrinsically has small distance between charge layers. Consequently, electrochemical capacitors can store more charge and have higher energy density then conventional ones. Furthermore, their charge/discharge time is in the order of seconds to minutes compared to the order of 10^{-3} and 10^{-6} seconds for normal capacitors [149].

When compared to the batteries, process that happens inside EC is physical in nature and it is non-Faradaic i.e., no charge transfer occurs. This means that this process is highly reversible compared to irreversible redox reactions in batteries and consequently ECs can be cycled more than half million times. Furthermore, charge realise is not limited by kinetic rates of the chemical reactions, and hence ECs intrinsically exhibit higher power densities than batteries. Although they can store more charge (higher energy density) than conventional capacitors, still they can store 3-30 times less energy than batteries. Thus, ECs found their applications in transportation industry to bridge the gaps of batteries in so called hybrid energy storage systems.

Recently a term supercapattery (supercapacitor + battery) was coined to put under same umbrella devices that take advantage of both non-faradaic and faradaic type of charge storage at either electrode [150]. One of those devices is lithium-ion capacitor that is combination of

active carbon (EC side) and lithiated graphite (battery side). Lithium-ion capacitor offers advantages compared to ECs such as higher voltage window and higher energy density.

3.2 Battery modelling

Modelling of the batteries and its behaviour is of crucial importance. Models are useful in the design stage of the cell, for the simulation of the behaviour on the system- and cell-level, for the parameter estimation that are used in BMS and EMS. Most commonly, batteries are modelled using one of three types of models: physics based (electrochemical) models, empirical models and equivalent circuit models.

3.2.1 Physical models

Physics-based models, also called electrochemical models, are based on first principles that account for underlying chemical and physical processes inside cells. They give insight into microscopic behaviours such as concentration dynamic, in addition to the macroscopic quantities that can be observed, such as terminal voltage and temperature [151]. Due to their explicit physical meaning, these models are the most accurate. Also, these models help predict the ageing of the battery and possible failure modes [152]. Furthermore, thermal effects can be simulated with high accuracy. Being very precise, these models are naturally used during cell design. However, they are not suitable to be implemented on microcontrollers for real-time estimation and monitoring due to their large computational complexity, as explained later.

Doyle, Fuller and Newman developed the most used electrochemical model in the middle of the 1990s, the so-called DFN or pseudo 2D (P2D) model [153]. The model assumes porous electrodes and concentrated solution spaced in two dimensions (x,r). X-direction represents the path of lithium through the electrolyte, whereas r represents radial travel of ions into and out from active material spherical particle as shown in Figure 3.15. The model accounts for all relevant processes, namely diffusion in electrolyte and solid phase, ohm's law in electrolyte and solid phase, charge conservation in electrodes and separator, and kinetic equation on the surface of each particle in each electrode [154]. It consists of several non-linear partial differential and algebraic equations. Therefore, a closed-form solution is usually never obtained, so numerical techniques such as finite element, finite difference, and finite volume methods are employed. For this reason, these models are not suitable to be implemented on the microcontroller for BMS systems, even though they are the most accurate ones.

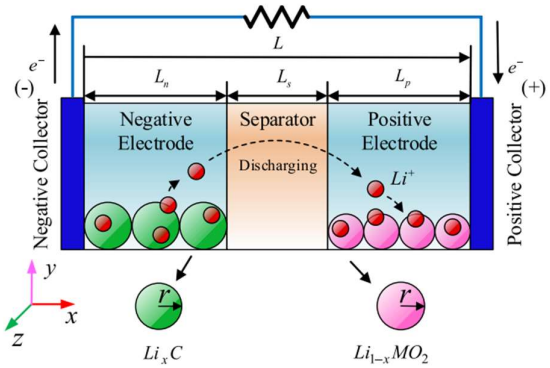


Figure 3.15 Schematic of P2D model.

Numerous techniques exist to simplify the P2D model into more usable forms. Some use numerical tools for approximation such as proper orthogonal decomposition and Padé approximation, whereas others use model simplification such as single-particle model (SPM) [152]. For example, in an SPM model (Figure 3.16), each electrode is modelled as a single spherical particle. Consequently, this model requires less numerical effort for solving and exhibits lower run times. Nonetheless, the solution in closed form is also rarely obtained. Therefore, mentioned approximation techniques transfer partial differential equations into ordinary differential equations in so-called reduced-order models.

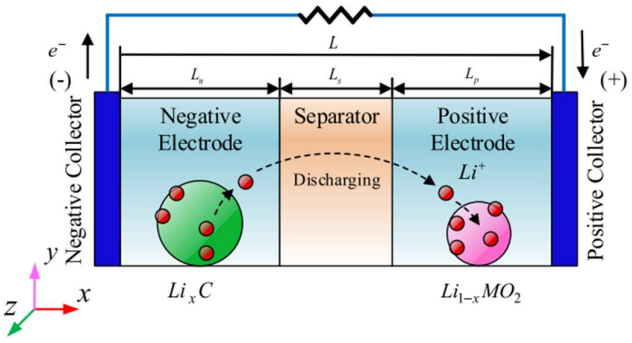


Figure 3.16 Schematic of SPM.

As an interim conclusion, the electrochemical models are the most accurate battery models. They require high computational power to be solved, usually using software such as COMSOL and techniques such as the finite difference method. Despite its advantage, these models require inputs that cannot be easily obtained, such as electrode thickness, electrolyte properties, and similar, making it unfavourable for characterisation studies of the already existent cells [151]. Furthermore, electrochemical models are not suitable for control purposes in BMS, where states are observed and estimated. Finally, electrochemical models are appropriate for predicting the ageing of the battery in terms of SEI growth and capacity fade.

3.2.2 Empirical models

Empirical models describe the specific battery behaviour using various functions and formulas. Since these models employ past experimental data, predictions may be poor for other battery operating conditions [152]. For example, Peurket's law can be used to successfully determine the capacity for constant current discharge. However, this model cannot be applied for a dynamically varied current and it cannot predict the terminal voltage behaviour of the cell.

Under this wide category are the majority of lifetime and aging models. For example, in [155], a capacity fade, ratio of current capacity and nominal capacity, due to cycling is evaluated in terms of temperature (T), cycle depth (cd) and number of cycles (nc) of a commercial LFP/C cell. Albeit the function that predicts capacity fade (C_{fade}) shown in (3.6) includes most of the important factors, it has been obtained using specific pre-defined charge and discharge cycle. However, if battery is cycled under different current profiles, it might not experience the same aging profile. For instance, the equation might be changed if different average SoC cycling point and different charge and discharge rates were selected. Finally, in real applications, especially in electric vehicles, batteries are discharged with cycles that cannot be predicted easily.

$$C_{fade}(nc, T, cd) = 0.00024e^{0.02717T} \cdot 0.02982cd^{0.4904} \cdot nc^{0.5} \tag{3.6}$$

Another famous empirical model is created by Olivier Tremblay and due to its simplicity, it is implemented in Matlab/Simulink as generic battery model [156]. In fact, this model is improved version of Shepherd's model and it relies only on the information provided in datasheets for model parametrisation instead of conducting set of experiments [157]. The battery terminal voltage during discharge is expressed by (3.7):

$$V_t = E_o - K\frac{Q}{Q - it}it - Ri + Ae^{-Bit} - K\frac{Q}{Q - it}i \tag{3.7}$$

where V_t is the battery terminal voltage, E_o battery nominal voltage, R battery internal resistance, i current through the battery terminals, it battery current integrated over time, i.e., actual charge extracted during discharge, Q nominal capacity, and K, A, and B constants that can be calculated as explained in [158].

This model shows excellent behaviour when battery is discharged with constant current. However, the shortcomings of the model are constant internal resistance over all SoC range, sensitivity on the accuracy of provided discharge/charge curves by the manufacturer, and low

accuracy when discharged with high C rates [159], [160]. Finally, this model didn't prove the satisfying accuracy to be used for dynamic performance evaluation [159].

3.2.3 Equivalent Circuit Models

The equivalent circuit models (ECM) were developed to bridge the disadvantages of electrochemical and empirical models. ECM are semi-empirical models because experiments must be performed to extract the model parameters, the same as for empirical models. However, ECM offer more flexibility, i.e., they can model with sufficient accuracy the profiles that were not used for parameter characterisation. As the name implies, the ECMs use electrical circuits elements to describe the terminal voltage of batteries under dynamic current load profile. With some modifications, the model can also be adapted to predict the battery's temperature [161]. Due to the numerical simplicity, they are often implemented in BMS and used for electric vehicles' system-level [162].

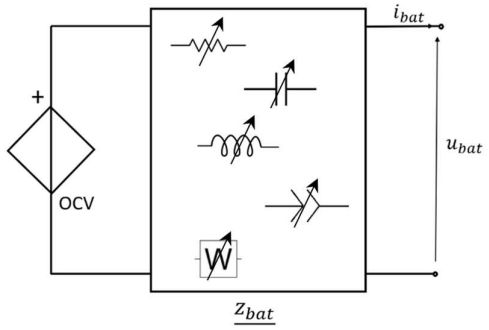


Figure 3.17 General representation of ECM with OCV and $\underline{z_{bat}}$.

The general ECM of the battery consists of two main elements, and it is shown in Figure 3.17. The first element is open-circuit voltage (OCV), modelled as a controlled voltage source due to its dependency on the battery's state of charge (SoC). The second element is the impedance network ($\underline{z_{bat}}$) consisting of variable inductances, resistances, capacitors, and constant phase elements. In the following subsections, the modelling and parameter identification of each of the circuit parts is explained. Moreover, as both OCV and impedance depend on SoC, subsection 3.2.6 briefly discusses the methods of SoC calculation and identification. Historically there have been many ECMs and in the following paragraphs the reasoning behind them will be presented.

3.2.4 OCV

The OCV identification is an essential part of the modelling process since OCV is one of the battery model's main components. It results as part of complex physical behaviour during the intercalation and de-intercalation of the lithium-ions [116]. The OCV is a battery parameter that especially varies with respect to the SoC. Therefore, a proper correlation between OCV and SoC must be established. Continuous and discrete (i.e., incremental) methods are often used to determine OCV(SoC) function [163].

3.2.4.1 Continuous methods

During continuous OCV identification, a sufficiently low discharge constant current (e.g., C/40) is applied to a fully charged battery [164]. Low discharge current will decrease the SoC of the battery and, at the same time, keep it in an equilibrium state. Consequently, the measured battery terminal voltage can be considered to represent OCV with enough accuracy. Because OCV expresses hysteresis, i.e., different OCV curves are obtained during charge and discharge, the same load current must be applied for the charging process. This procedure takes at least 80 hours without considering the charging period and the rest time between charge and discharge periods. This method is advantageous because the OCV mapping is done continuously.

If the long waiting times are undesirable or unacceptable, several experiments with a high constant discharge current can be performed. During continuous constant current discharge, battery terminal voltage can be described by:

$$V_{t,xC} = OCV - RI_{xC} \tag{3.8}$$

where $V_{t,xC}$ is the terminal voltage during constant current discharge with xC rate (I_{xC}) and R is the internal resistance. Equation (3.8) has two unknowns, OCV and internal resistance; thus, another equation is required to solve for two unknowns. Therefore, discharging the battery with two different C rates (I_{x_1C} and I_{x_2C}) suffice to calculate OCV as shown below:

$$R = \frac{V_{t,x_1C} - V_{t,x_2C}}{I_{x_2C} - I_{x_1C}} \tag{3.9}$$

$$OCV = V_{t,x_1C} + RI_{x_1C} \tag{3.10}$$

This concept is taken even further in [165], where datasheet constant discharge information is used to obtain OCV. Usually, battery manufacturers provide several constant current discharge curves. Assuming that n discharge curves are given, there are $m = \binom{n}{2} = \frac{n!}{(n-2)!2!}$ possible combinations to select a system of two equations. For example, in case of $n = 4$ curves (e.g., 0.2C, 0.5C, 1C, 2C) there are $m = 6$ combination pairs namely: (0.2C,0.5C), (0.2C,1C),

(0.2C,2C), (0.5C,1C), (0.5C,2C) and (1C,2C). Each of those m systems can be solved using (3.9) and (3.10), which results in m solutions for internal resistance and OCV. Finally, OCV can be calculated as average of all solutions.

$$OCV = \frac{1}{m}\sum_{i=1}^{m} OCV_i \tag{3.11}$$

3.2.4.2 Discrete methods

The second option is to measure OCV at specific SoC points that are defined in advance, e.g., in SoC intervals of 10%, i.e., [100%, 90%, 80%, …, 20%, 10%]. The battery is driven to the demanded SoC level by applying a constant current pulse of a certain duration and amplitude. Equation (3.12) relates the battery's capacity in Ah, duration and amplitude of the pulse with the desired SoC change in %.

$$\Delta SoC[\%] = \frac{I_{pulse}[A]\Delta t_{pulse}[s]}{Q[Ah]36} \tag{3.12}$$

Once the current pulse is removed, the battery voltage does not return immediately to equilibrium OCV state but only after some relaxation time, as demonstrated in Figure 3.18. Therefore, to correctly capture OCV, an adequate rest time must be applied. However, there must be a consensus between accuracy and time. Longer rest times will result in a better representation of OCV. For example, if two hours rest time is considered and 10% SoC decrease, the total experimental procedure would last 21 h. If more precision is required in the SoC interval, e.g., $\Delta SoC = 5\%$ which is not uncommon, the total time would rise to 42 h. If hysteresis is vital for the study, the procedure must be repeated for the charging process, doubling the experiment time. In the literature, no consensus is achieved on the good relaxation time and SoC voltage range. Relaxation time can be as low as 5 minutes and high as 5 h [163].

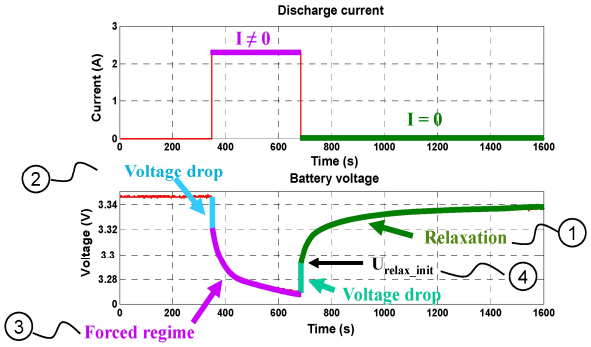


Figure 3.18 Battery terminal voltage response after discharge [166].

Another discrete methodology is to perform a similar experiment without waiting for the voltage to relax. In [167], the 15 minutes long current pulses with an amplitude of 0.4C with the rest time of 1 minutes between them were used. In this case, a lower boundary for OCV during discharge is obtained. Therefore, it is imperative to repeat the same test for charging and obtain the upper boundary and find the real OCV as the average of two. This procedure is illustrated in Figure 3.19 and Figure 3.20.

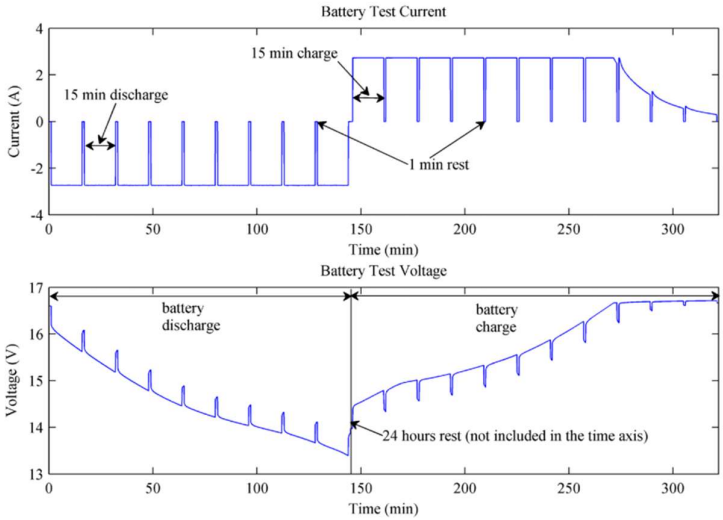


Figure 3.19 Voltage evolution during OCV characterisation with 1 minute relaxation with respect to time [167].

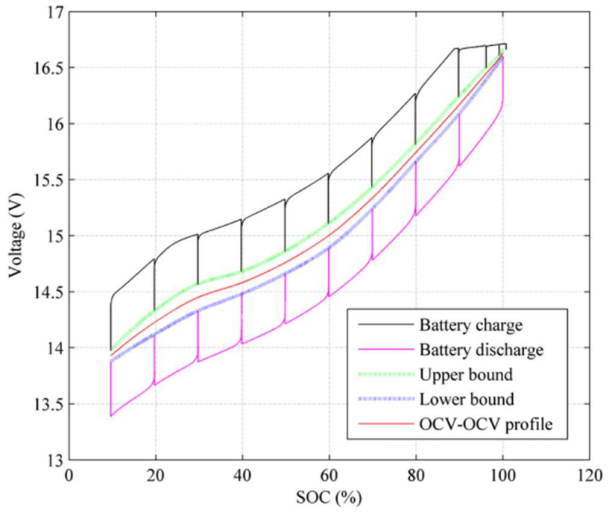


Figure 6. SOC-OCV profile extraction

Figure 3.20 Voltage evolution during OCV characterisation with 1 minutes relaxation with respect to SoC [167].

3.2.4.3 Software implementation

Once OCV(SoC) function is found, the model should be implemented on a simulation platform. This is usually performed either through lookup tables or obtaining analytical formula of OCV vs SOC. In the case of lookup tables, interpolation techniques are used to obtain OCV between the measured and known points. However, a precaution should be taken because the same interpolation technique might give different results for different battery chemistries. The second option is to find an analytical equation that relates SoC and OCV. Many studies have been performed, and the selected equation type depend on the battery chemistry. In [168], it was shown that the best model is polynomial for NMC and NCA chemistries, whereas for LFP,

the best model is logarithmic. The differences that arise are from the fact that distinctive chemistries result in different OCV shapes, as shown in section 3.1.4.

3.2.5 Impedance

The impedance part of the battery ECM can be obtained by analysing either the impedance spectrum in the frequency domain or by analysing voltage waveforms in the time domain. The frequency method is based on electrochemical impedance spectroscopy (EIS), which relates the physical phenomena inside the battery with the electric circuit elements. On the other hand, only a voltage waveform for a given current profile is analysed during the time domain impedance analysis, not requiring the EIS equipment.

3.2.5.1 Analysis of the impedance in the frequency domain

EIS is a non-intrusive process in which the complex impedance of the electrochemical system is determined for a given range of frequencies. An appropriate equivalent electrical circuit topology and its parameters can be generated by analysing the acquired impedance spectrum. A sinusoidal current/voltage is applied to the system during EIS, and voltage/current response is measured. The response also has a sinusoidal waveform with the same frequency, but it is different in amplitude and phase, as shown in (3.13) and (3.14).

$$u(t) = U\sqrt{2}\,cos(2\pi ft+\varphi_U) \tag{3.13}$$

$$i(t) = I\sqrt{2}\,cos(2\pi ft+\varphi_I) \tag{3.14}$$

Then, complex impedance is calculated as:

$$\underline{Z} = Ze^{j\varphi} = Z\,(cos\,\varphi + j\,sin\,\varphi) \tag{3.15}$$

where $Z = U/I$ and $\varphi = \varphi_U - \varphi_I$. In cases when current is used as a stimulus of the system, the procedure is called galvanostatic EIS (GEIS). In contrast, it is called potentiostatic EIS (PEIS) if the voltage is applied and the current is measured. The choice of EIS depends on the electrochemical system under study and the phenomena that are desired to be investigated. In the case of lithium-ion batteries, both techniques are used equally, but GEIS is preferable since lithium-ion batteries are inherently low impedance devices. Thus, even a small voltage amplitude (~mV) can potentially result in current amplitudes in the range of A, pushing the battery from its equilibrium point, a vital condition for successful EIS.

The EIS spectrum is generally presented in terms of impedance's imaginary and real part in a so-called Nyquist plot. Due to historical reasons, the y-axis represents a negative imaginary part of the impedance, i.e., the negative imaginary axis is pointing upwards. The typical

Nyquist plot of lithium-ion battery is shown in Figure 3.21. Three distinct regions can be observed from the figure, each corresponding to different processes occurring in a lithium-ion battery with their respective impedance contribution.

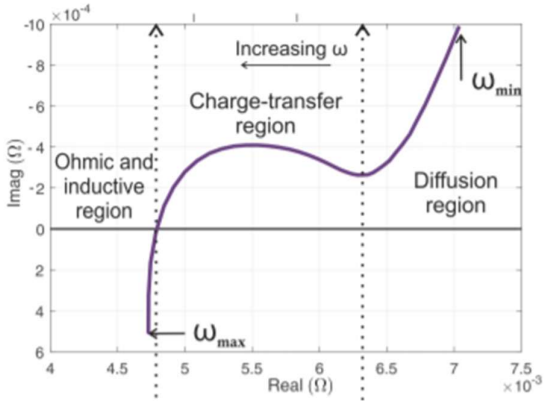


Figure 3.21 Spectrum of lithium-ion battery [169].

Before explaining how different parts of the spectrum can be modelled using various circuit elements and their combinations, a review of the most commonly used circuit elements in battery analysis is presented first. Table 3.2 gives the complex impedance and its real and imaginary parts of an inductor, capacitor, resistor, constant phase element (CPE), and Warburg element, whose spectrum is shown in Figure 3.22 and Figure 3.23.

Table 3.2 The complex impedance of the essential circuit elements for ECM.

Element	Complex Impedance	Real part	Imaginary part
Inductor (L)	$\underline{z_L} = j\omega L$	0	ωL
Capacitor (C)	$\underline{z_C} = \frac{1}{j\omega C}$	0	$-\frac{1}{\omega C}$
Resistor (R)	$\underline{z_R} = R$	R	0
CPE, (Q,α)	$\underline{z_{CPE}} = \frac{1}{Q(j\omega)^{\alpha}}$	$\frac{1}{Q\omega^{\alpha}} cos\left(\alpha\frac{\pi}{2}\right)$	$-\frac{1}{Q\omega^{\alpha}} sin\left(\alpha\frac{\pi}{2}\right))$
Warburg (W)	$\underline{z_W} = \frac{W}{\sqrt{j\omega}}$	$\frac{W}{\sqrt{2\omega}}$	$-\frac{W}{\sqrt{2\omega}}$

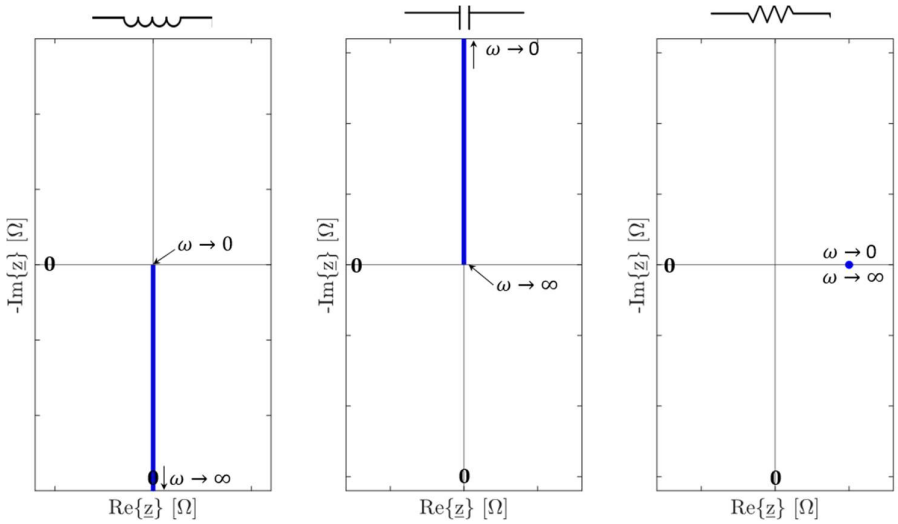


Figure 3.22 Spectrum of inductor, capacitor, and resistor.

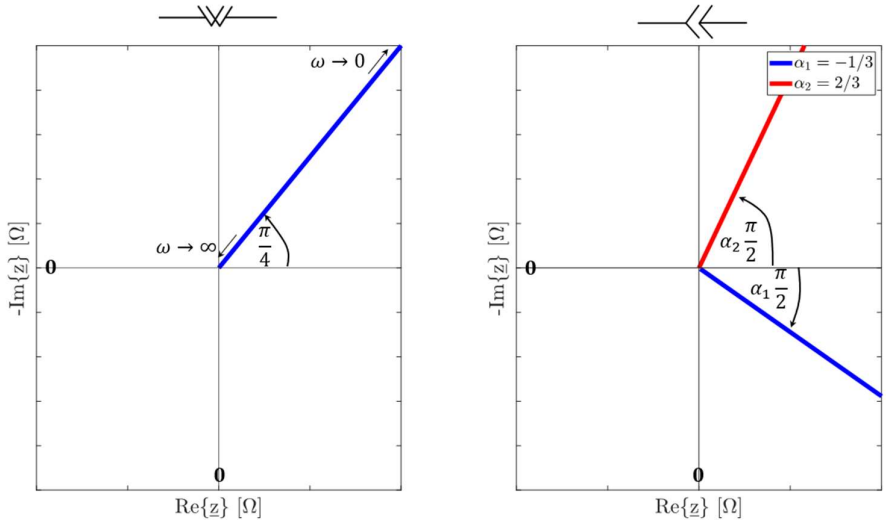


Figure 3.23 Spectrum of Warburg impedance and CPE.

Whereas resistor, capacitor, and inductor are extensively used in electrical engineering, the Warburg impedance and CPE are rarely used. The Warburg impedance is characterised by the Warburg coefficient W (unit of W is $\Omega^{-1}s^{0.5}$) and by a line in the Nyquist plot that makes a 45° angle with x-axis as shown in the left part of Figure 3.23. The Warburg impedance originates from the diffusion process inside the battery. The formula from Table 3.2 assumes a semi-infinite diffusion. However, practically in batteries, diffusion never occurs in semi-infinite space. Therefore, finite models are more appropriate depending on the electrode's boundary condition reflectivity: transmissive (3.16) or reflective (3.17), where l_T is the thickness of the diffusion layer, and D is the diffusion coefficient of the diffusing species [170], [171]. (3.16) is also called a finite length Warburg (FLW) impedance, whereas (3.17) is called finite space Warburg (FSW) impedance, and their spectrum is shown in Figure 3.24.

$$\underline{z_W} = \frac{W}{\sqrt{j\omega D}} tanh(l_T\sqrt{j\omega/D}) \tag{3.16}$$

$$\underline{z_W} = \frac{W}{\sqrt{j\omega D}} cotanh(l_R\sqrt{j\omega/D}) \tag{3.17}$$

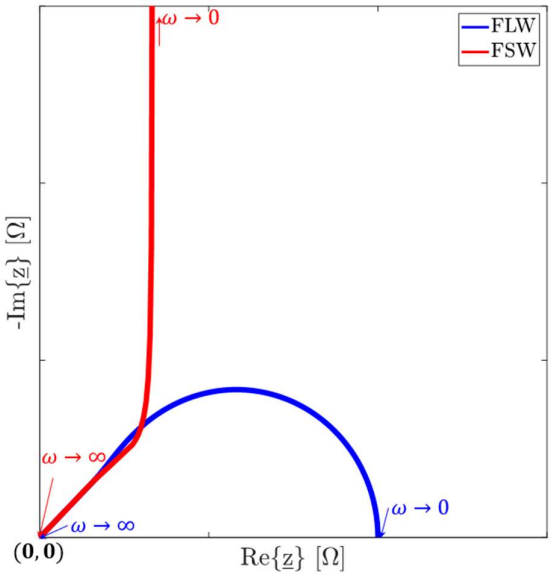


Figure 3.24 Spectrum of FSW and FLW impedance.

The constant phase element is an element that has two parameters, Q and α. The unit of Q is $\Omega^{-1}s^{\alpha}$ whereas α is dimensionless and ranges between -1 and 1. As the name implies, depending on the value α, different arguments, i.e., phases, can be obtained. Thus, CPE is represented as a straight line in the Nyquist plot with α 90° angle towards the x-axis. The CPE can be considered as a generalisation of the previous four elements. If $\alpha = 1$, CPE becomes a pure capacitor and for $\alpha = -1$ pure inductor. If $\alpha = 0$ CPE behaves as pure resistance with $R = 1/Q$. On the other hand, if $\alpha = 0.5$, CPE becomes a well-known semi-infinite diffusion Warburg element.

However, these elements are rarely used alone but rather in series or parallel combinations with other elements. For example, from Table 3.2, it can be deduced that adding a resistor in series with an impedance element will only shift the spectrum to the right on the real axis, as shown in Figure 3.25.

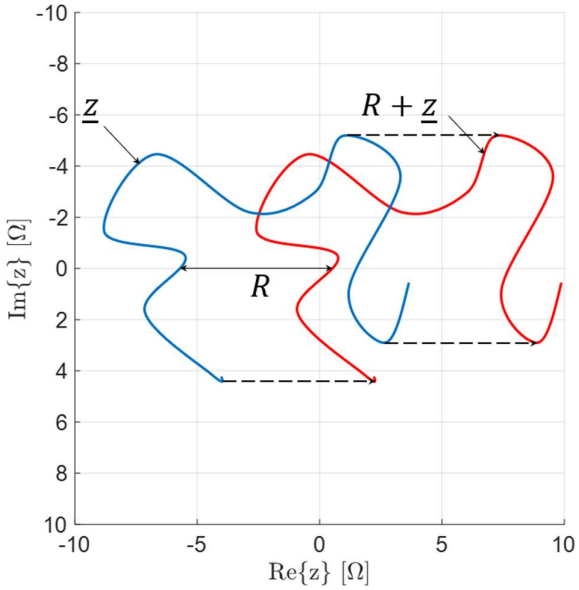


Figure 3.25 Effect of series resistance to impedance spectrum.

When it comes to a parallel combination of resistor and other elements, the new spectrum isn't easily obtained as in the case of series configuration, and even a shape is not preserved. For example, equations (3.18)-(3.20) describe the impedance of a parallel RC circuit.

$$\underline{z_{RC,\|}} = \frac{R}{1 + jRC\omega} \tag{3.18}$$

$$Re\{z_{RC,\|}\} = \frac{R}{1 + (wRC)^2} \tag{3.19}$$

$$Im\{z_{RC,\|}\} = -\frac{wR^2C}{1 + (wRC)^2} \tag{3.20}$$

With mathematical manipulations, the equations (3.19) and (3.20) can be combined into one:

$$\left(Re\{z_{RC,\|}\} - \frac{R}{2}\right)^2 + Im\{z_{RC,\|}\}^2 = \left(\frac{R}{2}\right)^2 \tag{3.21}$$

which represents the equation of a circle with centre (R/2,0) and R/2 radius, as shown in the left part of Figure 3.26. Of course, because $Im\{z_{RC,\|}\}$ is negative for all frequencies, only the upper semi-circle circle is considered. Therefore, a capacitor spectrum line is transformed into a semi-circle when paralleled with a resistor. Similarly, a parallel combination of CPE and resistor, also called ZARC (3.22), results in an interesting shape. Removing w from the equation, a new equation (3.23) is obtained. Therefore, a circuit composed of resistor and CPE produces a semi-depressed circle, i.e., an arc, as represented in the right part of Figure 3.26.

$$\underline{z_{RQ,\|}} = \underline{z_{ARC}} = R \parallel \frac{1}{Q(j\omega)^\alpha} = \frac{R}{1 + QR(j\omega)^\alpha} \tag{3.22}$$

$$\left(Re\{\underline{z_{ARC}}\} - \frac{R}{2}\right)^2 + \left(Im\{\underline{z_{ARC}}\} - \frac{R}{2}cot\left(\frac{\alpha\pi}{2}\right)\right)^2 = \left(\frac{R}{2}csc\left(\frac{\alpha\pi}{2}\right)\right)^2 \quad (3.23)$$

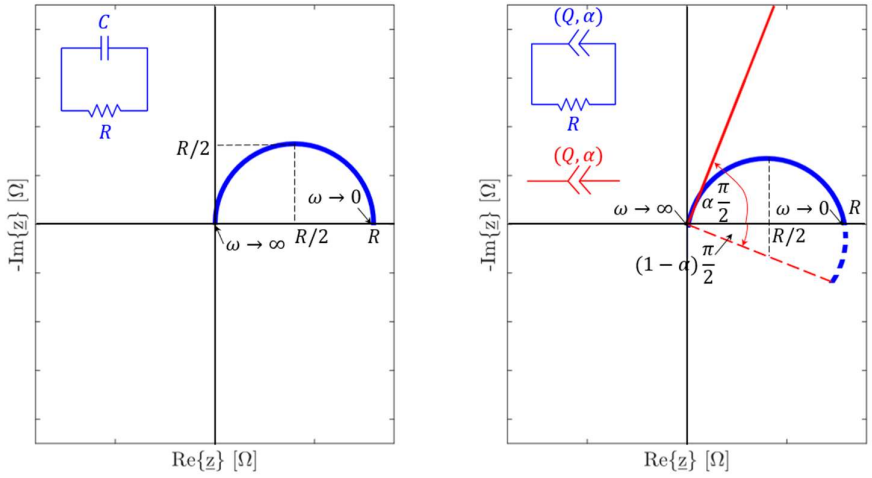


Figure 3.26 Spectrum of parallel RC circuit (left) and parallel RQ circuit, i.e., ZARC (right).

At this point, the spectrum from Figure 3.21 can be analysed, and an equivalent circuit can be constructed. First, at high frequencies (f>1kHz), electromagnetic phenomena dominate. The impedance graph intersects the real axis at almost -90° degrees which indicates inductive behaviour. Furthermore, the impedance plot is shifted to the right by a specific value, representing the instantaneous series resistance. Therefore, this impedance part can be modelled with a series RL circuit. Then, there is a middle frequency range (1kHz>f>1Hz) in which electrode kinetics, i.e., charge-transfer phenomena, are dominantly manifested. However, secondary effects such as double-layer capacitance can also appear. They are usually described with a depressed semicircle which is entirely modelled with a ZARC element. Finally, in the low-frequency range (f<1Hz), diffusion effects dominate the battery behaviour. This effect is usually characterised by a straight line with the 45° slope, i.e., Warburg impedance. However, that part can also be modelled as a constant phase element with different slope angles depending on the obtained spectrum. Thus, finally, the impedance network shown in Figure 3.27 can represent the battery behaviour accurately.

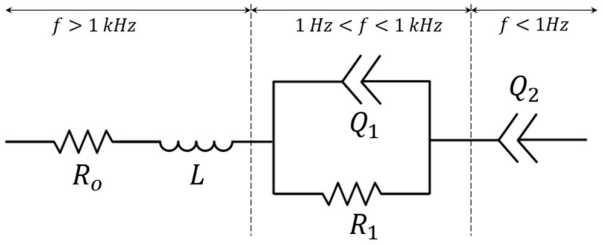


Figure 3.27 The ECM model using CPEs.

The above circuit represents a more generalised version of the historical Randles model (Figure 3.28), which modelled the middle-frequency range with a circle (i.e., parallel RC) and low-frequency diffusion with Warburg impedance.

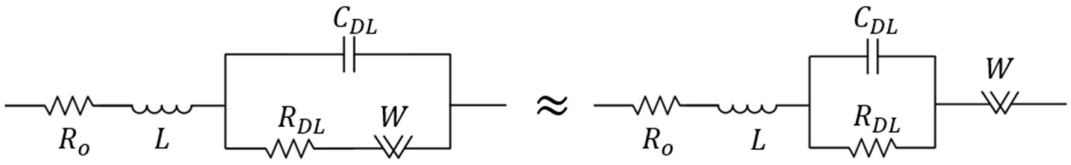


Figure 3.28 Randless model of battery and its approximation [172].

In both cases, the impedance of ZARC and parallel RC element collapses to a resistor in the low-frequency range, in addition to the inductor behaving as a short circuit. Therefore, Ro and R1 (or Rdl) can be combined in one resistor, i.e., total internal resistance and together with Q or W create a series RQ battery model as demonstrated in Figure 3.29.

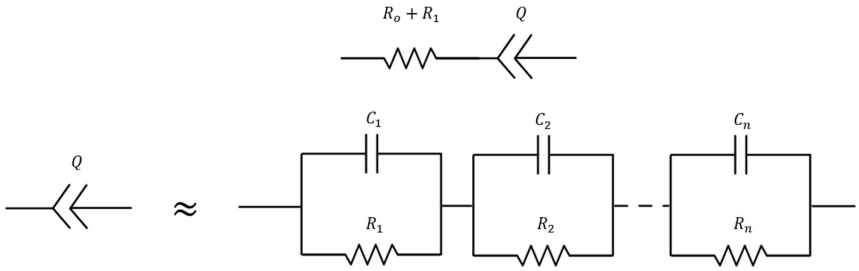


Figure 3.29 Reduced ECM (above) and CPE approximation (below).

However, both CPE and W cannot be simulated in commercial software of electric circuits. Consequently, their impedance cannot be analysed in the time domain. These circuits are analysed using fractional order calculus, in which these elements are ‘’solved’’ using definitions of Grünwald–Letnikov, Riemann–Liouville or Caputo [154]. Alternatively, the response of W and CPE elements can be approximated with several parallel RC circuits in series (Figure 3.29) [173], which leads to the well-known Thevenin equivalent circuit in Figure 3.30. In the case of $n = 0$, the circuit is commonly called the Rint model, which is usually used

for design purposes as it cannot represent the dynamic behaviour of the battery. For this purpose, the circuit with $n >= 1$ is used. Of course, depending on the accuracy, the number of RC circuit pairs will increase or decrease. Usually, 2 RC circuits represent a reasonable balance between the accuracy and time of the simulation.

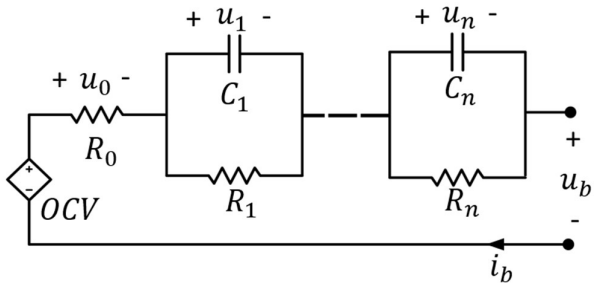


Figure 3.30 Thevenin ECM with n parallel RC pairs.

No matter what circuit is selected, commercial software such as Zfit can find the most appropriate circuit parameters to fit the obtained spectra for a given frequency range. However, as the Thevenin ECM consist of conventional electric circuit elements, they can also be parametrised using time-domain analysis, which is the topic of interest of the next section.

3.2.5.2 Time-domain impedance analysis

In frequency domain impedance analysis, the parameters of ECM are found so that the ECM has the identical impedance spectra as the battery's one obtained through EIS. Compared to the frequency method parameters of ECM in the time domain are found such that ECM and battery have the same voltage response for the predefined current profile. Therefore, a current profile is imposed to the battery system in a time-domain evaluation, and voltage response is measured and used for model parametrisation. Consequently, for the time domain method, an experiment must be performed in which the specific current profile is applied to the battery so that parameters can be extracted adequately.

It is essential to mention that for this procedure, the OCV must be known a priori. Thus, the voltage over impedance network can be known as the difference between OCV and measured terminal voltage, and in fact, the parameters are calculated such that voltage over impedance during the experiment matches the ECM's one. Additionally, the impedance parameters depend on the battery's SoC. Therefore, one of the objectives is to apply such a current pattern that can be used both for OCV and impedance parameter estimation with respect to SoC. Luckily, the OCV incremental extraction technique is also used for successful RC parameter estimation.

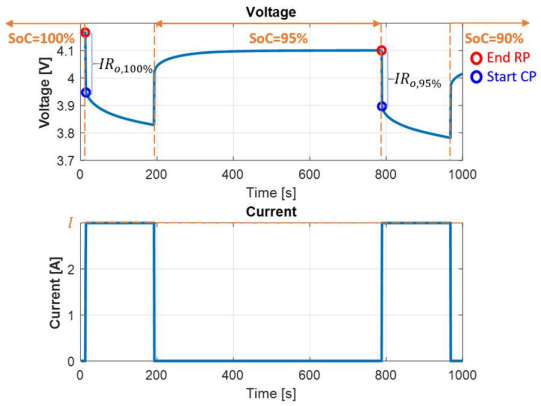


Figure 3.31 Incremental SoC identification [174].

In Figure 3.31, two current pulses decrease SoC by 5%, starting from 100%. As explained in section 3.2.4.2, OCV is obtained as the last point of rest period (RP) before applying the next current pulse. The instantaneous resistance can be calculated either from moment when the pulse is applied or from the instance when current is removed from the batter as:

$$R_o = \begin{cases} \dfrac{u_b(t_{pulse}^-) - u_b(t_{pulse}^+)}{I_b} \\ \dfrac{u_b(t_{relax}^+) - u_b(t_{relax}^-)}{I_b} \end{cases} \tag{3.24}$$

Once the OCV and Ro are known, the voltage of the RC circuit pairs (u_τ) can be calculated as in:

$$u_\tau = \sum_{i=1}^{N} u_i = OCV - R_o i_b - u_b \tag{3.25}$$

When u_τ is obtained, many techniques can be used to find R and C parameters. The most popular are analytical and curve-fitting methods [174]. Depending on whether current is present or not, a voltage of a parallel RC circuit can take one of the two forms:

$$u_{RC,\|} = \begin{cases} U_0 e^{-\frac{t}{RC}}, & I = 0 \\ RI + (U_0 - RI)e^{-\frac{t}{RC}} & I \neq 0 \end{cases} \tag{3.26}$$

where U_0 is the voltage initial condition. In case of analytical methods, numerous assumptions are made in order to simplify the calculations. First of all, most of the analytical methods focus on relaxation part of the voltage, as the equation describing that part is more convenient for analytical manipulation. Nonetheless, if multiple RC circuits are used assumptions about time constant are made. For instance, if the last part of the RP is analysed the assumption made is that response of the other RC circuits with faster time constants has subsided [175]. On the

other hand, the analytical method using current pulse (CP) are rarely used. Another common assumption is about the initial conditions. It is assumed that current and relax periods are long enough so that RC circuits reached their steady state. Contrary, the curve fitting method uses non-linear least squares. As the analytical equations that describe relaxation and pulse periods are known, curve fitting procedure returns as result parameters R and C that provide the best curve fit [176], [177]. Also, several assumptions are made during this technique, for example, completely ignoring the pulse period when analysing the relaxation phase.

In Chapter 5 of this thesis, the modelling technique that was developed rectifies the problems mentioned above. First, it considers the pulse and relaxation parts as unseparated processes, and as such, no assumptions are made regarding dynamics and initial conditions. Also, analysing CP allows investigation of current level on parameter variations, effectively creating parameter lookup tables that depend on current rate and SoC.

3.2.6 State of Charge

SoC is a state of battery that is physically related to the average concentration of active material ($c_{s,avg}$) remaining in the cell. In the case of lithium-ion batteries, that material is lithium. In a fully charged cell (SoC=100%), all lithium that participates in energy conversion is stored in the negative electrode. However, as already explained, the negative electrode is usually always oversized to prevent the ageing mechanisms that are dominant during undercharge and overcharge [178]. Therefore, the concentration level that corresponds to the fully charged state ($c_{s,avg,100\%}$) is always less than the maximum allowable lithium concentration in the negative electrode $c_{s,avg,max}$. Similarly, when fully discharged (SoC=100%) the concertation of lithium in negative electrode ($c_{s,avg,0\%}$) never reaches zero, $c_{s,avg,0\%} > 0$. Finally, the SoC can be defined as ratio:

$$SoC = \frac{c_{s,avg} - c_{s,avg,0\%}}{c_{s,avg,100\%} - c_{s,avg,0\%}} \tag{3.27}$$

Unfortunately, the average lithium concentration is a quantity that is not measurable, so SoC should be calculated using different approaches from quantities that can be observed, such as voltage and current. For example, the OCV(SoC) function is bijective, which means that only one SoC value exists for a single OCV value. Thus, if OCV is identified, then SoC is identified as well. However, OCV cannot also be measured during battery operation as measured terminal voltage equals OCV only when the battery has been at rest for a specific

amount of time. Therefore, most of the methods rely on current measurement in so-called Coulomb counting [153]. SoC at time t is defined as:

$$SoC(t) = SoC(t_0) - \frac{1}{Q_{tot}} \int_{t_0}^{t} \eta(\tau) I(\tau) d\tau \tag{3.28}$$

where $SoC(t_0)$ is the initial value of SoC at the time t_0, Q_{tot} is the total capacity of the battery, I is battery current ($I > 0$ during discharge, $I < 0$ during charge) and η coulombic efficiency ($\eta = 1$ during discharge, $\eta < 1$ during charge). Even though the coulomb counting method brings a lot of advantages compared to the electrochemical definition, several problems are countered in practice. First of all, the current measurement is never precise due to the presence of noise and sensor drifts. In the case of current sensor drift, the error would accumulate over time due to integrator in open loop and lead to unreliable SoC estimates. Furthermore, due to ageing effects Q_{tot} changes over time, also leading to incorrect SoC estimation. Finally, the initial value is seldom known in real-time applications unless the initial starting point is fully charged or discharged battery [140].

Hence, in applications such as electric vehicles, the coulomb counting method is combined with battery models in a closed-loop to improve the accuracy. Particle filters are statistical methods that estimate states under uncertainties such as noise. However, as particle filters cannot be conveniently implemented on a microcontroller, sequential probabilistic interference is used, with the most popular one being the Kalman filter [140]. The Kalman filtering iteration diagram is shown in Figure 3.32. Depending on the type of filter (linear, extended or unscented), initialisation, prediction, correction, and Kalman filter gain calculation blocks would have different equations. As already mentioned, a valid battery model should exist for this SoC technique that can be implemented on a microcontroller, usually an ECM, which can be represented in state space and discretised using standard methods. In brief, the Kalman filter works by comparing the measured battery voltage and predicted voltage. Then, the error is fed to the Kalman gain calculator used to correct the predictions for future calculations until the error between measured and predicted states falls under the acceptable predefined error boundary.

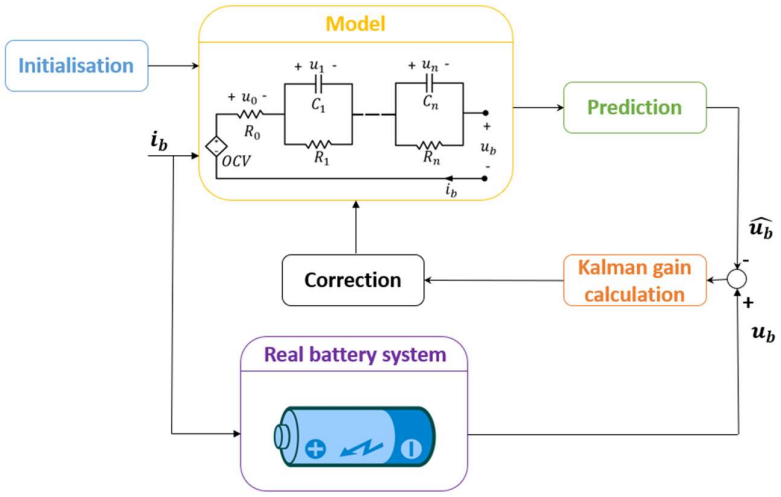


Figure 3.32 General Kalman filter iteration diagram.

3.2.7 Conclusion on battery modelling

Depending on the application or problem statement a suitable battery model can be selected. In Table 3.3 three presented modelling techniques are compared.

Table 3.3 Comparison of battery models.

	Complexity	Accuracy	Application
Electrochemical	Very high	Very High	Battery design, Degradation mechanism
Reduced order	High – very high	High – very high	Control, SOC estimation
ECM	Low- High	Low- High	Real time control and SoC estimation
Empirical	Low	Low	Constant current operation, cycling capacity fade, calendar aging

4 Chapter: Dynamic modelling of ETS's drive and model's employment

In Chapter 2, various ETSs were described: external ETS (Taxibot, Mototok etc.), geared NLG on-board ETS (Wheeltug and DLR) and geared MLG on-board ETS (EGTS). In this chapter, the last of five developed aircraft taxiing systems is explained in detail. The further analyses of ESS performance assume that aircraft is equipped with this particular ETS and hence, it is analysed and modelled in depth. The ETS under question came as a result of collaboration between the University of Nottingham (UoN) on one side and Safran, Airbus, Adeneo and DLR system under the CleanSky Joint Technology Initiative, for continuing the work of [179] and developing on-board ETS for MLG [180], [181]. The collaboration was primarily driven by the need for improving the ETS reliability while minimising its overall weight. Hence, the direct-drive solution was selected as the most appropriate one.

The developed ETS consists of two high torque density gear-less traction machines (TMs), each mounted directly inside the wheel of the respective MLG (i.e., left 'L' and right 'R'). The TM is a double star three-phase Permanent Magnet Synchronous Motor (PMSM) powered from two separate 2-level voltage source inverters (VSIs) connected to the same DC-link of 540 V, as depicted in Figure 4.1 [182]. In Figure 4.1, the APU S/G and ESS are connected to the DC link with dashed black lines only indicating possible options of HET (APU S/G only), HET+ (APU S/G and ESS) and AET (ESS only).

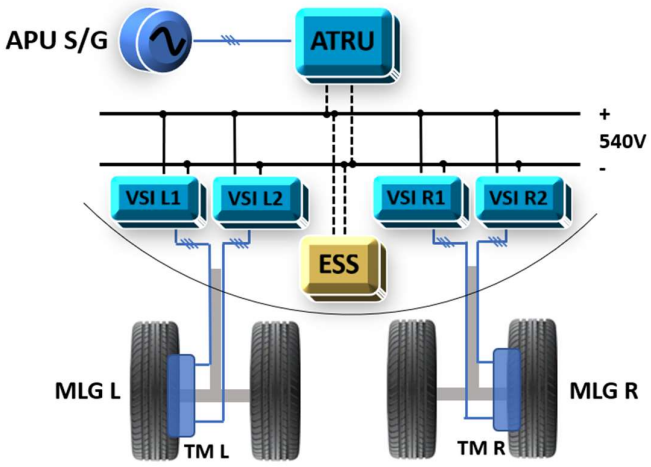


Figure 4.1 The direct drive ETS system developed by the University of Nottingham and Co.

The proposed TM was first tested at the UoN laboratories using commercial power converters and a dSPACE microcontroller platform. In Figure 4.2, the assembled TM coupled

on the testing angle plate is shown, where the gearbox is only used for testing purposes to cope with the load machine rated torque. After the preliminary tests at UoN facilities, the TM was fed by the power electronics converters developed by Adeneo and controlled with the control algorithm written by the DLR. The second stage of the test campaign was carried out in Safran Landing Systems laboratories in France, where the whole electric drive system was tested up to TRL5 standards in a realistic environment [21].

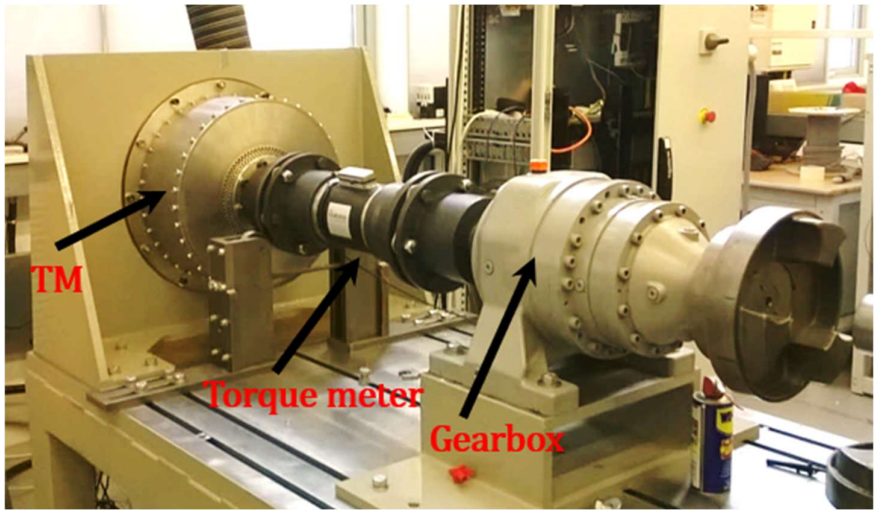


Figure 4.2 The test bed for analysis of electric drive system at the UoN.

4.1 The TM description

The implementation of TM inside the MLG represents significant challenge due to the confined and limited space available in the gear cavity. Considering as benchmark aircraft an Airbus A320, the back and front envelopes of its MLG were identified as suitable locations for the TM since two twin TMs could be fitted, as highlighted in Figure 4.3. To deal with the demanding space requirements, a PMSM was selected due to the superior power density compared to other electrical machine topologies.

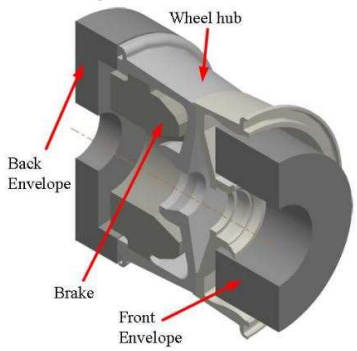


Figure 4.3 Wheel hub of the A320 MLG [179].

The TM design process led to a machine featuring a record-holding peak torque density of 65 Nm/kg (the number refers to the active weight of 108 kg with 7 kNm peak torque) [181], resulting in a total torque at wheels of 14 kNm. These superb values were achieved by implementing several torque enhancement techniques [183], [184]. Firstly, an outer rotor configuration was preferred to the more conventional inner rotor arrangement for the reasons listed below:

• Assuming electrical machines with similar performance characteristics, outer rotor motors are axially shorter than their inner rotor counterpart enabling a more compact design that is more suitable for in-wheel operations. Additionally, a bigger rotor eases the coupling between motor and wheel for the specific application at hand.

• Comparing electrical machines with the same external diameter, the outer rotor configuration is characterised by a longer radius at the air gap than the inner rotor one. Such particularity positively impacts the torque production, making the outer rotor appropriate for direct-drive applications.

Considering the PMs layout, a five-stage Halbach array configuration, represented in Figure 4.4, was favoured because a stronger magnetic field is produced with the same PM volume. Hence, a higher flux density at the air gap is achieved, resulting in enhanced torque capability. Although the indisputable benefit of the Halbach array arrangement, it is also true that its employment adds manufacturing complexity and inflates the TM cost. The selection of materials played a critical role in pushing the torque density performance of the designed TM. Advanced materials such as Cobalt Iron for the stator and rotor core laminations and Samarium Cobalt for the PMs were chosen, with a remanence field of 1.04 T. The former features very high saturation limits, thus extending the magnetic loading, while the latter provides outstanding performance at high operating temperatures. Indeed, due to the location of the TM, only a forced-air cooling system was allowed for thermal management. Hence PMs are likely to experience high temperatures, which might be a source of demagnetisation issues.

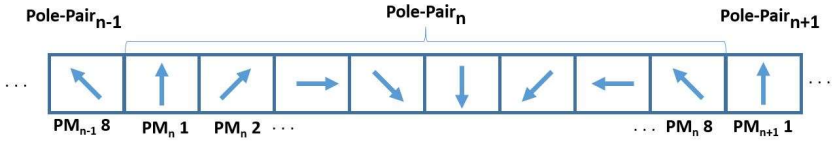


Figure 4.4 Magnetisation direction of PMs inside five-stage Halbach array configuration.

Apart from the significant torque density level, the TM should ensure a satisfactory availability due to the safety-critical nature of the application under study. Therefore, a double

star winding configuration (i.e., dual-channel power lane) was adopted to improve the fault-tolerant ability of the TM. The machine adopts asymmetric configuration in which two stars are displaced by 30°. This choice is preferable than symmetrical configuration (60° displacement between stars) also for the reasons of improved fault-tolerant ability [185].

The challenges caused by the landing and take-off speeds were addressed by short-circuiting the TM winding terminals at the VSI level. This strategy is feasible because the TM is designed according to a fault-tolerant approach. Indeed, the maximum absolute value of braking torque occurs at very low speed, and the ensuing short-circuit current is contained below the TM rated value. On the one hand, such design choice allows mitigating the risks associated with the short circuit currents (i.e., over-temperature and permanent magnet demagnetisation). On the other hand, the resulting braking torque value at the aircraft landing and take-off speeds is relatively low (i.e., well below the TM rated torque) that can be easily overcome by the jet engines' thrust during take-off. The parameters of the manufactured TM are given in Table 4.1.

Table 4.1 The parameters of the designed TM.

Parameter	Value
Slots/poles	36/42
I_{max} [A]	223
T_{max} [kNm]	7
Remanent PM flux density [T]	1.04
PM/Laminations material	SaCo/CoFe
DC link voltage [V]	540

4.2 2D Finite Element Model of TM

This chapter aims to develop the whole ETS's model, including aircraft dynamics and formulation of control systems. Firstly, to obtain a dynamic model of the machine, the TM model in MagNet finite element software is created. The scripting procedure was used because it allowed for more accessible parameters' modifications such as speed, d-axis and q-axis currents, simulation parameters (such as mesh size and time step) etc. The FE model also allowed for a better understanding of the machine's working principles and performance analysis, in addition to the acquisition of parameters necessary for obtaining the analytical model such as inductance matrix and permanent flux density. Figure 1.5 presents the construction slice lines/arcs of the model, whereas the total model with construction slice surfaces is shown in Figure 4.6. In Figure 4.7, 1/3 section of the model shows the phase windings distribution illustrating distinct slot concentrated double-layer configuration. Also, the magnetisation direction of one pole pitch is shown. In the following sections, the developed

model is employed to analyse the machine's performance and gather parameters necessary for dynamic model establishment.

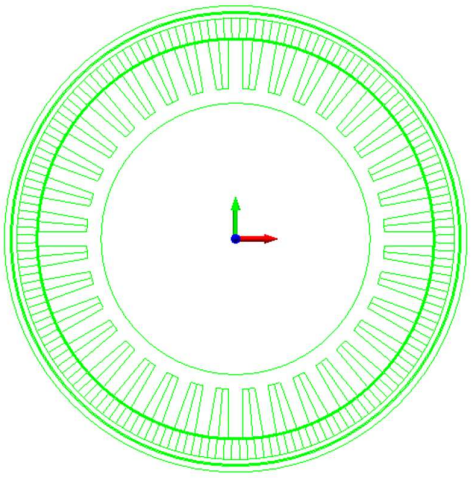


Figure 4.5 Construction slice line/arcs of the 2D FE model.

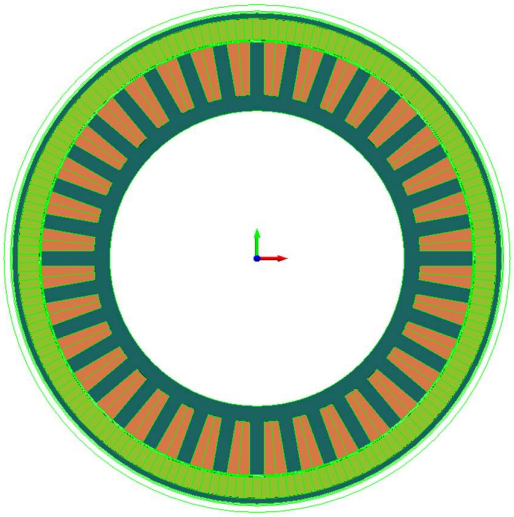


Figure 4.6 Construction slice surfaces of the 2D FE model.

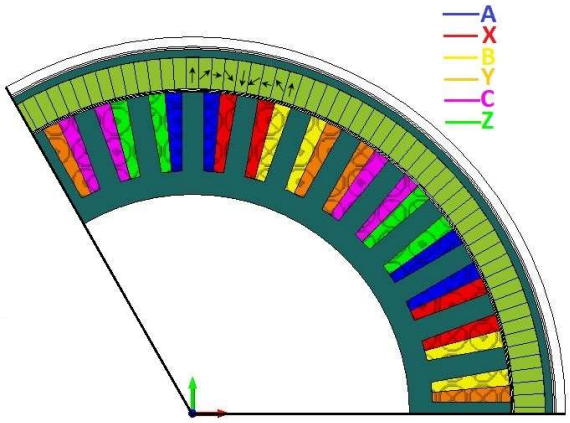


Figure 4.7 A 1/3 of the 2D FE model illustrating magnetisation directions and phase windings arrangement.

4.3 Performance analysis of the TM and parameters calculation

4.3.1 No-load analysis

No-load operation of PMSM consists in speed driven shaft with open phase windings, i.e., no current applied to them. Due to the presence of PMs, stator windings are exposed to the time varying flux linkage, hence, quantities that can be obtained from no-load analysis are the phase back-emf and PM flux linkage. Eight different simulations with speeds from 20 to 160 rpm with step of 20 rpm were performed to analyse no-load operation. PM flux linkage amplitude is a parameter that does not depend on the speed, and the waveforms are shown in Figure 4.8.

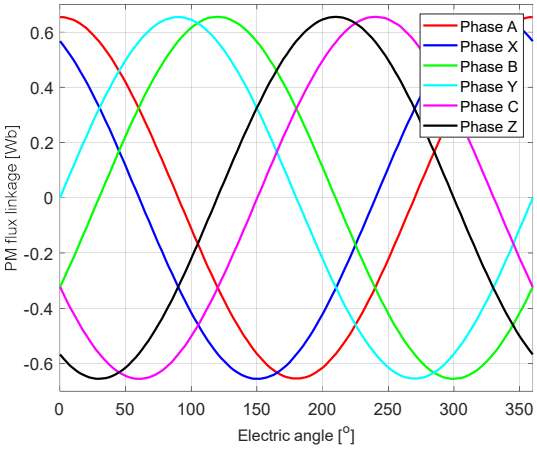


Figure 4.8 PM flux linkage during no-load analysis.

The peak value is $\psi_{pm} = 0.654$ Wb and it can be noticed that waveforms of the 2nd star (*xyz*) are shifted by +30°. Thus, the PM flux linkage can be written in vector form as in (4.1) where ω_e is electric speed in rad/s.

$$[\boldsymbol{\psi_{pm}}] = \begin{bmatrix} \psi_{pm,a} \\ \psi_{pm,b} \\ \psi_{pm,c} \\ \psi_{pm,x} \\ \psi_{pm,y} \\ \psi_{pm,z} \end{bmatrix} = \psi_{pm} \begin{bmatrix} sin\,(\omega_e t + \varphi_a) \\ sin\,(\omega_e t + \varphi_a - 120°) \\ sin\,(\omega_e t + \varphi_a + 120°) \\ sin\,(\omega_e t + \varphi_a + 30°) \\ sin\,(\omega_e t + \varphi_a - 90°) \\ sin\,(\omega_e t + \varphi_a + 150°) \end{bmatrix} \tag{4.1}$$

In Figure 4.9 the back-emf of phase a with 8 different speeds is shown, whereas in Figure 4.10 back-emf of all phases for the speed of 120 rpm are shown. This allows to extract the back-emf constant as 0.64 Vs/radel or 13.5 Vs/radmech. In [186], the back-emf was experimentally measured for 80.8 rpm which resulted in value slightly lower than 110V, whereas 3D FE returned slightly above 116V, compared to 2D FE model developed in this work which returned 114V. The error of 3.63% can be attributed to machine and assembly tolerances.

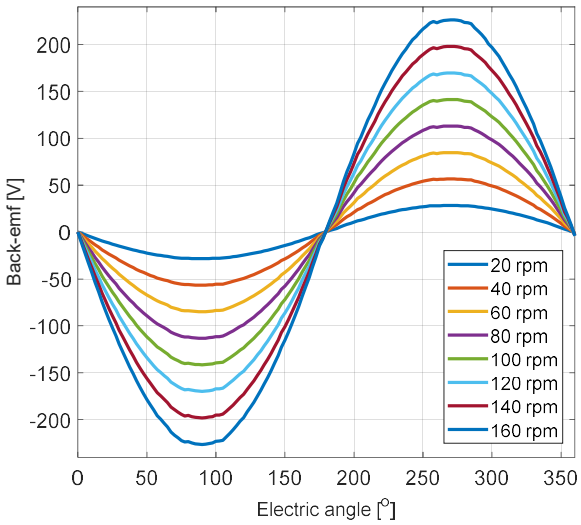


Figure 4.9 Back-emf of phase a for eight different speeds.

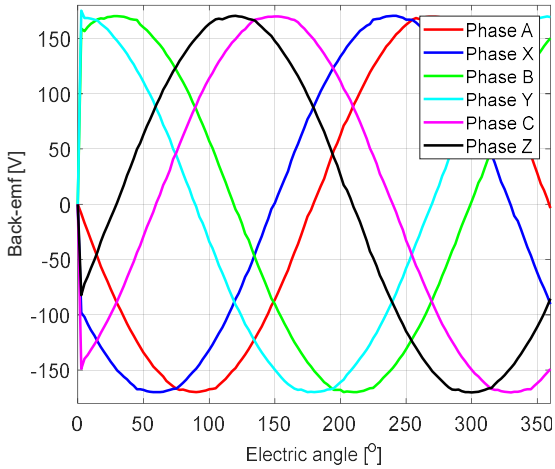


Figure 4.10 Back-emf of all six phases for fixed speed of 120 rpm.

4.3.2 Torque versus current

The torque and torque constant for symmetrical operation (i.e., both stars are fed with the same currents) are shown in Figure 4.11 for nine different values of i_q, from 25 A to 223 A in steps of 25 A. It can be noticed that the saturation effect becomes dominant after 100 A. For example, the torque constant value drops from 41 Nm/A to 31.4 Nm/A for maximum allowable current of 223 A, representing a drop of 23.4%. In Figure 4.12 torque and torque constant for single-star operation are shown. As expected, with only one star being powered, the saturation occurs with higher currents levels (around 175 A) and hence the drop in torque constant for 223 A is only 9.2%, compared to 23.4% when both stars are powered. In this thesis, the operation of machine always assumes symmetrically powered stars.

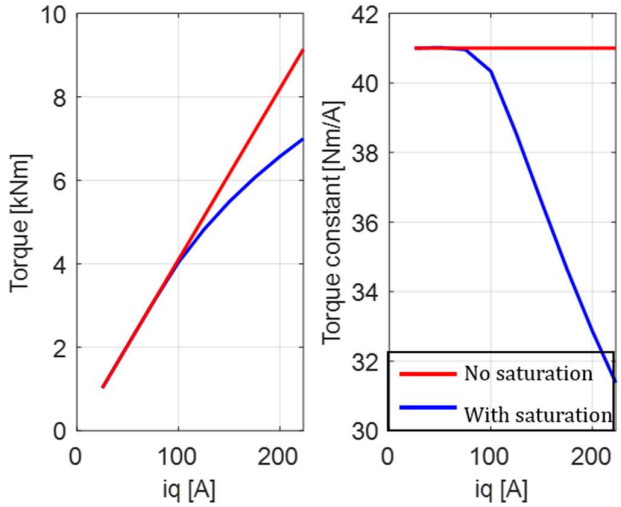


Figure 4.11 Torque (left) and torque constant (right) versus i_q for $i_d = 0$ for symmetrical operation.

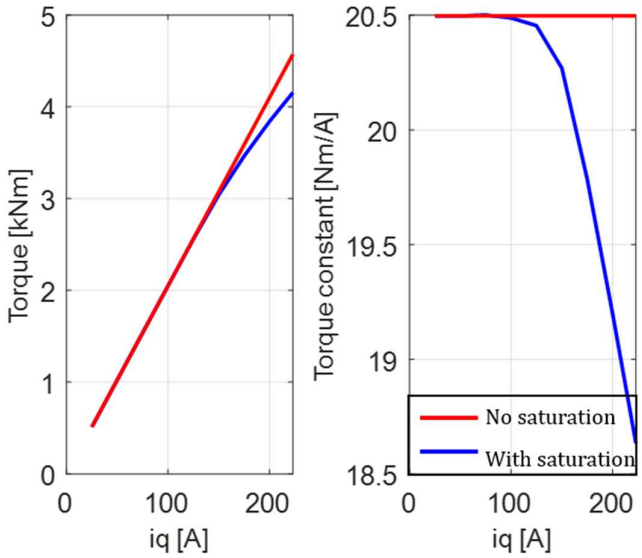


Figure 4.12 Torque (left) and torque constant (right) versus i_q and $i_d = 0$ for single-star operation.

The effect of negative d-axis current on torque performance was also investigated. Two i_d values of -50 A and -100 A with i_q values of up to 200 A in steps of 25 A. The results are shown in Figure 4.13. During operations in linear mode, the injection of i_d current doesn't change the torque value as expected since machine doesn't have saliency. However, in saturation region the anisotropy and consequently the reluctance torque ensue. Therefore, the torque constant of this machine is described as multivariable function of i_q and i_d, $k_t(i_q, i_d)$.

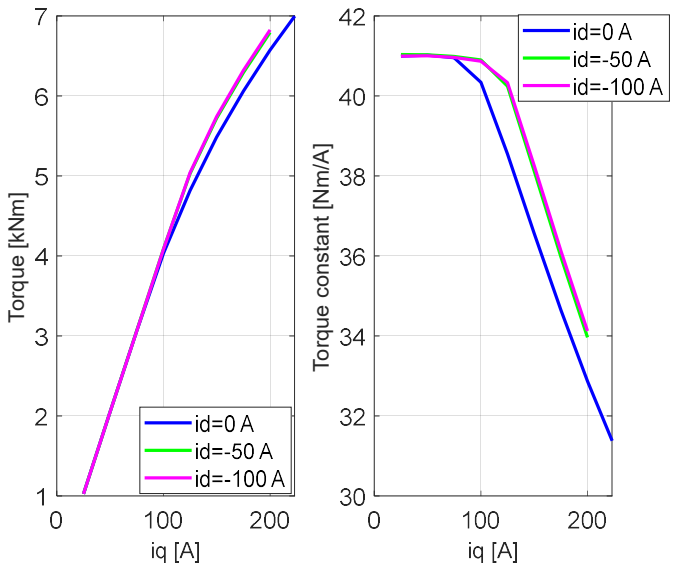


Figure 4.13 Torque (left) and torque constant (right) versus i_q for different i_d values during symmetrical operation.

In terms of phase voltages, at 80.8 rpm and with $i_q = 223\text{A}$, $i_d = 0$ the peak voltage achieves 270 V which means that DC link voltage limit of 540V is reached and further increase in speed should require field weakening. The power at which this happens is 59.2 kW.

4.3.3 Efficiency map

Efficiency map is a useful tool when evaluating the performance of machines that operate with dynamic duty cycles, such as traction application. The efficiency map is plotted in terms of contour plots imposed on a shaft torque-speed plane (T, Ω). Practically, it informs about the efficiency of each operating point. Therefore, a set of simulations with different torque values (i.e., i_q values) and speeds must be performed. In total 61 simulations were performed with speeds between 20 rpm and 160 rpm and step of 20 rpm. 36 simulations were carried out in constant torque region and additional 25 simulations in constant power mode considering the power limit of 60 kW. The winding ohmic and lamination iron losses are calculated in each of the 61 simulations and are added to the shaft power in order to evaluate efficiency at those certain operating points using (4.2), where Ω is the mechanical speed. The mechanical losses due to application's low speed are neglected. A 2D interpolation technique is used to obtain efficiency over the whole torque-speed plane. The efficiency map of the machine is shown in Figure 4.14.

$$\eta(T, \Omega) = \frac{T\Omega}{T\Omega + P_{cu} + P_{Fe}} \tag{4.2}$$

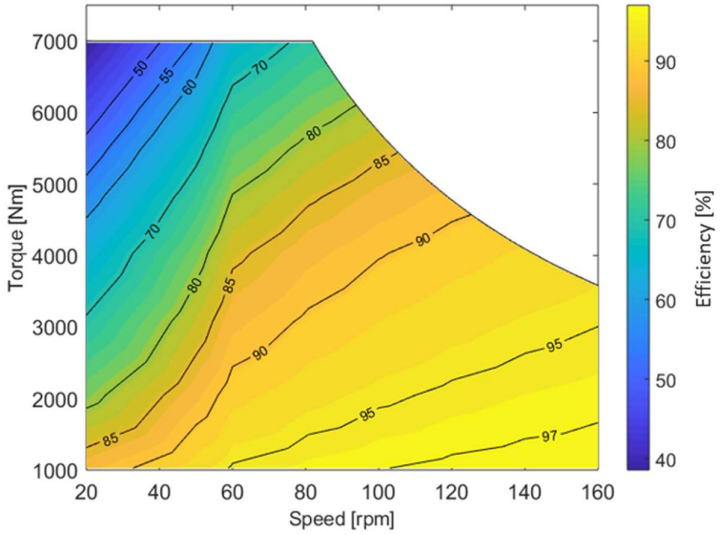


Figure 4.14 The efficiency map of the TM.

4.3.4 Inductances and resistance

Inductances are one of the most important parameters of any electric machine. The flux linkage of one phase of electric machine arises due to current flow in that phase, current flow in other phases, and due to flux created by PMs. Therefore, the flux linkage of phase j (ψ_j) in a machine that has n phases can be expressed as in equation (4.3):

$$\psi_j = \sum_{k=1}^{n} L_{jk} i_k + \psi_{pm,j}, \qquad j = 1,2,\dots,n \tag{4.3}$$

where $L_{jk} i_k$ represents the flux created in phase j due to current flow in phase k. If $j = k$, the L_{jk} is called a self-inductance of phase j and if $j \neq k$ it is called mutual inductance between phases j and k. Finally, $\psi_{pm,j}$ is the flux linkage due to PMs already defined in (4.1). In case of six-phase machine, equation (4.3) can be written in a more usual matrix form as below:

$$\begin{bmatrix}\psi_a\\ \psi_b\\ \psi_c\\ \psi_x\\ \psi_y\\ \psi_z\end{bmatrix} = \begin{bmatrix} L_{aa} & L_{ab} & L_{ac} & M_{ax} & M_{ay} & M_{az}\\ L_{ba} & L_{bb} & L_{bc} & M_{bx} & M_{by} & M_{bz}\\ L_{ca} & L_{cb} & L_{cc} & M_{cx} & M_{cy} & M_{cz}\\ M_{xa} & M_{xb} & M_{xc} & L_{xx} & L_{xy} & L_{xz}\\ M_{ya} & M_{yb} & M_{yc} & L_{yx} & L_{yy} & L_{yz}\\ M_{za} & M_{zb} & M_{zc} & L_{zx} & L_{zy} & L_{zz}\end{bmatrix}\begin{bmatrix}i_a\\ i_b\\ i_c\\ i_x\\ i_y\\ i_z\end{bmatrix} + \begin{bmatrix}\psi_{pm,a}\\ \psi_{pm,b}\\ \psi_{pm,c}\\ \psi_{pm,x}\\ \psi_{pm,y}\\ \psi_{pm,z}\end{bmatrix} \tag{4.4}$$

or more conveniently in a vector format

$$[\boldsymbol{\psi}] = \underline{[\boldsymbol{L}]}[\boldsymbol{i}] + [\boldsymbol{\psi_{pm}}] \tag{4.5}$$

where $[\boldsymbol{\psi}]$ and $[\boldsymbol{i}]$ are 6x1 vectors of flux linkage and current respectively,

$$[\boldsymbol{i}] = [i_a \quad i_b \quad i_c \quad i_x \quad i_y \quad i_z]^T;\ [\boldsymbol{\psi}] = [\psi_a \quad \psi_b \quad \psi_c \quad \psi_x \quad \psi_y \quad \psi_z]^T \tag{4.6}$$

and $\underline{[\boldsymbol{L}]}$ is the inductance matrix 6x6 written in a block matrix form as

$$\underline{[\boldsymbol{L}]} = \begin{bmatrix} \underline{[\boldsymbol{L_{abc,s1}}]}_{3x3} & \underline{[\boldsymbol{M_{s1s2}}]}_{3x3} \\ \underline{[\boldsymbol{M_{s2s1}}]}_{3x3} & \underline{[\boldsymbol{L_{xyz,s2}}]}_{3x3} \end{bmatrix} \tag{4.7}$$

Matrices $\underline{[\boldsymbol{L_{abc,s1}}]}$ and $\underline{[\boldsymbol{L_{xyz,s2}}]}$ represent the self-inductances and mutual inductances between phases of single stars *abc* (star 1) and *xyz* (star 2) respectively. Similarly, matrices $\underline{[\boldsymbol{M_{s1s2}}]}$ and $\underline{[\boldsymbol{M_{s2s1}}]}$ represent the coupling between phases of different stars, i.e., mutual inductances between phases of stars 1 and 2 respectively.

Another notation commonly used is $\boldsymbol{f_{abc,s1}}$ and $\boldsymbol{f_{xyz,s2}}$ where $\boldsymbol{f}$ represents either voltage, current or flux linkage 3x1 vector of star 1 and 2 respectively as in:

$$[\boldsymbol{f}_{\boldsymbol{abc,s1}}] = [f_a\ f_b\ f_c]^T; [\boldsymbol{f}_{\boldsymbol{xyz,s2}}] = \left[f_x\ f_y\ f_z\right]^T \tag{4.8}$$

Therefore, flux equations of both stars can be written as:

$$\left[\boldsymbol{\psi}_{\boldsymbol{abc,s1}}\right] = \underline{\left[\boldsymbol{L}_{\boldsymbol{s,abc}}\right]}\left[\boldsymbol{i}_{\boldsymbol{abc,s1}}\right] + \underline{\left[\boldsymbol{M}_{\boldsymbol{s1s2}}\right]}\left[\boldsymbol{i}_{\boldsymbol{xyz,s2}}\right] + \left[\boldsymbol{\psi}_{\boldsymbol{pm,abc,s1}}\right] \tag{4.9}$$

$$\left[\boldsymbol{\psi}_{\boldsymbol{abc,s2}}\right] = \underline{\left[\boldsymbol{L}_{\boldsymbol{s,xyz}}\right]}\left[\boldsymbol{i}_{\boldsymbol{xyz,s2}}\right] + \underline{\left[\boldsymbol{M}_{\boldsymbol{s2s1}}\right]}\left[\boldsymbol{i}_{\boldsymbol{abc,s1}}\right] + \left[\boldsymbol{\psi}_{\boldsymbol{pm,xyz,s2}}\right] \tag{4.10}$$

Finite element analysis is used to find each element of the afore-mentioned matrices. From (4.3), it is apparent that inductance L_{jk} can be calculated as

$$L_{jk} = \left.\frac{\psi_j}{i_k}\right|_{\psi_{pm}=0, i_m=0}, m = \overline{1,n}\ except\ k \tag{4.11}$$

Therefore, a set of simulations in which PMs are ‘’turned off’’, and only one phase excited with DC current are carried out to calculate the elements of inductance matrix. For example, by exciting the phase b with DC current and measuring flux in all other phase, the second row of matrix $\underline{[\boldsymbol{L}]}$ can be calculated.

After performing the set of simulations and analysing the results, the matrices take form of the following configuration:

$$\underline{\left[\boldsymbol{L}_{\boldsymbol{s,abc}}\right]} = \begin{bmatrix} L_s & 0 & 0 \\ 0 & L_s & 0 \\ 0 & 0 & L_s \end{bmatrix}, \underline{\left[\boldsymbol{L}_{\boldsymbol{s,xyz}}\right]} = \begin{bmatrix} L_s & 0 & 0 \\ 0 & L_s & 0 \\ 0 & 0 & L_s \end{bmatrix} \tag{4.12}$$

$$\underline{\left[\boldsymbol{M}_{\boldsymbol{s1s2}}\right]} = \begin{bmatrix} M_s & 0 & -M_s \\ -M_s & M_s & 0 \\ 0 & -M_s & M_s \end{bmatrix}, \underline{\left[\boldsymbol{M}_{\boldsymbol{s2s1}}\right]} = \begin{bmatrix} M_s & -M_s & 0 \\ 0 & M_s & -M_s \\ -M_s & 0 & M_s \end{bmatrix} \tag{4.13}$$

where $L_s = 3.95$ mH and $M_s = 1.03$ mH. From above, it can be noticed that there is no coupling between phases of the same star, i.e., self-inductance matrices are diagonal. However, there is coupling between certain phase pairs of different stars. For example, phase *a* is coupled with phases *x* and *z* and not to *y*. The reason for weak coupling is due to the use of double-layer fractional slot windings where a phase is coupled only to neighbouring phases which in case of phase *a* are *x* and *z*. In [186], 3D FE reported phase inductance of 4 mH whereas the measured one was 4.2 mH which represents good agreement.

Finally, the phase resistance has been calculated using ohmic losses in copper obtained from MagNet simulations using equation (4.14). Averaging over all simulations, phase resistance amounts to $R = 0.158\ \Omega$.

$$R = \frac{P_{cu,total}/6}{I_{rms}^2} = \frac{P_{cu,total}}{3I_{peak}^2} \tag{4.14}$$

4.4 QD Model development

Numerous modelling methods of 6-phase machine exist, but the two most widespread ones are vector space decomposition (VSD) and two-individual three-phase method [187]. The latter one assumes modelling in *qd0* frame and it is more favorable if the machine is powered from two separate inverters [188], thus this modelling approach has been selected in this thesis. The modelling process slightly differs from the standard procedure as for conventional 3-phase machines, due to the additional phase coupling induced by the second set of 3-phase winding. Nonetheless, all rotating vectors are projected to the unique *qd0* reference frame with d-axis aligned with the vector of PM flux linkage, where angle θ is measured from the magnetic axis of phase *a* to the q-axis as in [189] (Figure 4.15).

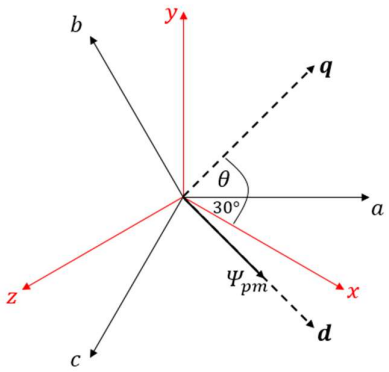


Figure 4.15 *qd0* frame orientation.

Matrix $[\boldsymbol{K}(\theta)]$, which transforms *abc* to *qd0* variables, is defined in (4.15), whereas the transformation matrix associated to the variables of winding *xyz* is $[\boldsymbol{K}(\theta + 30°)]$ [190]. Transformation equations are presented in (4.16) and (4.17), where $\boldsymbol{f}_{qd0} = [f_q\ f_d\ f_0]^T$ represents either current, voltage or flux linkage values in rotating reference frame and the subscripts s1 and s2 stand for the winding sets *abc* and *xyz* respectively.

$$[\boldsymbol{K}(\theta)] = \frac{2}{3}\begin{bmatrix} cos(\theta) & cos(\theta - \frac{2\pi}{3}) & cos(\theta + \frac{2\pi}{3}) \\ sin(\theta) & sin(\theta - \frac{2\pi}{3}) & sin(\theta + \frac{2\pi}{3}) \\ \frac{1}{2} & \frac{1}{2} & \frac{1}{2} \end{bmatrix} \tag{4.15}$$

$$[\boldsymbol{f}_{qd0,s1}] = [\boldsymbol{K}(\theta)][\boldsymbol{f}_{abc}], [\boldsymbol{f}_{abc}] = [\boldsymbol{K}(\theta)]^{-1}[\boldsymbol{f}_{qd0,s1}] \tag{4.16}$$

$$[\boldsymbol{f}_{qd0,s2}] = [\boldsymbol{K}(\theta + 30°)][\boldsymbol{f}_{xyz}], /\boldsymbol{f}_{xyz}] = [\boldsymbol{K}(\theta + 30°)]^{-1}[\boldsymbol{f}_{qd0,s2}] \tag{4.17}$$

It is well-known that time domain phase voltage equation of PM machine (4.18) transfers into *qd0* domain as equation (4.19) where ω_e represents electric speed, i.e., $p\Omega$.

$$[\boldsymbol{v}] = [\boldsymbol{R}][\boldsymbol{i}] + \frac{d[\psi]}{dt} = [R][i] + \frac{d}{dt}([\boldsymbol{L}][\boldsymbol{i}] + [\boldsymbol{\psi_{pm}}]) \tag{4.18}$$

$$\downarrow$$

$$\left[v_{qd0}\right] = [R]\left[i_{qd0}\right] + \frac{d\left[\psi_{qd0}\right]}{dt} + \omega_e\left[\psi_{qd}\right];\ \left[\psi_{qd}\right] = \begin{bmatrix} \psi_d \\ -\psi_q \\ 0 \end{bmatrix} \tag{4.19}$$

In case of two stars the equations become:

$$\left[v_{qd0,s1}\right] = [R]\left[i_{qd0,s1}\right] + \frac{d\left[\psi_{qd0,s1}\right]}{dt} + \omega_e\left[\psi_{qd,s1}\right];\ \left[\psi_{qd,s1}\right] = \begin{bmatrix} \psi_{d,s1} \\ -\psi_{q,s1} \\ 0 \end{bmatrix} \tag{4.20}$$

$$\left[v_{qd0,s2}\right] = [R]\left[i_{qd0,s2}\right] + \frac{d\left[\psi_{qd0,s2}\right]}{dt} + \omega_e\left[\psi_{qd,s2}\right];\ \left[\psi_{qd,s2}\right] = \begin{bmatrix} \psi_{d,s2} \\ -\psi_{q,s2} \\ 0 \end{bmatrix} \tag{4.21}$$

where $[\boldsymbol{\psi_{qd0,s1}}] = [\boldsymbol{K}(\theta)][\boldsymbol{\psi_{abc}}]$ and $[\boldsymbol{\psi_{qd0,s2}}] = [\boldsymbol{K}(\theta + 30)]\left[\boldsymbol{\psi_{xyz}}\right]$. Therefore, using (4.16), (4.17) and (4.20) flux linkage of star 1 in *qd0* domain can be expressed as:

$$[\boldsymbol{\psi_{qd0,s1}}] = [\boldsymbol{K}(\theta)]\underline{[\boldsymbol{L_{abc}}]}[\boldsymbol{i_{abc}}] + [\boldsymbol{K}(\theta)]\underline{[\boldsymbol{M_{s1s2}}]}\left[\boldsymbol{i_{xyz}}\right] + [\boldsymbol{K}(\theta)]\left[\boldsymbol{\psi_{pm,abc}}\right] \tag{4.22}$$

First and second term of the above equation can be further expanded as:

$$\begin{aligned}[\boldsymbol{\psi_{qd0,s1}}] = {} & [\boldsymbol{K}(\theta)]\underline{[\boldsymbol{L_{abc}}]}[\boldsymbol{K}(\theta)]^{-1}\left[\boldsymbol{i_{qd0,s1}}\right] \\ & + [\boldsymbol{K}(\theta)]\underline{[\boldsymbol{M_{s1s2}}]}[\boldsymbol{K}(\theta + 30)]^{-1}\left[\boldsymbol{i_{qd0,s2}}\right] + [\boldsymbol{\psi_{qd0,s1,pm}}]\end{aligned} \tag{4.23}$$

whereas third term becomes

$$[\boldsymbol{\psi_{qd0,s1,pm}}] = \left[0\ \psi_{pm}\ 0\right]^T \tag{4.24}$$

Similarly, the same procedure can be done for the star 2, and therefore, the final flux equation of the machine in *qd0* frame is written as below:

$$\begin{bmatrix} \boldsymbol{\psi_{qd0,s1}} \\ \boldsymbol{\psi_{qd0,s2}} \end{bmatrix} = \underline{\left[\boldsymbol{L_{qd0}}\right]}\begin{bmatrix} \boldsymbol{i_{qd0,s1}} \\ \boldsymbol{i_{qd0,s2}} \end{bmatrix} + \begin{bmatrix} \boldsymbol{\psi_{qd0,s1,pm}} \\ \boldsymbol{\psi_{qd0,s1,pm}} \end{bmatrix} \tag{4.25}$$

in which

$$\begin{aligned}&\underline{\left[\boldsymbol{L_{qd0}}\right]} \\ &= \begin{bmatrix} [\boldsymbol{K}(\theta)]\underline{[\boldsymbol{L_{abc}}]}[\boldsymbol{K}(\theta)]^{-1} & [\boldsymbol{K}(\theta)]\underline{[\boldsymbol{M_{s1s2}}]}[\boldsymbol{K}(\theta + 30°)]^{-1} \\ [\boldsymbol{K}(\theta + 30°)]\underline{[\boldsymbol{M_{s2s1}}]}[\boldsymbol{K}(\theta)]^{-1} & [\boldsymbol{K}(\theta + 30°)]\underline{\left[\boldsymbol{L_{xyz}}\right]}[\boldsymbol{K}(\theta + 30°)]^{-1} \end{bmatrix}\end{aligned} \tag{4.26}$$

$$\begin{bmatrix} \boldsymbol{\psi_{qd0,s1,pm}} \\ \boldsymbol{\psi_{qd0,s1,pm}} \end{bmatrix} = \begin{bmatrix} 0 & \psi_{pm} & 0 & 0 & \psi_{pm} & 0 \end{bmatrix}^T \tag{4.27}$$

Each of the blocks of the $\underline{\boldsymbol{[L_{qd0}]}}$ represents specific inductance matrix in *qd0* domain. By applying matrix multiplications, the resulting matrices in *qd0* domain become diagonal:

$$\boldsymbol{[L_{qd0,s1}]} = [\boldsymbol{K}(\theta)]\underline{\boldsymbol{[L_{abc}]}}[\boldsymbol{K}(\theta)]^{-1} = \begin{bmatrix} L_{q1} & 0 & 0 \\ 0 & L_{d1} & 0 \\ 0 & 0 & L_{01} \end{bmatrix} \tag{4.28}$$

$$\boldsymbol{[L_{qd0,s2}]} = [\boldsymbol{K}(\theta + 30°)]\underline{\boldsymbol{[L_{xyz}]}}[\boldsymbol{K}(\theta + 30°)]^{-1} = \begin{bmatrix} L_{q2} & 0 & 0 \\ 0 & L_{d2} & 0 \\ 0 & 0 & L_{02} \end{bmatrix} \tag{4.29}$$

$$\boldsymbol{[M_{qd0,s1s2}]} = [\boldsymbol{K}(\theta)]\underline{\boldsymbol{[M_{s1s2}]}}[\boldsymbol{K}(\theta + 30°)]^{-1} = \begin{bmatrix} M_{q1} & 0 & 0 \\ 0 & M_{d1} & 0 \\ 0 & 0 & M_{01} \end{bmatrix} \tag{4.30}$$

$$\boldsymbol{[M_{qd0,s2s1}]} = [\boldsymbol{K}(\theta + 30°)]\underline{\boldsymbol{[M_{s2s1}]}}[\boldsymbol{K}(\theta)]^{-1} = \begin{bmatrix} M_{q2} & 0 & 0 \\ 0 & M_{d2} & 0 \\ 0 & 0 & M_{02} \end{bmatrix} \tag{4.31}$$

where $L_{q1} = L_{d1} = L_{01} = L_{q2} = L_{d2} = L_{02} = L_s = 3.95$ mH, and $M_{q1} = M_{d1} = M_{01} = M_{q2} = M_{d2} = M_{02} = \sqrt{3}M_s = 1.78$ mH. Finally, the machine's equations in scalar form are written as in (4.32) and equivalent circuit is presented in Figure 4.16.

$$\begin{cases} V_{q,s1} = Ri_{q,s1} + L_q \dfrac{di_{q,s1}}{dt} + M_q \dfrac{di_{q,s2}}{dt} + \omega_e L_d i_{d,s1} + \omega_e M_d i_{d,s2} + \omega_e \psi_{pm} \\ V_{d,s1} = Ri_{d,s1} + L_d \dfrac{di_{d,s1}}{dt} + M_d \dfrac{di_{d,s2}}{dt} - \omega_e L_q i_{q,s1} - \omega_e M_q i_{q,s2} \\ V_{q,s2} = Ri_{q,s2} + L_q \dfrac{di_{q,s2}}{dt} + M_q \dfrac{di_{q,s1}}{dt} + \omega_e L_d i_{d,s2} + \omega_e M_d i_{d,s1} + \omega_e \psi_{pm} \\ V_{d,s2} = Ri_{d,s2} + L_d \dfrac{di_{d,s2}}{dt} + M_d \dfrac{di_{d,s1}}{dt} - \omega_e L_q i_{q,s2} - \omega_e M_q i_{q,s1} \end{cases} \tag{4.32}$$

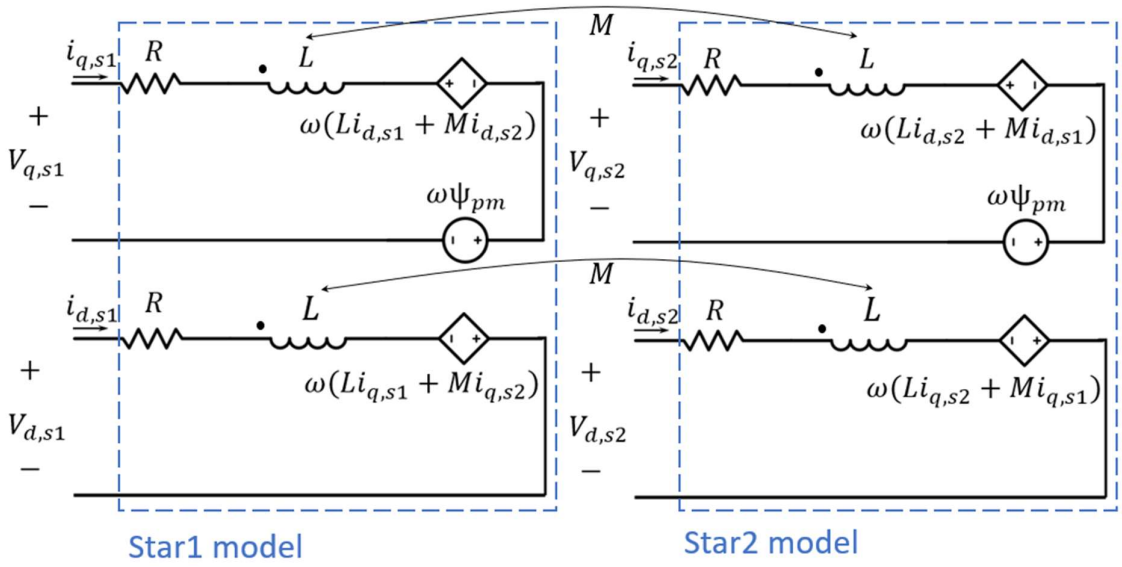


Figure 4.16 The *qd0* equivalent circuit of machine used for ETS.

In order to conclude the model, torque equation is needed. Torque is calculated as the sum of torques produced by each star T_{s1} and T_{s2} [188]:

$$T = T_{s1} + T_{s2} \tag{4.33}$$

$$T_{s1} = \frac{3}{2}p\left(\psi_{d1}i_{q1} - \psi_{q1}i_{d1}\right) \tag{4.34}$$

$$T_{s2} = \frac{3}{2}p\left(\psi_{d2}i_{q2} - \psi_{q2}i_{d2}\right) \tag{4.35}$$

By expanding (4.34) and (4.35) and including equations for flux, torque becomes:

$$T_{s1} = \frac{3}{2}p(\psi_{pm}i_{q1} + \left(L_{d1} - L_{q1}\right)i_{q1}i_{d1} - M_{q1}i_{q2}i_{d1} + M_{d1}i_{d2}i_{q1} \tag{4.36}$$

$$T_{s2} = \frac{3}{2}p(\psi_{pm}i_{q2} + \left(L_{d2} - L_{q2}\right)i_{q2}i_{d2} - M_{q2}i_{q1}i_{d2} + M_{d2}i_{d1}i_{q2} \tag{4.37}$$

Considering that $L_{q1} = L_{d1} = L_{q2} = L_{d2}$ and that $M_{q1} = M_{d1} = M_{q2} = M_{d2}$ torque formula simplifies to:

$$T = \frac{3}{2}p\psi_{pm}\left(i_{q1} + i_{q2}\right) \tag{4.38}$$

4.5 Verification of the QD model

The qd model of the machine, i.e., equations (4.32) and (4.38), is developed under the assumption of linear operation without the effect of the saturation. In order to take saturation into the account, a following approach is taken. Equation (4.38) can be re-written as considering symmetrical operation, i.e., $i_{q1} = i_{q2} = i_q$.

$$T = \frac{3}{2} p\psi_{pm}(i_{q1} + i_{q2}) = 3p\psi_{pm} i_q = k_t(i_q, i_d) i_q \tag{4.39}$$

The torque constant has been calculated for various (i_q, i_d) pairs in section 4.3.2. Therefore, $\psi_{pm}(i_q, i_d)$ can be calculated as

$$\psi_{pm}(i_q, i_d) = \frac{k_t(i_q, i_d)}{3p} \tag{4.40}$$

and used in equations (4.32) to account for the saturation. In Table 4.2 the difference between FE model and *qd0* model in the symmetrical operation with $i_d = 0$ A and 80.8 rpm is shown. Both torque and maximum phase voltage are shown for both MagNet 2D FE model and *qd0* model. In Table 4.3 speed is kept constant at 40 rpm and id is -100 A. As expected, the torque showed excellent agreement with average error that is less than 0.05% and voltage average error of 2.3%. Voltage error increases in saturation region and with very high currents (above 200A) and it can be as high as 5%, which is still good agreement between analytical and FE model.

Table 4.2 Comparison of FE and *qd0* model for 80.8 rpm and id=0A.

i_q [A]	T_{FE} [Nm]	T_{qd0} [Nm]	$100\frac{T_{FE} - T_{qd0}}{T_{FE}}$ [%]	V_{FE}^{MAX} [V]	V_{qd0}^{MAX} [V]	$100\frac{V_{FE}^{MAX} - V_{qd0}^{MAX}}{V_{FE}^{MAX}}$ [%]
25	1023.00	1024.95	0.19	122.22	122.24	0.02
50	2048.93	2051.01	0.10	134.55	133.64	0.68
75	3069.49	3071.81	0.08	149.67	148.48	0.80
100	4030.99	4033.58	0.06	167.52	164.77	1.67
125	4815.40	4818.16	0.06	187.39	180.83	3.63
150	5482.68	5485.76	0.06	208.90	198.55	5.21
175	6059.71	6062.94	0.05	230.53	217.91	5.79
200	6569.67	6573.11	0.05	253.81	238.64	6.36
223	6994.33	6998.11	0.05	271.88	258.67	5.11

Table 4.3 Comparison of FE and *qd0* model for 40 rpm and id=-100A.

i_q [A]	T_{FE} [Nm]	T_{qd0} [Nm]	$100\frac{T_{FE} - T_{qd0}}{T_{FE}}$ [%]	V_{FE}^{MAX} [V]	V_{qd0}^{MAX} [V]	$100\frac{V_{FE}^{MAX} - V_{qd0}^{MAX}}{V_{FE}^{MAX}}$ [%]
25	1024.94	1024.94	0.0	30.70	30.27	1.38
50	2050.29	2050.29	0.0	43.91	43.47	0.99
75	3072.05	3072.05	0.0	57.14	56.65	0.86
100	4087.06	4087.06	0.0	70.41	69.82	0.85
125	5041.88	5041.88	0.0	83.68	82.79	1.07
150	5740.11	5740.11	0.0	96.38	95.15	1.27
175	6321.33	6321.33	0.0	108.22	107.56	0.62
200	6824.55	6824.55	0.0	119.21	120.06	0.72

4.6 3-phase voltage source inverter modelling

As mentioned in section 1.4.1, the average modelling of power electronics is essential for fast system-level simulations of forward models of traction drives. The typical configuration

of a conventional 3-phase 2-level VSI is depicted in Figure 4.17. The voltage equation of the switching model of the inverter can be represented as in (4.41) using matrix form.

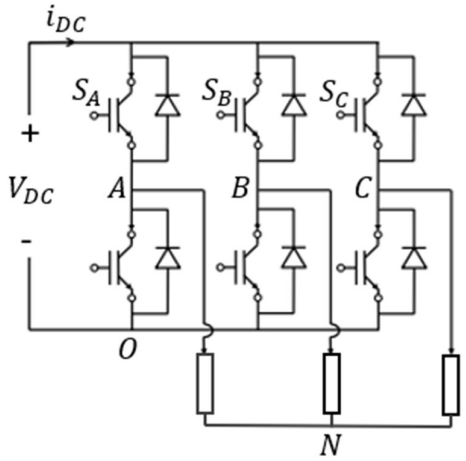


Figure 4.17 3-phase 2-level voltage source inverter.

$$\begin{bmatrix} V_{AO} \\ V_{BO} \\ V_{CO} \end{bmatrix} = \begin{bmatrix} S_A & 0 & 0 \\ 0 & S_B & 0 \\ 0 & 0 & S_C \end{bmatrix} \begin{bmatrix} V_{DC} \\ V_{DC} \\ V_{DC} \end{bmatrix} \tag{4.41}$$

In (4.41) S_i is the switching function defined as

$$S_i = \begin{cases} 1, upper\ switch\ of\ leg\ i\ is\ closed \\ 0, bottom\ switch\ of\ leg\ i\ is\ closed \end{cases}, i \in \{A, B, C\}$$

The phase voltages, V_{iN}, are defined as difference between leg midpoint and neutral point potentials:

$$\begin{bmatrix} V_{AN} \\ V_{BN} \\ V_{CN} \end{bmatrix} = \begin{bmatrix} V_{AO} - V_{NO} \\ V_{BO} - V_{NO} \\ V_{CO} - V_{NO} \end{bmatrix} \tag{4.42}$$

where

$$V_{NO} = \frac{V_{AO} + V_{BO} + V_{CO}}{3} \tag{4.43}$$

Therefore, phase voltages in terms of switching function can be written as:

$$\begin{cases} V_{AN} = \dfrac{2S_A - S_B - S_C}{3} V_{DC} \\ V_{BN} = \dfrac{-S_A + 2S_B - S_C}{3} V_{DC} \\ V_{CN} = \dfrac{-S_A - S_B + 2S_C}{3} V_{DC} \end{cases} \tag{4.44}$$

As already mentioned, in order to have lower computational burden, inverters' equations will first be averaged over one switching period T_{sw} using operator (4.45). More details about the procedure can be found in [191].

$$\overline{x(t)} = \frac{1}{T_{sw}} \int_{t}^{t+T_{sw}} x(\tau)\, d\tau \tag{4.45}$$

It can be shown that averaged switch functions in triangular carrier PWM modulation are:

$$\overline{S_i} = \frac{1}{2}(1 + m_i^*) \tag{4.46}$$

where m_i^* is the modulating index of the ith phase. Thus, applying averaging operator to (4.44) gives averaged voltage equations:

$$\overline{V_{iN}} = \overline{d_i} V_{DC}, i \in \{A, B, C\}; \begin{cases} \overline{d_A} = \dfrac{2\overline{S_A} - \overline{S_B} - \overline{S_C}}{3} \\ \overline{d_B} = \dfrac{-\overline{S_A} + 2\overline{S_B} - \overline{S_C}}{3} \\ \overline{d_C} = \dfrac{-\overline{S_A} - \overline{S_B} + 2\overline{S_C}}{3} \end{cases} \tag{4.47}$$

In order to connect VSI model to the already developed qd electric circuit model of the machine, (4.47) is also transferred to *qd0* reference frame using $[\boldsymbol{K}(\theta)]$ yielding (4.48). The process of obtaining *qd0* duty cycles is shown in Figure 4.18.

$$\begin{bmatrix} V_{q,s1} \\ V_{d,s1} \\ V_{q,s2} \\ V_{d,s2} \end{bmatrix} = \begin{bmatrix} d_{q,s1} \\ d_{d,s1} \\ d_{q,s2} \\ d_{d,s2} \end{bmatrix} V_{DC} \tag{4.48}$$

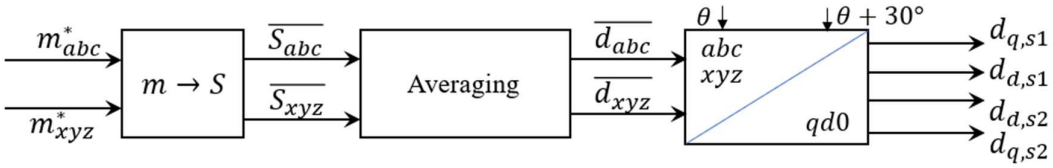


Figure 4.18 The procedure of obtaining *qd0* duty cycles form modulation signals in time domain.

To accomplish the VSI model, DC link current should also be modelled. It can be found by balancing power extracted from the DC link and power absorbed by the inverter as in (4.49) and (4.50). Averaged *qd0* models of the VSIs are shown in Figure 4.19.

$$i_{DC} V_{Dc} = \frac{3}{2}(V_{d,s1} i_{d,s1} + V_{q,s1} i_{q,s1} + V_{d,s2} i_{d,s2} + V_{q,s2} i_{q,s2} \tag{4.49}$$

$$i_{DC} = \frac{3}{2}(d_{d,s1}i_{d,s1} + d_{q,s1}i_{q,s1} + d_{d,s2}i_{d,s2} + d_{d,s2}i_{q,s2}) \tag{4.50}$$

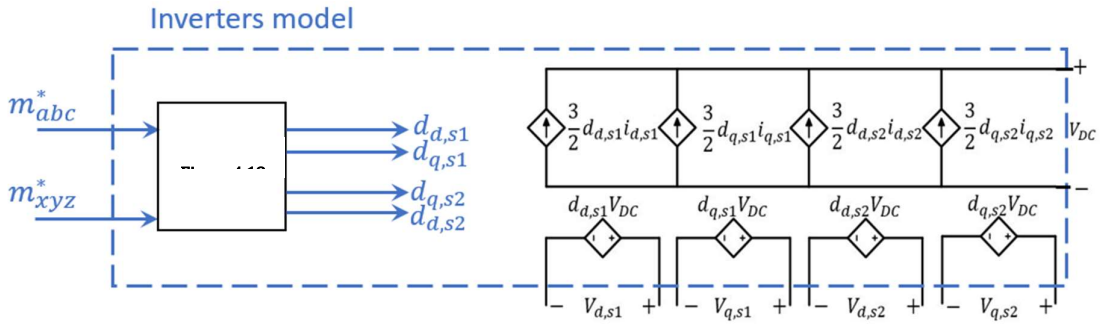


Figure 4.19 Averaged *qd0* model of 3-phase 2-level VSI.

Inverters are highly efficient devices with efficiencies above 95% [192]. The two main source of power converter inefficiencies come from semiconductor-based switches, and they are namely conduction and switching losses. During its ON state, the current (i_{ON}) flows through whilst there is voltage across the switch (V_{ON}). On the other hand, switching losses occur during the transition between ON and OFF sates as there is brief period where current and voltage coexist as shown in Figure 4.20 [111].

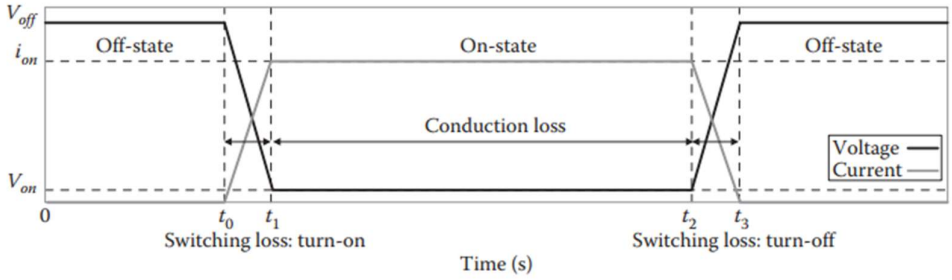


Figure 4.20 Electrical waveforms and generated losses.

Conduction losses can be calculated using equation (4.51) while switching losses using (4.52), where E_{ON} and E_{OFF} are energy dissipated during switch commutation. It is evident that only switching losses depend on the switching frequency.

$$P_{cond} = i_{on}V_{on} \tag{4.51}$$

$$P_{switch} = (E_{on} + E_{off})f_{sw} \tag{4.52}$$

As inverters use sine PWM, the average conduction losses of one inverter leg can be written as

$$P_{cond} = \frac{V_{T0} + V_{D0}}{\pi} I_{peak} + \frac{R_{T0} + R_{D0}}{4} I_{peak}^2 + 2m \cos\varphi \left(\frac{V_{T0} - V_{D0}}{8} I_{peak} + \frac{R_{T0} - R_{D0}}{3\pi} I_{peak}^2\right) \quad (4.53)$$

where V_{T0} and V_{D0} are forward voltages and R_{T0} and R_{D0} are ON resistances of transistor and diode respectively, m is the modulation index and φ is phase angle between output current and voltage and I_{peak} is the amplitude of the output current [193]. The envisaged power converters to drive this machine are SKAI inverters from Semikron with half-bridge SKM300GB12E4 which information can be found in [194]. Using equations from above and information form datasheet it can be concluded that during most operating points the inverter operates more efficiently than PMSM. Therefore, its losses could be neglected comparing to machine's and hence in further analysis the inverter was modelled as lossless device.

4.7 Control system development

The forward-facing model of the whole ETS consists not only of the physical models of the aircraft dynamics, traction machine and inverters (Figure 4.21) but also from the control layer responsible for driving the aircraft with the pre-given speed drive cycle, i.e., speed reference. Therefore, the control layer uses as its inputs speed reference and feedback signals from the physical layer: speed and currents (yellow coloured). As a result, it outputs the modulation signalsm^*_{abc} and m^*_{xyz} that forces the inverters to produce currents necessary for torque generation at the machine's shaft that drives the aircraft with the desired speed.

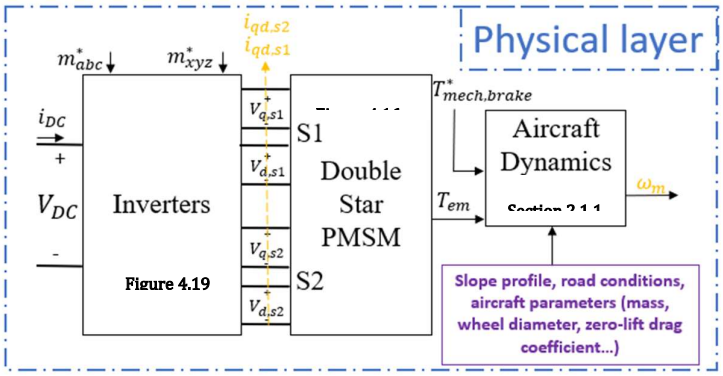


Figure 4.21 Physical layer of the ETS model.

The preferred speed control system of the selected ETS is a well-known two nested control loops approach consisting of speed and current loops. The speed control loop implements a conventional PI controller with an anti-windup mechanism. Additionally, speed reference is pre-filtered to reduce the overshoot during the transient. Before passing the desired torque

reference, i.e., the output of the speed PI controller, further on to the next block in the loop, a power limit is considered. Therefore, the reference torque is compared to the limiting torque (T_{lim}), which corresponds to the power limit (P_{lim}) of 50 kW, resulting in the total power transferred to the road never being greater than 100 kW. The reasoning behind selecting this value is due to the desired constant force/constant power acceleration profile. The constant power acceleration is described by differential equation (4.54). Unfortunately, the solution in closed form is challenging to obtain, so numerical software like Simulink are used.

$$m\frac{dv}{dt} = \frac{P}{v} - mgi_{eq,\%} \tag{4.54}$$

In Figure 4.22 and Figure 4.23, the constant force/constant power acceleration is simulated using Airbus A320 as an example with the power limit of 100 kW. The constant force value is selected to be 25 kN which corresponds to 14 kNm torque at the wheels. In Figure 4.22, the equivalent slope is kept at 0.8%, varying the aircraft's mass from 69 t to the MTOW of 79 t. It can be noticed that in all scenarios, aircraft accelerates within acceptable margins of the requirements outlined by EGTS. For example, the heaviest 79 t aircraft would achieve 20 knots in 100 s instead of 90 s, which is interpreted as acceptable. On the other hand, in Figure 4.23, the weight is kept at 79 t whereas $i_{eq,\%}$ is varied. It can be seen that even with MTOW of 79 t, the aircraft accelerates to 20 knots in around 90 seconds for most of the cases, except at $i_{eq,\%} = 1\%$. Similarly stands for acceleration of active runway crossing, all of them are achieved in around 20 seconds.

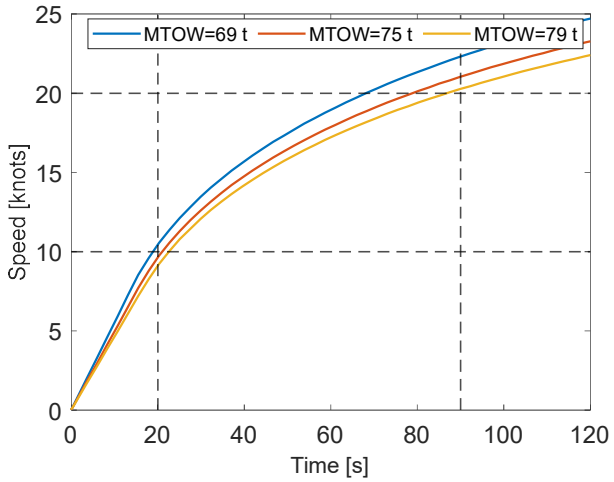


Figure 4.22 The acceleration profiles with $i_{eq,\%}$=0.8% and three different values of MTOW.

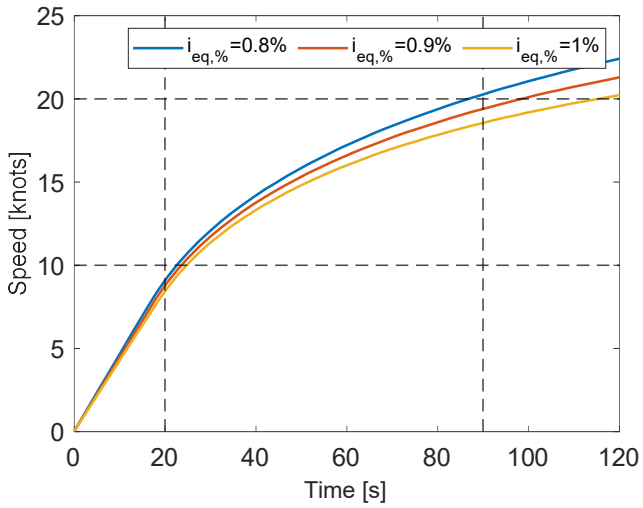


Figure 4.23 The acceleration profiles with MTOW=79 t and three different values of $i_{eq,\%}$.

Of course, setting a higher P_{lim} would result in faster acceleration and fulfilling the requirements even in the worst-case scenarios. However, in this case, a higher power would be demanded from the energy storage or APU S/G. 100 kW represents a trade-off between acceptable kinematic performances and required rated maximum power from the energy source.

Another thing to mention is the inclusion of mechanical brakes. As the minimum electromagnetic torque that machines can provide is negative 14 kNm (as there are two TMs installed), the aircraft would decelerate with very slow rates. It would take an Airbus A320 almost 24 s to decelerate to a standstill from 20 knots. Therefore, a mechanical break needs to be included in the model in conjugation with the electromagnetic torque. Three breaking strategies can be selected in the model.

- Strategy one, i.e., maximum regeneration (MAX), uses only electromagnetic torque, and hence it maximises the regenerated energy. On the other hand, due to the low torque values, safety is compromised, as explained.
- Accordingly, strategy two, i.e., minimum regeneration (MIN), includes not only electromagnetic torque but also a mechanical brake. In this strategy, the deceleration time is minimised, and the mechanical brake will add any value needed to achieve -30 kNm total braking torque. Due to the short deceleration times, the regenerated energy is the lowest in this strategy.
- Finally, strategy three (BLEND), is developed to blend two approaches. The mechanical brake is engaged only in emergency braking events (e.g., 20 knots to a

standstill), as in strategy two. During other braking events, the mechanical brake assists the electromagnetic one by adding -1.5 kNm per wheel. In strategies two and three, once the speed is within acceptable error from the speed reference, the mechanical brake is disengaged. Then the electromagnetic torque of –3 kNm brakes the aircraft until the desired reference. All mentioned PI controllers, calculations and control logic are included in the so-called "pilot model" block in Figure 4.24.

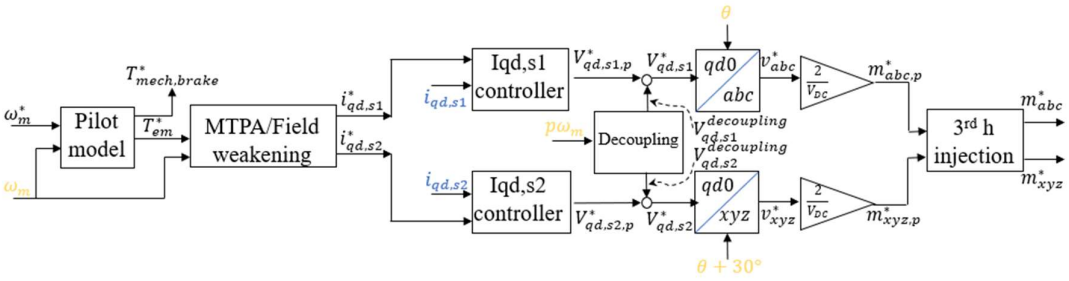


Figure 4.24 Control layer of the ETS model.

Once the proper torque reference is generated, it is then sent to the MTPA block. The MTPA is implemented using the indirect method, meaning that based on the instantaneous speed and torque reference, the block will calculate needed q-axis and d-axis currents considering the voltage and current limitations [195]. The MTPA block is implemented using a C-script block in which the field weakening equations are implemented based on the developed model assuming symmetrical operation. The current PI controllers use the same configuration as speed ones, and they output needed d- and q-axis voltages ($V^*_{qd,p}$) The difference is that decoupling values for d- and q-axis voltage values must be added to achieve the correct V^*_{qd} references. The decoupling values are:

$$\begin{cases} V_{q,s1}^{decpupling} = \omega L_d i_{d,s1} + \omega M_d i_{d,s2} + \omega \psi_{pm} \\ V_{d,s1}^{decpupling} = -\omega L_q i_{q,s1} - \omega M_q i_{q,s2} \\ V_{q,s2}^{decoupling} = \omega L_d i_{d,s2} + \omega M_d i_{d,s1} + \omega \psi_{pm} \\ V_{d,s2}^{decpupling} = -\omega L_q i_{q,s2} - \omega M_q i_{q,s1} \end{cases} \quad (4.55)$$

The references V^*_{qd} are then transferred to *abc* and *xyz* voltages and scaled with (Vdc/2) to obtain the modulation indexes of phases prior to the additional manipulation: $m^*_{abc,p}$and $m^*_{xyz,p}$. In order to extend the voltage range during which the inverter is in linear mode, a third harmonic injection is used where the $m_{3h,abc}$ is calculated using (4.56) [196]. The same applies to star *xyz*.

$$m_{3h,abc} = \frac{1}{2}\left(min\left(m^*_{a,p}, m^*_{b,p}, m^*_{c,p}\right) + max(m^*_a, m^*_b, m^*_c)\right) \tag{4.56}$$

$$m^*_{abc} = m^*_{abc,p} + m_{3h,abc} \tag{4.57}$$

Finally, the reference modulation signals undergo transformations explained in Figure 4.18, in which the required duty cycles in the *qd0* domain are calculated. They act as input to the inverter model, and together with machine and aircraft dynamics, they complete the whole model of ETS shown in Figure 4.25. The battery block, as already mentioned uses the equivalent circuit model and several commercially available lithium-ion cell are modelled in the next chapter.

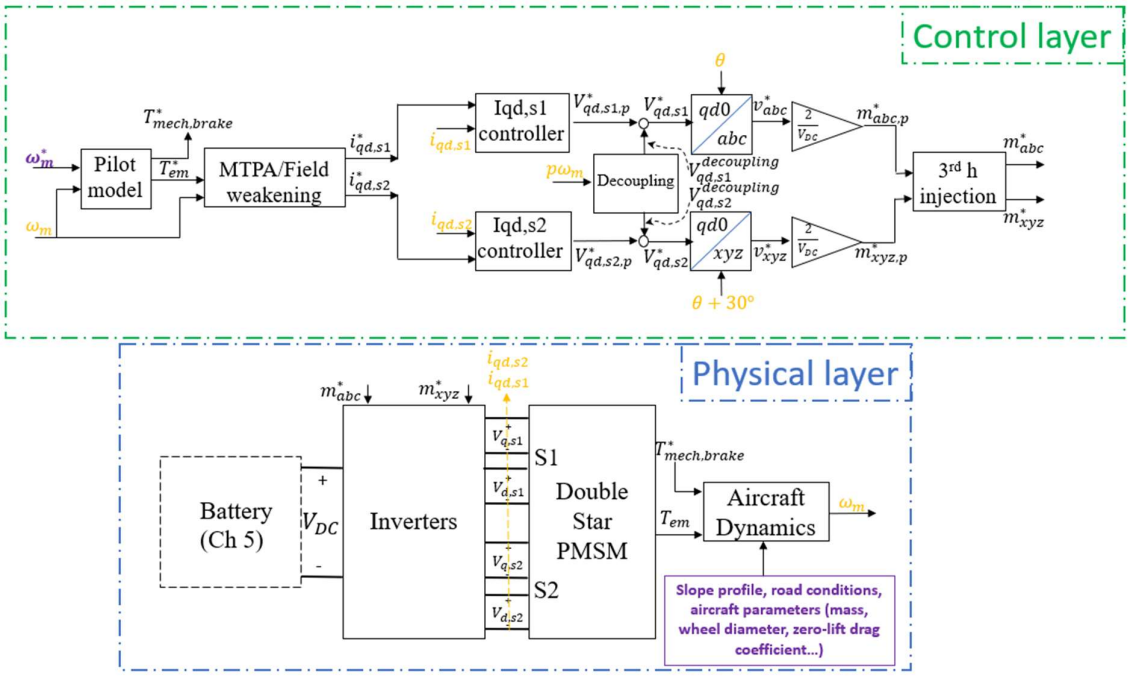


Figure 4.25 The full forward-facing model of the ETS including aircraft dynamics.

4.8 Employment of the model and interim conclusions

In this section, the ETS under study is analysed for several drive cycles to demonstrate the effectiveness of the developed model. The primary input to the model is the desired speed profile, i.e., the reference drive cycle. It is widely accepted in the automotive sector that the drive cycles are helpful tools in assessing the performance of vehicles in terms of pollutant emissions and fuel consumption [182]. For example, in the EU, the legislative drive cycle called New European Drive Cycle (NEDC) has been in use since 2000. In contrast, in the United States, numerous test cycles exist, such as Urban Dynamometer Driving Schedule (UDDS) and the New York City Cycle (NYCC) [197]. All these cycles try to represent

common patterns encountered during motorway and urban (city) driving. Unfortunately, such legislative cycles do not exist for ET applications yet. However, most ET manufacturers designed their systems to follow the EGTS requirements.

Two partial drive cycles from Safran that represent two taxiing scenarios were available at hand, namely, Amsterdam Schiphol (AMS) Taxi-Out (T-O) and London Heathrow (LHR) Taxi-In (T-I). The fragmentary information was reconstructed with the help of an extensive literature review presented in Chapter 2 and using the already published ET drive cycle from the Smart Ground Operations (SGO) Cleansky Project project [198]. The reference speed cycles in knots are presented in Figure 4.26, whereas the cycle from [198] is shown in Figure 4.27 in m/s (20 knots = 10.29 m/s). The authors in [199] and [100] analysed conventional taxiing cycles logged using GPS device whilst being onboard. Analysis of a total of 36 obtained cycles showed that taxiing patterns could be categorised into unrestricted and restricted profiles. During the unrestricted cycle, the aircraft taxis to the runway without any stops. On the other hand, multiple stops occur during the restricted taxiing cycle due to traffic and active runway crossings, such as AMS T-O and LHR T-I. Therefore, besides those two cycles, a Berlin Tegel (TXL) T-O cycle from [199] (Figure 4.28) is adapted and used as another reference cycle. Considering that 40 km/h is slightly above 20 knots, a reference cycle presented in Figure 4.29 is created using only the last 5 minutes (between 200 and 500 sec) of the initial cycle from Figure 4.28.

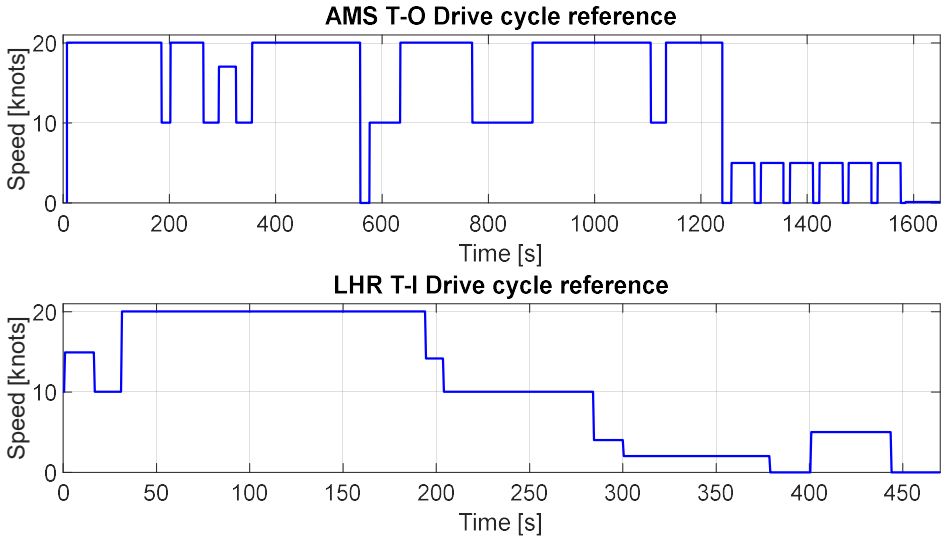


Figure 4.26 AMS T-O and LHR T-I reference drive cycles.

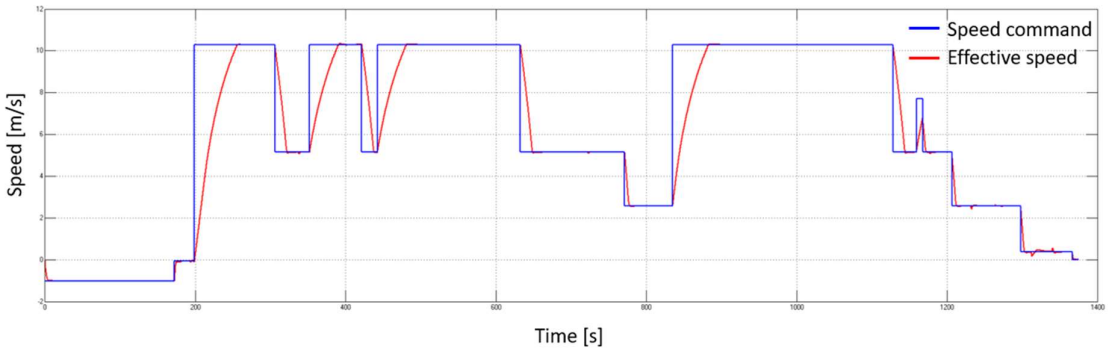


Figure 4.27 Speed curves during testing of control system for Cleansky project SOG [198].

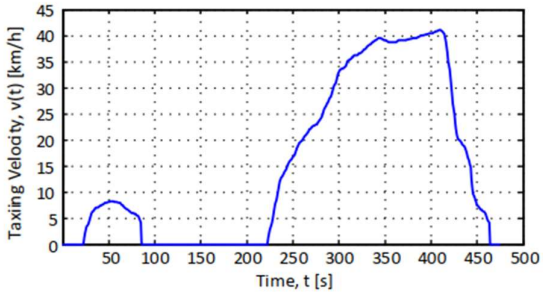


Figure 4.28 TXL T-O drive cycle [199].

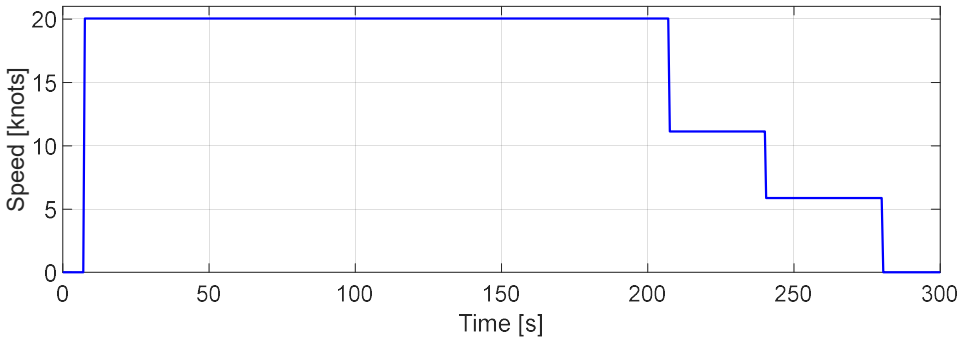


Figure 4.29 TXL T_O reference cycle adapted from Figure 4.28

Additional inputs to the model are aircraft and road load information. Therefore, in the mask of the model (Figure 4.30), the user can select the aircraft type (A320, B737, E family, B777, B787), which automatically fixes wheel tyre radius and $c_{d0,taxiing} * A$ product. However, the user can input the mass as it is a variable parameter that depends on the mission profile. When it comes to the road load, the rolling resistance is modelled using (2.9) and (2.10) with $V^* = 10$ knots, $c_{rr,0}$= 0.008, and Δc_{br}= 0.0084. The rolling resistance is made invariant of the cycle selection. On the other hand, each drive cycle has its associated slope profile, which, if needed, can be modified. Finally, the model allows for selecting three braking strategies explained in detail in section 4.7.

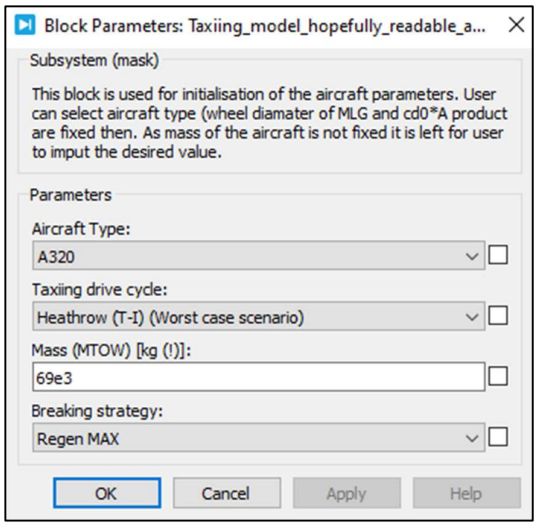


Figure 4.30 Mask of the created model in PLECS 4.4.

4.8.1 A320 analysis

An Airbus A320 with a mass of 69 t under AMS T-O requirements with maximum regeneration braking strategy has been selected to demonstrate the model's capabilities. It can be seen from Figure 4.31 that the aircraft manages to follow the speed reference closely except during acceleration and deceleration events when it obeys the powertrain constraints explained in section 4.7. The aeroplane accelerates from 0 to 20 knots in less than 90 seconds following the pattern from Figure 4.22, which shows that powertrain constraints have been implemented correctly and that the control system is working properly. Furthermore, the torque and power at the wheel and power at the DC link are plotted in Figure 4.32 and Figure 4.34. It can be noticed that power at the wheel follows the imposed limitation as expected, but power at the DC link is above 50 kW. This behaviour is due to the machine's efficiency at low speeds, a problem whose implications were discussed in section 4.3.3. The peak power during acceleration is 73.2 kW, representing an average efficiency of 68.3%, which is in line with the machine's efficiency map. Therefore, it is once again highlighted that power limit value should be selected to satisfy the kinematic requirements without representing systematic stress on the power generation system. On the other hand, the minimum power reached at the DC link is -47.8 kW during braking events.

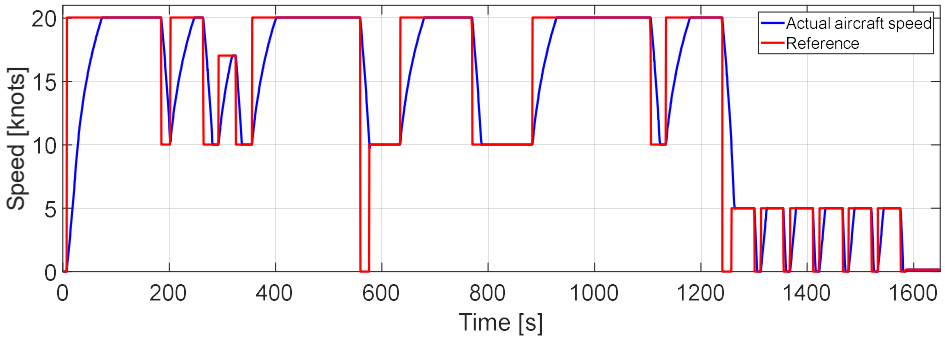


Figure 4.31 The speed profile of an A320 with 69 t under AMS T-O and maximum regeneration scenario.

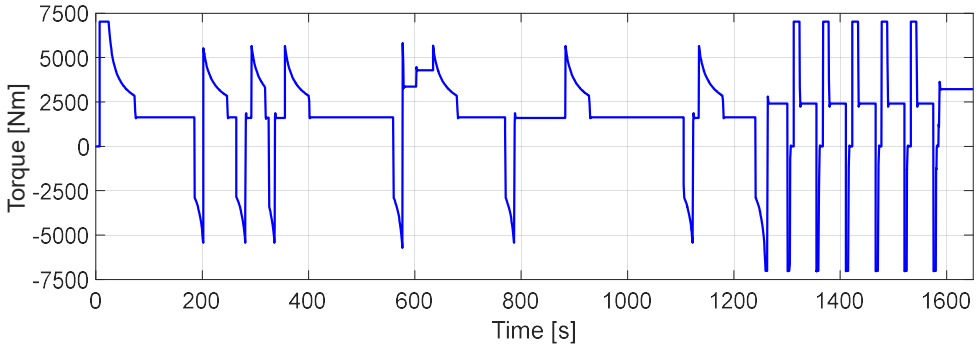


Figure 4.32 The TM's torque profile of an A320 with 69 t under AMS T-O and maximum regeneration scenario.

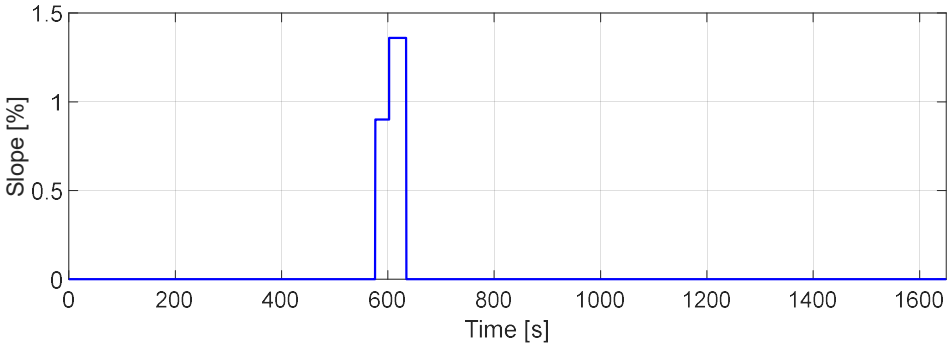


Figure 4.33 The slope profile of AMS T-O drive cycle.

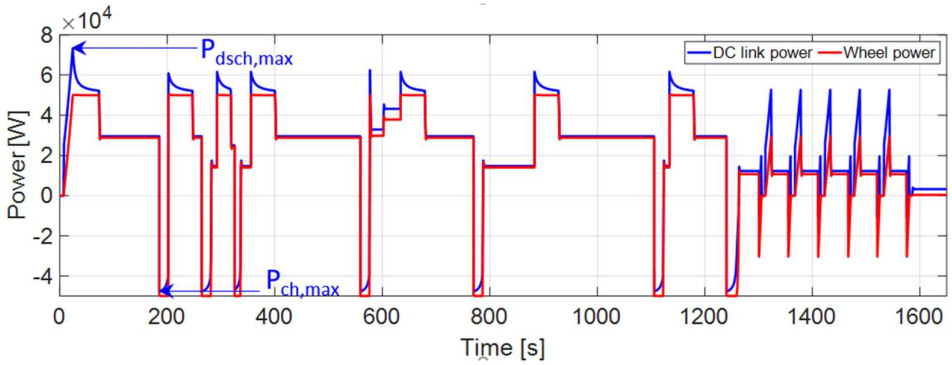


Figure 4.34 The DC link and wheel power profiles of an A320 with 69 t under AMS T-O and maximum regeneration scenario.

The required energy for this taxiing scenario can be calculated by integrating power profiles, and energy curves are shown in Figure 4.35. The total energy needed for the propulsion (E_{prop}) is 12.43 kWh, whereas 1.49 kWh can be regenerated (E_{regen}) during braking events. Therefore, a total required energy (E_{tot}) of 10.94 kWh is needed in this scenario, of which the regeneration provides 13.62%.

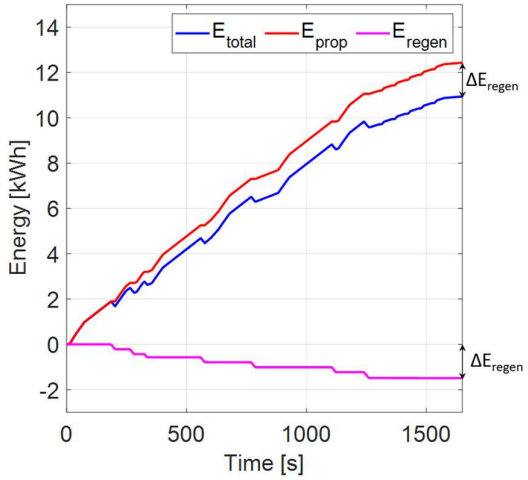


Figure 4.35 The energy profiles of an A320 with 69 t under AMS T-O and maximum regeneration scenario.

Before proceeding to the analysis of energy consumption for different braking strategies and different taxiing cycles, the performance of an A320 is also analysed with various weights with a minimum regeneration strategy. The acceleration follows the theoretical profiles closely from Figure 1.22, whereas aircraft decelerates faster due to the selected braking procedure than the profile from Figure 4.31. It can be noticed that maximum discharge power doesn't vary with the mass. The most power demanding event, acceleration from 0 to 20 knots, will always result in 73.2 kW peak power, and deceleration from 20 knots to zero will always result in a peak value of -47.8 kW.

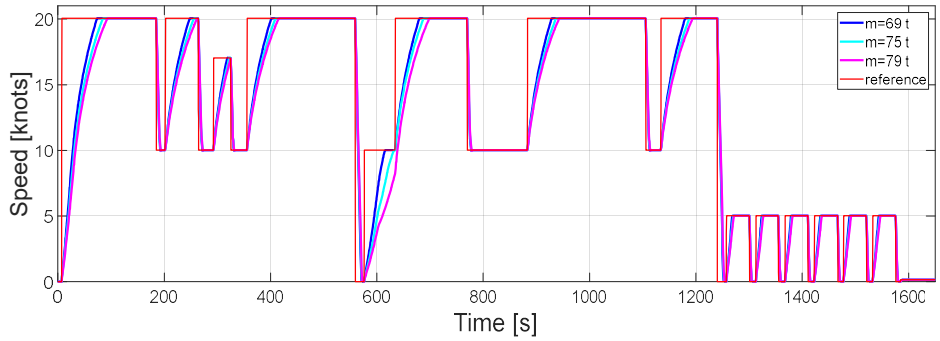


Figure 4.36 The speed profiles of an A320 under AMS T-O and minimum regeneration scenario for three different aircraft mass.

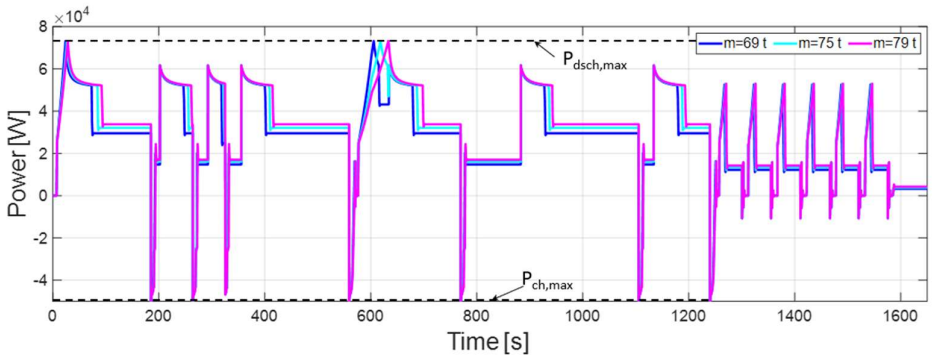


Figure 4.37 The DC link power profiles of an A320 under AMS T-O and minimum regeneration scenario for three different aircraft mass.

4.8.2 Power demands and energy consumption analysis

The energy consumption is analysed for three different drive cycles and three different braking strategies. The results of the AMS T-O cycle are presented in Table 4.4 to Table 4.6. As expected, the required total energy is highly dependent on the mass of the aircraft and the selected braking strategy. It is the highest for aircraft with 79 t and minimum regeneration (13.87 kWh), where it is the lowest for 69 t and maximum regeneration (10.94 kWh). The difference of 2.93 kWh represents 26.7% of the E_{tot} for the first case. It can be noticed that a maximum of 13.62% of energy can be obtained through regeneration depending on the braking strategy. The energy consumption is calculated per aircraft mass (i.e., F_1 [Wh/kg]), but as E_{tot} depends on the length of the cycle, specific energy consumption per aircraft mass and distance (i.e., F_2 [Wh/(kgkm)]) is also reported. The length of 11.42 km shouldn't be surprising as the most used Polderbaan runway at AMS is 7 km north of the terminal building [200]. In Figure 4.38, the typical taxiing route at AMS of 8 km is shown.

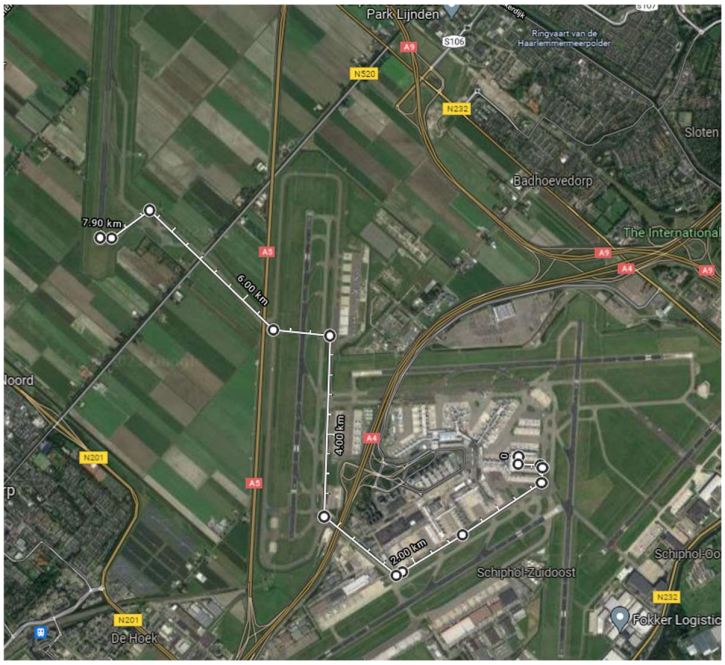


Figure 4.38 The typical taxi-out route at AMS.

Table 4.4 Energy consumption for A320 with 69 t under AMS T-O cycle.

	P_{avg} [kW]	E_{prop} [kWh]	E_{tot} [kWh]	E_{regen} [kWh]	$\frac{E_{regen}}{E_{prop}}$ [%]	$F_1 \left[\frac{Wh}{kg}\right]$	d [km]	$F_2 \left[\frac{Wh}{kgkm}\right]$
MAX	23.87	12.43	10.94	1.49	13.62	0.159	11.42	0.0139
BLEND	25.61	12.74	11.74	1	8.52	0.170	11.12	0.0153
MIN	26.79	12.86	12.28	0.58	4.72	0.178	11	0.0162

Table 4.5 Energy consumption for A320 with 75 t under AMS T-O cycle.

	P_{avg} [kW]	E_{prop} [kWh]	E_{tot} [kWh]	E_{regen} [kWh]	$\frac{E_{regen}}{E_{prop}}$ [%]	$F_1 \left[\frac{Wh}{kg}\right]$	d [km]	$F_2 \left[\frac{Wh}{kgkm}\right]$
MAX	25.85	13.41	11.85	1.56	13.16	0.158	11.33	0.0139
BLEND	27.69	13.76	12.69	1.07	8.43	0.169	10.96	0.0154
MIN	28.97	13.9	13.28	0.62	4.67	0.177	10.84	0.0163

Table 4.6 Energy consumption for A320 with 79 t under AMS T-O cycle.

	P_{avg} [kW]	E_{prop} [kWh]	E_{tot} [kWh]	E_{regen} [kWh]	$\frac{E_{regen}}{E_{prop}}$ [%]	$F_1 \left[\frac{Wh}{kg}\right]$	d [km]	$F_2 \left[\frac{Wh}{kgkm}\right]$
MAX	27.14	14.05	12.44	1.61	12.94	0.157	11.26	0.0140
BLEND	28.91	14.36	13.25	1.11	8.38	0.168	10.81	0.0155
MIN	30.26	14.53	13.87	0.65	4.69	0.176	10.69	0.0164

On the other hand, a much shorter (5 min) and non-restricted Berlin Taxi-Out cycle requires a maximum of 2.69 kWh, an 81.5% decrease of the most requiring Schiphol scenario. Also, due to fewer stop and go patterns, the regenerated energy is less in absolute value than the Schiphol scenarios, but similar values are obtained in terms of regeneration rate in percentage. The reason why TXL's cycles are unrestricted can be seen from the airport taxiway plan and

typical taxiing route (2.1 km) as laid out in Figure 4.39. The results for different aircraft mass are shown in Table 4.7 to Table 4.9. For the purpose of fair analysis, a longer unrestricted taxiing cycle (i.e., 7.8 min) is considered with a prolonged cruising phase as shown in Figure 4.40, whose results are presented in Table 4.10 and Table 4.12. As expected, the regenerated energy is the same, but the required propulsion energy is almost doubled. This alteration results in a lower energy recovery ratio of only 7% in its best-case scenario.



Figure 4.39 Typical TXL T-O route.

Table 4.7 Energy consumption for A320 with 69 t under TXL T-O cycle.

	P_{avg} [kW]	E_{prop} [kWh]	E_{tot} [kWh]	E_{regen} [kWh]	$\frac{E_{regen}}{E_{prop}}$ [%]	$F_1 \left[\frac{Wh}{kg}\right]$	d [km]	$F_2 \left[\frac{Wh}{kgkm}\right]$
MAX	24.36	2.29	2.03	0.26	12.81	0.029	2.17	0.0136
BLEND	24.96	2.29	2.08	0.21	10.10	0.030	2.16	0.0140
MIN	26.64	2.33	2.22	0.11	4.95	0.032	2.14	0.0150

Table 4.8 Energy consumption for A320 with 75 t under TXL T-O cycle.

	P_{avg} [kW]	E_{prop} [kWh]	E_{tot} [kWh]	E_{regen} [kWh]	$\frac{E_{regen}}{E_{prop}}$ [%]	$F_1 \left[\frac{Wh}{kg}\right]$	d [km]	$F_2 \left[\frac{Wh}{kgkm}\right]$
MAX	26.16	2.45	2.18	0.27	12.39	0.029	2.13	0.0136
BLEND	26.88	2.47	2.24	0.23	10.27	0.030	2.12	0.0141
MIN	28.68	2.51	2.39	0.12	5.02	0.032	2.07	0.0154

Table 4.9 Energy consumption for A320 with 79 t under TXL T-O cycle.

	P_{avg} [kW]	E_{prop} [kWh]	E_{tot} [kWh]	E_{regen} [kWh]	$\frac{E_{regen}}{E_{prop}}$ [%]	$F_1 \left[\frac{Wh}{kg}\right]$	d [km]	$F_2 \left[\frac{Wh}{kgkm}\right]$
MAX	27.36	2.56	2.28	0.28	12.28	0.029	2.11	0.0137
BLEND	28.08	2.57	2.34	0.23	9.83	0.030	2.09	0.0142
MIN	30	2.62	2.5	0.12	4.80	0.032	2.07	0.0153

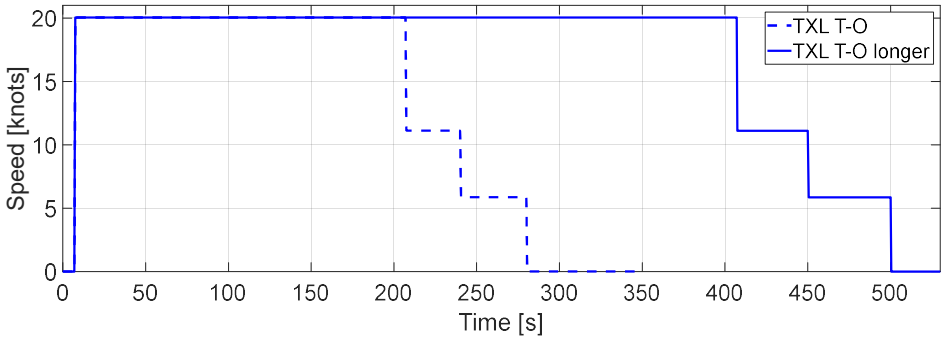


Figure 4.40 The prolonged unrestricted TXL-TO in comparison to TXL-TO.

Table 4.10 Energy consumption for A320 with 69 t under prolonged TXL T-O cycle.

	P_{avg} [kW]	E_{prop} [kWh]	E_{tot} [kWh]	E_{regen} [kWh]	$\frac{E_{regen}}{E_{prop}}$ [%]	$F_1 \left[\frac{Wh}{kg}\right]$	d [km]	$F_2 \left[\frac{Wh}{kgkm}\right]$
MAX	25.47	4.01	3.75	0.26	6.93	0.054	4.32	0.0126
BLEND	25.88	4.02	3.81	0.21	5.51	0.055	4.31	0.0128
MIN	26.76	4.05	3.94	0.11	2.79	0.057	4.29	0.0133

Table 4.11 Energy consumption for A320 with 75 t under prolonged TXL T-O cycle.

	P_{avg} [kW]	E_{prop} [kWh]	E_{tot} [kWh]	E_{regen} [kWh]	$\frac{E_{regen}}{E_{prop}}$ [%]	$F_1 \left[\frac{Wh}{kg}\right]$	d [km]	$F_2 \left[\frac{Wh}{kgkm}\right]$
MAX	27.58	4.33	4.06	0.27	6.65	0.054	4.29	0.0126
BLEND	27.92	4.34	4.11	0.22	5.35	0.055	4.28	0.0128
MIN	28.94	4.38	4.26	0.12	2.82	0.057	4.25	0.0134

Table 4.12 Energy consumption for A320 with 79 t under prolonged TXL T-O cycle.

	P_{avg} [kW]	E_{prop} [kWh]	E_{tot} [kWh]	E_{regen} [kWh]	$\frac{E_{regen}}{E_{prop}}$ [%]	$F_1 \left[\frac{Wh}{kg}\right]$	d [km]	$F_2 \left[\frac{Wh}{kgkm}\right]$
MAX	28.94	4.54	4.26	0.28	6.57	0.054	4.26	0.0127
BLEND	29.28	4.55	4.31	0.23	5.34	0.055	4.25	0.0128
MIN	30.23	4.59	4.45	0.12	2.70	0.056	4.22	0.0133

Finally, taxi-in operations are equally important to analyse as they are typically shorter than taxi-in, and inherently, more braking occurs due to the initial non-zero speed. An LHR taxi-in cycle of 500 s is used, and the results are shown in Table 4.13 to Table 4.15. It can be noticed that aircraft traverse distance of 2.5 km, a usual taxi-in distance at Heathrow Airport as shown in Figure 4.41. During taxi-in, the aircraft is lighter, and 4 t has been accounted for the fuel required for a mission (e.g., AMS-LHR or TXL-LHR).



Figure 4.41 Typical taxi-in route at LHR.

Table 4.13 Energy consumption for A320 with 65 t under LHR T-I cycle.

	P_{avg} [kW]	E_{prop} [kWh]	E_{tot} [kWh]	E_{regen} [kWh]	$\frac{E_{regen}}{E_{prop}}$ [%]	$F_1 \left[\frac{Wh}{kg}\right]$	d [km]	$F_2 \left[\frac{Wh}{kgkm}\right]$
MAX	16.77	2.53	2.19	0.33	15.07	0.034	2.55	0.0132
BLEND	17.16	2.53	2.24	0.29	12.95	0.034	2.55	0.0135
MIN	18.31	2.56	2.39	0.18	7.53	0.037	2.53	0.0145

Table 4.14 Energy consumption for A320 with 71 t under LHR T-I cycle.

	P_{avg} [kW]	E_{prop} [kWh]	E_{tot} [kWh]	E_{regen} [kWh]	$\frac{E_{regen}}{E_{prop}}$ [%]	$F_1 \left[\frac{Wh}{kg}\right]$	d [km]	$F_2 \left[\frac{Wh}{kgkm}\right]$
MAX	18.31	2.74	2.39	0.35	14.64	0.034	2.54	0.0133
BLEND	18.69	2.74	2.44	0.3	12.30	0.034	2.55	0.0135
MIN	19.91	2.79	2.6	0.19	7.31	0.037	2.51	0.0146

Table 4.15 Energy consumption for A320 with 75 t under LHR T-I cycle.

	P_{avg} [kW]	E_{prop} [kWh]	E_{tot} [kWh]	E_{regen} [kWh]	$\frac{E_{regen}}{E_{prop}}$ [%]	$F_1 \left[\frac{Wh}{kg}\right]$	d [km]	$F_2 \left[\frac{Wh}{kgkm}\right]$
MAX	19.30	2.88	2.52	0.36	14.29	0.034	2.53	0.0133
BLEND	19.69	2.88	2.57	0.31	12.06	0.034	2.52	0.0136
MIN	20.99	2.93	2.74	0.19	6.93	0.037	2.5	0.0146

It can be concluded that specific energy consumption depends mainly on cycle type, cycle length and braking strategy. The upper and lower boundaries were identified using four typical electric taxiing cycles. For example, the specific energy consumption ranges between 0.0126 and 0.0139 Wh/(kgkm) for the maximum regeneration case and between 0.0134 and 0.0165 Wh/(kgkm) for the minimum regeneration case. These estimates can be used at the initial design stage of energy storage for aircraft electric taxiing operations.

For instance, if the energy storage is designed for the worst-case cycle (AMS T-O and LHR T-I) and blend braking strategy, roughly a 17.24 kWh storage is needed for 79 t aircraft and 13.93 kWh for 69 t, assuming the storage is charged fully at AMS and will be recharged again

at LHR. If 80% DoD is considered and 90% efficiency, the values increase to 23.94 kWh and 19.34 kWh, respectively, for 79 t and 69 t A320. Only taxi-out cycles are analysed regarding the peak required power as they are more demanding due to high acceleration events. As seen, when it comes to a maximum charge and discharge power, it is the same for all scenarios due to powertrain limitations. However, the average power is different, and it varies from 24 kW to 30 kW for different taxi-out patterns.

In the following chapters the models of various lithium-ion batteries are presented. In Chapter 6, the battery models and model developed in this chapter are joined to form a versatile model of battery powered electric taxiing system.

5 Chapter: Battery modelling

In this chapter, ECMs of several commercially available cylindrical lithium-ion battery cells are developed. As already mentioned in the introduction, the model-based design approached is adopted in this thesis in which model simulation's data are used to inform system architecture decisions, to validate battery energy storage selection against predefined performance requirements and to analyse trade-offs. In the first part of this chapter, the datasheet information about the selected cells is provided and the test rig and experimental tests used to determine ECM's parameters are described. In the second part, the post-processing procedure is explained in detail starting from the data preparation and actual parameter identification. The chapter is finalised by presenting the equivalent model validation results.

5.1 Battery selection

For this project eight off-the-shelf cylindrical lithium-ion cells were selected to be modelled and analysed for ET application. The selection covers all range of energy and power densities (i.e., HE, HP, and MEP cells) and wide range of available chemistries. The selected cells are namely: INR35E, INR 30Q and INR 20S from Samsung, M1B from A123, VTC6 from Sony, NCR B from Panasonic, and MJ1 and HG2 from LG Chem. The datasheet characteristics of the cells are given in Table 5.1.

Table 5.1 Datasheet characteristics of the selected cells.

	Capacity [Ah]	Nominal voltage [V]	Max continuous discharge $I_{cell,max}$ [A]	Mass [g]	Energy density [Wh/kg]	Power density [W/kg]	
NCR B	3.35	3.6-3.7	6.7	47.5	257.42	514.84	HE
MJ1	3.5	3.6-3.65	10	49	260.71	744.90	HE
INR 35E	3.5	3.6	8	48.3	260.87	604.55	HE
HG2	3	3.6	20	48	225.00	1520.83	MEP
VTC6	3	3.6	20	45.5	237.36	1604.40	MEP
INR 30Q	3	3.6	20	48	225.00	1520.83	MEP
INR 20S	2	3.6	20	48	150.00	1520.83	HP
A123	2.5	3.3	50	76	108.55	2171.05	HP

The materials used in positive and negative electrode are not disclosed by the manufacturers. Luckily, the composition of the selected cells was analysed and researched thoroughly in the literature using scanning electron microscopy (SEM), energy dispersive x-ray spectroscopy (EDX or EDS), and X-ray diffraction (XRD) [201], [202]. Therefore, nowadays, the content of the electrodes is usually known. Normally, small variations might occur as battery manufacturers constantly improve their cells. The materials of the selected cells are given in Table 5.2.

Table 5.2 Positive and negative electrode materials of the selected cells [201], [202].

Cell	Positive Electrode	Negative Electrode
Panasonic NCR B	NCA	Graphite silicon doped
LG MJ1	NMC 811	Graphite silicon doped
Samsung INR 35E	NCA	Graphite silicon doped
LG HG2	NMC 811	Graphite silicon doped
Sony VTC 6	NCA	Graphite silicon doped
Samsung INR 30Q	NCA	Graphite silicon doped
Samsung INR 20S	NMC n/a	n/a
A123 M1B	LFP	Graphite

It can be noticed that all negative electrodes use silicon doped graphite for the reasons explained in Chapter 3. On the other side the positive electrode covers all major Li-ion chemistries used already in traction application such as LFP, NCA and NMC 811. The information for Samsung INR20s were difficult to find. It is only known that the cathode has NMC, but the ratio of materials is not known.

Even though LG MJ1 and LG HG2 both utilise high energy materials, they have different power densities. This is because there is a function between the capacity and power density of 18650 cells are closely related. As the volume is constant, more capacity means more active material at the expense of current collectors and tabs etc, i.e., at the expense of high current discharge rate. Therefore, doubling power density is paid with 15% degradation in energy density. The new cell case 21700 have almost 50% higher volume and capacity high up to 5 Ah (Samsung INR 50E) allowing for better ration of active to inactive material resulting in higher energy densities [203].

The most important benefit of cylindrical cell compared to other cell formats is that they are produced in high volumes, and consequently having low price ($/Wh) and high availability. The manufacturing process of these cells is well developed and the behaviour of these cells under normal and overload conditions was thoroughly studied and reported in the literature [204]. Contrary, pouch and prismatic cells are not mass produced and their size is not standardised, which means battery pack manufacturer cannot change cell suppliers easily. Additionally, the pouch cells noticeably expand and swell during lifetime which requires further safety precautions. Compared to pouch and prismatic cells that can have high capacity, the cylindrical cells are normally characterised by low cell capacity. This is beneficial in case of thermal runaway as smaller cells release less energy and risk of thermal propagation is reduced. Thus, battery systems using cylindrical cells have higher number of cells in parallel which complicates the BMS and thermal management system [205]**.** However, this problem is drastically reduced with high capacity 21700 cells as mentioned before. In terms of effectiveness of battery packaging, i.e., in terms of gravimetric and volumetric density on pack

level, there is a 20% of unused space due to circular cross-section. However, this allows for easier implementation of serpentine cooling plates with coolant running through it, an optimise cooling system patented by Tesla [206].

5.2 Test rig description and experiment sequence explanation

5.2.1 Test rig description

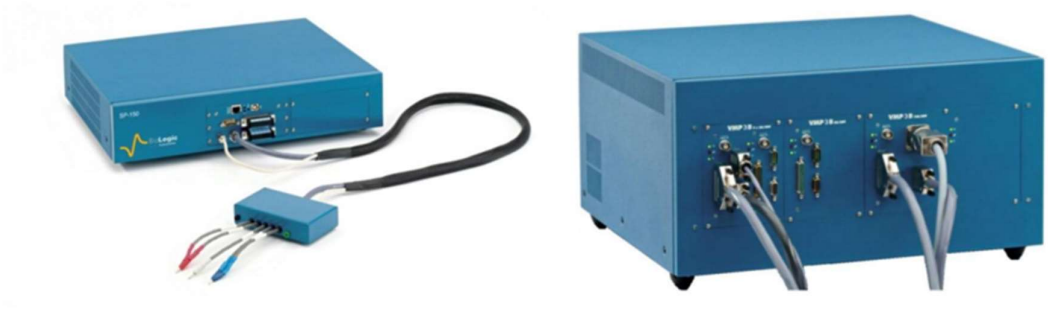


Figure 5.1 Biologic SP-150 (left) and 20 A VMP3 booster.

As already explained in Chapter 3, certain test procedures must be designed and performed for a successful parametrisation of ECM. The equipment used for this is a Biologic SP-150 potentiostat/galvanostat and VMP3 booster shown in Figure 5.1. Since the maximum current that the potentiostat can provide to the cell is only 1 A, a booster VMP3 was used which can provide maximum of 20 A. The potentiostat is connected via USB connection to the host PC and it is controlled using the dedicated EC Lab software. On the test side, the booster is connected to the cell using the four wire connection shown in Figure 5.2. Black thick wires are power connections which provide the controlled current to be injected into the cell, whereas the thin black wires are the voltage sensing connections which provide voltage information to the test equipment. Finally, the SP-150 and VMP3 are connected through a DB25 connector cable used for control and communication.

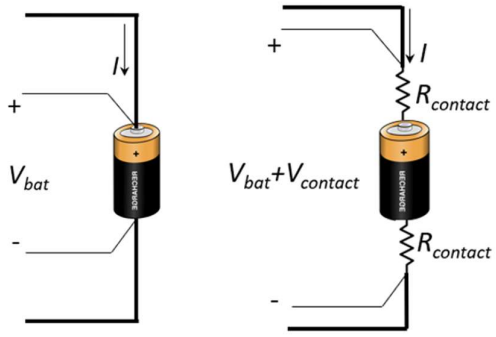


Figure 5.2 Four wire connection: correct (left) and incorrect (right).

Four wire sensing is used to remove from the measurements the voltage drop across the cables and contacts due to the applied currents. Therefore, voltage measurement must be taken directly off the cell electrode's surface, otherwise a contact resistance will be included in the measurement as shown in Figure 5.2 [207]. In that regard, a special battery cell holder from Arbin instruments was used with its separate power and sense connectors as shown in Figure 5.3. Once the cell is inserted in the holder, the sense pin is retracted using spring and it is in contact with the cell's electrode centre, whereas the current is supplied through outer brass assembly (Figure 5.4). In the bottom part of Figure 5.4 the side view of cell's connection to the holder is shown clearly indicating the correct four wire connection. The holder's screw and bolt mechanism allowed for straightforward connection booster wires using crocodile clamps as shown in Figure 5.5.

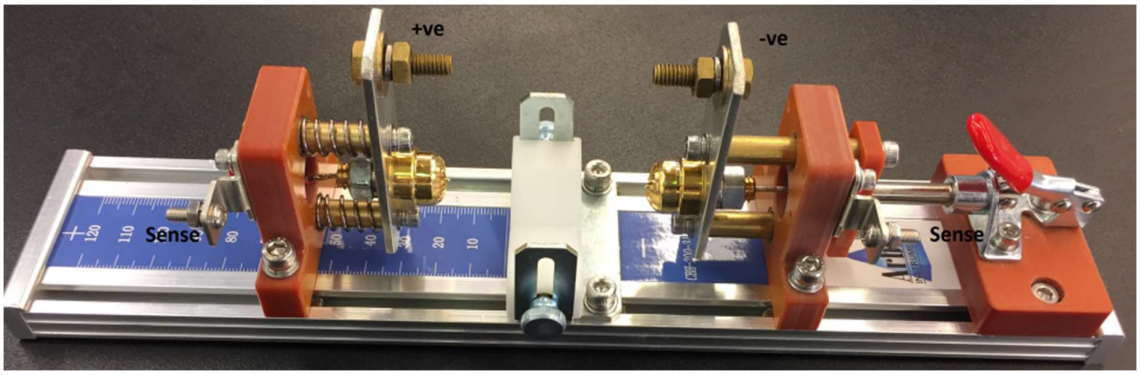


Figure 5.3 Cylindrical cell holder for currents up to 200A from Arbin instruments.

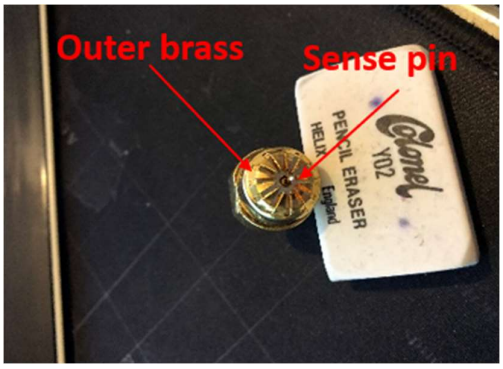


Figure 5.4 The holder's connector (top) and its side view connection to the cell (bottom).

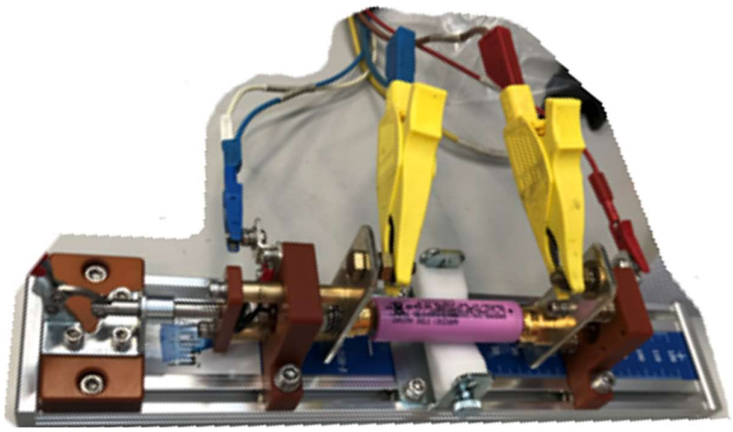


Figure 5.5 Cell, holder, and its connection to the booster wires.

5.2.2 Sequence explanation

As previously explained in Chapter 3, in order to parametrise ECMs, several characterisation tests must be performed on each cell. In this work the tests are designed with the purpose of identifying OCV(SoC) dependency and impedance parameters in respect to SoC and current rate by imposing discharging pulsed current waveforms to the cell. Due to the addition of the current rate influence investigation, the total time for the experimental procedure increases markedly compared to considering only a SoC dependency. Therefore, several sets of measures were taken to bring the total experimental time down to reasonable levels. Some of these measures are of the organisational nature, such as charging procedure, whereas others are related to directly shortening the test procedure which required modification of standard parametrisation algorithms. In the following paragraphs the methodology is explained in detail.

In all conducted tests, the initial SoC of battery was 100% which means that cells had to be fully charged prior to starting the testing. As characterisation is used only during discharge procedure, the charging of the cell is performed using constant current constant voltage protocol. The values for the charge cut-off voltage and tapered current are different for each battery cell and are usually reported in a datasheet. The potentiostat at hand features only one channel, meaning only one cell could be connected to it at any time, a constraint that severely impacted the testing capacity and increased the total time required for the testing. To alleviate this problem, two commercially available battery chargers (Xtar VP4 Plus Dragon Charger and Nitecore Digicharger D4) were acquired so the full charging of the cells required before the actual testing started, could be performed independently from SP-150, essentially increasing the testing capacity of SP-150 by allowing for simultaneous charging and testing procedures

of different cells. This meant that while test is performed on cell ‘’A’’ using SP-150, a cell ‘’B’’ could be fully charged at the same time using external chargers and be ready for the testing after cell ‘’A’’ actual tested, ended. If the potentiostat was used for both charging and test procedures, the ‘’B’’ cell could only be charged after the testing of ‘’A’’ has finished. Consequently, the experiment time would have been increased which was unacceptable considering that 8 cells had to be tested with several experiments ran on each cell. Once connected to the potentiostat, the CC-CV charging is finished in case the cells were not fully charged, or due to the self-discharge that might have occurred (usually around 0.5-1 % of SoC) and cells are rested for 20 minutes before beginning pulse testing procedure.

Pulse discharge current profiles are used for both OCV and impedance extraction with differences in number of applied pulses, i.e., number of SoC points at which identification is done. In both tests, applied current profile brings the cell SoC to the points of 90%, 80%, 70%, 60%, 50%, 40%, 30%, and 20%, whereas two additional SoC points, 95% and 10%, are added for OCV test. During the OCV test, pulses with $I_{cell,max}/2$ are applied to the cell spaced by 1h to allow cell to rest and properly capture OCV at the end of the rest period.

Regarding impedance parametrisation, in total four to five tests are performed for each cell with current pulses of different rates. The rates are selected to cover all range from 1C to max C rate in four or five points. Due to different current rates, pulse durations are different in each test and can be calculated using (3.24). The rest times are selected to be 20 minutes mainly for the reason of shortening total experiment time. Cutting the rest period by 40 minutes compared to 1h in [208], results in 33 hours of shorter testing duration per cell. The justification for the shorter rest time is as following:

- OCV and impedance identification are separated into two tests, compared to standard methods in which OCV and impedance parameters are obtained from the same test. Therefore, a long rest time is not required between pulses during impedance identification.
- The introduction of current rate investigation requires a new approach in parametrisation of the ECMs that focuses on data acquired during both pulse and rest periods. This is contrary to traditional methods that mainly focus on only the rest period using analytical equations with assumptions that are only true if a long rest time is applied.

- The developed method in this thesis takes into consideration the fact that the RC circuit dynamics is still on-going at the end of the rest period and no assumptions are made about the initial conditions in terms of voltages of EC branches.

5.2.2.1 EC Lab implementation of the sequences

The technique used to create the testing sequence is the Galvanostatic Cycling with Potential Limitation (GCPL), in which a constant predefined current is imposed to the cell but with predefined voltage potential limitations for both charging and discharging to make sure the health of the cell under test is not affected by a potential overcharge/discharge. Additionally, the rest periods are embedded in the procedure after each current pulse. Thus, GCPL is the most appropriate technique to define a customised sequence of current pulses and rest periods to the cell using the loop function of the software. As explained in Chapter 3, the value of current and its duration depends on the cell's capacity, and the desired SoC decrement. However, there are commonalities for all cell testing procedures. First of all, the sampling time is selected to 1s, the lowest possible. However, the GCPL5 technique allows for faster sampling time for few seconds after the current has been applied to the cell. Therefore, this technique is used as it allowed for capturing the high frequency dynamics with more precision. Since the rated voltage of all the battery cells is in the range between 0-5 V (except the LFP with 0-4 V), the voltage sensor resolution for all measurements is 200 μV or 0.2 mV.

Therefore, five or six tests per cell were performed for extracting the parameters of the ECM (OCV and impedance). The results of these experiments are also used to validate the developed model. Additionally, in order to validate the created model under the ET drive cycle, additional one or two tests are performed, with an imposed power profile (Power Profile Importation, i.e., GPW) from AMS T-O. ET power profiles are defined as presented in Chapter 4, and scaled according to the cell's maximum charge and discharge rates, preventing the cell from being stressed beyond its datasheet specifications. The overall experimental procedure is shown in Figure 5.6.

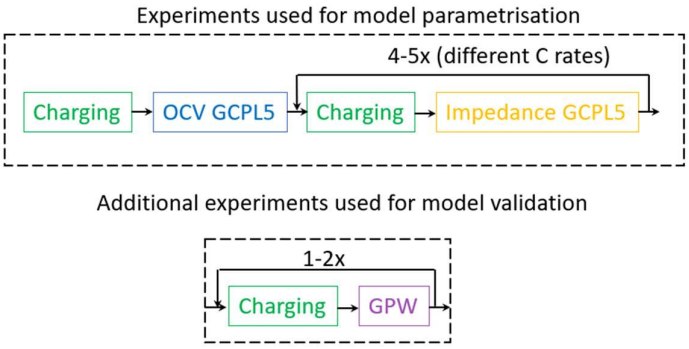


Figure 5.6 The overall test procedure for one cell.

The charging, OCV GCLP5, and impedance GCPL5 blocks are detailed in Figure 5.7. As mentioned, most of the initial full charging process is performed under CC/CV procedure using external chargers. Then, SP-150 finalises the CC/CV procedure using the GCPL5 technique. A constant charging current, according to datasheet for each cell, is applied until the maximum cell voltage (V_{max}) is reached, when the SP-150 switches to potentiostatic mode and keeps the cell voltage constant at V_{max} while cell current slowly decays to zero. Once, the cell charging current goes below the charge cut-off current, the CV voltage part is finished, and the cell is rested for 20 minutes before applying the other steps of the GCPL5 sequence. The OCV GCPL5 and impedance GCPL5 tests are different in number of applied pulses and the rest time between pulses, as previously explained. Throughout the test, the cell voltage condition ($V_{cell}>V_{min}$) is continuously checked. Once the condition is not met, the pulse is stopped and the sequence proceeds to the next step, i.e., relaxation. This occurs always during the last pulse (i.e., SoC decreasing from 20% to 10%) and only with pulses of high current amplitude.

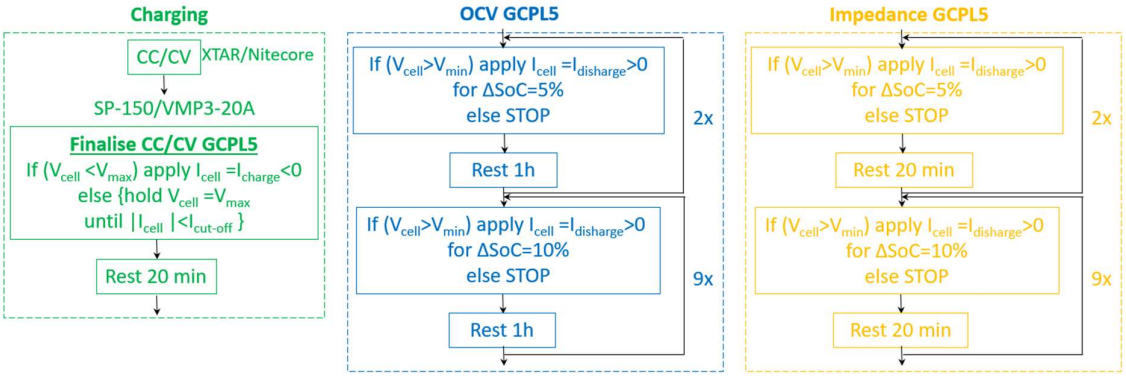


Figure 5.7 Flowchart of the Charging, OCV GCPL5 and Impedance GCPL5 sequences in more detail.

After characterisation tests are finished, the dynamic power profiles representative of ET application are applied to the cell with the purpose of validating the created models. Dynamic power profiles tests are designed such that power cycles discharge the cell within 90%-20%

SoC window, i.e., DoD of 70%, a typical SoC window extensively used in electric traction applications where the current capability of the cell is maximum [209]. Thus, prior to GPW, a cell is discharged to 90% SoC using GCPL5 after which a dynamic power profile, i.e., a scaled ET power profile, is applied to the cell which is indicated in Figure 5.8. As GPW sequence doesn't allow for minimum voltage condition implementation, the ET power profiles are scaled in such a way that the cell's SoC never drops below 20%. However, as it will be seen later, some scaled profiles do not discharge the cell to 20% at all. In this case, another cycle is applied again after rest period of 20 minutes with same stop and loop conditions. More on this will be explained in the section 5.5. The voltage waveforms of those experiment are compared with simulation results for validation purposes. Considering that a total of 7-8 experiments on average are ran per cell, for 8 cells it result in a total of 56 experiments performed.

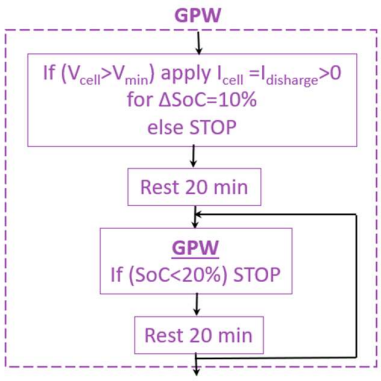


Figure 5.8 GPW test procedures in more detail.

5.3 Post-processing and data analysis

After the tests have been finished, the EC Lab software allows for raw data collected during the experiment to be extracted in .txt format for further processing. In this case, data was prepared in Microsoft Excel before it was imported to MATLAB for fundamental processing and curve fitting. The significant information that was extracted are array of time, current, voltage, and cell charge in Ah. Because several experiments were performed, an array of structures was created where each structure has fields that are the mentioned arrays. Later in the postprocessing process other fields are added.

Initial postprocessing includes identification of significant points, i.e., time instants, during experiments which are namely, the end of rest period, the start of pulse, the end of pulse, and the start of rest period. As explained in Chapter 3, these points are used to identify the OCV points (end of rest period) whilst the other points are used to calculate instantaneous resistance

as in (3.37). In Figure 5.9, the waveforms and key points during the 1.5C rate pulse experiment done on the Samsung INR35E cell, are shown.

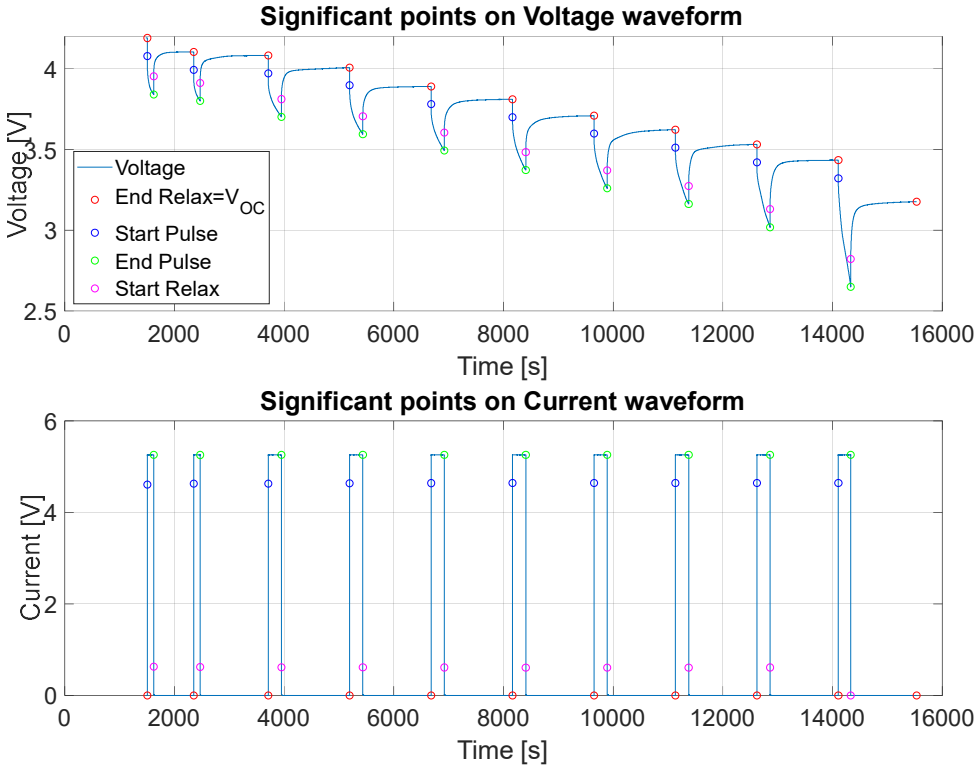


Figure 5.9 The voltage and current waveforms and their significant points during 1.5C rate pulse experiment for the Samsung INR35E cell.

5.3.1 OCV engineering

As already mentioned, the OCV points are extracted at the end of each 1h rest period during OCV GCPL5 experiment. Therefore, the SoC points at which OCV is identified are: [100, 90, 80, 70, 60, 50, 40, 30, 20] %. However, the pulse experiments shouldn't be ignored as they can contain information that complement OCV results. First, the OCV values at 95% and 10% can be known from pulse experiments. Those values are not as accurate as if they were extracted after 1h relaxation, but those points are important for the shape of the OCV curves that exhibits high non-linearities in the (95-100) % and (0-20) % SoC regions, as illustrated in Figure 5.10.

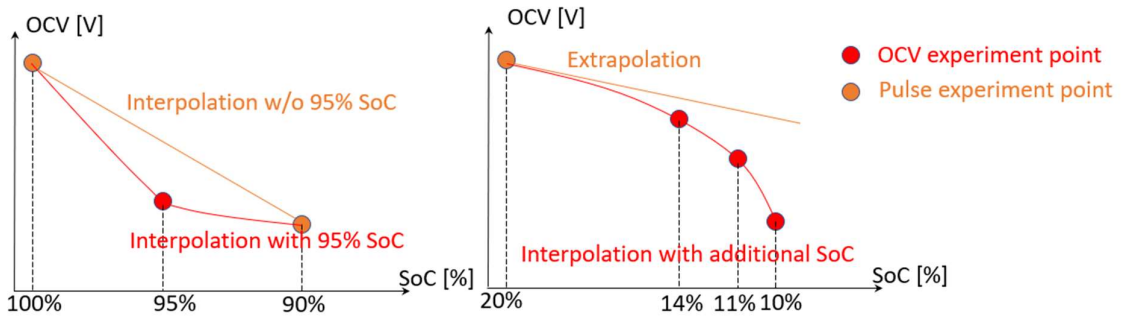


Figure 5.10 Identifying the non-linearities in OCV curves.

When it comes to lower region, more than one SoC point can be used for improved interpolation. Sometimes the condition $V_{cell}<V_{min}$ is achieved before SoC reaches 10% [210]. So, at times the last point during experiment is determined at greater than 10% SoC. This usually happens when high C current rates are applied. As OCV rapidly decays below 20% SoC, additional points from impedance experiment have to be used instead on relying on simple extrapolation methods using only the 30% and 20% SoC points from the OCV experiment.

A final factor to be considered is the time scale of the whole experiment cycle. OCV tests were the last experiments performed in the whole testing cycle, at the end of May 2021. On the other hand, the pulse experiments were performed from the end of February 2021 until the end of April 2021. Therefore, as the tests were performed under different ambient conditions, sometimes the OCV point after 1h was not the highest, because specific SoC points are very sensitive to temperature variation [211]. Additionally, the OCV tests were performed only with a single current level, whereas impedance is characterised at several currents, including $I_{cell,max}$. Therefore, the real OCV point, i.e., the "engineered" one, is always selected as the highest value available from the pool of points consisting of several points after 20 minutes and one point after 1h as shown in Figure 5.11. This procedure doesn't cause significant errors. If the acceptable difference between "engineered" OCV point and 1h point is 5mV, 92.5% of all cases fall under this condition, whereas that percentage increases to 96.25% if the error is increased to 10mV.

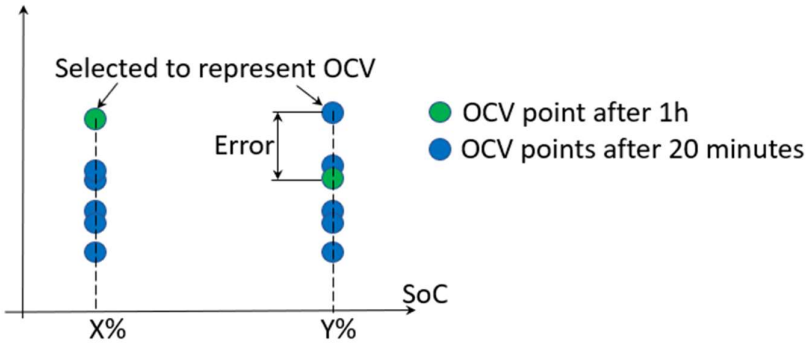


Figure 5.11 Engineering of the OCV points.

In Figure 5.12, as an example, nine points from OCV experiment and six additional points from pulse experiments are shown for the LG HG2 cell. As evident, this improves the spline interpolation process in non-linear and nearby SoC regions. Finally, the engineered OCV curves of all the selected battery chemistries are shown in Figure 5.13.

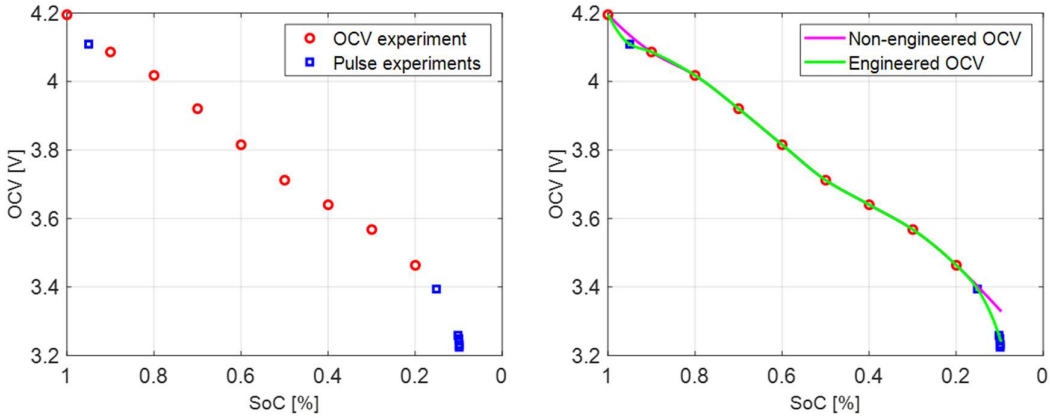


Figure 5.12 Difference between engineered and non-engineered OCV for LG HG2 cell.

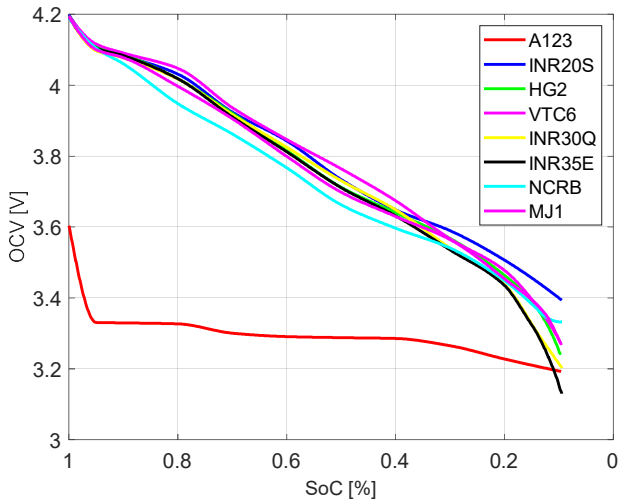


Figure 5.13 Engineered OCV curves for all the eight selected cells.

5.3.2 RC network voltage calculation (V_τ)

Once the relation between OCV and cell capacity is known, OCV(Q), an OCV versus experiment time should be calculated, OCV(t). This process was performed by combining the measured discharge capacity during experiment, Q(t) and previously calculated OCV(Q). In Figure 5.14 the process of obtaining OCV(t) is schematically shown whereas A123 M1B cell is taken as example and its OCV versus time is shown in Figure 5.15.

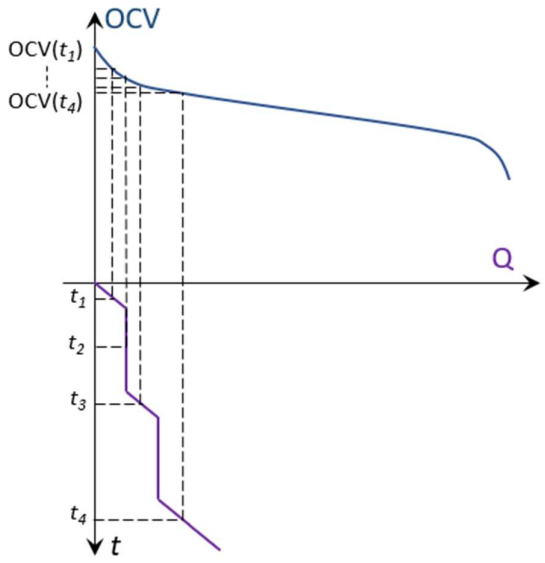


Figure 5.14 Process of finding OCV(t) from OCV(Q) and Q(t).

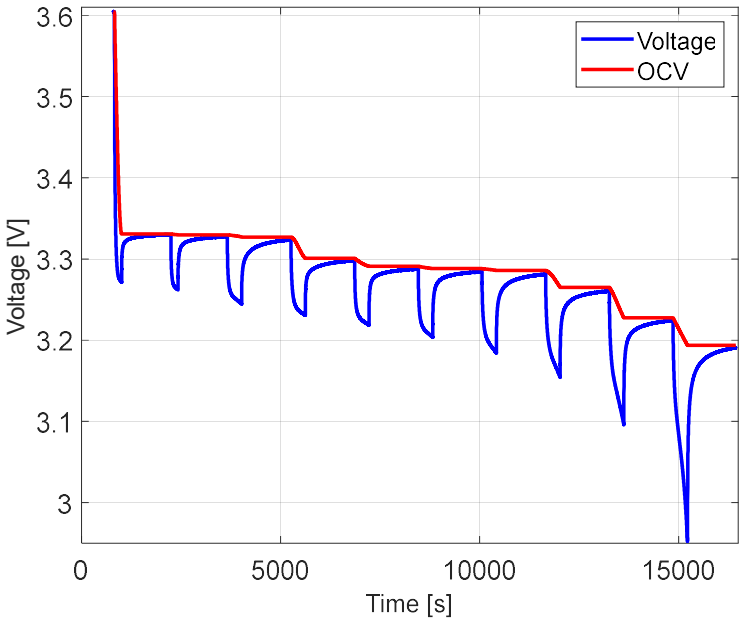


Figure 5.15 Cell terminal voltage and OCV during 1C pulse experiment for A123 M1B.

In order to obtain the voltages over the RC network, i.e., $V_\tau(t)$, an instantaneous resistance should also be calculated. Using the identified key points of interest, the resistance can be calculated at the beginning and end of each pulse using equations (3.1) and (3.2). The results for Samsung INR20S cell are shown in Figure 5.16 (interpolated), whereas the averaged instantaneous resistance for all SoC points and all C-rates is shown in Table 5.3. Additionally, the AC resistance at 1kHz has been shown for the cells from datasheet or from other papers. The calculated values showed good agreement.

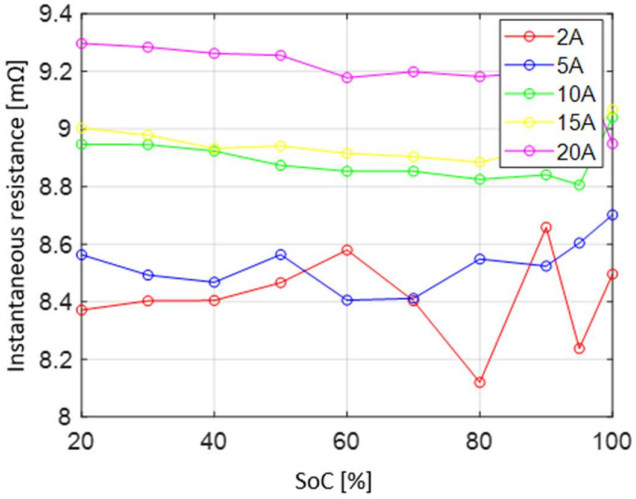


Figure 5.16 The instantaneous resistance at the beginning of pulse period for Samsung INR20S.

Table 5.3 The average instantaneous resistance for all selected cells.

Name	Average resistance [mΩ]	Resistance @1kHz
A123 M1B	5.8	6 [212]
Samsung INR20S	8.8	<15 [213]
LG HG2	14.5	15 [202], <20 [214]
Sony VTC6	12.6	13 [215]
Samsung INR30Q	12.4	13 [202], <26 [216]
Samsung INR 35E	21.1	21 [202], <35 [217]
Panasonic NCRB	36.5	37 [202]
LG MJ1	28.8	28 [202]

Before proceeding to calculate V_τ, it is important to take into consideration that the instantaneous resistance value is not constant during the pulse, because the SoC changes. Because the high frequency resistance values can be calculated only during current steps, which means at the beginning and the end of each current pulse, a linear relation can be established. Therefore, V_τ is calculated using (5.1). The V_τ waveform for A123 cell and 4C rate is shown in Figure 5.17.

$$V_\tau(t) = OCV(t) - V(t) - R_i(t)I \tag{5.1}$$

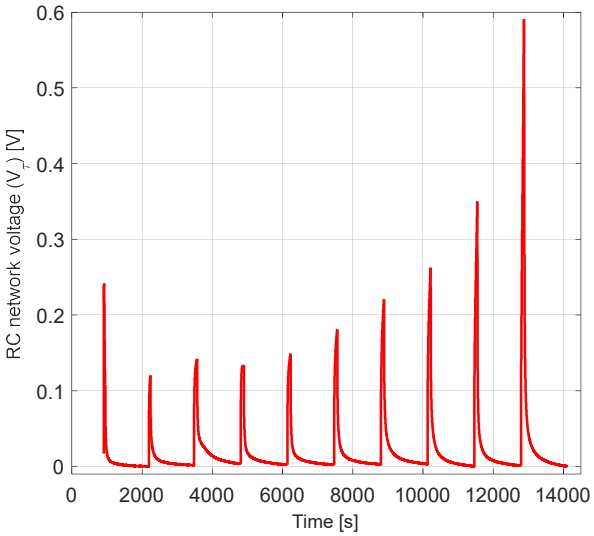


Figure 5.17 V_τ waveform for 4C pulse rate for A123 M1B cell.

As the OCV curve is extracted during 1h experiment it is evident that at some SoC points V_τ doesn't reach zero, i.e., steady state, as 20 minutes isn't enough for the battery to reach it. Compared to other parametrisation methods, namely analytical, where it is assumed that towards the end of the rest period the battery reaches steady state, in 20 minutes case that assumption cannot be made. Therefore, a curve fitting procedure is used to fit V_τ and find parameters of equivalent circuit model. Compared to traditional estimation methods which fit only relaxation period, the fitting in this thesis is performed for both pulse and relaxation period

and no hypotheses are made regarding the initial conditions. Therefore, for the curve fitting algorithm of V_τ is separated into pulse and relax periods for the more convenient analysis which is explained in the next section.

5.4 Curve fitting procedure

As explained in Chapter 3, the voltage of parallel RC circuit, during constant current application and rest periods, is described with equations in (3.26). For convenience, the equations are repeated here using notations more suitable for the fitting algorithm process. In (5.2) and (5.3) the $U_{0i,Pk}$ and $U_{0i,Rk}$ are initial voltages of the ith RC branch at the beginning of the kth constant pulse (CP) and the kth rest period (RP) respectively, whereas $\tau_{i,Pk}$ and $\tau_{i,Rk}$ are time constants of the ith RC branch during the kth CP and RP, respectively.

$$u_{i,Pk} = U_{0i,Pk}e^{-\frac{t}{\tau_{i,Pk}}} + \left(1 - e^{-\frac{t}{\tau_{i,Pk}}}\right)R_i I, \qquad I \neq 0 \tag{5.2}$$

$$u_{i,Rk} = U_{0i,Rk}e^{-\frac{t}{\tau_{i.Rk}}}, \qquad I = 0 \tag{5.3}$$

Commonly only two RC pairs are used in the battery simulations studies having the faster time constant in the order of seconds and the slower one in the range of tens or hundreds of seconds [175]. However, as mentioned, due to the GCPL5 technique, a charge transfer dynamic can be captured, so the additional third parallel RC circuit is added in this thesis. Therefore, the fitting equations that will be used in this work are:

$$f_{P,k} = a + \left(U_{01,Pk} - a\right)e^{-bt} + c + \left(U_{02,Pk} - c\right)e^{-dt} + e + \left(U_{03,Pk} - e\right)e^{-gt} \tag{5.4}$$

$$f_{R,k} = U_{01,Rk}e^{-mt} + U_{02,Rk}e^{-nt} + U_{03,Rk}e^{-pt} \tag{5.5}$$

In (5.4) and (5.5) $f_{P,k}$ and $f_{R,k}$ are used to fit the kth pulse and relaxation part of V_τ respectively. During each fit, the unknown coefficients (a, b, c, d, e, g, m, n and p) are obtained. They are related to the parameters of the ECM and can be determined by comparing equations (5.2) and (5.3) with (5.4) and (5.5). Hence, parameters of the equivalent circuit during the pulse (i.e., I≠0) are calculated as:

$$\begin{cases} R_{1,Pk} = \dfrac{a}{I}, \tau_{1,Pk} = \dfrac{1}{b}, C_{1,Pk} = \dfrac{\tau_{1,Pk}}{R_{1,Pk}} \\ R_{2,Pk} = \dfrac{c}{I}, \tau_{2,Pk} = \dfrac{1}{d}, C_{2,Pk} = \dfrac{\tau_{2,PN}}{R_{2,PN}}, \quad I \neq 0 \\ R_{3,Pk} = \dfrac{e}{I}, \tau_{3,Pk} = \dfrac{1}{g}, C_{3,Pk} = \dfrac{\tau_{3,Pk}}{R_{3,Pk}} \end{cases} \tag{5.6}$$

Likewise, ECM's parameters in relaxation (i.e., no current) are obtained as:

$$\begin{cases} R_{1,Rk} = \dfrac{U_{01,Rk}}{I}, \tau_{1,Rk} = \dfrac{1}{m}, C_{1,Rk} = \dfrac{\tau_{1,Rk}}{R_{1,Rk}} \\ R_{2,Rk} = \dfrac{U_{02,Rk}}{I}, \tau_{2,Rk} = \dfrac{1}{n}, C_{2,Rk} = \dfrac{\tau_{2,Rk}}{R_{2,Rk}}, \quad I = 0 \\ R_{3,Rk} = \dfrac{U_{03,Rk}}{I}, \tau_{3,Rk} = \dfrac{1}{p}, C_{3,Rk} = \dfrac{\tau_{3,Rk}}{R_{3,Rk}} \end{cases} \tag{5.7}$$

As it can be seen from (5.4) and (5.5), the values of $U_{0i,Pk}$ and $U_{0i,Rk}$ are either needed for curve fitting or are treated as unknowns and are set as output of fitting algorithm along with *a*, *b*, *c*, *d*, *e*, *g*, *m*, *n* and *p*. Compared to other parametrisation methods, in this approach, no assumptions are made regarding initial voltages. Instead, initial voltages can be analytically calculated before each CP and RP fitting procedure and used as known coefficients during curve fitting. Practically, the initial voltage of the ith branch at the beginning of the kth CP is equal to the ith branch relaxation voltage prior to the pulse at the time t_{relax} (i.e., at the end of (k-1)th RP) $u_{i,R(k-1)}(t = t_{relax})$. Similarly, the initial voltage of the ith branch at the beginning of the kth RP is equal to the ith branch pulse voltage at the time t_{pulse} (i.e., end of the kth CP) $u_{i,PN}(t = t_{pulse})$. It is evident that the procedure requires that the fitted voltages are known before each $U_{0i,PN}$ and $U_{0i,RN}$ calculations which is the basis for the developed algorithm shown in Figure 5.18.

$$U_{0i,Pk} = u_{i,R(k-1)}(t = t_{relax}) = U_{0i,R(k-1)} e^{-\frac{t_{relax}}{\tau_{i,R(k-1)}}} \tag{5.8}$$

$$U_{0i,Rk} = u_{i,Pk}(t = t_{pulse}) = U_{0i,Pk} e^{-\frac{t_{pulse}}{\tau_{i,Pk}}} + \left(1 - e^{-\frac{t_{pulse}}{\tau_{i,Pk}}}\right) R_{1,Pk} I \tag{5.9}$$

Initial conditions for the first CP are equal to zero (i.e., $U_{01,Pi} = 0$) since the system is in equilibrium before the test. By using (5.4), V_τ is fitted for the 1st CP (i.e. the coefficients *a*, *b*, *c*, *d*, *e* and *g* are determined), from which initial conditions for the 1st RP can be computed using (5.9). Similarly, then, by using (5.5) V_τ is fitted for the 1st RP (i.e. coefficients, m, n and p are calculated). Thus, initial conditions for 2nd CP can be determined (5.8). This procedure is repeated until the last RP is reached (i.e., k=N), as shown in the flowchart in Figure 5.18 and Figure 5.19.

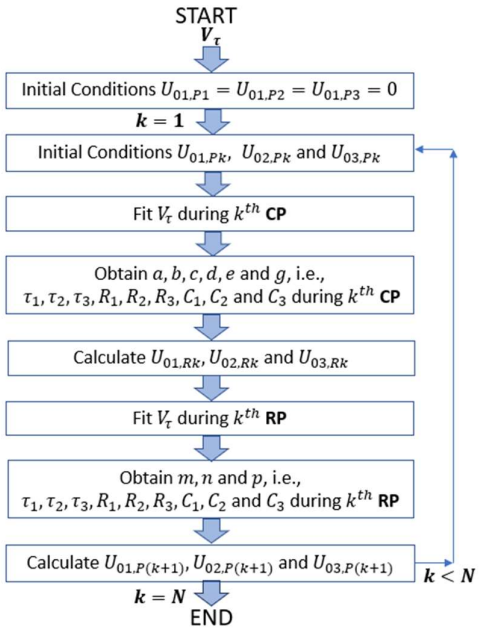


Figure 5.18 The flowchart of the developed algorithm for ECM parametrisation [174].

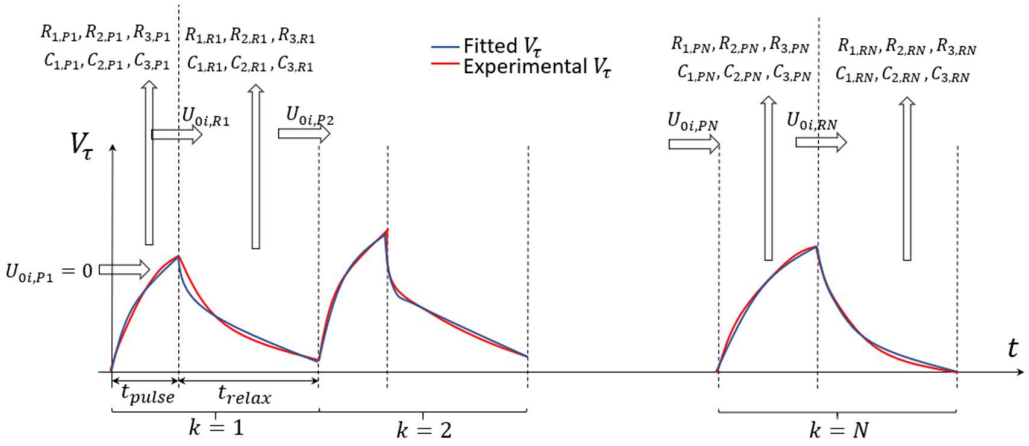


Figure 5.19 The fitting procedure shown using waveforms.

5.4.1.1 Fitting procedure

The fitting procedure uses the non-linear least squares method by employing MATLAB's embedded curve fitting features. Due to the nature of the proposed algorithm, a programmatic curve fitting that uses *fit* function is selected over the interactive toolbox. Since fitting equations (5.4) and (5.5) are not listed under standard equation types, a *fittype* function is used to create non-linear exponential equations that are passed as arguments of the *fit* function. The selected algorithm used for the fitting procedure is a default *Trust-Region* with the robust option disabled. As with any non-linear curve fitting application, the algorithm requires initial guess (i.e., starting point), the lower and upper boundary for the unknown parameters, i.e., for *a*, *b*,

c, *d*, *e*, *g*, *m*, *n* and *p*. Additionally, the numerical algorithms that perform the non-linear least squares are sensitive to mentioned parameter's boundaries and starting points. In the following paragraphs, it is explained how they are varied to achieve a better fit.

First, it has been noticed that the algorithm performs better, i.e., it achieves better fit, during the pulse period. This is because the calculated initial voltages used to fit the relaxation waveform are calculated after the pulse waveform has been fitted, meaning that those values are fixed in (5.5). However, if the fit is performed without initial voltage constraints, i.e., if $U_{01,Rk}$, $U_{02,Rk}$ and $U_{03,Rk}$ are treated as unknowns, it would result in similar initial voltages and time constants but for different RC circuits. Thus, adding initial voltage constraint impairs the fitting procedure of the relaxation forms from the mathematically ideal one. It can be observed from [175] that the initial voltage of the slowest time constant RC circuit can practically be obtained as the intersection of the y-axis and extension of the tail of the relaxation waveform. Therefore, by analysing the relaxation waveform before pulse fitting, the slowest RC circuit can be ''forced'' to end pulse period at the expected voltage range, which is used as an initial condition for fit during relaxation. A straight line, created from the two points that lie on relaxation waveform, $(t_1, y_{relax}(t_1))$ and $(t_2, y_{relax}(t_2))$ (Figure 5.20), is used to estimate the initial condition of the slowest RC circuit during the relaxation period. A point where the line intersects the y-axis (V_{exp}) is analytically calculated prior to every pulse fit, and it is used as one of the fitting constraints during the pulse.

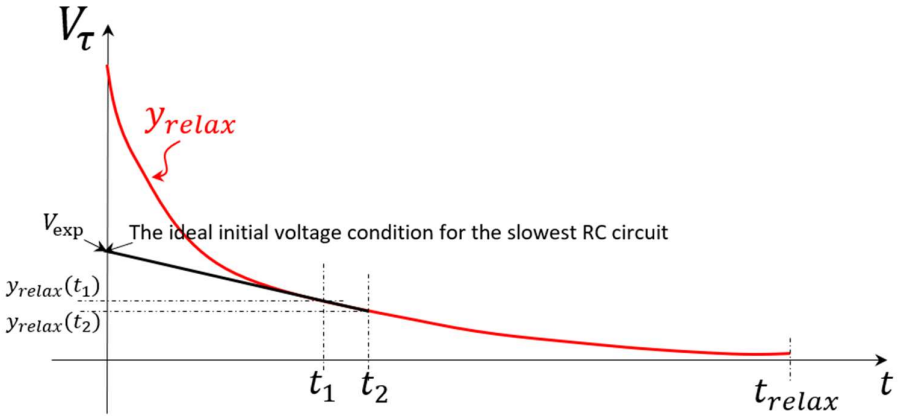


Figure 5.20 Relaxation waveform and auxiliary line used for initial voltage estimation.

Suppose that the calculated initial voltage of the slowest RC circuit ($U_{01,RN}$) doesn't fall within ($0.9V_{exp}$,$1.1V_{exp}$) interval, $y_{pulse,fit1}$ in Figure 5.21. In this case, the fit is performed again by changing the starting values and the boundaries of the *a* and *b* parameters. It is essential to mention that parameter *a* physically represents the steady state voltage, i.e., voltage when

current is applied for long time ($t \to \infty$) as shown in Figure 5.21. However, during the short pulse this condition is most likely not achieved. Therefore, algorithm will adjust the parameter's a upper boundary and perform the fit again until $U_{01,RN}$ falls within the defined region as shown in Figure 5.21. As an illustration, if the a_1 is the upper boundary in the first iteration, the fit will never reach the expected range. If the upper limit is increased to a_2 in the second iteration, with parameter b being also varied, the initial voltage will fall within the predefined interval. This procedure is done in a loop for 40 iterations which can stop earlier if the initial voltage condition is met.

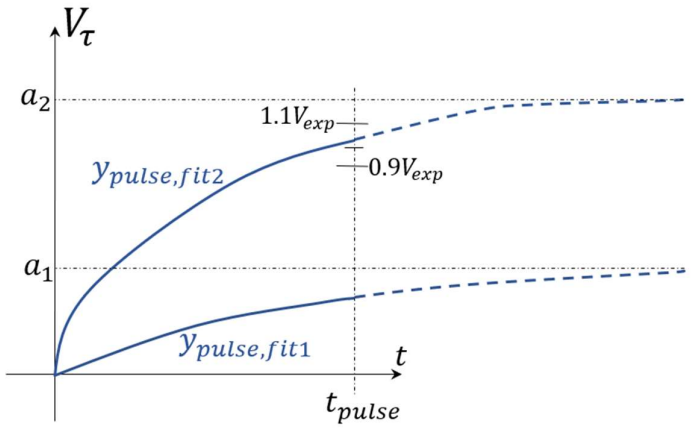


Figure 5.21 The pulse fitting loop procedure of the slowest RC circuit.

As already mentioned, this procedure reduces the error during the relaxation period at the expense of the goodness of fit during the pulse. It has been observed that adding weights to specific parts of the curve enhances the fit. Ten times more weights are put on points following current pulse steps for duration of 1s, in order to catch the charge-transfer dynamics better. Another important aspect that affects the result is the boundaries of the parameters in which the fitting algorithm searches for parameters and the starting point. The explanation for the a and b parameters was given above. When it comes to c and e parameters, their lower boundary is zero volts. However, the upper boundaries are 0.75Vmax and Vmax, respectively, where Vmax is the maximum V_τ during the pulse. The starting point is selected to be in the middle between minimum and maximum. When it comes to time constants, d and e are in $[10^{-2},10]$ and $[10,10^5]$ range, respectively. Finally, the relaxation parameters, m, n and p, have the same boundaries as the pulse ones.

In Figure 5.22 the V_τ fitting results are shown for INR30Q cell during 1C pulse experiment. Additionally, the waveforms of three RC pairs are shown as well as the auxiliary line. As expected from the procedure, the green waveform during pulse ends in the vicinity of V_{exp} to

ensure for the acceptable fit during relaxation. The absolute error between experimental and fitted V_τ are shown in Figure 5.23. Finally, in Figure 5.24 the cell's terminal voltage during pulse experiment is compared to the fitted one. It can be noticed that good fit is obtained. In the following section the model and errors are discussed in more detail.

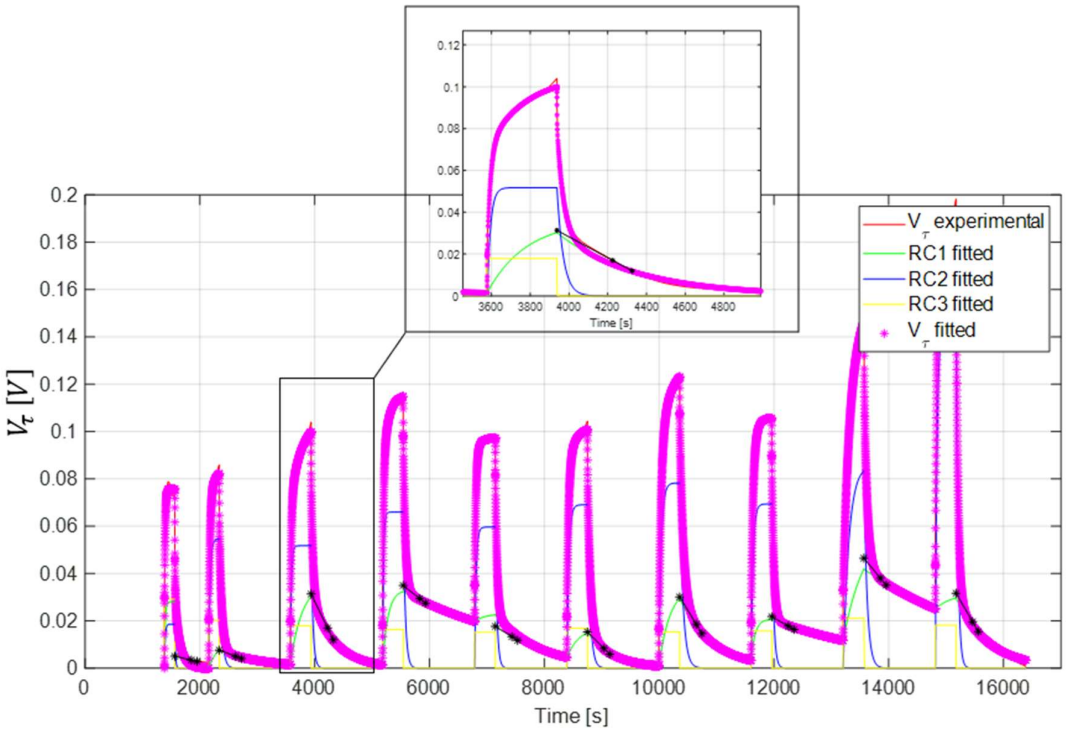


Figure 5.22 Experimental and fitted V_τ with three RC waveforms for INR30Q cell with 1C pulse.

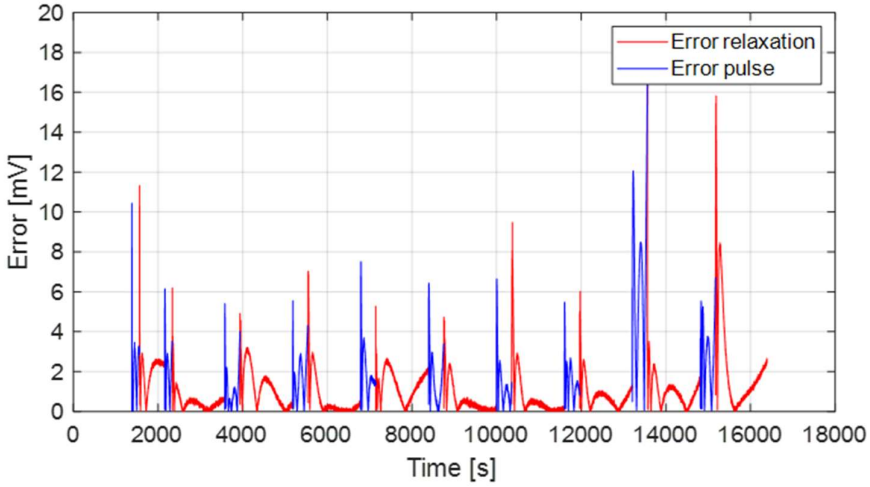


Figure 5.23 Absolute error between experimental and fitted V_τ for INR30Q cell with 1C pulse.

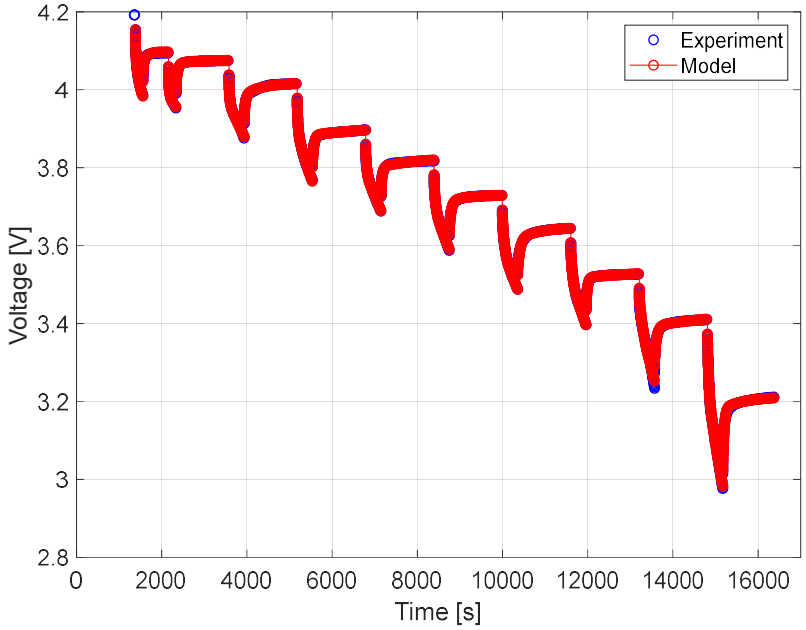


Figure 5.24 The experimental and fitted voltage at cell terminals of the INR30Q cell during 1C pulse experiment.

5.4.1.2 Fitting results and battery cell parameters

The red waveform from Figure 5.24 is obtained simply by subtracting fitted V_τ and voltage drop over instantaneous resistance form from the identified OCV from OCV GCPL5 test. The accuracy of the curve fitting procedure for the different cells and different pulse experiments are summarised in Table 5.4. The parameter selected to represent the goodness of fit, i.e., difference between model and experiment, is the root mean square absolute error (RMSAE) for all sampled points during the test. It can be noticed that in most of the experiments the RMSAE is less than 5 mV which is a good fit according to [218].

Table 5.4 Accuracy of the fitting procedure for all battery cells during impedance estimation tests.

	Test N° 1		**Test N° 2**		**Test N° 3**		**Test N° 4**		**Test N° 5**	
	I [A]	**RMSAE [mV]**	**I [A]**	**RMSAE [mV]**	**I [A]**	**RMSAE [mV]**	**I [A]**	**RMSAE [mV]**	**I [A]**	**RMSAE [mV]**
M1B	2.5	**6.4**	5	**5.6**	10	**5.7**	15	**6.5**	20	**7.4**
INR20S	2	**1.4**	5	**2.4**	10	**3.2**	15	**4.3**	20	**5.8**
HG2	3	**2.2**	5	**2.4**	10	**3.4**	15	**4.4**	20	**5.9**
VTC6	3	**2.2**	5	**2.5**	10	**3.7**	15	**5.1**	20	**5.7**
INR30Q	3	**2.1**	6	**2.7**	10.5	**4**	15	**5.2**	N/A	N/A
INR 35E	3.5	**3.1**	5.25	**4.2**	7	**5.3**	8	**6.8**	N/A	N/A
NCRB	1.7	**1.7**	3.4	**2.9**	5.1	**4.4**	6.8	**6.7**	N/A	N/A
MJ1	3.5	**2.4**	5.25	**2.9**	7	**3.5**	10	**4.8**	N/A	N/A

However, the results in the above table are obtained purely on assessing the error between experimentally obtained and mathematically fitted waveforms from previous section. As already explained, the parameters of RC circuit are calculated form the fitted waveforms which

means that each waveform has its corresponding R and C values. During relaxation period SoC doesn't change, meaning that relaxation RC parameters are identified for set of discrete SoC points. During battery application, SoC changes continuously, therefore the results should be interpolated, and in this work a linear interpolation is used to estimate battery cell parameters between two known SoC points. Another point to be considered is that relaxation period are calculated for each impedance identification test. As battery cell must have unique parameters value during relaxation (I=0), compared to RC parameters when current is applied (I≠0), the calculated relaxation parameters are averaged over four or five experiments performed (depending on the cell). An identical procedure is performed with the instantaneous resistance.

When it comes to RC parameters obtained from fitting the waveform during pulse, the procedure is different. The SoC during current pulse discharge is not constant, so calculated parameters can be arbitrarily assigned to any SoC point within the SoC variation during the pulse. In this work it is assumed that parameter is valid for the lowest value SoC achieved during that pulse, so that pulse and relaxation parameters are assigned to the same SoC value which makes easier the postprocessing in terms of interpolation. The battery cell parameters for LG MJ1 cell are shown in Figure 5.25 and Figure 5.26.

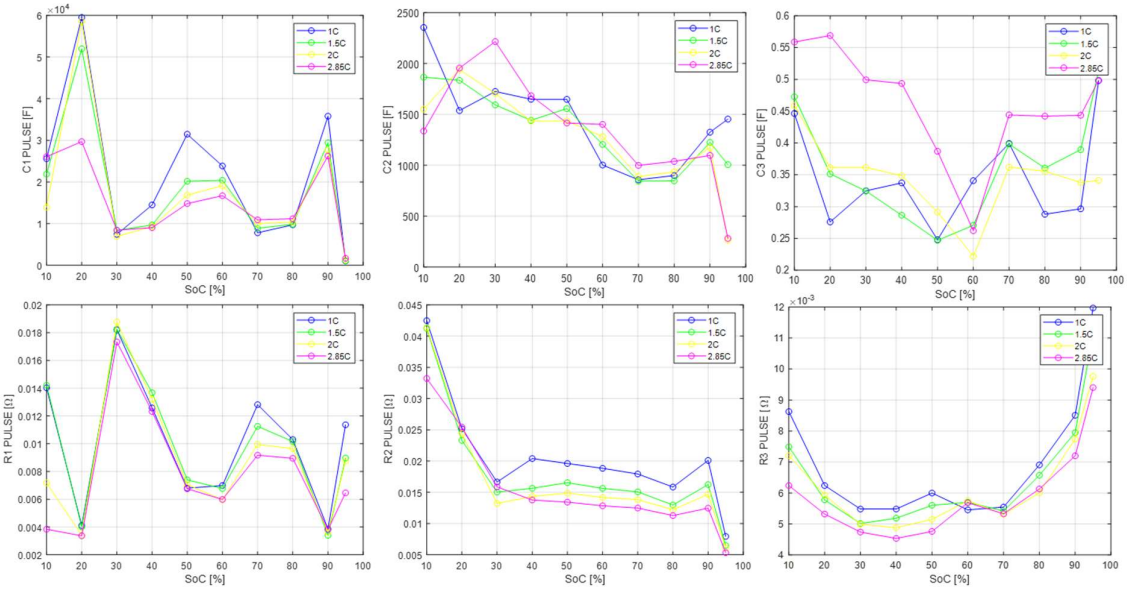


Figure 5.25 Value of the three RC parameters extracted during the pulse for LG MJ1 cell.

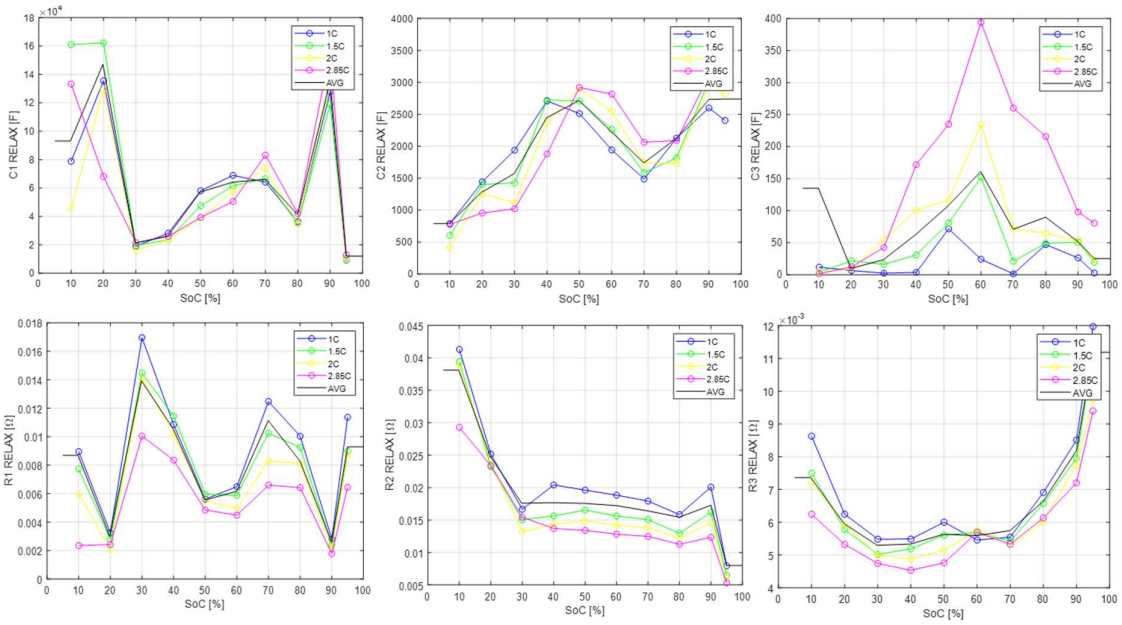


Figure 5.26 Value of the three RC parameters extracted during the relaxation for LG MJ1 cell.

5.5 Model validations

In order to additionally validate the accuracy of the model, an equivalent circuit is created in MATLAB/Simulink. The RC parameters are embedded inside 2D lookup table (SoC and current as inputs) whereas OCV and instantaneous resistance are in the form of 1D lookup table with SoC as input as shown in Figure 5.27. The SoC is calculated using Coulomb counting method for the reasons given in Chapter 3.

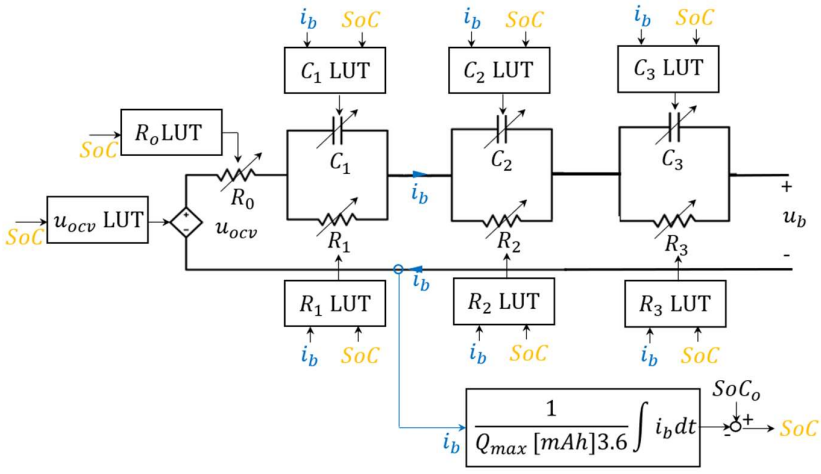


Figure 5.27 Implementation of battery cell model in Simulink/MATLAB using ECM with 3 RC pairs and 1D and 2D lookup tables.

The circuit above is the actual model of battery cell and thus is further used to assess the difference between model and experiment. Initially, the accuracy of the model is assessed by

applying to it the same current profiles as during impedance estimation tests, with RMSE and maximum relative error (MxRE) shown in Table 5.5 - Table 5.7. The three tables show results for three different cells, i.e., HE, HP and MEP. The errors values are calculated separately for the [10,100] % and [20,90] % SoC ranges and shown in both mV and %. It needs to be specified that in the [20,90] % SoC region, only portion of the waveform was analysed and besides RMSAE also root mean square relative error (RMSRE), mean absolute error (MAE) and mean relative error (MRE) are shown. As the parameters are not constant during the pulse and as there are unique relaxation parameters and instantaneous resistance, the error increases as expected compared to the mathematical ideal fit from Table 5.4.

Table 5.5 The accuracy of HG2 cell model for five pulse tests.

		SoC=[100-10]%		SoC=[90-20]%					
N°	**I [A/C]**	**RMSAE [mV]**	**RMSRE [%]**	**RMSAE [mV]**	**RMSRE [%]**	**M_xRE [%]**	**$RMSAE_{pulse}$ [mV]**	**MAE_{pulse} [mV]**	**MRE_{pulse} [%]**
1	3/1	7.04	0.223	**5.51**	0.148	0.478	**3.84**	6.07	0.08
2	5/1.67	7.99	0.255	**5.06**	0.139	0.515	**3.05**	6.37	0.08
3	10/3.33	9.24	0.298	**6.44**	0.177	0.748	**3.01**	8.46	0.13
4	15/5	9.88	0.312	**8.34**	0.234	1.528	**3.22**	10.62	0.16
5	20/6.67	10.88	0.324	**11.15**	0.322	3.029	**4.01**	14.49	0.19

Table 5.6 The accuracy results of INR20S cell model for five pulse tests.

		SoC=[100-10]%		SoC=[90-20]%					
N°	**I [A/C]**	**RMSAE [mV]**	**RMSRE [%]**	**RMSAE [mV]**	**RMSRE [%]**	**M_xRE [%]**	**$RMSAE_{pulse}$ [mV]**	**MAE_{pulse} [mV]**	**MRE_{pulse} [%]**
1	2/1	4.47	0.142	**5.15**	0.134	0.54	**3.89**	6.13	0.068
2	5/2.5	5.14	0.16	**5.02**	0.134	0.506	**2.55**	6.51	0.097
3	10/5	7.9	0.227	**7.41**	0.198	0.913	**2.91**	9.82	0.144
4	15/7.5	8.92	0.258	**8.03**	0.217	1.59	**2.9**	11.49	0.153
5	20/10	10.45	0.31	**8.94**	0.247	2.157	**2.72**	12.21	0.151

Table 5.7 The accuracy results of INR35E cell for four pulse tests.

		SoC=[100-10]%		SoC=[90-20]%					
N°	**I [A/C]**	**RMSAE [mV]**	**RMSRE [%]**	**RMSAE [mV]**	**RMSRE [%]**	**M_xRE [%]**	**$RMSAE_{pulse}$ [mV]**	**MAE_{pulse} [mV]**	**MRE_{pulse} [%]**
1	3.5/1	9.37	0.308	**6.17**	0.173	0.579	**4.41**	7.62	0.1
2	5.25/1.75	9.8	0.315	**7.72**	0.219	0.812	**4.2**	8.72	0.14
3	7/2	11.22	0.346	**10.87**	0.301	1.354	**4.84**	10.36	0.22
4	8/2.28	12.41	0.371	**13.39**	0.382	2.756	**5.51**	11.4	0.27

In the last step, the cell models are verified when a dynamic power profile, that is a scaled representation of the ET application, is applied. The ET power profiles obtained in Chapter 4 are scaled in such a manner that after scaling down, the cell is not exposed to power values outside its limits.

As already mentioned in section 5.2.2.1, depending on the battery capacity and power limitations, some of the scaled power profiles discharge the battery cell less than 70% DoD. In this case when the initial cycle is finished, the cell is left to rest for 20 minutes and then it is

discharged again, with the purpose of analysing the model with estimated parameters over the full SoC range. This is the case of INR35E cell, with capacity of 3.5Ah and maximum continuous discharge current of 8A, for which almost two full taxiing profiles can be applied with DoD of slightly above 70%, i.e., 72%. The results for this cell are shown in Figure 5.28 - Figure 5.33.

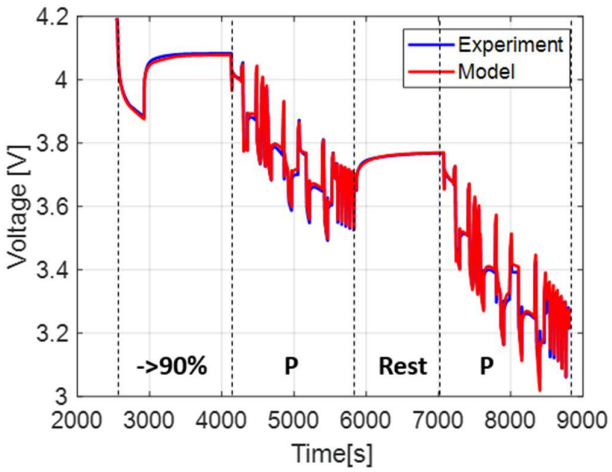


Figure 5.28 Voltage at the cell terminals of the model and experiment during dynamic power profile for INR35E.

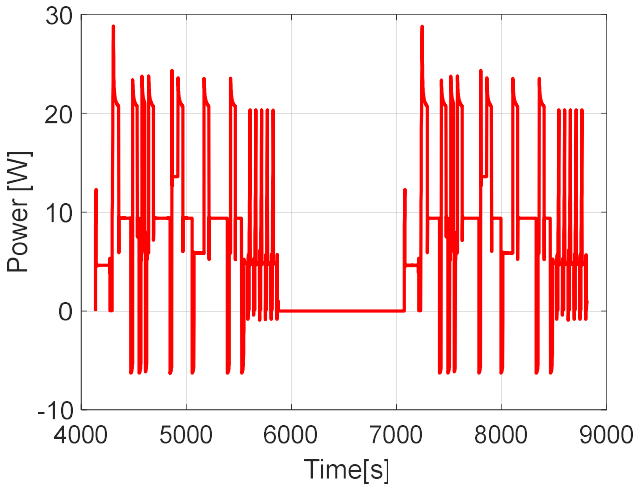


Figure 5.29 Dynamic power profile applied to the INR35E cell discharging it from 90% to 20% SoC.

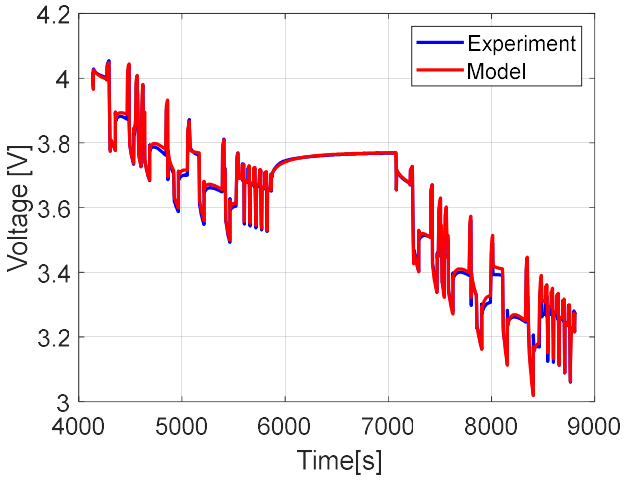


Figure 5.30 Voltage at the cell terminals of the model and experiment during dynamic power profile for INR35E (zoomed 4000s to 9000s).

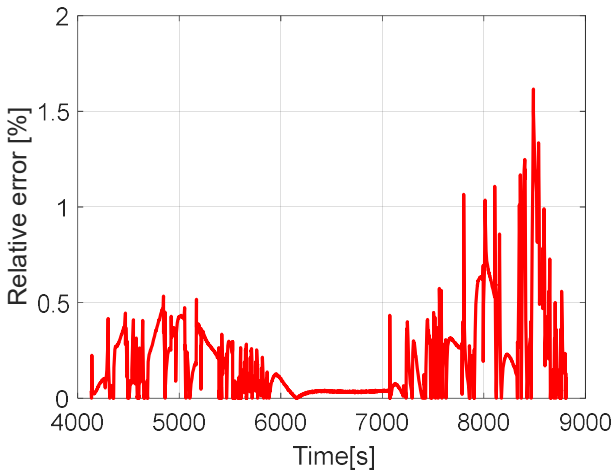


Figure 5.31 Relative error of terminal voltage during dynamic power profile for INR35E (zoomed 4000s to 9000s).

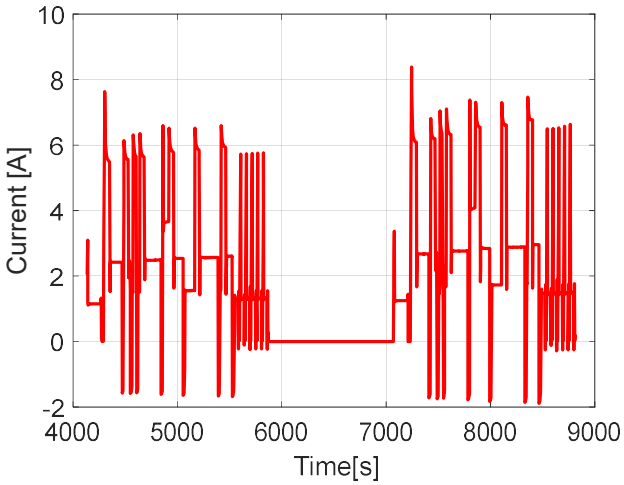


Figure 5.32 Current of the INR35E cell model during the power profile.

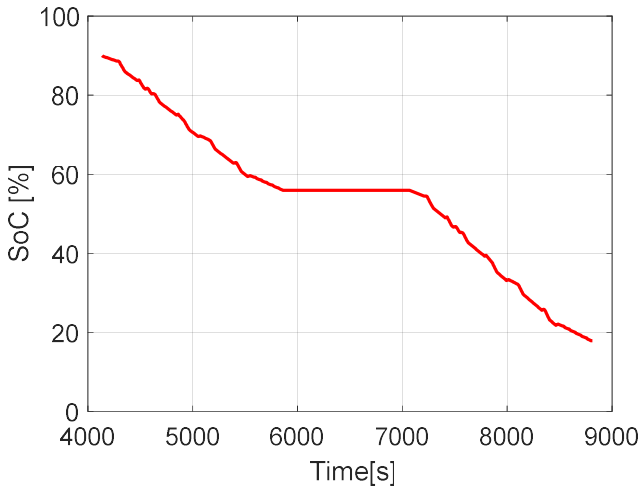


Figure 5.33 SoC of INR35E cell during power profile.

In contrast to the way the testing of INR35E cell was done, for smaller/weaker cells, the applied scaled profile would discharge that battery cell to 20% before completing one full taxiing cycle, which is the case for, e.g., INR20S cell. If this is the case, a modified power profile is created and applied, by scaling it in such a way that the application of the full taxing cycle would result in exactly 70% DoD, i.e., 90% to 20% SoC. Figure 5.34 - Figure 5.39 show the comparative results for INR20S cell , where the results on the left side are for the scaled profile that hits the battery limits before it ends, whereas the results on the right side are with the further scaled profile that makes sure the energy consumed allows discharge of the cell to the specified DoD.

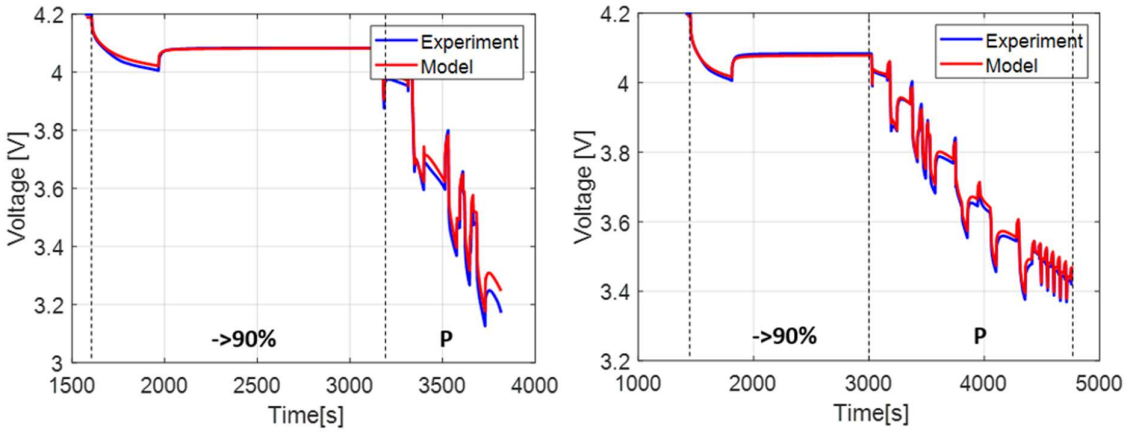


Figure 5.34 Voltage at the cell terminals of the model and experiment during two dynamic power profiles for INR20S.

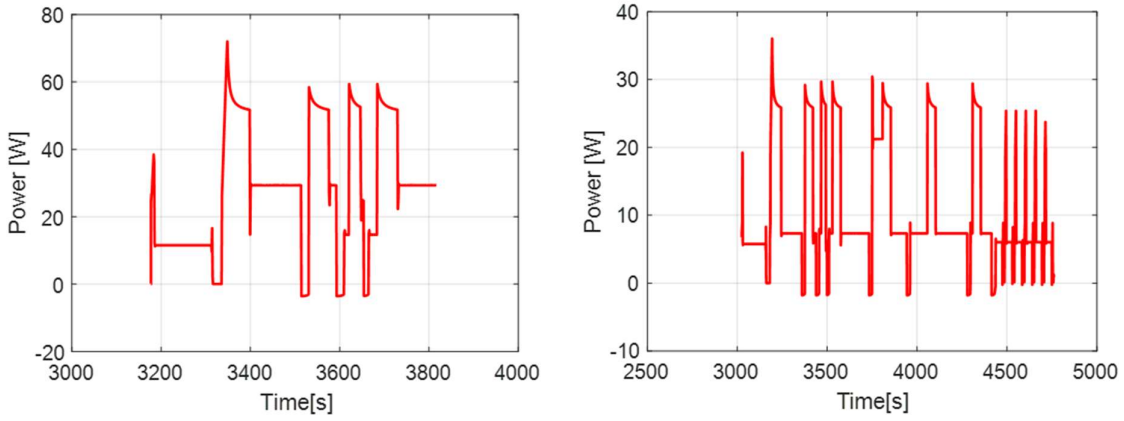


Figure 5.35 The two dynamic power profiles applied to the INR20S cell.

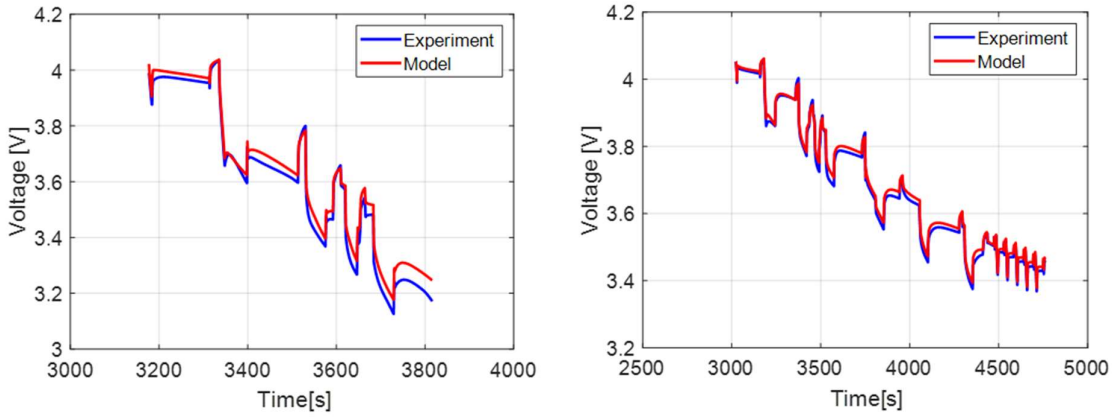


Figure 5.36 Voltage of the model and experiment during dynamic power profiles for INR20S (zoomed).

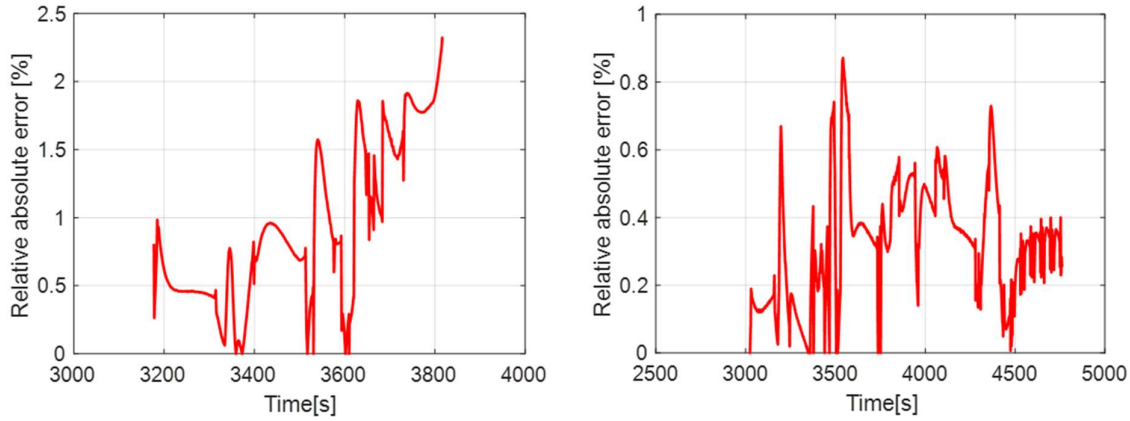


Figure 5.37 Relative error of terminal voltage during dynamic power profiles for INR20S.

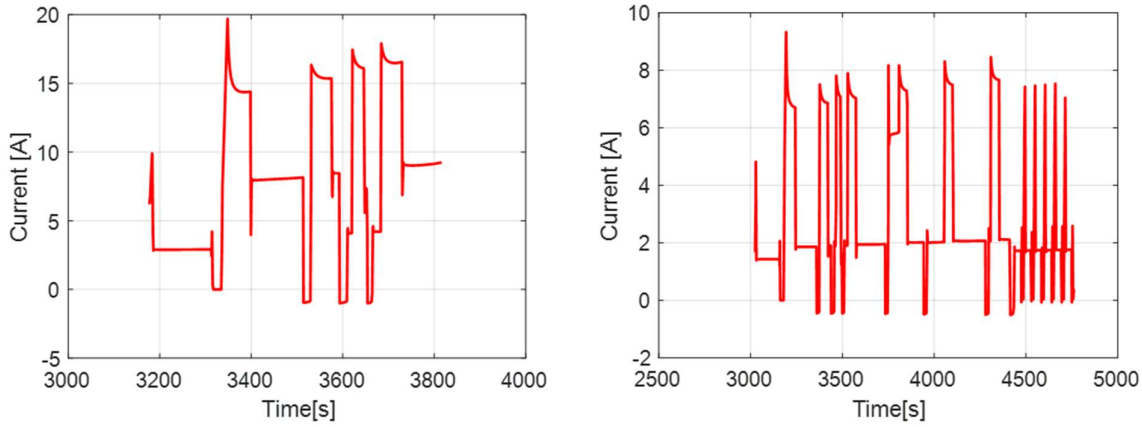


Figure 5.38 Current of the INR20S cell model during the power profiles.

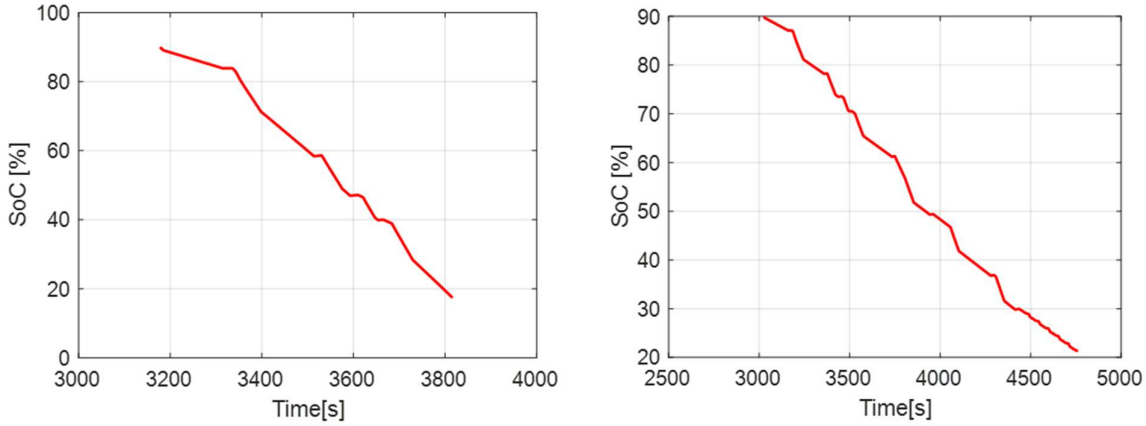


Figure 5.39 SoC of INR20S cell during power profiles.

As it can be concluded from the figures above that in general, the models that were using the parameters identified with the proposed methodology showed good agreement with the experiments. The biggest error occurs when the full scaled cycles would deplete battery more than 70% DoD, i.e., more power intensive profile. In this case, cell is discharged with currents that are close to its maximum continuous C-rates continuously for several minutes as seen in Figure 5.38 (left). This results in inevitable temperature raise which the developed model does not account for. The relative error evolution is shown in Figure 5.37 (left), and it clearly be seen that with time progression, i.e., as the cell temperature is expected to increase, the error increases as well. When the power profile is further scaled to prevent the load consuming more energy that would reduce the DoD below the minimum threshold, it results in smaller error. In this case, the applied currents are lower (Figure 5.38 (right)) and consequently the temperature increase will be lower. The minimum error is achieved for cells whose original scaled profile depletes the cell less than 70%. This scenario happens for cells that have high capacity and lower maximum discharge current. The results of the three experiments presented above are

shown in Table 5.8 for [90-20] % SoC range. The last column represents the percentage of test time during which the relative error is less than 1%.

Table 5.8 Errors for three representative power profiles.

	RMSAE [mV]	RMSRE [%]	MxRE [%]	% of time RE <1%
INR35E	10.37	0.303	1.62	98.34
INR20S full	13.52	0.37	0.87	100
INR20S	35.71	1.04	1.91	64.8

5.6 Conclusion

In this chapter, eight cylindrical lithium-ion cells are modelled, with the aim of using developed models for the analysis of potential use of battery energy storage in ET application through a model-based design approach. The developed models were validated against pulse and dynamic experiments and showed good agreement. The models can predict battery behaviour over a wide SoC range (DoD=70%) and wide current range with acceptable errors. It has also been found that when the applied profile drives cells to their limits, the model tends to lose its accuracy due to temperature increase of the experimental cells and rise of non-linearities.

Thus, the model of the cells could be further improved using environmental chambers to account for ambient temperature and performing parameterisation experiments for several temperature values. For example, if five temperature values and current levels are to be selected, a total of 25 experiments had to be done in addition to 5 new experiments for OCV extraction, i.e., 30 per cell. It means that the total experiment time would increase at least five times including prolongation of the validation experiments. Therefore, in this case, with eight batteries and one channel available for testing, the experimental procedure would last between 6 and 8 months of everyday activities. Additionally, the accuracy of the model could be improved by including the inner cell temperature estimator. Considering that one of the objectives of this thesis is to propose an ETS model that encompasses all parts of the system, including control, the long temperature experiments should be included in future studies, for which this work should represent a starting point.

6 Chapter: The full model of ETS

In this chapter, the aircraft dynamics, electric drive, and battery cells models, developed in Chapters 2, 4 and 5, are all combined into a unique forward-facing dynamic model of ETS. The developed model can be used for design purposes, observing interactions between different system parts, and developing low- and high-level controls such as energy management strategies. However, this chapter focuses on the performance analysis of batteries composed of HE and HP cells modelled in Chapter 5. Several batteries with different energy content are evaluated regarding weight, energy recovery analysis and economic merit.

6.1 The battery rating selection

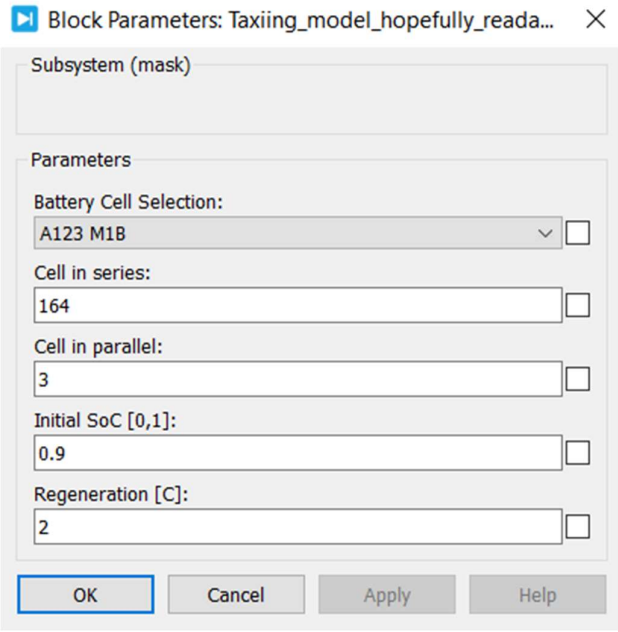


Figure 6.1 The mask of the battery pack block.

The whole system model includes the battery model with a mask as shown in Figure 6.1 and the aircraft model mask as shown in Figure 4.30. The main selection criterium for any battery is the cell type. Once the cell type is selected, the number of cells in series (N_s) and parallel (N_p) should be decided. If those two parameters are left unconstrained, an infinite number of batteries could be analysed for this application. The N_s and N_p depend on the imposed design constraints such as energy content, continuous peak power, pulse peak power, weight, volume etc. For the analysis in this section, two constraints are selected:

1. Nominal battery voltage to equal 540 V.
2. Maximum continuous power to equal 75 kW.

The first constraint fixes N_s for each cell type as in:

$$N_s = \frac{540\ V}{V_{cell,nom}\ [V]} \tag{6.1}$$

As already discussed in Chapter 2, the battery is directly connected to the inverter without the DC/DC converter. This means that the battery must provide sufficient voltage for the proper operation of the electric drive unit. Therefore, the battery's nominal voltage is constrained to 540 V. As the battery voltage is variable, the voltage fed to the drive will be either higher or lower than 540 V depending on the battery SoC. Because the field weakening strategy is implemented, the drive can cope with lower voltage levels.

Another premise outlined in Chapter 2 is that the ETS will be analysed as AET, i.e., no APU to behave as a backup if the battery cannot provide the necessary power. Thus, battery power rating must be designed in such a way to allow for acceleration from 0 to 20 knots, as the most critical power event, at all SoC. Therefore, the second constraint is forcing the battery's maximum continuous power rating to be 75 kW. This approach is more conservative than if the battery's maximum power was designed to match the aircraft max speed cruise of 20 knots (~30 kW), as batteries can be exposed to pulses above its maximum continuous power for specific amounts of time. However, the battery would then regularly be exposed to power pulses above its rated value, reducing the lifecycle, which is critical for this operation. Using the selected approach, the battery can provide 75 kW even at low SoC states, allowing for unplanned active runway crossing before take-off at the end of the taxiing cycle. This also means that battery cell current will rarely exceed $I_{cell,max}$ which supports the battery's lifetime. Additionally, oversizing the battery in terms of power also ensures that the battery can provide the power necessary for critical events at the end of life.

Once the number of cells in series is determined, a string (configuration of N_sS1P) is formed. That one string has its energy content and continuous power rating defined in (6.2) and (6.3), which do not satisfy the needs of electric taxiing.

$$P_{string,max} = N_s V_{cell,nom} I_{cell,max} \tag{6.2}$$

$$E_{string} = N_s V_{cell,nom} Q \tag{6.3}$$

Therefore, the number of strings in parallel is determined as

$$N_p = \left\lceil \frac{75\ kW}{P_{string,max}\ [kW]} \right\rceil \tag{6.4}$$

where $\lceil * \rceil$ symbol represents the round up to integer function. Once N_s and N_p are selected, batteries can be analysed. The batteries, first of all, mainly differ in energy content which can be calculated as in:

$$E_{bat} = N_p N_s V_{cell,nom} Q_{cell} \quad (6.5)$$

$$E_{usable} = N_p N_s V_{cell,nom} Q_{cell} DoD \quad (6.6)$$

As explained previously, the DoD considered in this study is 70%, i.e., 90-20% SoC range. In Table 6.1, the parameters of eight batteries are shown, each composed of one cell type from the analysed set of cells in Chapter 5.

Table 6.1 Battery specifications.

	Ns	Np	Ntot	m_{bat} [kg]	E_{bat} [kWh]	E_{usable} [kWh]
NCR B	148	21	3108	147.63	38	26.60
MJ1	149	14	2086	102.21	26.47	18.53
INR 35E	150	18	2700	130.41	34.02	23.81
HG2	150	7	1050	50.4	11.34	7.938
VTC6	150	7	1050	47.77	11.34	7.938
INR 30Q	150	10	1500	72	16.2	11.34
INR 20S	150	7	1050	50.4	7.56	5.29
A123	164	3	492	37.39	4.06	2.84

As it can be noticed, the cells with a higher (P/E) ratio result in batteries with less energy, and the cells with a lower (P/E) ratio result in higher energy content. The benefit of having less energy is that the battery is lighter, which will result in less consumption during flight. Still, the question is how many taxiing cycles this energy content can sustain. On the other hand, a larger battery will carry more energy and be available for more cycles, increasing battery life. The mentioned aspects are analysed for the eight selected battery types in the next section.

Once the N_s and N_p are selected, the cell models developed in Chapter 5 are scaled to battery model using equations:

$$R_{bat} = \frac{N_s}{N_p} R_{cell} \quad (6.7)$$

$$C_{bat} = \frac{N_p}{N_s} C_{cell} \quad (6.8)$$

$$Q_{bat} = N_s Q_{cell} \quad (6.9)$$

$$OCV_{bat} = N_s OCV_{cell} \quad (6.10)$$

6.1.1 BMS considerations

Each battery needs a BMS to ensure safe operation of system and operator. Lithium- ion cells can enter thermal runaway due to numerous reasons, main ones being overheating, over-charge, over-discharge and mechanical abuse. Therefore, BMS must monitor states of battery and react in timely manner when detecting suspicious behaviour. For this purpose, voltage, current and temperature are sensed among other parameters. However, some important parameters such as SoC are estimated and most advanced BMS use filtering techniques such as Extended Kalman Filter. Another function of the BMS is to limit the performance of battery when needed in a way that it doesn't comprise the mission. The design of a sophisticated BMS is necessary to ensure longevity and performance since battery behaviour can change over time [219]. As battery ages the capacity decreases (capacity fade) and internal resistance increases (power fade) and thus BMS for mission critical applications, such as ET, must have health tracker implemented in their algorithms [220]. The performance analysis in the section ahead was perform for begging of life and the impact that ageing has on financial revenue for airlines and is discussed in section 6.3.1.

As total percentage of recuperated energy depends on cells' limitation regeneration limit is imposed in the model, meaning that the implemented BMS logic would prevent cells being charged with higher rates than rated. The regeneration limit can be changed by the user according to the selected cell as it can be seen in Figure 6.1.

Finally, the alternative approach in battery performance modelling, once a thermal and mechanical design are advanced, is scaling the drive cycle to the cell level. By doing this, a busbar resistance between the cells can be included, as well as appropriate thermal models of the cooling system. Additionally, this modelling approach allows for analysis of how different position of the cell within the pack impacts the temperature of the cells. As this modelling approach requires a more mature design stage, in this work a first approach has been selected.

6.2 The battery results and discussion

6.2.1 HE batteries

It is essential to mention that another parameter that can be selected is battery regeneration rate, as seen in Figure 6.1. The standard charge continuous rates are applied for all batteries. Still, as braking events are of short time scales, the battery can accept higher charging rates so that parameter is left to be selected by the user, and as it will be seen, how it affects the regeneration capabilities.

Table 6.2 Panasonic NCRB battery performance for A320 69t during AMS T-O for three braking strategies.

	E_{prop} [kWh]	E_{tot} [kWh]	E_{regen} [kWh]	$\frac{E_{regen}}{E_{prop}}$ [%]	$\Delta\frac{E_{regen}}{E_{prop}}$ [%]	SoC_{end} [%]	DoD [%]
MAX	12.43	11.74	0.69	5.55	8.07	58.87	31.13
BLEND	12.69	11.97	0.72	5.67	2.85	58.14	31.86
MIN	12.86	12.55	0.31	2.41	2.31	56.64	33.36

In Table 6.2, the results of the battery composed of NCRB cells are shown for 69t A320 aircraft and three braking strategies under AMS T-O cycle. Compared to the results of Chapter 4 (Table 4.8), the impact of the battery's regeneration capability can be seen. According to datasheet [221], the standard charging current for NCRB cell is 0.5C, and it has been selected during the maximum regeneration strategy. It can be noticed that 5.55% of propulsion energy can be recovered with this battery, which represents a drop of 8.07% compared to the theoretical maximum of 13.62% for this strategy. When it comes to blend and minimum regeneration strategy, a limit of 0.75C is selected for cell charging limit because the braking events are shorter and can tolerate a higher charging rate as presented in [222] for NCR cell. From the above table, it is clear that blend strategy is the best choice as it can achieve savings as much as during maximum regeneration strategy and it also provides extra safety. Thus, for the other batteries, only blend strategy is considered, and the results for AMS, TXL and LHR are shown in figures and tables below for 69t A320 aircraft.

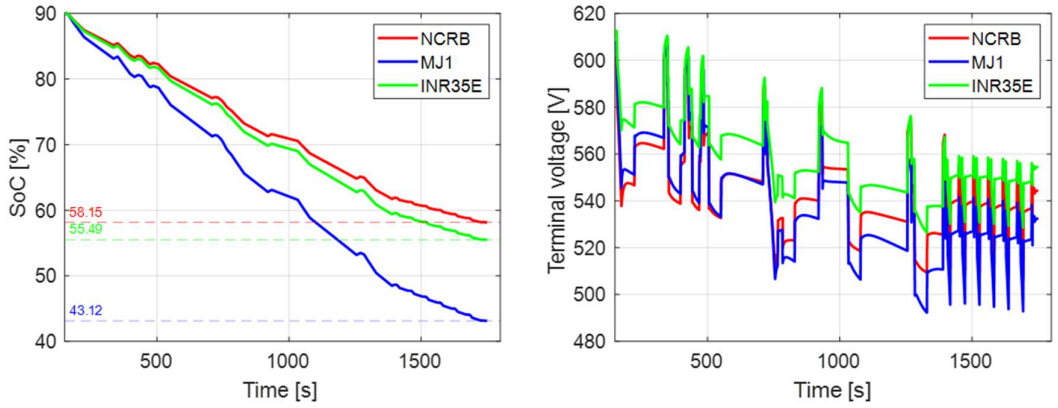


Figure 6.2 SoC (left) and terminal voltage (right) during AMS T-O for blend braking strategy for three HE batteries employed in 69t A320.

Table 6.3 HE battery performance for A320 69t during AMS T-O for blend braking strategy.

	E_{prop} [kWh]	E_{tot} [kWh]	E_{regen} [kWh]	$\frac{E_{regen}}{E_{prop}}$ [%]	$\Delta\frac{E_{regen}}{E_{prop}}$ [%]	SoC_{end} [%]	DoD [%]	N	η [%]
NCRB	12.69	11.97	0.72	5.67	2.85	58.15	31.85	2	93.7
MJ1	12.69	12.18	0.51	4.02	4.50	43.12	46.88	1	93.2
INR35E	12.69	12.04	0.65	5.12	3.40	55.49	34.51	2	94.6

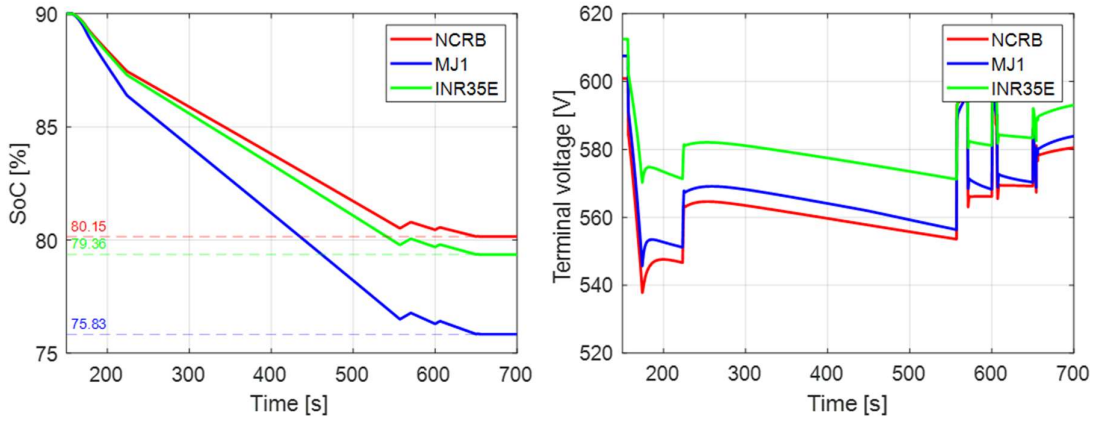


Figure 6.3 SoC (left) and terminal voltage (right) during TXL T-O for blend braking strategy for 69t A320.

Table 6.4 HE battery performance for A320 69t during TXL T-O (unrestricted) for blend braking strategy.

	E_{prop} [kWh]	E_{tot} [kWh]	E_{regen} [kWh]	$\frac{E_{regen}}{E_{prop}}$ [%]	$\Delta\frac{E_{regen}}{E_{prop}}$ [%]	SoC_{end} [%]	DoD [%]	N	η [%]
NCRB	4.02	3.86	0.16	3.98	1.53	80.15	9.85	7	94.4
MJ1	4.02	3.90	0.12	2.99	2.52	75.83	14.17	4	94.4
INR35E	4.02	3.87	0.15	3.73	1.78	79.36	10.64	6	95.8

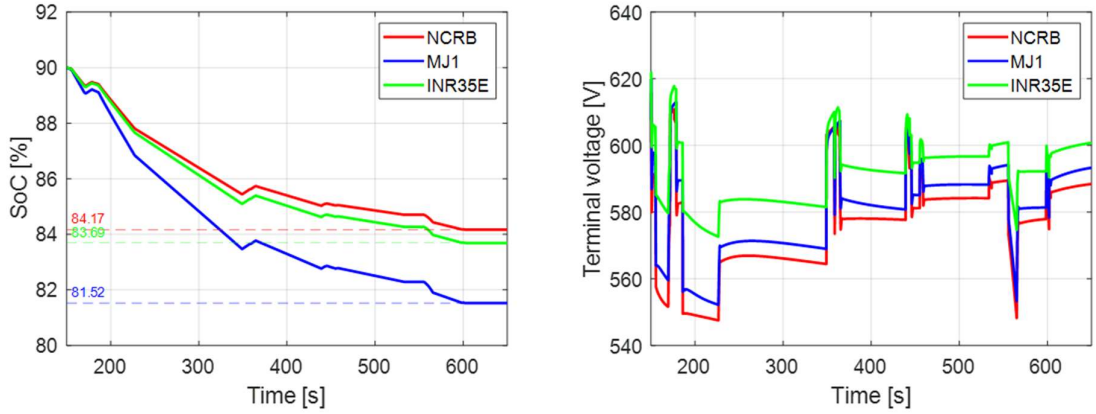


Figure 6.4 SoC (left) and terminal voltage (right) during LHR T-I for blend braking strategy for 69t A320.

Table 6.5 HE battery performance for A320 65t during LHR T-I for blend braking strategy.

	E_{prop} [kWh]	E_{tot} [kWh]	E_{regen} [kWh]	$\frac{E_{regen}}{E_{prop}}$ [%]	$\Delta\frac{E_{regen}}{E_{prop}}$ [%]	SoC_{end} [%]	DoD [%]	N	η [%]
NCRB	2.52	2.30	0.22	8.73	4.22	84.17	5.83	12	95.6
MJ1	2.52	2.35	0.17	6.75	6.2	81.52	8.48	8	95.5
INR35E	2.52	2.31	0.21	8.33	4.62	83.69	6.31	11	96.8

The first thing that can be noticed for all three taxiing cycles is that the most energy can be harvested with a Panasonic NCRB battery, even though all cells have a similar charge rate, i.e., 2.62 A and 2.51 A (i.e., 0.75C for all cells). This is because the NCRB battery has the most cells in parallel due to the lowest discharge P/E ratio.

As the most energy abundant, the NCR battery can sustain the most cycles on one charge, i.e., 2 AMS T-O or 7 TXL T-O or 12 LHR T-I. Further analysis of the potential number of flight missions that can be done on one charge depends on the charging strategies. If the aircraft is charged after every flight, the battery should provide energy for one T-O and one T-I cycle. This option is viable as the typical turnaround time is 45 minutes, and during this time, the battery can be charged with a 70% SoC window while passengers disembark and board. In this scenario, all HE batteries can provide energy for the worst-case scenario, AMS T-O and LHR T-I with the following DoD, 37.7%, 55.4% and 40.8% for NCRB, MJ1 and INR35E, respectively.

Another option is for batteries to be charged after one aircraft rotation, i.e., after two flights. This option might be favourable by budget airlines famous for having very short turnaround times of 25 minutes [223]. Additionally, using the charging infrastructure and electricity at the non-hub airports, where companies don't have available discounts like ones at their hub airports, might result in higher operational costs. Therefore, this option should be investigated as well.

Unfortunately, none of the HE batteries from Table 6.1 can sustain two AMS T-O and two LHR T-I on one charge. However, it is highly unlikely to have two worst-case taxiing scenarios during one aircraft rotation. Therefore, the less strict and more realistic worst-case scenario should be adopted. If one AMS T-O, one TXL T-O and two LHR T-I is assumed as worst-case, the following DoDs of 55.4%, 78%, 57.8% can be obtained for NCRB, MJ1 and INR35E, respectively. Even though DoD for MJ1 exceeds 70% DoD (i.e., 8% below 20% SoC), this is an acceptable event as it wouldn't happen frequently. It is fair to note that NCRB could also sustain two AMS T-O and two LHR T-I by dipping into reserves below 20% SoC by 5.4% SoC.

It is common for all batteries made from HE cells to sustain the worst-case scenario of one flight mission, i.e., longest taxi-out (AMS) and longest taxi-in (LHR), on one charge. Regarding the second charging strategy, only NCRB can sustain two AMS and two LHR cycles by dipping into reserves below 20% SoC. On the other hand, MJ1 and INR35E can support a less strict worst-case scenario of one AMS T-O cycle, one TXL (unrestricted) T-O and two LHR T-I cycles. Considering that the average DoD for taxi-out is 25% and for taxi-in 7%, the aircraft using these battery types can, in most cases, fulfil one full rotation (return flight) on one charge.

Being the lightest HE battery, MJ1 is a good choice, and it can sustain worst-case scenarios for both charging strategies. However, its lifecycle might be compromised due to deeper DoD compared to NCRB with shallower DoD. Additionally, the NCRB battery offers the higher regeneration capability of all battery types, but it is the heaviest and would result in more fuel consumption during flight. These aspects are analysed in section 6.3.1 from the financial point of view.

Regarding differences between the two charging strategies, it is crucial to consider the number of rotations aircraft make during the day. Typical A320 makes six short-haul flights per day, i.e., three rotations [76]. Therefore, the battery would be discharged and charged with a deep SoC window three times a day or discharged and charged with a shallow SoC window six times a day. An in-depth study analysing the lifecycle of this application should be considered for future research. The second charging option reduces operational costs, but the lifecycle could be more compromised. However, statistical analysis should be performed when more cycles become available to examine what percentage of taxiing missions would have the worst-case scenario. Finally, the operations can be improved if the battery is charged during the flight, which means it wouldn't have to be sized for taxiing at the destination airport. However, there are no regulations about charging energy storage during commercial flights, which is highly unlikely to be approved due to safety issues related to charging at low temperatures.

6.2.2 MEP batteries

The results for MEP batteries for AMS T-O cycle for the same aircraft and braking strategy are shown in Figure 6.5, Figure 6.6 and Table 6.6. As expected, due to lower energy content, the batteries cannot complete the entire AMS T-O cycle. Samsung INR30Q can perform 75% of the cycle, whereas HG2 and VTC6 can deliver around 48.5% of the cycle. When they could sustain the cycle, the average total regenerated energy is 2%, which is lower than for HE batteries. In this segment of the cycle, batteries experienced lower efficiency.

As already mentioned, the field weakening strategy is implemented. In this case, for all three batteries, the voltage reaches critical low points when a negative id current is injected. This suggests that lower battery voltage (at 20% SoC) is not dangerous to electric drive with an adequately designed MTPA and field weakening strategy. The developed model could be used for further improvements on MTPA based on a lower number of cells in series.

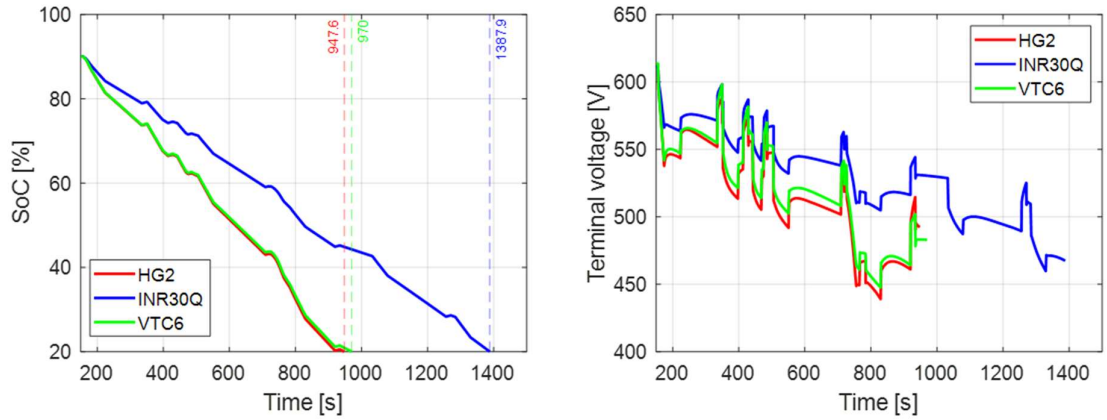


Figure 6.5 SoC (left) and terminal voltage (right) during AMS T-O for blend braking strategy for three MEP batteries employed in 69t A320.

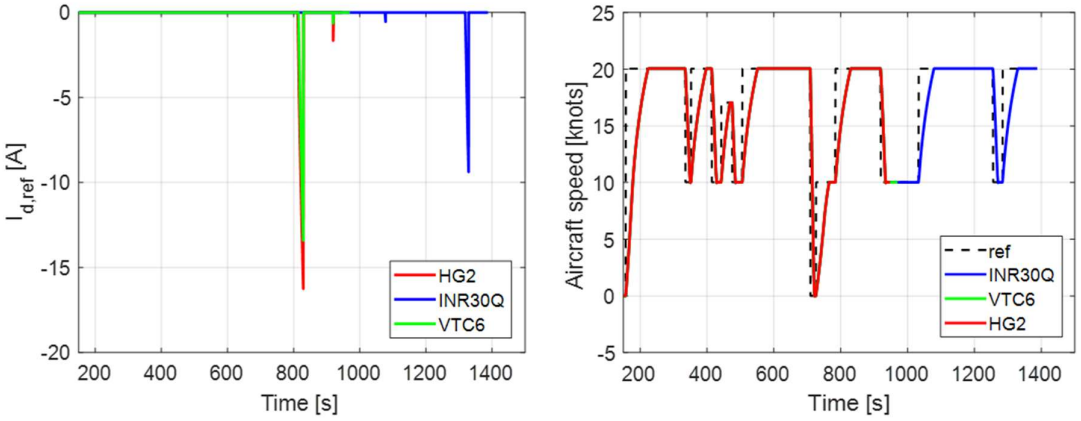


Figure 6.6 $I_{d,ref}$ (left) and aircraft speed (right) during AMS T-O for blend braking strategy for three MEP batteries employed in 69t A320.

Table 6.6 MEP battery performance for A320 69t during AMS T-O for blend braking strategy.

	E_{prop} [kWh]	E_{tot} [kWh]	E_{regen} [kWh]	$\frac{E_{regen}}{E_{prop}}$ [%]	[%]	η [%]
HG2	7.57	7.41	0.16	2.11	48.34	90.9
INR30Q	11.27	11.00	0.27	2.40	75.03	93.6
VTC6	7.65	7.50	0.15	1.96	49.70	91.2

When it comes to TXL T-O cycle, all MEP batteries can sustain at least two cycles, except INR30Q, which can support three. It is fair to compare regeneration capability to HE batteries for this cycle. Even though the MEP cells have higher power than HE cells, the regeneration capabilities in terms of C rate are the same, which due to lower capacity resulted in lower absolute charge rate. It is emphasised that the model allows for this change, and different regeneration rates can be further investigated with more aggressive regeneration.

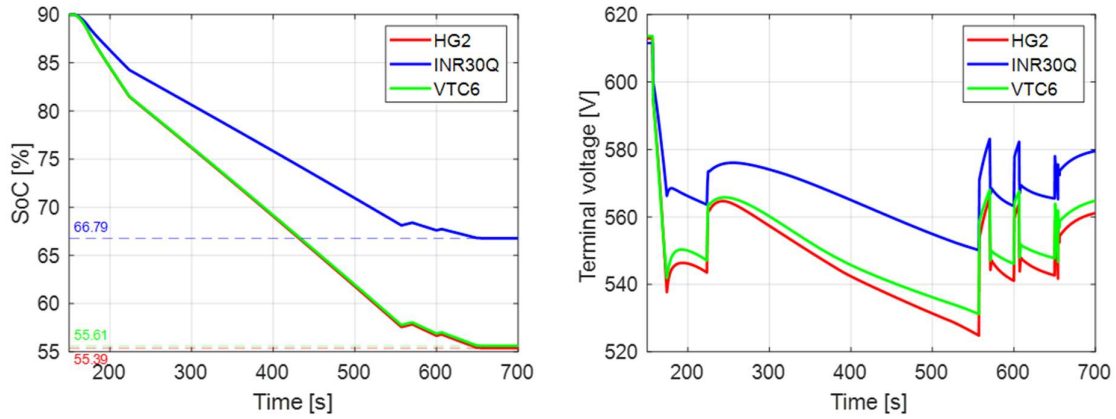


Figure 6.7 SoC (left) and terminal voltage (right) during TXL T-O (unrestricted) for blend braking strategy for three MEP batteries employed in 69t A320.

Table 6.7 MEP battery performance for A320 69t during TXL T-O for blend braking strategy.

	E_{prop} [kWh]	E_{tot} [kWh]	E_{regen} [kWh]	$\frac{E_{regen}}{E_{prop}}$ [%]	$\Delta\frac{E_{regen}}{E_{prop}}$ [%]	SoC_{end} [%]	DoD [%]	N	η [%]
HG2	4.02	3.96	0.06	1.49	4.02	55.39	34.61	2.00	93.7
INR30Q	4.02	3.94	0.08	1.99	3.52	66.79	23.21	3.00	95.4
VTC6	4.02	3.96	0.06	1.49	4.02	55.61	34.39	2.00	93.5

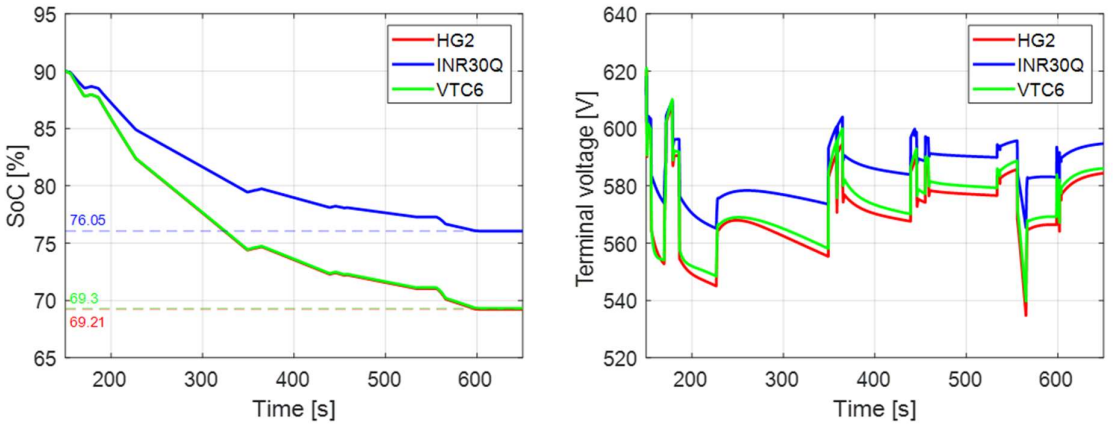


Figure 6.8 SoC (left) and terminal voltage (right) during LHR T-I for blend braking strategy for three MEP batteries employed in 69t A320.

Table 6.8 MEP battery performance for A320 65t during LHR T-I for blend braking strategy.

	E_{prop} [kWh]	E_{tot} [kWh]	E_{regen} [kWh]	$\frac{E_{regen}}{E_{prop}}$ [%]	$\Delta\frac{E_{regen}}{E_{prop}}$ [%]	SoC_{end} [%]	DoD [%]	N	η [%]
HG2	2.52	2.44	0.08	3.17	9.78	69.21	20.79	3.00	95.5
INR30Q	2.52	2.41	0.11	4.37	8.58	76.04	13.96	5.00	96.9
VTC6	2.52	2.44	0.08	3.17	9.78	69.30	20.70	3.00	95.5

When it comes to charging strategies, all MEP batteries can sustain the worst-case scenario, which is one TXL T-O and one LHRT-I. However, only INR30Q has enough energy to sustain

one rotation on a full charge and be charged at the home airport. Therefore, these batteries are more suitable for the first charging scenario and are lighter than HE batteries, resulting in less fuel consumption during the flight. However, they would be deeply cycled three times a day and reach the end of life sooner than HE batteries. This would also result in often pack replacement costs, more maintenance etc.

6.2.3 HP batteries

Based on previous analysis it is obvious that HP batteries cannot sustain the full AMS T-O. INR20S can sustain one TXL T-O or one LHR T-I, whereas A123 can barely sustain one LHR T-I. Thus, it can be concluded that HP batteries should be used only if the second charge scenario is adopted. Additionally, HP batteries must be oversized in terms of power in order to meet the energy requirements of one TXL T-O and LHR T-I. Therefore, simulated HP batteries differ from Table 6.1 in such a way that they have more cells in parallel and to meet the required energy content. The N_p for A123 battery is increased from 3 to 7 whereas for INR20S from 7 to 9. The results are shown below.

As it can be seen both INR20S and A123 can deliver one worst-case scenario of the second charging strategy. However, as their weights are 64.8 kg and 87.24 kg respectively, they don't offer weight advantages compared to MEP batteries. The benefit is that batteries are oversized in terms of power and practically, from the kinematic performance point of view they should be fine throughout their lifetime as A123 is LFP chemistry which offers more lifecycle compared to its MEP counterpart. Additionally, LFP cells are safer and not prone to thermal runways. Also, as charge rate of A123 cell varies between 1C and 4C [137], a value of 2C has been selected in this work, resulting in the regenerated energy being the highest using this battery.

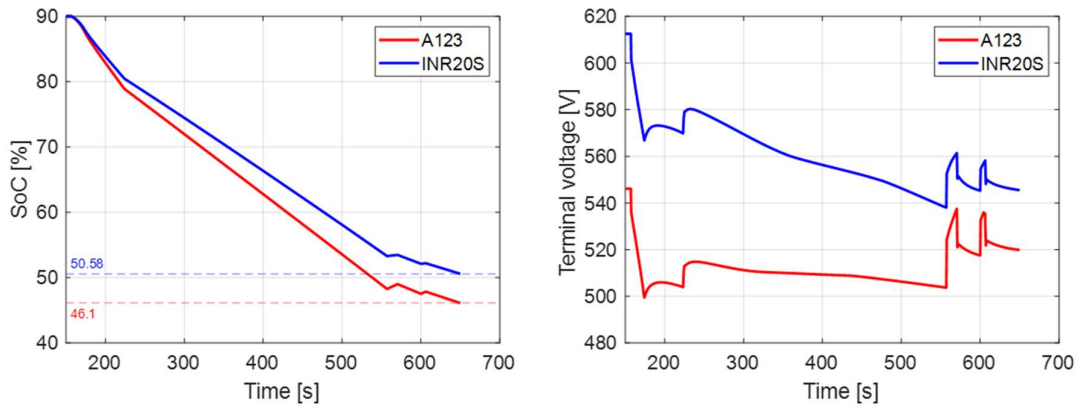


Figure 6.9 SoC (left) and terminal voltage (right) during TXL T-O (unrestricted) for blend braking strategy for three HP batteries employed in 69t A320.

Table 6.9 HP battery performance for A320 69t during TXL T-O for blend braking strategy.

	E_{prop} [kWh]	E_{tot} [kWh]	E_{regen} [kWh]	$\frac{E_{regen}}{E_{prop}}$ [%]	$\Delta\frac{E_{regen}}{E_{prop}}$ [%]	SoC_{end} [%]	DoD [%]	N	η [%]
INR20S	4.01	3.98	0.03	0.75	4.76	50.57	39.43	1	94.68
A123	4.01	3.91	0.1	2.5	3.05	46.09	43.91	1	95.71

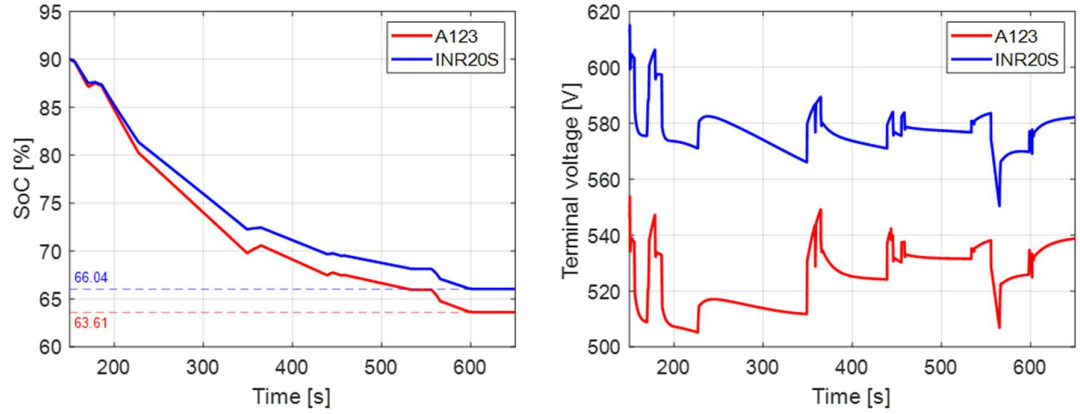


Figure 6.10 SoC (left) and terminal voltage (right) during LHR T-I for blend braking strategy for three MEP batteries employed in 65t A320.

Table 6.10 HP battery performance for A320 65t during LHR T-I for blend braking strategy.

	E_{prop} [kWh]	E_{tot} [kWh]	E_{regen} [kWh]	$\frac{E_{regen}}{E_{prop}}$ [%]	$\Delta\frac{E_{regen}}{E_{prop}}$ [%]	SoC_{end} [%]	DoD [%]	N	η [%]
INR20S	2.52	2.47	0.05	1.98	10.97	66.03	23.97	2	96.36
A123	2.52	2.37	0.15	5.95	7	63.61	26.39	2	96.6

6.3 Discussion summary

The following discussion should be seen in the light of available drive cycles, used road load conditions, selected electric drive, and chosen design constraints for batteries. The developed model allows for effortless change, which means that other studies can be performed

easily when more data are available from the airports and airlines. Finally, as already mentioned, this discussion aims not to propose the best battery but rather to explain which battery works better for which scenario and what considerations must be taken to make faster decisions when more data are available.

As batteries are sized considering power requirement, half of the selected batteries have energy content only for one TXL T-O and one LHR T-I cycle, with a certain reserve that is either high or low. Thus, only the first charging strategy is analysed. The reason for selecting a short taxi-out profile is that in the future, ET operations are expected to be autonomous, connected, and optimised at the airport level to eliminate events of lengthy taxiing procedures. Thus, the aircraft with ETS would be prioritised and assigned shorter and unrestricted taxiing routes.

For the presented sizing approach, batteries using HE cells are oversized in terms of energy due to low power density. Thus, they are depleted with a shallow DoD window, the average being 18.4 %. As already mentioned, these batteries have enough energy content for the full rotation, which appears beneficial if charging for some reason is not available at the destination airport. On the other hand, the MEP HG2 and VTC6 batteries can be used only for the first charging strategy. In contrast, the INR35E battery can be used in the second charging strategy but with the extended available SoC window, e.g., 95% to 15% SoC, i.e., 80% DoD. HG2 and VTC6 batteries are similar in all aspects. They can sustain the proposed cycles with a DoD of around 55% but with a low reserve margin and with a weight of approximately 50 kg. On the other hand, INR30Q is slightly heavier, but its depth of discharge is 37.17%, guaranteeing a longer lifecycle compared to HG2 and VTC6. Nonetheless, MEP batteries would age quicker compared to HE batteries due to deep cycling that would occur six times a day, but the aircraft would consume less fuel during flight as they are lighter. Consequently, the MEP batteries would have to be replaced frequently, which would lead to increased battery cost and maintenance. In the following subsection, battery replacement costs and extra fuel costs are compared for different batteries. The most significant disadvantage of HE batteries is the weight. The lightest of them, LG MJ1, has NMC chemistry, which is inherently safer than the NCA of Panasonic NCRB. Thus, MJ1 cells appear to be the preferred choice if a battery were to be made with high energy content. Finally, HP batteries can sustain little or no margin and are heavier than MEP batteries. However, the A123 battery, which uses LFP cells, has excellent cycle life compared to NMC and NCA and would age the slowest of all batteries. However,

the A123 battery doesn't have a margin in this case as seen in Table 6.11. In the following subsection, battery replacement costs and extra fuel costs are compared for different batteries.

Table 6.11 The expected DoD and reserve for taxiing mission consisting of TXL T-O and LHR T-I.

	NCRB	MJ1	NR35E	HG2	INR30Q	VTC6	INR20S	A123
DoD [%]	15.68	22.65	16.95	55.4	37.17	55.09	63.4	70.3
Reserve [%]	54.32	47.35	53.05	14.6	32.83	14.91	6.6	No reserve

6.3.1 Battery replacement cost vs extra fuel cost

As already mentioned, the cost of frequent and lightest MEP battery changes might be higher than the cost of extra fuel used for carrying batteries. In this section, these expenses are investigated and compared for several batteries. The reason for not analysing all of them is that the lifecycle of lithium-ion batteries depends on chemistry, DoD, charge/discharge rates, temperature, etc. Additionally, the same chemistries of different manufacturers will exhibit different lifecycle behaviours. Therefore, it is ungrateful to estimate lifecycle for various applications, as cells should be cycled using the exact drive cycles of the application to predict lifetime with high accuracy. However, using simple formulas can give an idea of the expected lifetime. In [202], [224], several commercial lithium-ion 18650 cells were analysed in terms of cycle life and some of them are used in this study, such as NCRB, MJ1, HG2, and A123. Therefore, only these four batteries are analysed in this section over the expected five-year period of operations.

First, the extra fuel consumption during flight is studied. The AET scenario is compared to conventional ET with APU, i.e., HET. The differences between CT and HET are not the scope of this research, and it is assumed that HET brings cost benefits compared to CT, as discussed in Chapter 2. Therefore, only the impact of APU fuel removal and the addition of batteries on extra fuel burn during flight is analysed. This comparison might seem unfair as AET is envisaged to be used in the future generation narrow body aircraft with modified electrical systems, whereas HET is the technology that can be retrofitted to the existing aircraft. Therefore, the actual weight difference will differ from the selected one. However, the analysis gives insight of today's battery technology limitations and how requirements on system level in terms of weight can be derived.

Using a typical APU fuel consumption curve that can be found in [31], the fuel need for HET can be calculated. In the worst-case scenario, the APU burns 44.3 kg during AMS T-O [182]. Even though that is a small amount, the procedure is still not emission and noise-free. Therefore, adding any batteries from Table 6.1 will increase fuel consumption during flight. In

literature [49], [64], [76], it is averaged that A320 burns around 0.03 kg of fuel per added kg of payload per hour. As already mentioned, ET is most suitable for short-haul flights of 1 h, and with that utilisation, aircraft can make up to four rotations per day [50] and this maximum value is used for below analysis. It is important to note that parameters from Table 6.12 are for batteries per wheel, so their weight should be doubled for analysis on extra fuel consumption during flight. In the same table, extra fuel consumption in kg and its cost equivalent is presented considering the price of aircraft fuel to be 0.72 $/kg [225]. It is important to mention that there are other savings that can be obtained using AET such as savings in cabling mass but they are not included in this study.

Table 6.12 Extra cost of fuel per flight needed for carrying more weight due to battery addition.

	Mass [kg]	Difference [kg]	Extra fuel [kg]	Extra cost [$/flight]
NCRB	295.26	250.96	7.53	5.43
MJ1	204.42	160.12	4.8	3.47
HG2	100.8	56.5	1.7	1.22
A123	174.49	130.19	3.9	2.82

The extra cost generated by carrying more weight might be offset as some batteries will have a shorter life cycle and would have to be replaced several times during the five-year analysed period. As already mentioned in [202], [224], the number of cycles for different cells and different DoDs are analysed and for clarity are summarised here in Table 6.13. It is essential to mention that these cells were discharged with standard rates in the datasheet (1C/0.5C), and in reality, less lifecycle is expected.

The given datasets are fitted using exponential least squares to calculate the expected lifecycle for the DoD of interest from Table 6.11. Considering that the battery would be cycled 14600 cycles in 5 years (i.e., eight flights per day for five years) number of replacements can be calculated, and it is shown in Table 6.14. Finally, the cost of battery installation and change per flight can be calculated considering 140$/kWh for the battery pack [226] and an additional 500$ per replacement for the maintenance.

Table 6.13 Number of cycles before reaching EOL for commercial 18650 cells and different DoDs.

	DoD=100%	DoD=60% (80% for MJ1)	DoD=20% (60% for MJ1)
NCRB	300	1167	8000
MJ1	300	2000	2333
HG2	400	3083	11000
A123	5000	30000	50000

Table 6.14 Cost of battery installation and replacement per flight over five years period.

	Total Energy [kWh]	Installation +Replacement	Cost of battery installation and replacement [$/flight]
NCRB	76	1+1	1.49
MJ1	52.94	1+0	0.51
HG2	22.68	1+4	1.22
A123	16.24	1+0	0.16

Finally, the last thing to be considered is the electricity price for charging. Assuming 0.25 $/kWh (price of electricity in the UK in January 2022), the cost of energy per mission is calculated and presented in Table 6.15. The HG2 has the highest electricity cost per flight as the required energy per mission is the highest. This is due to the fact that HG2 has the lowest efficiency over the high DoD window which can be seen from Table 6.6. Finally, the total extra cost per flight is shown in Table 6.16.

Table 6.15 Cost of electricity per flight.

	Total Energy [kWh]	DoD [%]	Energy for the mission [kWh]	Cost of electricity [$/flight]
NCRB	76	15.68	11.92	2.98
MJ1	52.94	22.65	11.99	3
HG2	22.68	55.4	12.56	3.14
A123	16.24	70.03	11.41	2.85

Table 6.16 Total extra cost per flight.

	Cost of extra fuel [$/flight]	Cost of battery installation and replacement [$/flight]	Cost of electricity [$/flight]	Total additional cost [$/flight]
NCRB	5.43	1.49	2.98	9.78
MJ1	3.47	0.51	3	6.88
HG2	1.22	1.22	3.14	5.56
A123	2.82	0.16	2.85	5.81

The analysis showed that HG2 and A123 batteries have a similar total extra cost per flight for the given scenarios and prices. This means that burning more fuel in the case of HP LFP batteries can be cancelled by repeated MEP battery replacement. However, the difference would increase in favour of MEP if more energy was required for LFP batteries to account for a certain energy margin. On the other hand, the difference would increase in favour of LFP batteries if battery cost is higher. The selected value of 140$/kWh is the price of EV battery packs at the moment, which reached mass production and their cost significantly dropped compared to ten years ago [226]. If the initial cost of ET batteries is higher, e.g., 200 kWh/kg the difference increases in favour of LFP (5.88$ compared to 6.03$ of MEP). On the other hand, if three rotations with 2h flights are considered as the typical aircraft daily utilisation, the extra fuel cost becomes the dominant factor and would be difficult to offset. Therefore, HP cells can be competitive to MEP cells under certain conditions, but further studies are needed

to assess the lifecycle, decide on mission margins properly, typical taxiing profiles and typical daily aircraft utilisation. If HP LFP cells offer a competitive cost increase per flight, it would be preferable over LG HG2 due to safer LFP chemistry.

6.4 Conclusions

In this chapter developed models from chapters 2, 4 and 5 were combined in a full model of ETS. The cell models developed in Chapter 5 are scaled to battery pack using equations (6.7)-(6.10) with the option to select the cell regeneration C rate. The number of cells in series and parallel is selected to fulfil the nominal voltage requirement of 540 V and the maximum power requirement of 75 kW. Batteries sized in this way will always be able to provide maximum power which is important for acceleration during critical events such as active runway crossing.

Due to different P/E ratios, batteries differ in energy rating. HE batteries with a low P/E ratio have a high energy rating compared to HP batteries with a high P/E ratio. The battery packs were simulated, and their performance was analysed for all three taxiing cycles for 69 t A320 aircraft. HE batteries can fulfil multiple taxiing cycles on one charge. For example, all HE batteries can sustain one AMS T-O, one TXL T-O and two LHR T-I on one charge. Contrary, only the INR35E MEP battery can be used for one rotation with shorter cycles, namely, two TXL T-O and two LHR T-I. HG2 and VTC6 batteries can be used only for the first charging strategy where they can sustain one TXL T-O and one LHR T-I with acceptable margins in case more energy has to be used. Finally, HP batteries couldn't fulfil two cycles, so their rating had to be revised and more strings added in parallel to meet the energy requirements of one TXL T-O and one LHR T-I. With this revised rating, the HP batteries became heavier compared to MEP ones with no energy reserve. However, the lifecycle analysis showed that HP batteries that use LFP chemistry could be competitive under certain conditions.

The rough estimation of the expected lifetime showed that MEP cells would have to be replaced 4 times over 5 years period of operation if they are being cycled eight times a day with TXL-LHR taxiing profiles. On the other hand, MJ1 and LFP wouldn't have to be replaced at all, whereas NCRB once. For the selected price of fuel, electricity, and battery pack the utilisation of HP LFP batteries is only 4.5% more costly compared to the HG2 battery with NMC chemistry. It has been shown, how modification of prices and typical aircraft utilisation can further increase or decrease the gap between these two batteries. Future studies can be

conducted, and more batteries simulated with different sizing constraints such as mass or energy in order to assess this application in more detail.

7 Chapter: Conclusions and Future Work

7.1 Conclusions

This thesis focused on the model-based design and analysis of the entire aircraft electric taxiing system, emphasising battery energy storage. The primary outcome of this work is the versatile model of the whole system (batteries, power converters, and electric machine) that also includes aircraft dynamics and road loads in addition to the control algorithms, both at system and component levels. The developed model is primarily used for preliminary sizing and analysis of battery energy storage. However, the model was also used to gain insights into interactions between different components and between control and components through closed-loop control, outline requirements specifications, and analyse system operations.

The need for emissions reductions at the airport level is explained in the Introduction (Chapter 1), and electric taxiing is introduced as one solution to this problem. Additionally, the modelling paradigms of traction drives, and their advantages and disadvantages are discussed in this part of the thesis. Due to the scope of the thesis, the forward modelling approach has been selected. Finally, it has been emphasised that in order to expedite ETS's introduction and reach the goal of zero-carbon taxiing by 2050, timely studies are needed on the system level, hence another reason for the model-based design and analysis.

A detailed review of ET operations and already developed ETS was presented in section 2.1 to help the reader understand why current aircraft taxiing procedures will be replaced with its electric counterpart and what benefits it would bring. Additionally, challenges for the implementation of these systems were also addressed. In section 2.2, a kinematic model of the aircraft was introduced with a detailed analysis of all parameters needed to implement it. The developed kinematic model was also used to analyse power and torque requirements at the aircraft wheels, which showed how current APU S/G cannot deliver stringent taxiing requirements solely and why this work focused on battery energy powered ETS, i.e., AET.

An essential part of this work is battery energy storage. Hence, an extensive literature review on different batteries was presented in section 3.1. The operation, benefits and disadvantages of several battery types such as lead-acid, nickel-cadmium, nickel-metal hydride and lithium-ion were shown. Lithium-ion batteries were selected as desired chemistry for this application due to their advantages and as being exclusively used in electric vehicles. Different positive and negative electrode materials were reviewed and how they affect the cell characteristics. The benefits and disadvantages of several lithium-ion types were discussed in

detail. In the second part of Chapter 3, several lithium-ion battery modelling techniques are given, focusing on the ECMs due to compatibility with the rest of the ETS model. The standard model parametrisation techniques were explained, highlighting their limitations.

The traction machine intended for direct drive ETS was introduced and explained in Chapter 4. The traction motor was first modelled in finite element software MagNet, which was used to extract the machine's parameters such as inductance matrix, permanent magnet flux etc. After the machine's parameters were acquired, the analytical model in the *qd* reference frame was developed. The FE and *qd* model showed good agreement for most operating points. Furthermore, three-phase VSI were also modelled in the *qd* reference frame and joined with machine's model. Finally, the whole system (including aircraft dynamics) is controlled through one speed and two current loops. The developed model includes three different speed taxiing profiles. It features drop-down menus and edit fields to select the aircraft model, mass, braking strategies and drive cycle. If needed, the slope profile can be imported as well. The employment of the model showed that for Airbus A320 with MTOW of 79t 150 kW is required for the needed acceleration. Additionally, the energy consumption is analysed for different regeneration strategies showing that consumption on average is between 0.0128 and 0.0142 kWh/(kgkm) for blend braking strategy.

As the final part of the system left to be modelled, eight commercially available cylindrical lithium-ion cells had been selected for the study covering all li-ion chemistries from HE to HP. A new modified parametrisation method was developed for cells at hand to model them within the acceptable time frame. Therefore, the postprocessing of the tests had to be modified with a significant difference, including the pulse waveform analysis and not neglecting the initial conditions. The developed ECMs were verified by comparing experimental test results with simulations using the scaled drive cycles, with errors within acceptable limits.

Finally, in Chapter 6, all developed models are combined. As one potential analysis, the selected batteries for discussion were sized to fulfil two criteria: V_{nom} and P_{max}. Those batteries were then analysed for different taxiing cycles. The study has shown that HE batteries designed with these constraints provide a higher lifetime because they have shallow DoD and can sustain several taxiing cycles on one charge. However, they are the heaviest, and study has shown they accumulate the most losses over the given period of operation. On the other hand, high power batteries can barely sustain the shortest cycle, which means they must be oversized in terms of power. Finally, the analysis has shown that MEP battery cells give the best balance in all aspects however LFP HP cells can be competitive depending on the aircraft utilisation, price

of electricity and battery pack. Additionally, the model showed further aspects, e.g., *id* current injection for field weakening during low DC voltage etc. Finally, it has been mentioned that battery selected for the analysis are not the proposed battery for ET application and that developed model allows for further in-depth studies of ET applications that would lead towards the battery decision. Some of the possible future works are discussed in following section.

7.2 Future Work

The model developed in this thesis has laid the foundations for several potential directions for further investigation of ETS. Despite the shortcomings, the author of this thesis believes that ETS will come into service in the near future, simultaneously as strict regulations regarding CO_2 come into force. The author also believes that the future of aircraft taxiing will be electric, autonomous and connected, similarly as with the automotive industry. Below is the following list of potential future studies:

- The availability of more than three drive cycles would be beneficial as it would identify typical electric taxiing patterns that could help in designing and analysing ETS with more statistical confidence. In contrast to the EVs and HEVs, where the benchmarking drive cycles exist (e.g., UDDS and NEDC etc.), no legally (standard) defined drive cycles exist to assess the performance of ETS, both HET and AET, such as emissions, fuel economy, drivability etc. After the extensive literature review on the topic demonstrated in this thesis, typical ET requirements are outlined. Nonetheless, more research is needed for statistical analysis of taxiing profiles at major world airports, focusing on duration, rolling resistance coefficients, slopes, etc. This work should be performed in conjunction with airports and airlines, and the development of such standards is vital as more prototypes attempt to enter service.
- The findings in this thesis have already been used to analyse the impact of the battery size and type on the fuel consumption of HET and HET+ using offline optimisation method, while the constraints of the formulation were changed according to the three proposed energy management strategies (EMSs) [182]. As a continuation of this research, new EMSs can be analysed in addition to the more challenging online optimisation problems. The developed forward model of the system allows for the testing of such strategies and control methodologies.

- Another vital aspect of ET is scheduling and operation optimisation at the airport level. The taxiways and taxiing routes at every airport are predetermined and known in advance. Thus, the implementation of ETS would pave the way towards autonomous taxiing operations. In this scenario, an assigned taxiing route, which would result from higher hierarchy optimisation, can be logged into the electric taxiing control unit (ETCU) before every departure. The ETCU would then calculate the optimal EMS patterns offline, scheduling of the power devices etc.
- Potential direction is an economic analysis that would include more aspects such as weight savings during cabling, and more detailed cost models of charging infrastructure, electricity, battery cells, aircraft fuel, penalties for noise and CO2, and how those would affect the ET operations. Additionally, more in-depth lifecycle models adapted for this application would have to be developed to account for typical drive cycles to which these would be exposed.
- The effect of temperature should be considered not only for battery models but also for traction machines. The temperature is a significant environmental factor during ET because aircraft operate all year round in various geographical regions. Also, there is a temperature gradient with altitude, meaning that the battery would be exposed to cold temperatures for at least an hour during the flight. Additionally, it means that the battery would go through significant temperature changes before taxi-in, affecting its performance and should be thoroughly investigated.
- The case study presented in Chapter 6 assumes battery powered ETS, i.e., AET. As seen, no battery perfectly fits the requirements of ET alone. Some batteries are oversized in terms of energy, whereas others might be in terms of power. Therefore, a hybrid ESS can be analysed, where a smaller HE energy battery can be complemented with a high power device such as SC, and different combinations exist [227]. For example, a hybrid battery pack composed of HE and HP cells can be considered. Additionally, the developed model allows for analysis of HET and HET+ systems with APU power source.
- Regarding battery cell technology, the market should be monitored and examined frequently as more cells with high power capability, and excellent energy density (>200W h/kg) start becoming more commercially available such as 2170 cells. Additionally, lithium metal batteries can be used in the future, which offer higher

energy density but are limited with low cyclability at this commercial development stage.

- Finally, further study can be focused solely on the battery system's design once the requirements are known. This work would include the design of the cooling system, the battery management system, protection, mechanical casing, thermal and abuse testing etc.

List of references

[1] ATAG, “The economic & social benefits of air transport.” Accessed: Mar. 12, 2022. [Online]. Available: https://www.icao.int/meetings/wrdss2011/documents/jointworkshop2005/atag_socialbenefitsairtransport.pdf.

[2] Airbus, “Global Market Forecast; Cities, Airports & Aircraft (2019-2038),” 2019.

[3] M. Schaefer, “Methodologies for Aviation Emission Calculation - A comparison of alternative approaches towards 4D global inventories,” Berlin Univeristy of Technology, 2016.

[4] “Emissions - Overview of Aviation Sector.” https://www.easa.europa.eu/eaer/topics/overview-aviation-sector/emissions (accessed Feb. 28, 2022).

[5] “Effects of Novel Coronavirus (COVID-19) on Civil Aviation: Economic Impact Analysis.” Accessed: Feb. 28, 2022. [Online]. Available: http://www.asma.org/asma/media/AsMA/Travel-Publications/COVID-19/Effects-of-Novel-Coronavirus-(COVID-19)-on-Civil-Aviation-Economic-Impact-Analysis.pdf.

[6] Airbus S.A.S., “Global Market Forecast: Growing Horizons 2017/2036.” https://ec.europa.eu/transport/sites/transport/files/2016_eu_air_transport_industry_analyses_report.pdf [Accessed: 16 - May - 2018].

[7] Airbus, “Airbus Global Market Forecast 2021 - 2040,” [Online]. Available: https://www.airbus.com/en/products-services/commercial-aircraft/market/global-market-forecast.

[8] EUROCONTROL, “Forecast Update 2021-2027 European Flight Movements and Service Units - Three Scenarios for Recovery from COVID-19.” [Online]. Available: https://www.eurocontrol.int/sites/default/files/2021-10/eurocontrol-7-year-forecast-2021-2027.pdf.

[9] European Comission, “Flightpath 2050, Europe’s Vision for Aviation.” https://ec.europa.eu/transport/sites/transport/files/modes/air/doc/flightpath2050.pdf [Accessed: 16 - May - 2018].

[10] “French lawmakers approve a ban on short domestic flights.”

https://www.reuters.com/business/environment/french-lawmakers-approve-ban-short-domestic-flights-2021-04-11/ (accessed Mar. 01, 2022).

[11] V. Singh and S. K. Sharma, "Fuel consumption optimization in air transport: a review, classification, critique, simple meta-analysis, and future research implications," *Eur. Transp. Res. Rev.*, vol. 7, no. 2, 2015, doi: 10.1007/s12544-015-0160-x.

[12] "Continuous descent approach." https://en.wikipedia.org/wiki/Continuous_descent_approach (accessed Feb. 28, 2022).

[13] Airbus, "Descent Profile Optimisation (DPO)." https://aircraft.airbus.com/en/services/enhance/systems-and-airframe-upgrades/efficiency-sustainability-systems-upgrades/descent-profile-optimisation-dpo (accessed Mar. 12, 2022).

[14] "Destination 2050 - A route to net zero European aviation." [Online]. Available: https://www.destination2050.eu/wp-content/uploads/2021/03/Destination2050_Report.pdf.

[15] S. Bozhko, C. I. Hill, and T. Yang, "More-Electric Aircraft: Systems and Modeling," in *Wiley Encyclopedia of Electrical and Electronics Engineering*, 2018.

[16] L. Papini, P. Connor, C. Patel, L. Empringham, C. Gerada, and P. Wheeler, "Design and testing of electromechanical actuator for aerospace applications," *2018 25th Int. Work. Electr. Drives Optim. Control Electr. Drives, IWED 2018 - Proc.*, vol. 2018-Janua, pp. 1–6, 2018, doi: 10.1109/IWED.2018.8321392.

[17] B. Sarlioglu and C. T. Morris, "More Electric Aircraft: Review, Challenges, and Opportunities for Commercial Transport Aircraft," *IEEE Trans. Transp. Electrif.*, vol. 1, no. 1, pp. 54–64, 2015, doi: 10.1109/TTE.2015.2426499.

[18] G. Qiao, G. Liu, Z. Shi, Y. Wang, S. Ma, and T. C. Lim, "A review of electromechanical actuators for More/All Electric aircraft systems," *Proc. Inst. Mech. Eng. Part C J. Mech. Eng. Sci.*, vol. 232, no. 22, pp. 4128–4151, 2018, doi: 10.1177/0954406217749869.

[19] "787 No bleed systems: Saving fuel and enhancing operational efficiencies." https://www.boeing.com/commercial/aeromagazine/articles/qtr_4_07/article_02_4.html (accessed Mar. 01, 2022).

[20] G. Buticchi *et al.*, "On-Board Microgrids for the More Electric Aircraft — Technology Review," *IEEE Trans. Ind. Electron.*, vol. 66, no. 7, pp. 5588–5599, 2019, doi:

10.1109/TIE.2018.2881951.

[21] P. W. Tao Yang, Fei Gao, Serhiy Bozhko, “Power Electronic Systems for Aircraft,” in *Control of Power Electronic Converters and Systems Vol. 2*, 2018.

[22] V. Madonna, P. Giangrande, and M. Galea, “Electrical Power Generation in Aircraft: Review, Challenges, and Opportunities,” *IEEE Trans. Transp. Electrif.*, vol. 4, no. 3, pp. 646–659, 2018, doi: 10.1109/TTE.2018.2834142.

[23] E. Fleuti and S. Maraini, “Taxi-Emissions at Zurich Airport,” 2017. https://www.flughafen-zuerich.ch/-/jssmedia/airport/portal/dokumente/das-unternehmen/politics-and-responsibility/environmental-protection/technische-berichte/2017_taxi_study_zurichairport.pdf?vs=1#:~:text=The split of the taxi,22%25 (impact LTO). (accessed Mar. 06, 2022).

[24] “Aircraft on the ground CO2 reduction programme.” https://www.sustainableaviation.co.uk/wp-content/uploads/2018/06/Aircraft-On-the-Ground-CO2-Reduction-Programme-Best-Practice-Guidance.pdf (accessed Feb. 28, 2022).

[25] J. Li *et al.*, “Aircraft emission inventory and characteristics of the airport cluster in the Guangdong-Hong Kong-Macao Greater Bay area, China,” *Atmosphere (Basel).*, vol. 11, no. 4, 2020, doi: 10.3390/atmos11040323.

[26] “HEATHROW CARBON FOOTPRINT 2018.” https://www.heathrow.com/content/dam/heathrow/web/common/documents/company/heathrow-2-0-sustainability/futher-reading/Heathrow-Carbon-Footprint-report_2018.pdf (accessed Feb. 28, 2022).

[27] A. Ashok, “Reducing the air quality impacts of aircraft activity at airports,” MASSACHUSETTS INSTITUTE OF TECHNOLOGY.

[28] M. E. J. Stettler, G. S. Koudis, S. J. Hu, A. Majumdar, and W. Y. Ochieng, “The impact of single engine taxiing on aircraft fuel consumption and pollutant emissions,” *Aeronaut. J.*, vol. 122, no. 1258, pp. 1967–1984, 2018, doi: 10.1017/aer.2018.117.

[29] “Improving air quality around Heathrow.” http://airqualitynews.com/wp-content/uploads/2015/04/Air-Quality-Blueprint.pdf (accessed Feb. 28, 2022).

[30] L. Khammash, L. Mantecchini, and V. Reis, “Micro-simulation of airport taxiing procedures to improve operation sustainability: Application of semi-robotic towing

tractor," *5th IEEE Int. Conf. Model. Technol. Intell. Transp. Syst. MT-ITS 2017 - Proc.*, pp. 616–621, 2017, doi: 10.1109/MTITS.2017.8005587.

[31] F. Re, "Model-based Optimization, Control and Assessment of Electric Aircraft Taxi Systems," Technischen Universitat Darmstadt, 2017.

[32] J. Tao, J. Guo, and C. Liu, "A review of powered wheel for aircraft," *2016 IEEE Int. Conf. Aircr. Util. Syst.*, pp. 378–383, 2016, doi: 10.1109/AUS.2016.7748078.

[33] F. Ommi, G. Pourabedin, and K. Nekofa, "Evaluation of model and performance of fuel cell hybrid electric vehicle in different drive cycles," *World Acad. Sci. Eng. Technol.*, vol. 38, no. February, pp. 586–592, 2009.

[34] A. Baroutaji, T. Wilberforce, and A. G. Olabi, "Overview of hydrogen and fuel cells technology in the aviation sector," in *Proceedings of SEEP2018*, 2018, pp. 8–11.

[35] "Developing Sustainable Aviation Fuel (SAF)." https://www.iata.org/en/programs/environment/sustainable-aviation-fuels/ (accessed Mar. 06, 2022).

[36] "Possible Solutions for the Battery Problem on the Boeing 787." https://batteryuniversity.com/article/possible-solutions-for-the-battery-problem-on-the-boeing-787 (accessed Mar. 05, 2022).

[37] J. W. Bennett, "Fault Tolerant Electromechanical Actuators for Aircraft," University of Newcastle, 2010.

[38] "Safran suspends electric jet taxiing project after Airbus ends talks." https://www.reuters.com/article/businessNews/idCAKBN1Y72MN?edition-redirect=ca (accessed Mar. 01, 2022).

[39] S. Onori, *Hybrid Electric Vehicles - Energy Management Strategies*. Springer, 2016.

[40] D. D. Tran, M. Vafaeipour, M. El Baghdadi, R. Barrero, J. Van Mierlo, and O. Hegazy, "Thorough state-of-the-art analysis of electric and hybrid vehicle powertrains: Topologies and integrated energy management strategies," *Renew. Sustain. Energy Rev.*, vol. 119, p. 109596, 2020, doi: 10.1016/j.rser.2019.109596.

[41] L. Guzzella and A. Sciarretta, *Vehicle propulsion systems: Introduction to modeling and optimization*, vol. 9783642359. Springer, 2013.

[42] A. Cerofolini, "Optimal supervisory control of hybrid vehicles," Univeristy of Bologna,

2014.

[43] Lea Dorn-Gomba, “Multi-Source Inverter for Electrified Vehicles : Concept , Analytical Design , Efficiency Analysis , and Implementation,” McMaster University, 2018.

[44] R. U. I. Xiong, J. Cao, and Q. Yu, “Critical Review on the Battery State of Charge Estimation Methods for Electric Vehicles,” *IEEE Access*, vol. 6, p. 5, 2018, doi: 10.1109/ACCESS.2017.2780258.

[45] “ECCAIRS Aviation - Data Definition Standard.” https://www.icao.int/safety/airnavigation/AIG/Documents/ADREP Taxonomy/ECCAIRS Aviation 1.3.0.12 (VL for AttrID 391 - Event Phases).pdf (accessed Mar. 06, 2022).

[46] ICAO, *Annex 14, Volume I, Aerodrome Design and Operations*, vol. I, no. July. 2018.

[47] “Pushback.” https://skybrary.aero/articles/pushback (accessed Mar. 05, 2022).

[48] “Airport CDM Implementation - The Manual.” https://www.eurocontrol.int/sites/default/files/publication/files/2012-airport-cdm-manual-v4.pdf (accessed Jan. 14, 2019).

[49] Y. Nicolas, “eTaxi, taxiing aircraft with engines stopped.” http://www.smartcockpit.com/docs/taxiing-aircraft-with-engines-stopped.pdf (accessed Aug. 06, 2019).

[50] T. F. Johnson, “Electric Green Taxiing System (EGTS) for Aircraft.” https://tec.ieee.org/newsletter/march-april-2014/electric-green-taxiing-system-egts-for-aircraft (accessed Mar. 02, 2022).

[51] “Taxi times - Summer 2019.” https://www.eurocontrol.int/publication/taxi-times-summer-2019 (accessed Mar. 02, 2022).

[52] G. Pillirone, “Greener Aircraft Taxiing : Single-Engine Taxi-out Evaluations Aviation Commitment to Environmental Sustainability.” [Online]. Available: https://www.sesarju.eu/sites/default/files/documents/webinars/Guiseppe.pdf.

[53] C. Walker, “Heathrow Airport 2017 Emission Inventory,” 2018. [Online]. Available: http://www.heathrowairwatch.org.uk/documents/Heathrow_Airport_2017_Emission_Inventory_Issue_1.pdf.

[54] D. Bresser and S. Prent, “Sustainable taxiing: which route will we take?”

https://www.schiphol.nl/en/innovation/blog/sustainable-taxiing-which-route-will-we-take/ (accessed Mar. 02, 2022).

[55] ICAO, "Operational Opportunities to Reduce Fuel Burn and Emissions," 2014. [Online]. Available: http://www.icscc.org.cn/upload/file/20190102/Doc.10013-EN Operational Opportunities to Reduce Fuel Burn and Emissions.pdf.

[56] D. Bresser and S. Prent, "Single-Engine Taxiing; wouldn't it be better?" https://www.schiphol.nl/en/innovation/page/single-engine-taxiing/ (accessed Mar. 02, 2022).

[57] M. Groot, "The Impact of Electric Aircraft," Delft University of Technology, 2020.

[58] I. D. H. Balakrishnan, "Evaluation of strategies for reducing taxi-out emissions at airports," *Proc. 10th AIAA Aviat. Technol. Integr. Oper. Conf. (ATIO 2010), Fort Worth, Texas*, 2010.

[59] R. B. Transportation, of Sciences Engineering, and Medicine, *Deriving Benefits from Alternative Aircraft-Taxi Systems*. Washington, DC: The National Academies Press, 2016.

[60] M. Lukic, P. Giangrande, A. Hebala, S. Nuzzo, and M. Galea, "Review, Challenges, and Future Developments of Electric Taxiing Systems," *IEEE Trans. Transp. Electrif.*, vol. 5, no. 4, pp. 1441–1457, 2019, doi: 10.1109/TTE.2019.2956862.

[61] M. Lukic *et al.*, "State of the Art of Electric Taxiing Systems," 2018.

[62] N. Dzikus, R. Wollenheit, M. Schaefer, and V. Gollnick, "The Benefit of Innovative Taxi Concepts: The Impact of Airport Size, Fleet Mix and Traffic Growth," 2013.

[63] N. Dzikus, J. Fuchte, A. Lau, and V. Gollnick, "Potential for Fuel Reduction through Electric Taxiing," *11th AIAA Aviat. Technol. Integr. Oper. Conf.*, no. September, pp. 1–9, 2011, doi: 10.2514/6.2011-6931.

[64] D. Prent and S. Bresser, "What is sustainable taxiing? (Part 1) After our previous." https://www.schiphol.nl/en/innovation/page/what-is-sustainable-taxiing-part-1/ (accessed Mar. 02, 2022).

[65] H. Jakub, "Electric taxiing – Taxibot system," *Mag. avaiation Dev.*, vol. 2, no. 10, pp. 17–20, 2014.

[66] "Mototok." https://www.mototok.com/ (accessed Mar. 06, 2022).

[67] "BRITISH AIRWAYS' REMOTE-CONTROL PUSHBACK VEHICLES REACH RECORD 100,000 DEPARTURES." https://mediacentre.britishairways.com/pressrelease/details/86/Technology-379/11451#:~:text=British Airways has celebrated its,for the last two years. (accessed Mar. 06, 2022).

[68] S. Soepnel and P. C. Roling, "Impact of Electric Taxi Systems on Airport Apron Operations and Gate Congestion," *17th AIAA Aviat. Technol. Integr. Oper. Conf.*, 2017, doi: 10.2514/6.2017-4391.

[69] D. Bresser and S. Prent, "Sustainable taxiing: Taxibot trial." https://www.schiphol.nl/en/innovation/blog/sustainable-taxiing-taxibot-trial/ (accessed Mar. 06, 2022).

[70] "Aircraft Tractors Driven from the Cockpit Save Thousands of Tons of Fuel." https://www.innovations-report.com/html/reports/energy-engineering/aircraft-tractors-driven-from-the-cockpit-save-thousands-of-tons-of-fuel.html (accessed Mar. 06, 2022).

[71] "TaxiBot - Green revolution in airplane taxiing." http://docs.wixstatic.com/ugd/865bf2_9eb200929c4a42108ecf23d94e5c1379.pdf (accessed Mar. 06, 2022).

[72] Amsterdam Airport Schiphol, "Sustainable taxiing and the Taxibot," 2020. https://www.schiphol.nl/en/download/b2b/1594319068/40LYaERw5x8BuRuXpVQkiK.pdf (accessed Mar. 06, 2022).

[73] "Honeywell, Safran Demo Electric Taxiing System For Airlines." https://www.ainonline.com/aviation-news/air-transport/2013-06-18/honeywell-safran-demo-electric-taxiing-system-airlines (accessed Mar. 06, 2022).

[74] E. D. Ganev, "Electric Drives for Electric Green Taxiing Systems," *IEEE Electrif. Mag.*, no. December, pp. 10–24, 2016, doi: 10.4271/2016-01-2013.

[75] G. Evgeni, C. Chiang, L. Fizer, and E. Johnson, "Electric Drives for Electric Green Taxiing Systems," *SAE Int. J. Aerosp.*, vol. 9, no. 1, pp. 62–73, 2016.

[76] J. A. Stockford, C. Lawson, and Z. Liu, "Benefit and performance impact analysis of using hydrogen fuel cell powered e-Taxi system on A320 class airliner," *Aeronaut. J.*, vol. 123, no. 1261, pp. 378–397, 2019, doi: 10.1017/aer.2018.156.

[77] "Electric green taxiing system Presentation to Arts et Métiers," 2013. Accessed: Mar.

06, 2022. [Online]. Available: https://recette-ec.soce.fr/manifestation_cr/678_compte_rendu.pdf.

[78] P. C. Roling, P. Sillekens, R. Curran, and W. D. Wilder, "The effects of Electric Taxi Systems on airport surface congestion," *15th AIAA Aviat. Technol. Integr. Oper. Conf.*, no. June, pp. 1–10, 2015, doi: 10.2514/6.2015-2592.

[79] D. Švragulja, "Masures for improving fuel efficiency by implementing electric taxi system." https://repozitorij.fpz.unizg.hr/islandora/object/fpz:141/preview (accessed Jan. 14, 2019).

[80] A. Osorio and M. Zorrilla, "The EGTS: When the Aerospace Ecosystem is not Ready," *2018 IEEE ANDESCON, ANDESCON 2018 - Conf. Proc.*, 2018, doi: 10.1109/ANDESCON.2018.8564729.

[81] European Comission (March 2017), "Annex VI : 6 th Call for Proposals (CFP06) - List and Full Description of Topics." https://ec.europa.eu/research/participants/portal/doc/call/h2020/jti-cs2-2017-cfp06-air-01-25/1762608-cfp06_description_of_topics_en.pdf (accessed May 16, 2018).

[82] "Boeing Demonstrates New Technology for Moving Airplanes on the Ground." https://boeing.mediaroom.com/2005-08-01-Boeing-Demonstrates-New-Technology-for-Moving-Airplanes-on-the-Ground (accessed Apr. 24, 2019).

[83] "The FUTURE of PUSHBACK is ELECTRIC! Without a pushback truck! Explained by CAPTAIN JOE." https://www.youtube.com/watch?v=2BZbHAJQ70s (accessed Mar. 06, 2022).

[84] "WheelTug Presents Video of TestDrive Success." https://www.wheeltug.com/?p=2209 (accessed Mar. 06, 2022).

[85] M. Schrier, F. Rinderknecht, and H. Hellstern, "Electric Wheel Hub Motor for Aircraft Application," *Int. J. Renew. Energy Res.*, vol. 1, no. 4, pp. 298–305, 2011, [Online]. Available: http://www.ijrer.org/index.php/ijrer/article/view/89.

[86] M. Schier, F. Rinderknecht, A. Brinner, and H. Hellstern, "High Integrated Electric Machine for Aircraft Autonomous Taxiing," *Int. Conf. Electr. Veh. Renew. Energies (EVER 11)*, 2011.

[87] F. Re, "Viability and state of the art of environmentally friendly aircraft taxiing systems," *2012 Electr. Syst. Aircraft, Railw. Sh. Propuls.*, pp. 1–6, 2012, doi:

10.1109/ESARS.2012.6387462.

[88] "DLR Airbus A320 ATRA taxis using fuel cell-powered nose wheel for the first time." https://www.dlr.de/dlr/en/desktopdefault.aspx/tabid-10204/296_read-931/#/gallery/2078 (accessed Jul. 02, 2018).

[89] T. Q. Hua, H. S. Roh, and R. K. Ahluwalia, "Performance assessment of 700-bar compressed hydrogen storage for light duty fuel cell vehicles," *Int. J. Hydrogen Energy*, vol. 42, no. 40, pp. 25121–25129, 2017, doi: 10.1016/j.ijhydene.2017.08.123.

[90] "WheelTug Certification Plan Receives FAA approval." https://www.ultra-pcs.com/wheeltug-receives-faa-approval/ (accessed Mar. 06, 2022).

[91] D. Bresser and S. Prent, "Is sustainable taxiing possible at a busy Schiphol." https://www.schiphol.nl/en/innovation/page/is-sustainable-taxiing-possible-at-a-busy-schiphol/ (accessed Mar. 06, 2022).

[92] M. N. Postorino, L. Mantecchini, and E. Gualandi, "Integration between aircraft and handling vehicles during taxiing procedures to improv e airport sustainability," *Int. J. Transp. Dev. Integr.*, vol. 1, no. 1, pp. 28–42, 2017, doi: 10.2495/TDI-V1-N1-28-42.

[93] I. Chakraborty, D. R. Trawick, D. N. Mavris, M. Emeneth, and A. Schneegans, "A Requirements-driven Methodology for Integrating Subsystem Architecture Sizing and Analysis into the Conceptual Aircraft Design Phase," no. June, pp. 1–24, 2014, doi: 10.2514/6.2014-3012.

[94] N. E. Daidzic, "Determination of taxiing resistances for transport category airplane tractive propulsion," *Adv. Aircr. Spacecr. Sci.*, vol. 4, no. 6, pp. 651–677, 2017, doi: 10.12989/aas.2017.4.6.651.

[95] J. Sun, J. M. Hoekstra, and J. Ellerbroek, "Aircraft Drag Polar Estimation Based on a Stochastic Hierarchical Model," 2018, [Online]. Available: http://resolver.tudelft.nl/uuid:9977a616-4506-4acb-9d27-b9e27f9ddb8d.

[96] M. Ploechl, P. Lugner, and E. Johannes, "Basics of Longitudinal and Lateral Vehicle Dynamics," in *Road and off-Road Vehicle System dynamics Handbook*, CRC press, 2014.

[97] O. Grigore-Müler and M. Barbelian, "Regenerative braking for aircraft landing roll phase using an electric machine," *13th Int. Conf. Optim. Electr. Electron. Equip.*, pp. 584–593, 2012.

[98] I. Chakraborty, “Subsystem Architecture Sizing and Analysis for Aircraft Conceptual Design,” no. December, pp. 1–325, 2015, [Online]. Available: https://smartech.gatech.edu/bitstream/handle/1853/54427/CHAKRABORTY-DISSERTATION-2015.pdf.

[99] Hakan Gürocak, *INDUSTRIAL MOTION CONTROL MOTOR SELECTION, DRIVES, CONTROLLER TUNING, APPLICATIONS*. John Wiley & Sons, Ltd, 2016.

[100] M. T. E. Heinrich, F. Kelch, P. Magne, and A. Emadi, “Regenerative Braking Capability Analysis of an Electric Taxiing System for a Single Aisle Midsize Aircraft,” *IEEE Trans. Transp. Electrif.*, vol. 1, no. 3, pp. 298–307, 2015.

[101] M. T. E. Heinrich, F. Kelch, P. Magne, and A. Emadi, “Investigation of regenerative braking on the energy consumption of an electric taxiing system for a single aisle midsize aircraft,” *IECON Proc. (Industrial Electron. Conf.*, pp. 3023–3029, 2014, doi: 10.1109/IECON.2014.7048940.

[102] “Tyre Information.” https://www.bridgestone.com/products/speciality_tires/aircraft/products/applications/pdf/tire_applications.pdf (accessed Feb. 27, 2019).

[103] “APU products.” http://pwaeropower.com/en/apu-engine-center/our-products (accessed Mar. 06, 2022).

[104] “AUXILIARY POWER UNITS (APU).” https://www.pwc.ca/en/products-and-services/products/auxiliary-power-units (accessed Mar. 06, 2022).

[105] R. Morris *et al.*, “SafeTug Semi-Autonomous Aircraft Towing Vehicles.” [Online]. Available: https://nari.arc.nasa.gov/sites/default/files/Morris_SafeTugFinalReport.pdf.

[106] F. Kelch, Y. Yang, B. Bilgin, and A. Emadi, “Investigation and design of an axial flux permanent magnet machine for a commercial midsize aircraft electric taxiing system,” *IET Electr. Syst. Transp.*, vol. 8, no. 1, pp. 52–60, 2018, doi: 10.1049/iet-est.2017.0039.

[107] S. Roggia, F. Cupertino, C. Gerada, and M. Galea, “Two-dimensional analysis for conical permanent magnet motors,” *2018 XIII Int. Conf. Electr. Mach.*, pp. 1008–1014, 2018, doi: 10.1109/ICELMACH.2018.8507047.

[108] S. Roggia, F. Cupertino, C. Gerada, and M. Galea, “A Two-Degrees-of-Freedom System for Wheel Traction Applications,” *IEEE Trans. Ind. Electron.*, vol. 65, no. 6, pp. 4483–4491, 2018.

[109] S. Roggia, F. Cupertino, C. Gerada, and M. Galea, "Axial Position Estimation of Conical Shaped Motors for Aerospace Traction Applications," *IEEE Trans. Ind. Appl.*, vol. 53, no. 6, pp. 5405–5414, 2017.

[110] M. Eshani, Y. Gao, S. Gay, and A. Emadi, *Modern electric, hybrid electric and fuel cell vehicles 2nd. Edition*. 2010.

[111] A. Emadi, *Advanced Electric Drive Vehicles*. CRC press.

[112] G. Plett, *Battery Managment Systems - Volume I - Battery modeling*. Artech House.

[113] M. Salomon, "ELECTROLYTES | Overview," in *Encyclopedia of Electrochemical Power Sources*, 2009, pp. 134–139.

[114] "Lithium battery." https://theory.labster.com/lithium-battery/ (accessed Mar. 13, 2022).

[115] M. Alipour, C. Ziebert, F. V. Conte, and R. Kizilel, "A Review on Temperature-Dependent of Lithium-Ion Cells," *Batteries*, vol. 6, no. 3, p. 35, 2020.

[116] T. B. Reddy and D. Linden, *Linden's handbook of batteries*, 4th ed. Mc Graw Hill, 2011.

[117] Y. L. Ding, "Automotive Li-Ion Batteries: Current Status and Future Prespectives," University of Waterloo, 2014.

[118] R. Korthauer, *Lithium-ion batteries: Basics and applications*. Springer, 2018.

[119] Q. Li, J. Chen, L. Fan, X. Kong, and Y. Lu, "Progress in electrolytes for rechargeable Li-based batteries and beyond," *Green Energy Environ.*, vol. 1, no. 1, pp. 18–42, 2016, doi: 10.1016/j.gee.2016.04.006.

[120] B. Scrosati, J. Garche, and W. Tillmetz, *Advances in Battery Technologies for Electric Vehicles*. Woodhead Publishing Series in Energy: Number 80, 2015.

[121] C. Julien, A. Mauger, K. Zaghib, and H. Groult, "Comparative Issues of Cathode Materials for Li-Ion Batteries," *Inorganics*, vol. 2, no. 1, pp. 132–154, 2014, doi: 10.3390/inorganics2010132.

[122] C. Julien, A. Mauger, A. Vijh, and K. Zaghib, *Lithium Batteries: Science and Technology*. Springer, 2015.

[123] A. Konarov, S. T. Myung, and Y. K. Sun, "Cathode materials for future electric vehicles and energy storage systems," *ACS Energy Lett.*, vol. 2, no. 3, pp. 703–708, 2017, doi: 10.1021/acsenergylett.7b00130.

[124] K. A. Murashko, “Thermal modelling of commercial lithium-ion batteries,” Lappeenranta University of Technology, 2016.

[125] N. Nitta, F. Wu, J. T. Lee, and G. Yushin, “Li-ion battery materials: Present and future,” *Mater. Today*, vol. 18, no. 5, pp. 252–264, 2015, doi: 10.1016/j.mattod.2014.10.040.

[126] Z. Jian, W. Wang, M. Wang, Y. Wang, N. Auyeung, and M. Liu, “Al 2 O 3 coated LiCoO 2 as cathode for high-capacity and long-cycling Li-ion batteries,” 2018.

[127] C. M. Julien and A. Mauger, “NCA, NCM811, and the route to Ni-Richer lithium-Ion batteries,” *Energies*, vol. 13, no. 23, 2020, doi: 10.3390/en13236363.

[128] M. K. Gulbinska, *Lithium-ion Battery Materials and Engineering*, vol. 111. Springer, 2014.

[129] J. Yamaki, “Secondary Batteries - Lithium Rechargeable Systems | Overview,” in *Encyclopedia of Electrochemical Power Sources*, 2009, pp. 1–26.

[130] T. Wöhrle, “Potential Saving of Cobalt and Natural Graphite by Applying FiveVB Cell Chemistry in next generation,” 2016. [Online]. Available: https://ec.europa.eu/research/participants/documents/downloadPublic?documentIds=080166e5af271ab3&appId=PPGMS.

[131] J. Kim, H. Lee, H. Cha, M. Yoon, M. Park, and J. Cho, “Prospect and Reality of Ni-Rich Cathode for Commercialization,” *Adv. Energy Mater.*, vol. 8, no. 6, pp. 1–25, 2018, doi: 10.1002/aenm.201702028.

[132] H. Berg, *Batteries for Electric Vehicles; Materials and Electrochemistry*. Cambridge Univeristy Press, 2015.

[133] P. Kurzweil, “Chapter 16 - Lithium Battery Energy Storage: State of the Art Including Lithium–Air and Lithium–Sulfur Systems,” in *Electrochemical Energy Storage for Renewable Sources and Grid Balancing*, P. T. Moseley and J. Garche, Eds. Amsterdam: Elsevier, 2015, pp. 269–307.

[134] F. Li *et al.*, “Graphite-Embedded Lithium Iron Phosphate for High-Power-Energy Cathodes,” *Nano Lett.*, vol. 21, no. 6, pp. 2572–2579, 2021, doi: 10.1021/acs.nanolett.1c00037.

[135] X. Zeng *et al.*, “Commercialization of Lithium Battery Technologies for Electric Vehicles,” *Adv. Energy Mater.*, vol. 9, no. 27, 2019, doi: 10.1002/aenm.201900161.

[136] Z. Ahsan *et al.*, "Recent progress in capacity enhancement of LiFePO4cathode for Li-Ion batteries," *J. Electrochem. Energy Convers. Storage*, vol. 18, no. 1, 2021, doi: 10.1115/1.4047222.

[137] "Nanophosphate® High Power LithiumIon Cell ANR26650M1-B." https://www.batteryspace.com/prod-specs/6610.pdf (accessed Mar. 05, 2022).

[138] N. Omar, P. Van den Bossche, T. Coosemans, and J. Van Mierlo, "Peukert revisited-critical appraisal and need for modification for lithium-ion batteries," *Energies*, vol. 6, no. 11, pp. 5625–5641, 2013, doi: 10.3390/en6115625.

[139] R. Fu *et al.*, "Comparison of lithium-ion anode materials using an experimentally verified physics-based electrochemical model," *Energies*, vol. 10, no. 12, pp. 1–20, 2017, doi: 10.3390/en10122174.

[140] G. Plett, *Battery Management Systems. Volume II Equivalent-Circuit Methods*. Artech House, 2015.

[141] X. Han *et al.*, "A review on the key issues of the lithium ion battery degradation among the whole life cycle," *eTransportation*, vol. 1, no. August, p. 100005, 2019, doi: 10.1016/j.etran.2019.100005.

[142] "70 AMP HOUR CELL." https://altairnano.com/products/70-amp-hour-cell/ (accessed Mar. 05, 2022).

[143] M. Brunell, "Modelling and Predictive Performance of Lithium Titanate," University of Wawrick, 2020.

[144] M. N. Obrovac and V. L. Chevrier, "Alloy negative electrodes for Li-ion batteries," *Chem. Rev.*, vol. 114, no. 23, pp. 11444–11502, 2014, doi: 10.1021/cr500207g.

[145] J. Betz, G. Bieker, P. Meister, T. Placke, M. Winter, and R. Schmuch, "Theoretical versus Practical Energy: A Plea for More Transparency in the Energy Calculation of Different Rechargeable Battery Systems," *Adv. Energy Mater.*, vol. 9, no. 6, pp. 1–18, 2019, doi: 10.1002/aenm.201803170.

[146] M.-T. von Srbik, "Advanced Lithium-Ion Battery Modelling for Automotive Applications," Imperial College London, 2015.

[147] "KOKAM Li-ion/Polymer Cell." https://kokam.com/wp-content/uploads/2016/03/SLPB-Cell-Brochure.pdf (accessed Mar. 05, 2022).

[148] R. J. Brod, “Batteries for Sustainability,” Springer, 2012.

[149] A. González, E. Goikolea, J. A. Barrena, and R. Mysyk, “Review on supercapacitors: Technologies and materials,” *Renew. Sustain. Energy Rev.*, vol. 58, pp. 1189–1206, 2016, doi: 10.1016/j.rser.2015.12.249.

[150] G. Z. Chen, “Supercapacitor and supercapattery as emerging electrochemical energy stores Supercapacitor and supercapattery as emerging electrochemical energy stores,” *Int. Mater. Rev.*, vol. 62, no. 4, pp. 173–202, 2017, doi: 10.1080/09506608.2016.1240914.

[151] G. Fan, X. Li, and M. Canova, “A reduced-order electrochemical model of li-ion batteries for control and estimation applications,” *IEEE Trans. Veh. Technol.*, vol. 67, no. 1, pp. 76–91, 2018, doi: 10.1109/TVT.2017.2738780.

[152] R. Gu, P. Malysz, H. Yang, and A. Emadi, “On the suitability of electrochemical-based modeling for lithium-ion batteries,” *IEEE Trans. Transp. Electrif.*, vol. 2, no. 4, pp. 417–431, 2016, doi: 10.1109/TTE.2016.2571778.

[153] P. Weicker, *A system approach to lithium ion battery management*. Archtech House, 2014.

[154] R. Xiong, *Battery management algorithm for electric vehicles*. Springer, 2019.

[155] M. Swierczynski, D. I. Stroe, A. I. Stan, R. Teodorescu, and S. K. Kær, “Lifetime Estimation of the Nanophosphate LiFePO4/C Battery Chemistry Used in Fully Electric Vehicles,” *IEEE Trans. Ind. Appl.*, vol. 51, no. 4, pp. 3453–3461, 2015, doi: 10.1109/TIA.2015.2405500.

[156] “Generic battery model.” https://www.mathworks.com/help/physmod/sps/powersys/ref/battery.html (accessed Mar. 06, 2022).

[157] H. Hinz, “Comparison of lithium-ion battery models for simulating storage systems in distributed power generation,” *Inventions*, vol. 4, no. 3, 2019, doi: 10.3390/inventions4030041.

[158] O. Tremblay and L. A. Dessaint, “Experimental validation of a battery dynamic model for EV applications,” *World Electr. Veh. J.*, vol. 3, no. 2, pp. 289–298, 2009.

[159] J. Meng, G. Luo, M. Ricco, M. Swierczynski, D. I. Stroe, and R. Teodorescu, “Overview

of Lithium-Ion battery modeling methods for state-of-charge estimation in electrical vehicles," *Appl. Sci.*, vol. 8, no. 5, 2018, doi: 10.3390/app8050659.

[160] O. Tremblay, L. -a. Dessaint, and A.-I. Dekkiche, "A Generic Battery Model for the Dynamic Simulation of Hybrid Electric Vehicles," *2007 IEEE Veh. Power Propuls. Conf.*, no. V, pp. 284–289, 2007, doi: 10.1109/VPPC.2007.4544139.

[161] N. Watrin *et al.*, "Multiphysical Lithium-Based Battery Model for Use in State-of-Charge Determination," *IEEE Trans. Veh. Technol.*, vol. 61, no. 8, pp. 3420–3429, 2012.

[162] M. Chen and G. A. Rinc, "Accurate Electrical Battery Model Capable of Predicting Runtime and I – V Performance," *IEEE Trans. Energy Convers.*, vol. 21, no. 2, pp. 504–511, 2006, doi: 10.1109/TEC.2006.874229.

[163] M. Petzl and M. A. Danzer, "Advancements in OCV measurement and analysis for lithium-ion batteries," *IEEE Trans. Energy Convers.*, vol. 28, no. 3, pp. 675–681, 2013, doi: 10.1109/TEC.2013.2259490.

[164] G. Liebig, G. Gupta, U. Kirstein, F. Schuldt, and C. Agert, "Parameterization and validation of an electrochemical thermal model of a lithium-ion battery," *Batteries*, vol. 5, no. 3, 2019, doi: 10.3390/batteries5030062.

[165] N. Campagna *et al.*, "Battery models for battery powered applications: A comparative study," *Energies*, vol. 13, no. 15, 2020, doi: 10.3390/en13164085.

[166] A. Li, S. Pelissier, P. Venet, and P. Gyan, "Fast characterization method for modeling battery relaxation voltage," *Batteries*, vol. 2, no. 2, 2016, doi: 10.3390/batteries2020007.

[167] J. Li, M. Mazzola, J. Gafford, and N. Younan, "A new parameter estimation algorithm for an electrical analogue battery model," *Conf. Proc. - IEEE Appl. Power Electron. Conf. Expo. - APEC*, pp. 427–433, 2012, doi: 10.1109/APEC.2012.6165855.

[168] Q. Q. Yu, R. Xiong, L. Y. Wang, and C. Lin, "A comparative study on open circuit voltage models for lithium-ion batteries," *Chinese J. Mech. Eng. (English Ed.*, vol. 31, no. 4, pp. 0–7, 2018, doi: 10.1186/s10033-018-0268-8.

[169] J. Sihvo, T. Roinila, T. Messo, and D. Stroe, "Novel online fitting algorithm for impedance-based state estimation of Li-ion batteries," in *IECON 2019 - 45th Annual Conference of the IEEE Industrial Electronics Society*, 2019, pp. 4531–4536.

[170] V. F. Lvovich, *Impedance Spectroscopy - Applications to Electrochemical and*

Dielectric Phenomena. John Wiley & Sons, 2012.

[171] W. Wang, "MODELING , ESTIMATION AND BENCHMARKING OF LITHIUM ION ELECTRIC BICYCLE BATTERY," McMaster Univeristy, 2016.

[172] G. Saldana, J. I. S. Martin, I. Zamora, F. J. Asensio, and O. Onederra, "Analysis of the Current Electric Battery Models for Electric Vehicle Simulation," *Energies*, vol. 12, no. 14, p. 2750, 2019.

[173] N. Mijat, D. Jurisic, and G. S. Moschytz, "Analog Modeling of Fractional-Order Elements : A Classical Circuit Theory Approach," *IEEE Access*, vol. 9, pp. 110309–110331, 2021, doi: 10.1109/ACCESS.2021.3101160.

[174] M. Lukic, P. Giangrande, C. Klumpner, and M. Galea, "Novel parameter identification method for lithium-ion batteries based on curve fitting," *2020 IEEE Veh. Power Propuls. Conf. VPPC 2020 - Proc.*, 2020, doi: 10.1109/VPPC49601.2020.9330955.

[175] A. Hentunen, T. Lehmuspelto, and J. Suomela, "Time-domain parameter extraction method for thévenin-equivalent circuit battery models," *IEEE Trans. Energy Convers.*, vol. 29, no. 3, pp. 558–566, 2014, doi: 10.1109/TEC.2014.2318205.

[176] R. O. Nemes, S. Maria Ciornei, M. Ruba, and C. Martis, "Parameters identification using experimental measurements for equivalent circuit Lithium-Ion cell models," *2019 11th Int. Symp. Adv. Top. Electr. Eng. ATEE 2019*, pp. 1–6, 2019, doi: 10.1109/ATEE.2019.8724878.

[177] L. Zhang, H. Peng, Z. Ning, Z. Mu, and C. Sun, "Comparative research on RC equivalent circuit models for lithium-ion batteries of electric vehicles," *Appl. Sci.*, vol. 7, no. 10, 2017, doi: 10.3390/app7101002.

[178] C. D. Rahn and C. Y. Wang, *Battery Systems Engineering*. John Wiley & Sons, 2013.

[179] T. Raminosoa, T. Hamiti, M. Galea, and C. Gerada, "Feasibility and electromagnetic design of direct drive wheel actuator for green taxiing," *IEEE Energy Convers. Congr. Expo. Energy Convers. Innov. a Clean Energy Futur. ECCE 2011, Proc.*, pp. 2798–2804, 2011, doi: 10.1109/ECCE.2011.6064145.

[180] D. Golovanov, M. Galea, and C. Gerada, "High specific torque motor for propulsion system of aircraft," *2016 Int. Conf. Electr. Syst. Aircraft, Railw. Sh. Propuls. Road Veh. Int. Transp. Electrif. Conf. ESARS-ITEC 2016*, 2017, doi: 10.1109/ESARS-ITEC.2016.7841405.

[181] M. Galea, Z. Xu, C. Tighe, T. Hamiti, C. Gerada, and S. Pickering, "Development of an aircraft wheel actuator for green taxiing," *Proc. - 2014 Int. Conf. Electr. Mach. ICEM 2014*, pp. 2492–2498, 2014, doi: 10.1109/ICELMACH.2014.6960537.

[182] A. A. Recalde *et al.*, "Energy Storage System Selection for Optimal Fuel Consumption of Aircraft Hybrid Electric Taxiing Systems," *IEEE Trans. Transp. Electrif.*, vol. 7, no. 3, pp. 1870–1887, 2021, doi: 10.1109/TTE.2020.3039759.

[183] M. Galea, T. Hamiti, and C. Gerada, "Torque density improvements for high performance machines," *Proc. 2013 IEEE Int. Electr. Mach. Drives Conf. IEMDC 2013*, pp. 1066–1073, 2013, doi: 10.1109/IEMDC.2013.6556228.

[184] A. Hebala, O. Hebala, W. A. M. Ghoneim, and H. A. Ashour, "Multi-objective particle swarm optimization of wind turbine directly connected PMSG," *2017 19th Int. Middle-East Power Syst. Conf. MEPCON 2017 - Proc.*, vol. 2018-Febru, pp. 19–21, 2018, doi: 10.1109/MEPCON.2017.8301315.

[185] D. L. Sobczuk and M. Rolak, "Modeling and Control of PWM Fed 6-Phase Permanent Magnet Synchronous Machine," *Warsaw Univ. Technol.*, no. 1, pp. 58–61.

[186] M. Galea, "High performance , direct drive machines for aerospace applications . PhD thesis , University of Nottingham . High Performance , Direct Drive Machines for Aerospace Applications," Univeristy of Nottingham, 2013.

[187] Y. Hu, Z. Q. Zhu, and M. Odavic, "Comparison of Two-Individual Current Control and Vector Space Decomposition Control for Dual Three-Phase PMSM," *IEEE Trans. Ind. Appl.*, vol. 53, no. 5, pp. 4483–4492, 2017.

[188] J. Karttunen, S. Kallio, P. Peltoniemi, P. Silventoinen, and O. Pyrhönen, "Dual Three-Phase Permanent Magnet Synchronous Machine Supplied by Two Independent Voltage Source Inverters," in *International Symposium on Power Electronics Power Electronics, Electrical Drives, Automation and Motion*, 2012, pp. 741–747.

[189] K. Paul, W. Oleg, and Sudhoff Scott, *Analysis of Electric Machinery and Drive Systems*. IEEE Press, 2002.

[190] D. F. V. Garcia, J. Taylor, M. Mohamadian, D. Luedke, A. Emadi, and B. Bilgin, "A Comparative Analysis for Six-Phase Motor Configurations," *SAE Tech. Pap. 2020-01-0465*, 2020.

[191] S. Hiti, D. Boroyevich, and C. Cuadros, "Small-signal modeling and control of three-

phase PWM converters," in *Proceedings of 1994 IEEE Industry Applications Society Annual Meeting*, 1994, no. 4, pp. 1143–1150.

[192] S. Puranik and B. A. Bremdal, "Smart system of renewable energy storage based on INtegrated EVs and bA tteries to empower mobile, Distributed and centralised Energy storage in the distribution grid," *Deliv. D6.2; INVADE*, no. 731148, 2017.

[193] A. Fratta and F. Scapino, "Modeling inverter losses for circuit simulation," *PESC Rec. - IEEE Annu. Power Electron. Spec. Conf.*, vol. 6, no. 4, pp. 4479–4485, 2004, doi: 10.1109/PESC.2004.1354792.

[194] "SKM300GB12E4 IGBT Modules." https://www.semikron.com/products/product-classes/igbt-modules/detail/skm300gb12e4-22892077.html (accessed Sep. 01, 2022).

[195] R. Krishnan, *Permanent Magnet Synchronous and Brushless DC Motor Drives*. CRC press, 2010.

[196] R. De Donker, D. W. J. Pulle, and A. Veltman, *Advanced Electric Drives*. Springer.

[197] E. A. Grunditz, "Design and Assessment of Battery Electric Vehicle Powertrain, with Respect to Performance, Energy Consumption and Electric Motor Thermal Capability," Chalmers University of Technology.

[198] F. Re, "An Object-oriented Model for Development and Assessment of Green Taxiing Systems," *3AF Greener Aviat. Conf.*, no. March 2014, pp. 1–7, 2015.

[199] M. T. E. Heinrich, "On the Concept of Electric Taxiing for Midsize Commercial Aircraft: A Power System and Architecture Investigation," Mc Master University, 2015.

[200] "Why Is Amsterdam Schiphol's Polderbaan Runway So Far From The Terminal?" https://simpleflying.com/why-is-amsterdam-schiphols-polderbaan-runway-so-far-from-the-terminal/ (accessed Mar. 08, 2022).

[201] M. J. Lain, J. Brandon, and E. Kendrick, "Design strategies for high power vs. High energy lithium ion cells," *Batteries*, vol. 5, no. 4, 2019, doi: 10.3390/batteries5040064.

[202] F. C. Krause *et al.*, "Performance of Commercial Li-Ion Cells for Future NASA Missions and Aerospace Applications," *J. Electrochem. Soc.*, vol. 168, no. 4, p. 040504, 2021, doi: 10.1149/1945-7111/abf05f.

[203] J. B. Quinn, T. Waldmann, K. Richter, M. Kasper, and M. Wohlfahrt-Mehrens, "Energy Density of Cylindrical Li-Ion Cells: A Comparison of Commercial 18650 to the 21700

Cells," *J. Electrochem. Soc.*, vol. 165, no. 14, pp. A3284–A3291, 2018, doi: 10.1149/2.0281814jes.

[204] H. Chen *et al.*, "An experimental study on thermal runaway characteristics of lithium-ion batteries with high specific energy and prediction of heat release rate," *J. Power Sources*, vol. 472, no. February, p. 228585, 2020, doi: 10.1016/j.jpowsour.2020.228585.

[205] G. Fisher, "Pouch, Cylindrical or Prismatic: Which Battery Format Will Rule the Market?" https://www.addionics.com/post/pouch-cylindrical-or-prismatic-which-battery-format-will-rule-the-market (accessed Mar. 16, 2022).

[206] Q. Wang, B. Jiang, B. Li, and Y. Yan, "A critical review of thermal management models and solutions of lithium-ion batteries for the development of pure electric vehicles," *Renew. Sustain. Energy Rev.*, vol. 64, 2016.

[207] V. Muenzel *et al.*, "A Comparative Testing Study of Commercial 18650-Format Lithium-Ion Battery Cells," *J. Electrochem. Soc.*, vol. 162, no. 8, pp. A1592–A1600, 2015, doi: 10.1149/2.0721508jes.

[208] R. Zhang *et al.*, "Study on the characteristics of a high capacity nickel manganese cobalt oxide (NMC) lithium-ion battery-an experimental investigation," *Energies*, vol. 11, no. 9, 2018, doi: 10.3390/en11092275.

[209] M. A. Hannan, M. M. Hoque, A. Hussain, Y. Yusof, and P. J. Ker, "State-of-the-Art and Energy Management System of Lithium-Ion Batteries in Electric Vehicle Applications: Issues and Recommendations," *IEEE Access*, vol. 6, pp. 19362–19378, 2018, doi: 10.1109/ACCESS.2018.2817655.

[210] M. Masoudinejad, "Open-loop dynamic modeling of low-budget batteries with low-power loads," *Batteries*, vol. 6, no. 4, pp. 1–19, 2020, doi: 10.3390/batteries6040050.

[211] A. Farmann and D. U. Sauer, "A study on the dependency of the open-circuit voltage on temperature and actual aging state of lithium-ion batteries," *J. Power Sources*, vol. 347, 2017.

[212] "A123 26650m1b datasheet." https://www.batteryspace.com/prod-specs/6610.pdf (accessed Mar. 16, 2022).

[213] "Samsung INR20S datasheet." https://www.imrbatteries.com/content/samsung_20S.pdf (accessed Mar. 16, 2022).

[214] “LG HG2 datasheet.” https://www.batteryspace.com/prod-specs/9989.specs.pdf (accessed Mar. 16, 2022).

[215] “Sony VTC6 datasheet.” https://www.orbtronic.com/sony-vtc6-18650-battery-flat-top (accessed Mar. 16, 2022).

[216] “Samsung INR30Q datasheet.” https://eu.nkon.nl/sk/k/30q-specs.pdf (accessed Mar. 16, 2022).

[217] “Samsung INR35E datasheet.” https://www.orbtronic.com/content/samsung-35e-datasheet-inr18650-35e.pdf (accessed Mar. 16, 2022).

[218] G. L. Plett, “High-performance battery-pack power estimation using a dynamic cell model,” *IEEE Trans. Veh. Technol.*, vol. 53, no. 5, pp. 1586–1593, 2004, doi: 10.1109/TVT.2004.832408.

[219] N. A. Chaturvedi, K. Reinhardt, J. Christensen, J. Ahmed, and K. Aleksandar, “Algorithms for Advanced Battery-Management Systems,” *IEEE Control Syst. Mag.*, no. June 2010, pp. 49–68.

[220] A. Tomaszewska, M. Parkes, R. Doel, G. Offer, and B. Wu, “The Effects of Temperature and Cell Parameters on Lithium-Ion Battery Fast Charging Protocols: A Model-Driven Investigation,” *J. Electrochem. Soc.*, vol. 169, no. 6, p. 060542, 2022, doi: 10.1149/1945-7111/ac79d3.

[221] “Panasonic NCR18650B.” https://www.batteryspace.com/prod-specs/NCR18650B.pdf (accessed Mar. 11, 2022).

[222] P. Keil and A. Jossen, “Impact of Dynamic Driving Loads and Regenerative Braking on the Aging of Lithium-Ion Batteries in Electric Vehicles,” *J. Electrochem. Soc.*, vol. 164, no. 13, pp. A3081–A3092, 2017, doi: 10.1149/2.0801713jes.

[223] “Flights: Ryanair use this sneaky technique with plane seats to ensure speedy turnaround.” https://www.express.co.uk/travel/articles/1194648/ryanair-flights-seat-pocket-flight-turnaround-boarding-time (accessed Mar. 11, 2022).

[224] Y. Preger *et al.*, “Degradation of Commercial Lithium-Ion Cells as a Function of Chemistry and Cycling Conditions,” *J. Electrochem. Soc.*, vol. 167, no. 12, p. 120532, 2020, doi: 10.1149/1945-7111/abae37.

[225] “Jet Fuel Price Monitor.” https://www.iata.org/publications/economics/fuel-

monitor/Pages/index.aspx (accessed Feb. 25, 2022).

[226] "Battery Pack Prices Fall to an Average of $132/kWh, But Rising Commodity Prices Start to Bite." https://about.bnef.com/blog/battery-pack-prices-fall-to-an-average-of-132-kwh-but-rising-commodity-prices-start-to-bite/ (accessed Mar. 11, 2022).

[227] J. Cao and A. Emadi, "A new battery/ultracapacitor hybrid energy storage system for electric, hybrid, and plug-in hybrid electric vehicles," *IEEE Trans. Power Electron.*, vol. 27, no. 1, pp. 122–132, 2012, doi: 10.1109/TPEL.2011.2151206.